Chapter 1

PDFs, SHADOWING AND pA COLLISIONS

Convenors: *K.J. Eskola* [8,9], *J.W. Qiu* [18], *W. Geist* [13,14]

Editor: *K.J. Eskola* [8,9]

Contributors: *A. Accardi* [1,2], *N. Armesto* [3,4], *M. Botje* [5], *S.J. Brodsky* [6,7], *B. Cole* [1], *K.J. Eskola* [8,9], *G. Fai* [10], *L. Frankfurt* [11], *R.J. Fries* [12], *W. Geist* [13,14], *V. Guzey* [15], *H. Honkanen* [8,9], *V.J. Kolhinen* [8,9], *Yu.V. Kovchegov* [16], *M. McDermott* [17], *A. Morsch* [3], *J.W. Qiu* [18], *C.A. Salgado* [3], *M. Strikman* [19], *H. Takai* [20], *S. Tapprogge* [9], *R. Vogt* [21,22], *X.F. Zhang* [10]

[1] Columbia University, New York, NY, USA
[2] University of Heidelberg, Heidelberg, Germany
[3] CERN, Geneva, Switzerland
[4] University of Cordoba, Cordoba, Spain
[5] NIKHEF, Amsterdam, The Netherlands
[6] Stanford University, Stanford, CA, USA
[7] Thomas Jefferson National Accelerator Facility, Newport News, VA, USA
[8] University of Jyväskylä, Jyväskylä, Finland
[9] University of Helsinki, Helsinki, Finland
[10] Kent State University, Kent, OH, USA
[11] Tel Aviv University, Tel Aviv, Israel
[12] Duke University, Durham, NC, USA
[13] Louis Pasteur University, Strasbourg, France
[14] University of Notre Dame, Notre Dame, IN, USA
[15] Ruhr University, Bochum, Germany
[16] University of Washington, Seattle, WA, USA
[17] Liverpool University, Liverpool, UK
[18] Iowa State University, Ames, IA, USA
[19] Pennsylvania State University, University Park, PA, USA
[20] Brookhaven National Laboratory, Upton, NY, USA
[21] Lawrence Berkeley National Laboratory, Berkeley, CA, USA
[22] University of California, Davis, CA, USA

Abstract

This manuscript is the outcome of the subgroup 'PDFs, shadowing and pA collisions' from the CERN workshop 'Hard Probes in Heavy Ion Collisions at the LHC'. In addition to the experimental parameters for pA collisions at the LHC, the issues discussed are factorization in nuclear collisions, nuclear parton distribution functions (nPDFs), hard probes as the benchmark tests of factorization in pA collisions at the LHC, and semi-hard probes as observables with potentially large nuclear effects. Also, novel QCD phenomena in pA collisions at the LHC are considered. The importance of the pA programme at the LHC is emphasized.

1. WHY pA COLLISIONS: INTRODUCTION AND SUMMARY

K.J. Eskola, W. Geist and J.W. Qiu

Hard probes [1, 2] are high-energy probes of the quark–gluon plasma (QGP) which are produced in the primary partonic collisions. The production of hard probes involves a large transfer of energy-momentum at a scale $Q \gg \Lambda_{\rm QCD}$. Such hard probes include the production of Drell–Yan dileptons, massive gauge bosons, heavy quarks, prompt photons, and high-p_T partons observed as jets and high-p_T hadrons. In pp collisions, it is well established that the inclusive cross sections of these hard processes can be computed through collinear factorization, i.e. using short-distance cross sections of parton–parton scatterings and well-defined universal parton distribution functions (PDFs). While the partonic sub-cross sections and the scale evolution of the PDFs are calculable in perturbative QCD (pQCD), the PDFs contain nonperturbative information, which must be extracted from the measured cross sections of various hard processes.

Provided that leading-power collinear factorization is applicable also in AA collisions, the cross sections of hard probes can be used as benchmark cross sections against which the signals and properties of the QGP can be extracted. Therefore, *it is of extreme importance that the applicability of factorization be tested in pA interactions*, especially at the LHC where truly hard probes will finally become available for nuclear collisions.

In this document, we divide the hard probes into two classes according to their scales: hard probes and semi-hard probes. The hard probes refer to observables with hard partonic subprocesses of energy exchange Q greater than several tens of GeV, up to 100 GeV and higher. For these hard probes, the process-dependent nuclear effects (i.e. power corrections) should remain negligible. The semi-hard probes correspond to probes at moderate scales, Q of few GeV up to 10–20 GeV, where the process-dependent nuclear effects may already be sizeable in pA collisions and even larger in AA collisions. This document mainly addresses the hard and semi-hard probes in pA collisions from the factorization (large-scale) point of view but we also discuss (Section 7) other interesting new physics which can be explored in pA collisions at the LHC.

Section 2 summarizes the main machine parameters for the pA runs at the LHC as well as the acceptance regions of the ALICE, CMS and ATLAS detectors. In addition to protons, the LHC machine can accelerate light beams as dilute as the deuteron and as compact as the helium nucleus. The machine can also accelerate a variety of heavier nuclei ranging from oxygen to lead. All three complementary detectors, ALICE, CMS and ATLAS, have wide rapidity coverage for multiplicity measurements, the capability of precision centrality determination in pA collisions and excellent jet reconstruction efficiency for a range of transverse momentum, p_T, and pseudorapidity, η.

Experimental data become more valuable and powerful when there are theoretical calculations to compare with. Because of the nature of the strong interactions, our ability to do calculations and to make predictions for hard probes in hadronic collisions completely relies on factorization in QCD perturbation theory. For the hard probes, the benchmark tests, factorization can be expected to hold in pp, pA and

AA collisions. For the semi-hard probes, which are sensitive to the properties of nuclear matter via multiple parton scatterings, there is, however, a critical difference between pA and AA collisions: while factorization may be valid for such semi-hard observables in pA collisions, it can fail in AA collisions. Factorization in nuclear collisions is summarized in Section 3.

Nuclear parton distribution functions (nPDFs) are an essential ingredient in understanding the magnitude of the nuclear effects on the factorized hard probe cross sections. While AA collisions typically are too complex for detailed verification of the nPDF effects on the semi-hard probe cross sections, *pA collisions provide a much cleaner environment for studies of the nPDFs*. The pA collisions can also probe the spatial dependence of the nPDFs – an important issue in the studies of hard probes in different AA centrality classes as well as in understanding the origin of the nuclear effects (shadowing) on the nPDFs. We devote Section 4 to discussion of several aspects of the nPDFs, ranging from global DGLAP fits to studies of the origin of shadowing and diffractive phenomena, and PDFs in the gluon saturation region at small values of x and Q.

Section 5, 'The Benchmark Tests in pA', deals with hard probes for which the nonfactorizable nuclear effects, i.e. process-dependent power corrections, should remain negligible. For these large-Q processes, the factorizable nuclear effects (nuclear effects on the parton distributions) also remain small. We emphasize that it is very important to measure these processes in pA collisions at the LHC: universal nuclear effects that are internal to the nucleus would, if observed, confirm the practical applicability of factorization in hard nuclear processes and would establish a reliable reference baseline for AA. It would be especially important to verify at what scale the observed nuclear dependence becomes universal and is completely determined by that of the nPDFs. On the other hand, observation of any significant nuclear effects in pA would be a truly interesting and important signal of sizeable power corrections in the cross sections and thereby also of new multiple collision dynamics of QCD.

For nuclear collisions, the very large-scale processes with $Q \gtrsim 100$ GeV are in practice only available at the LHC, the ultimate hard probe machine. As shown in Table 1.1, due to the high cms-energy and luminosity – higher than in AA – the counting rates of the hard probes at the scale $Q \sim 100$ GeV in pA collisions will be large enough to give sufficient statistics for reliable measurements of the nuclear effects. For example, in a month (assumed to be 10^6 s) we expect about 3.3×10^8 jets with $E_T \geq 100$ GeV and $|\eta| \leq 2.5$ to be collected in pPb collisions at $\sqrt{s}$ = 8.8 GeV with the maximum machine luminosity 1.4×10^{30} cm^{-2}s^{-1} and 2.6×10^7 jets with the maximum ALICE luminosity 1.1×10^{29} cm^{-2}s^{-1} (for the luminosities, see Section 2.1). About half of these jets fall into the interval 100 GeV $\leq E_T \leq$ 120 GeV. The corresponding number of Z^0 bosons at $|y_Z| \leq 2.4$ is 6.8×10^6 in a month with the maximum machine luminosity and 5.4×10^5 with the maximum ALICE luminosity.

Table 1.1: Expected counting rates (in 1/s, with two significant digits) of jets with transverse energy $E_T \geq 100$ GeV and rapidity $|\eta| \leq 2.5$ (see Section 5.3), and heavy gauge bosons at rapidities $|y| \leq 2.4$ in pPb collisions at $\sqrt{s}$ = 8.8 TeV (see Section 5.1)

Luminosity (cm^{-2}s^{-1})	**Jets/s**	$\boldsymbol{Z^0}$**/s**	$\boldsymbol{W^+}$**/s**	$\boldsymbol{W^-}$**/s**
1.1×10^{29}	26	0.54	0.89	0.83
1.4×10^{30}	330	6.8	11	11

Section 6, 'Processes with Potentially Large Nuclear Effects', discusses the physics of the semi-hard probes. The theoretical reference cross sections for these processes inevitably contain some model dependence, causing unknown theoretical uncertainties in the corresponding cross sections in AA col-

lisions. For these semi-hard probes, it is even more important to experimentally confirm the reference cross sections in pA collisions because of the substantial non-universal nuclear dependence. That is, the reliable reference cross sections for semi-hard probes in AA can be obtained *only if the corresponding pA measurements are performed*. A concrete example of this is the clear suppression of hadrons with $p_T \lesssim 10$ GeV recently observed at RHIC in central AuAu collisions at $\sqrt{s} = 200$ GeV relative to the pp data [3–5]. Only with help of the p(d)A data is it possible to verify that the origin of the suppression indeed is the strongly interacting medium and not the nuclear effects, the process-dependent power corrections and/or nPDFs, in the production of 10–20 GeV partons. A significant suppression in p(d)A collisions would indicate that the nuclear effects, the process-dependent power corrections in particular, would play a major role in suppressing the hadron spectrum, especially so in AA collisions. In this case, the observed suppression in AuAu collisions would be only partly due to the dense medium. On the other hand, a significant enhancement (Cronin effect) in p(d)A collisions would also be a signal of sizeable nuclear effects which would cause an even stronger enhancement of 10–20 GeV parton production in AuAu collisions. In this case, the suppression observed in the AuAu data would, in fact, be stronger than expected based on the pp reference data. The new data on single hadron p_T distributions in dAu collisions at $\sqrt{s}$ = 200 GeV at RHIC [6–8] confirm the latter case by showing the absence of suppression or even the appearance of a Cronin-type enhancement up to $p_T \sim 8$ GeV, in contrast to the strong suppression observed in AuAu collisions. The experience at RHIC clearly demonstrates that in order to measure the detailed properties of the strongly interacting matter (Equation of State, degrees of freedom, degree of thermalization, etc.) produced at the LHC, one needs precise knowledge of the absolute reference cross sections *where the nuclear effects are constrained by those measured in pA collisions*.

Apart from the connection to the QGP signals, we emphasize the importance of measuring the magnitude of the nuclear effects on hard and semi-hard probes in pA relative to pp. It is only through these measurements, where we can separate the universal nuclear dependence of the nPDFs from the process-dependent power corrections due to rescattering in nuclear matter, that we can differentiate the contributions to the nuclear dependence. Then it is possible to determine when and where new QCD phenomena, such as gluon saturation at the scale of a few GeV, set in.

Finally, in Section 7, 'Novel QCD Phenomena in pA Collisions at the LHC', we emphasize the fact that pA collisions per se offer lots of new interesting QCD phenomena to explore, such as the breaking down of the leading twist QCD for a wide range of momentum transfer due to increase of the gluon fields at small x, related phenomena of p_T broadening of the forward spectra of leading jets and hadrons, strong quenching of the low p_T hadron production in the proton fragmentation region, and coherent diffraction into three jets.

In summary, the pA programme at the LHC serves a dual role. It is needed to calibrate the AA measurements for a sounder interpretation. It also has intrinsic merits in the framework of a more profound understanding of QCD (e.g. shadowing vs. diffraction, non-linear QCD and saturation, higher twists...). Thus, one should foresee three key steps in this programme: (1) (pp and) pPb runs with reliable determination of centrality at the same collision energy as PbPb interactions; (2) a systematic study of pA collisions, requiring a variety of collision energies and nuclei as well as a centrality scan; and (3) an interchange of p- and A-beams for asymmetric detectors. The expected physics output from measurements of hard and semi-hard probes in pA collisions at the LHC may be summarized as follows. We are able to

- test the predictive power of QCD perturbation theory in nuclear collisions by verifying the applicability of factorization theorems and the universality of the nPDFs through the hardest probes, only available at the LHC (Sections 3 and 5).
- measure the nuclear effects (internal to the nucleus) in the nPDFs over an unprecedented range of x and Q; investigate the interplay between the 'EMC' effect, nuclear shadowing and saturation as well as the transverse-coordinate dependence of the nPDFs; and possibly, discover a new state of matter, the colour glass condensate, by probing very soft gluons in heavy nuclei through the rapidity dependence (Section 4).

- determine the nuclear dependence of the cross sections of the semi-hard probes in pA collisions and study QCD multiple parton scattering in nuclear matter and its corresponding dependences beyond the universal nuclear effects included in the nPDFs (Section 6).
- extract excellent information on QCD dynamics in hadronization because normal nuclear matter acts like a filter for colour neutralization and parton hadronization and explore potential new QCD phenomena in pA collisions, such as diffraction into three jets, double PDFs, etc. (Section 7).
- use the hard and semi-hard probe cross sections as references for the QGP signals in AA collisions: the hard probes set the benchmark of the applicability of factorization while the semi-hard probes help to understand the size of the nuclear modifications not caused by the dense medium produced in AA collisions.

2. THE EXPERIMENTAL PARAMETERS FOR pA AT THE LHC

2.1. Constraints from the LHC Machine

A. Morsch

2.1.1. pA collisions as part of the LHC ion programme

The LHC ion programme has been reviewed in a recent LHC Project Report [9]. Whereas collisions between light ions are already part of the LHC Phase II programme, pA and pA-like collisions (i.e. pA, dA, αA) are part of the LHC upgrade programme. Collisions between protons and ions are in principle possible since two independent RF systems are already foreseen in the LHC nominal programme. However, pA collisions also require the availability of two independent timing systems. The necessary cabling is already included in the baseline layout. Acquisition of the dedicated electronics remains to be discussed.

The question whether dA collisions will be available in the LHC is still under investigation because the same source has to be used for the production of both protons and deuterons. Since proton availability is required for other CERN programmes in parallel with the LHC pA runs, the final answer will depend on the time required for the source to switch back and forth between proton and deuteron operation. Production of α particles in parallel with proton operation is simpler and can be considered as an interesting alternative to pA and dA collisions.

As an alternative, the AB Department is currently studying a new layout for Linac 3, with possibly two sources and a switch-yard allowing simultaneous production of two different types of ions, including deuterons and α.

2.1.2. Beam properties

At the LHC, protons and ions have to travel in the same magnetic lattice and hence the two beams have the same rigidity. This has several consequences for the physical properties of the collision system. The condition of having the same rigidity results in beam momenta p which depend on the atomic mass A and charge Z of the beam particles. For the nominal LHC bending field one obtains

$$p = 7 \ \mathrm{TeV} \, \frac{Z}{A} \, . \tag{1.1}$$

The centre-of-mass energy is given by

$$\sqrt{s} = 14 \ \mathrm{TeV} \, \sqrt{\frac{Z_1 Z_2}{A_1 A_2}} \, . \tag{1.2}$$

Since, in general, the two beams have different momenta, the rest system of the colliding particles does not coincide with the laboratory system. The rapidity of the centre-of-mass system relative to the

laboratory is

$$y_{\text{cent}} = \frac{1}{2} \ln \frac{Z_1 A_2}{Z_2 A_1} \,. \tag{1.3}$$

In Table 1.2 the properties of several collision systems of interest have been summarized together with their geometric cross sections.

Table 1.2: Geometric cross section, maximum centre-of-mass energy and rapidity shift for several collision systems

System	σ_{tot} **(barn)**	$\sqrt{s}_{\text{max}}$ **(TeV)**	**Rapidity shift**
p O	0.39	9.9	0.35
p Ar	0.72	9.4	0.40
p Pb	1.92	8.8	0.47
d O	0.66	7.0	0.00
d Ar	1.10	6.6	0.05
d Pb	2.58	6.2	0.12
α O	0.76	7.0	0.00
α Ar	1.22	6.6	0.05
α Pb	2.75	6.2	0.12

2.1.3. Luminosity considerations for pA collisions

Two processes limit the proton and ion beam lifetimes and, hence, the maximum luminosity [10]:

1 Beam–beam loss is due to hadronic interactions between the beam particles and proportional to the geometric cross section (see Table 1.2). For asymmetric beam intensities (different intensity proton and ion beams), the lifetime is proportional to the intensity of the higher intensity beam.

2 Intra-beam scattering increases the beam emittance during the run. Since the timescale of emittance growth is proportional to AZ, it mainly affects the ion beam.

It can be shown that maximizing the beam lifetime leads to solutions with asymmetric beam intensities (high-intensity proton beam, low-intensity ion beam). However, for the pA luminosity requirements published by the ALICE collaboration [11], it is rather the source intensity than the luminosity lifetime which limits the luminosity. Since high-intensity proton beams are readily available ($N_{\text{p}}^{\text{max}} = 10^{11}/\text{bunch}$) but ion sources can deliver only relatively small intensities, mainly limited by space charge effect in the SPS, these conditions also push the realistic scenarios towards asymmetric beams.

Table 1.3 shows the maximum intensities per bunch for Pb, Ar, and O. It has to be emphasized that these maximum intensities represent rough estimates and much more detailed studies are needed to confirm them. They are by no means to be quoted as official LHC baseline values. At these maximum intensities the transverse emittance growth time amounts to about 35 h. In the same table, the proton intensities needed to obtain the luminosities requested by ALICE are shown. In all cases these intensities are below $N_{\text{p}}^{\text{max}}$. Hence, higher luminosities from which CMS and ATLAS could profit can be envisaged, as shown in the last column.

Table 1.3: Maximum ion intensity per bunch, ALICE luminosity request, the proton intensity needed to fulfil the ALICE request and the maximum luminosity for $N_{\rm p} = 10^{11}$ for three different pA systems

System	$N_{\rm ion}^{\rm max}$ **(10^{10})**	**Luminosity (ALICE) ($\mathbf{cm^{-2}s^{-1}}$)**	$N_{\rm p}$ **(10^{10})**	**Max. luminosity ($\mathbf{cm^{-2}s^{-1}}$)**
p Pb	0.007	1.1×10^{29}	0.8	1.4×10^{30}
p Ar	0.055	3.0×10^{29}	0.27	1.1×10^{31}
p O	0.1	5.5×10^{29}	0.27	2.0×10^{31}

2.2. The ALICE Detector

M. Botje

2.2.1. Introduction

To study the properties of hadronic matter under conditions of extreme energy density the ALICE collaboration has designed a general purpose detector optimized to measure a large variety of observables in heavy-ion collisions at the LHC [12]. The apparatus will detect and identify hadrons, leptons and photons over a wide range of momenta. The requirement to study the various probes of interest in a very high multiplicity environment, which may be as large 8000 charged particles per unit of rapidity in central PbPb collisions, imposes severe demands on the tracking of charged particles. This requirement has led to a design based on high granularity, but slow, drift detectors placed in a large volume solenoidal magnetic field. Additional detectors augment the identification capabilities of the central tracking system which covers the pseudorapidity range $|\eta| \leq 0.9$. A forward muon spectrometer ($2.5 < \eta < 4.0$) provides measurements of the quarkonia state. Forward detectors provide global event properties by measurements of photon and charged particle multiplicities and forward calorimetry.

In addition to running with Pb beams at the highest available energy of $\sqrt{s}$ = 5.5 TeV, ALICE will take proton–proton (pp) and pA (pPb, maybe dPb or αPb) reference data. Note that there are restrictions imposed on the pA programme by both the LHC machine and the ALICE detector. First, the maximum luminosity is limited because of pile-up in the TPC to typically (10^{30},10^{29},10^{27}) cm^{-2}s^{-1} for pp, pPb and PbPb collisions, respectively. Second, the energy per nucleon of ions in the LHC bending field scales to the nominal proton beam energy (7 TeV) with the ratio Z/A so that the centre-of-mass energy per nucleon and the rapidity shift of the centre-of-mass with respect to the LHC system are $\sqrt{s} \approx$ (9, 6, 6) TeV and $\Delta y \approx$ (0.5, 0, 0) for pPb, dPb and αPb collisions, respectively, as given by Eqs. (1.2) and (1.3). A comparison of nominal pPb data with pp (14 TeV) or PbPb (5.5 TeV) therefore needs a good understanding of the energy dependence. Furthermore, the rapidity shift of $\Delta y \approx 0.5$ in pPb collisions needs a dedicated study of the ALICE acceptance. Whereas detailed simulations of PbPb and pp collisions are already well under way, a comprehensive study of the ALICE pA acceptance is not yet available.

In the following we will briefly describe the main components of the ALICE detector. For a recent, more detailed review, see Ref. [13] and references therein.

2.2.2. *The ALICE detector*

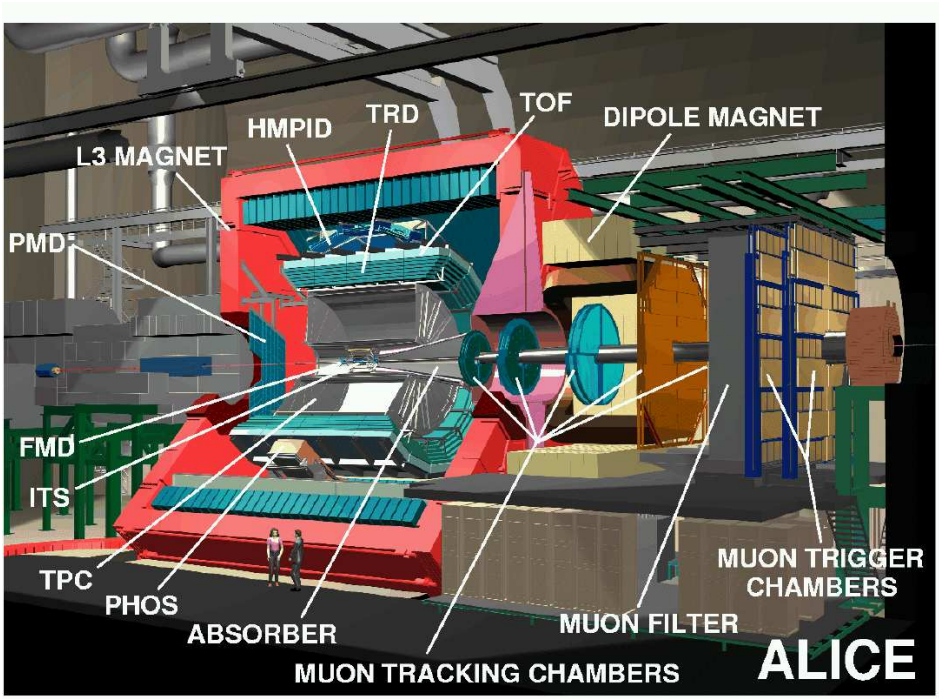

Fig. 1.1: Layout of the ALICE detector

The layout of the ALICE detector is shown in Fig. 1.1. The central barrel is placed inside the L3 magnet which provides a solenoidal field of up to 0.5 T. The choice of field is a compromise between low momentum acceptance ($\sim$ 100 MeV/c), momentum resolution and tracking and trigger efficiency. ALICE intends to run mostly with a higher field of 0.5 T to study high p_T probes but also with a lower field configuration of 0.2 T, which is optimal for soft hadronic physics.

The central tracking detector covers a range of $|\eta| < 0.9$ and the full range in azimuth. It consists of an inner tracking system (ITS) with six layers of high resolution silicon detectors located at a radial distance from the beam axis of r = 4, 7, 15, 24, 39 and 44 cm, respectively. The ITS provides tracking and identification of low-p_T particles and improved momentum resolution for particles at higher momenta which traverse the TPC. An impact parameter resolution of better than 100 μm allows for vertex reconstruction of hyperons and heavy quarks.

A time projection chamber (TPC) of 0.9 (2.5) m inner (outer) radius provides track finding, momentum measurement and particle identification via dE/dx with a resolution of better than 10%. Hadrons are identified in the TPC and ITS in the range $\sim$ 100–550 MeV/c and up to 900 MeV/c for protons. The overall efficiency of the ALICE tracking is estimated to be better than 90% independent of p_T down to 100 MeV/c.

One of the unique features of ALICE is its particle identification capability. First of all, a transition radiation detector (TRD) with an inner (outer) radius of 3 (3.5) m provides electron identification. The TRD allows for the measurement of light and heavy meson resonances, the dilepton continuum and open charm and beauty via their semileptonic decay channels. The fast tracking capability of the TRD can be used to trigger on high-p_T leptons and hadrons, providing a leading-particle trigger for jets.

Time-of-flight counters (TOF), covering the TPC geometrical acceptance, are installed at a radius of 3.5 m and have a time resolution of better than 150 ps. This detector will be able to identify π, K and protons in the semi-hard regime up to about 3 GeV/c.

A single-arm, high-resolution electromagnetic calorimeter (PHOS) is located 5 m below the interaction point and covers a range of $|\eta| \leq 0.12$ in pseudorapidity and $\Delta\phi$ = 100° in azimuth. The calorimeter is optimized to measure π^0, η and prompt photons in the energy range of one to several tens of GeV.

A RICH detector (HMPID) is positioned on top of the ALICE detector at about 4.5 m from the beam axis covering a range of $|\eta| < 0.5$ and $\Delta\phi$ = 57°. The RICH will extend the particle identification capabilities of the central barrel to $\approx$ 3 GeV/c for π/K and $\approx$ 5 GeV/c for K/p separation.

The forward muon spectrometer consists of an absorber, starting at 1 m from the vertex, followed by a dipole magnet with 3 Tm field integral, placed outside the central magnet, and 10 planes of high granularity tracking stations. The last section of the muon arm consists of a second absorber and two more tracking planes for muon identification and triggering. This detector is designed to measure the decay of heavy quark resonances (J/ψ, ψ', Υ, Υ' and Υ'') with sufficient mass resolution to separate the different states. The coverage is $2.5 < \eta < 4$ with p_T(single muon) > 1 GeV/c.

Several smaller detector systems located at small angles will measure global event characteristics. In particular, the FMD detectors measure the charged particle multiplicity in the ranges $-5.1 < \eta < -1.7$ and $1.7 < \eta < 3.4$ and full azimuth. The FMD and ITS combined will then cover most of the phase space ($-5.1 < \eta < 3.4$) for multiplicity measurements. Initial Monte Carlo studies indicate that a centrality determination in pA collisions with a resolution of about 2 fm might be within reach from a measurement of the total charged multiplicity.

To measure and to trigger on the impact parameter in heavy-ion collisions, the neutron and proton spectators will be measured by zero degree calorimetry. The neutron and proton spectators are separated in space by the first LHC dipole and measured by a pair of neutron and proton calorimeters installed at about 90 m both left and right of the interaction region. A centrality determination in pA collisions can be provided by measuring black ($p <$ 250 MeV, where p is the momentum in the rest system of nucleus A) and grey (p = 250–1000 MeV) protons and neutrons which are correlated with the impact parameter or, equivalently, with the number of collisions [14]. Initial simulations show that the ZDC acceptance for slow nucleons in pA collisions is quite large, see Fig. 1.2, so that such a centrality measurement in ALICE might be feasible. More detailed studies are currently under way.

2.3. The CMS Detector

W. Geist

The CMS detector at the LHC was conceived for optimal measurements of hard processes in pp collisions at a centre-of-mass energy $\sqrt{s}$ = 14 TeV and at a very high luminosity. Among the rare and hard processes are e.g. the production of Higgs- and SUSY-particles corresponding to mass/energy scales beyond 100 GeV; their decays yield charged leptons, photons, and weakly interacting particles as well as jets of hadrons. The CMS design is therefore driven by the need for

(i) a superb muon-system,
(ii) the best possible electromagnetic calorimeter (ECAL) compatible with (i), and
(iii) a high-performance tracking detector. The set-up is completed by
(iv) a large acceptance hadronic calorimeter (HCAL).

See Fig. 1.3 for a layout of the CMS detector.

Magnet. A direct consequence of these scientific goals is a strong (4 T) compact solenoid centred at the beam crossing; it bends the trajectories of charged particles in the plane perpendicular to the beam direction and thus facilitates the use of the position of the small-diameter beam for establishing primary and secondary vertices. Its length makes it possible to reconstruct tracks with good momentum resolution up to pseudorapidities $|\eta| \leq 2.4$. The field integral leads to transverse momentum resolutions $\delta p_T/p_T$

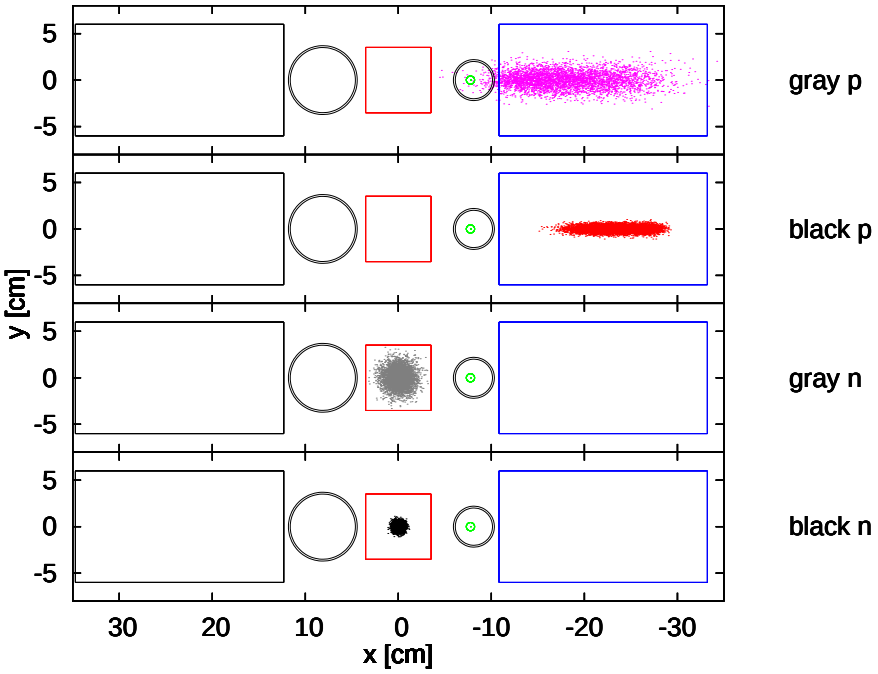

Fig. 1.2: Hit distribution of slow nucleons from pPb collisions at the front face of the ZDC. The squares at 0 (−20) cm indicate the neutron (proton) calorimeter. The Pb beam is visible inside one of the beam pipes (shown as circles) at about $x = -9$ cm.

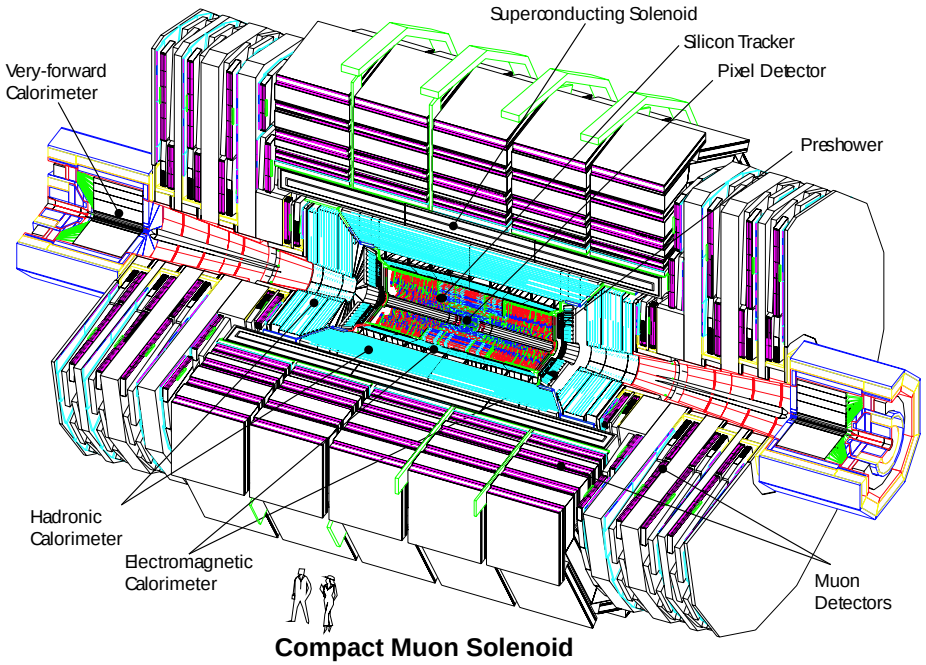

Fig. 1.3: Layout of the CMS detector

smaller than about 15% at p_T = 1 TeV/c. At the same time, particles with transverse momenta less than about 1 GeV/c spiral close to the beam line thereby reducing detector occupancies farther away.

Tracker. The all-Si tracker system of CMS consists of 13 cylindrical layers (3 layers of pixel detectors and 10 layers of strip-modules) as well as of forward-backward discs (2 pixel discs and 12 Si-strip discs) perpendicular to the beams. They complete the geometric acceptance for tracks up to $|\eta|$ = 2.4. The Si-detectors are characterized by fast response and very good spatial resolution. Four Si-strip layers are made of back-to-back ('double-sided') modules for quasi-3-dimensional space points. Good spatial resolution and low occupancies ($< 1\%$) in pp collisions at high luminosity result in track reconstruction efficiencies usually better than 98%, and better than 95% inside jets. The relative resolution for transverse momenta is expected to be $\delta p_T/p_T$ = (15 p_T + 5)%, with p_T in units of TeV, for $|\eta| \leq 1.6$. Furthermore, this system, in particular the pixel part, provides a reliable separation of primary vertices and secondary vertices due to B-decays.

Calorimeters. The electromagnetic and hadronic calorimeters surround the tracker system hermetically. They are positioned inside the coil of the magnet. Their large rapidity coverage ensures efficient detection of 'missing' transverse energy in the case of weakly-interacting particle production.

- ECAL: The barrel section of ECAL covers the rapidity range up to $|\eta|$ = 1.48. The forward part extends the acceptance to $|\eta| = 5$, where preshower detectors are also foreseen. The fine segmentation of the $PbWO_4$ crystals in rapidity and azimuth matches the transverse shower size from single $e^{\pm}$ and photons.
- HCAL: the hadronic calorimeter is also divided into a barrel part using copper-plastic tiles for $|\eta| \leq 3$ and a forward calorimeter which increases the acceptance up to $|\eta|$ = 5 and is based upon a fibre concept.

Muon detection. The muon chambers outside the magnet coil are grouped into stations of gaseous detector layers interleaved with the iron of the return yoke. They are protected by an absorber thickness of 10 interaction lengths in front of the first station and an additional 10 interaction lengths before the last station. Also, the muon system is organized into cylindrical and forward disc parts. It is a stand-alone system, capable of determining the muon momenta to very good precision.

Trigger. The CMS triggers select rare processes from the overwhelming rate of soft reactions at very high luminosities. The total rate of events to be transferred to a storage medium is limited to about 100 Hz. In order to cope with this low rate, the rate of individual triggers must be limited, typically by imposing a transverse momentum/energy cutoff.

2.3.1. CMS and pA collisions

While the first detailed investigations of CMS performance with PbPb collisions have been undertaken, this is not the case for pA collisions. However, no major problems are anticipated [15]. There are no a priori technical obstacles to running the CMS experiment at the lower pA- and AA-luminosities (see Section 2.1.) with e.g. lower p_T/energy thresholds and/or a lower magnetic field, as long as occupancy problems do not obstruct track reconstruction substantially. Global measurements corresponding to an increased acceptance at lower transverse momenta are very useful, given that the pA-collision energy will exceed that previously available by more than order of magnitude.

It should be emphasized that the TOTEM experiment will take data in conjunction with CMS. TOTEM needs a geometrical acceptance for secondary particles up to $|\eta|$ = 7. Furthermore, a 'zero-degree' calorimeter covering the range of beam rapidities is considered for CMS heavy-ion runs.

2.4. The ATLAS Detector

B. Cole, H. Takai, and S. Tapprogge

2.4.1. The ATLAS detector

The ATLAS detector is designed to study proton–proton collisions at the LHC design energy of 14 TeV in the centre of mass. The extensive physics programme pursued by the collaboration includes the Higgs boson search, searches for SUSY and other scenarios beyond the Standard Model, as well as precision measurements of processes within (and possibly beyond) the Standard Model. To achieve these goals at a full machine luminosity of 10^{34} cm^{-2}s^{-1}, ATLAS will have a precise tracking system (inner detector) for charged particle measurements, an as hermetic as possible calorimeter system, which has an extremely fine grain segmentation, and a stand-alone muon system. An overview of the detector is shown in Fig. 1.4.

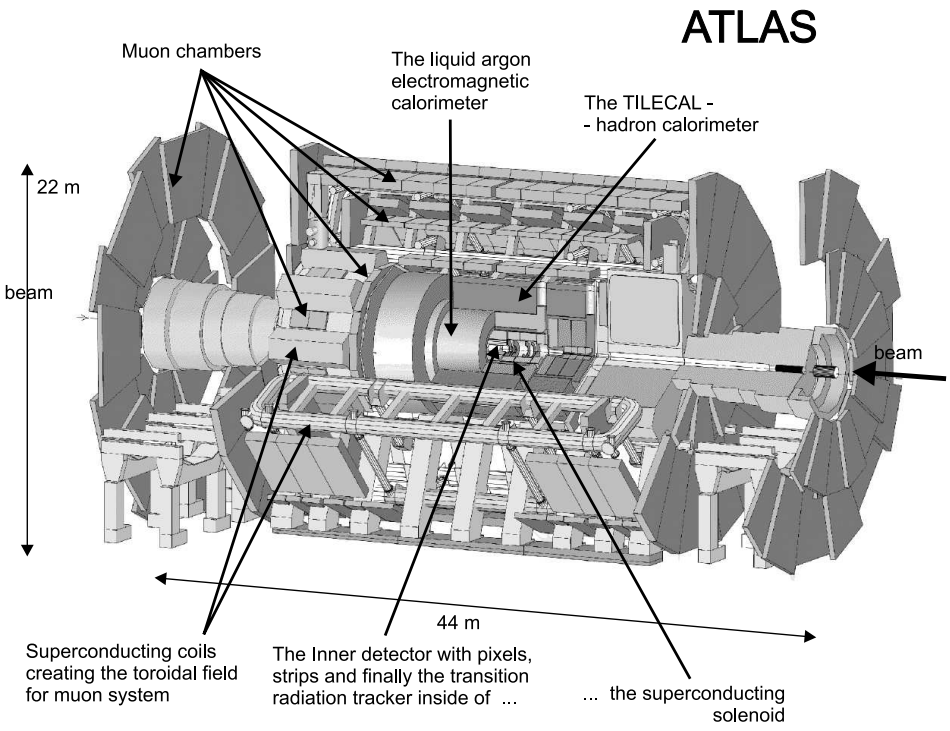

Fig. 1.4: The overall layout of the ATLAS detector

The inner detector is composed of a finely segmented silicon pixel detector, silicon strip detectors [Semiconductor Tracker (SCT)], and the Transition Radiation Tracker (TRT). The segmentation is optimized for proton–proton collisions at design luminosity. The inner detector system is designed to cover a pseudorapidity of $|\eta| < 2.5$ and is located inside a 2 T solenoid magnet.

The calorimeter system in the ATLAS detector surrounding the solenoid magnet is divided into electromagnetic and hadronic sections and covers pseudorapidity $|\eta| < 4.9$. The EM calorimeter is an accordion liquid argon device and is finely segmented longitudinally and transversely for $|\eta| \leq 3.1$. The first longitudinal segmentation has a granularity of 0.003×0.1 ($\Delta\eta \times \Delta\phi$) in the barrel and slightly coarser in the endcaps. The second longitudinal segmentation is composed of $\Delta\eta \times \Delta\phi = 0.025 \times 0.025$ cells and the last segment $\Delta\eta \times \Delta\phi = 0.05 \times 0.05$ cells. In addition, a finely segmented (0.025×0.1)

pre-sampler system is present in front of the electromagnetic (EM) calorimeter. The overall energy resolution of the EM calorimeter determined experimentally is $10\%/\sqrt{E}\oplus$ 0.5%. The calorimeter also has good pointing resolution, 60 mrad/$\sqrt{E}$ for photons, and a timing resolution of better than 200 ps for energy showers larger than 20 GeV.

The hadronic calorimeter is also segmented longitudinally and transversely. Except for the end-caps and the forward calorimeters, the technology utilized for the calorimeter is a lead-scintillator tile structure with a granularity of $\Delta\eta \times \Delta\phi = 0.1 \times 0.1$. In the endcaps the hadronic calorimeter is implemented in liquid argon technology for radiation hardness with the same granularity as the barrel hadronic calorimeter. The energy resolution for the hadronic calorimeters is $50\%/\sqrt{E}\oplus$ 2% for pions. The very forward region, up to η = 4.9, is covered by the Forward Calorimeter implemented as an axial drift liquid argon calorimeter. The overall performance of the calorimeter system is described in Ref. [16].

The muon spectrometer in ATLAS is located behind the calorimeters, thus shielded from hadronic showers. The spectrometer is implemented using several technologies for tracking devices and a toroidal magnet system which provides a 4 T field to have an independent momentum measurement outside the calorimeter volume. Most of the volume is covered by Monitored Drift tubes (MDTs). In the forward region, where the rate is high, Cathode Strip Chamber technology is chosen. The stand-alone muon spectrometer momentum resolution is of the order of 2% for muons with p_T in the range 10–100 GeV. The muon spectrometer coverage is $|\eta| < 2.7$.

The trigger and data acquisition system of ATLAS is a multi-level system which has to reduce the beam crossing rate of 40 MHz to an output rate to mass storage of O(100) Hz. The first stage (LVL1) is a hardware based trigger, making use of coarse granularity calorimeter data and dedicated muon trigger chambers only, to reduce the output rate to about 75 kHz, within a maximum latency of 2.5 μs.

The performance results mentioned here were obtained using a detailed full simulation of the ATLAS detector response with GEANT and have been validated by an extensive programme of test beam measurements of all components.

2.4.2. Expected detector performance for pA

The proton–nucleus events are asymmetric, with the central rapidity shifted by almost 0.5 units. In proton–nucleus runs it is expected that all of the subsystems will be available for data analysis. For the expected luminosity of 10^{29} cm^{-2}s^{-1} in pPb collisions, the occupancy of the detectors will be less than or at most comparable to the high luminosity proton–proton runs. The tracking will also benefit from not having up to 25 collisions (as in pp interactions at the design luminosity of 10^{34} cm^{-2}s^{-1}) in the same bunch crossing, but only a single event vertex. The detector acceptance for a pA run is the same as for pp and is shown in Table 1.4 (in the detector frame, see Section 2.1. for the rapidity shifts in the cms frame of the pA collisions).

The muon spectrometer will also benefit from the low luminosity proton–nucleus mode. In the high luminosity proton–proton runs, a large number of hits in the spectrometer comes from slow neutrons from previous interactions. These are not present in low luminosity runs. The only expected backgrounds are muons from π and K decays in flight. As has been shown for pp, a substantial number of these background muons are expected to be rejected when matching the track from the stand-alone muon system to a track in the inner detector is required.

2.4.3. The physics potential of ATLAS in pA

Measurements of proton–nucleus collisions at the LHC will not only provide essential control of the hard and semi-hard processes in heavy-ion collisions, but these measurements can also address physics that is, in its own right, of fundamental interest. The ATLAS detector provides an unprecedented opportunity to study proton–nucleus collisions in a detector with both large acceptance and nearly complete coverage of the various final states that can result from perturbative QCD processes.

Table 1.4: ATLAS detector acceptance for pA runs

Detector system	$\eta_{\max}$
Pixel	2.5
SCT	2.5
TRT	2.5
EM calorimeter	3.1
Hadronic calorimeter	4.9
Muon spectrometer	2.7

An important physics topic that can be addressed by proton–nucleus measurements in ATLAS is the applicability of factorization in hard processes involving nuclei. No detector that has studied either nuclear deep inelastic scattering or proton–nucleus collisions has been able to simultaneously study many different hard processes to explicitly demonstrate that factorization applies. In ATLAS, we will have the opportunity to study single jet and jet–jet events, photon–jet events, heavy quark production, Z^0 and $W^{\pm}$ production, Drell–Yan dilepton production, etc. and probe the physics of jet fragmentation in detail. With the wide variety of available hard processes that all should be calculable with the same parton distributions, we should be able to clearly demonstrate the success of factorization for the large-Q^2 processes.

The ATLAS inner detector has been designed to have good tracking efficiency in the momentum range of 1 GeV up to 1 TeV over the pseudorapidity range $|\eta| \leq 2.5$. The ability to reconstruct jets in ATLAS over a large pseudorapidity region (up to $|\eta| \leq 4.9$) and over the full azimuth would probe the onset of saturation effects in high p_T jets. One aspect of saturation that is not yet well understood is the effect on hard scattering processes for $Q^2 \sim Q_s^2$, where Q_s is the scale at which saturation sets in. It has been suggested that the gluon k_T distribution could be significantly modified well above Q_s. If so, then ATLAS should be able to study the Q^2 evolution of the saturation effects using photon–jet, $b\bar{b}$ and jet–jet measurements.

Detailed studies of the behaviour of jet fragmentation as a function of pseudorapidity could be used to determine whether the jet fragmentation is modified by the presence of the nucleus or its large number of low-x gluons. The observation or lack thereof of modifications to jet fragmentation could provide sensitive tests of our understanding of formation time and coherence in the re-dressing of the hard scattered parton and the longitudinal spatial spread of low-x gluons in a highly Lorentz-contracted nucleus.

3. QCD FACTORIZATION AND RESCATTERING IN pA COLLISIONS

J.W. Qiu

Perturbative QCD has been very successful in interpreting and predicting hadronic scattering processes in high energy collisions, even though the physics associated with an individual hadron wave function is nonperturbative. It is the QCD factorization theorem [17] that provides prescriptions to separate long- and short-distance effects in hadronic cross sections. The leading power contributions to a general hadronic cross section involve only one hard collision between two partons from two incoming hadrons of momenta p_A and p_B. The momentum scale of the hard collision is set by producing either a

heavy particle (like W/Z or virtual photon in Drell–Yan production) or an energetic third parton, which fragments into a hadron h of momentum p'. The cross section can be factorized as [17]

$$E_h \frac{d\sigma_{AB\to h(p')}}{d^3p'} = \sum_{ijk} \int dx' f_{j/B}(x') \int dx\, f_{i/A}(x) \int dz\, D_{h/k}(z)\, E_h \frac{d\hat{\sigma}_{ij\to k}}{d^3p'}(xp_A, x'p_B, \frac{p'}{z}) , \quad (1.4)$$

where $\sum_{ijk}$ runs over all parton flavours and all scale dependence is implicit. The $f_{i/A}$ are twist-2 distributions of parton type i in hadron A, and the $D_{h/k}$ are fragmentation functions for a parton of type k to produce a hadron h. For jet production, fragmentation from a parton to a jet, suitably defined, is calculable in perturbation theory and may be absorbed into the partonic hard part $\hat{\sigma}$. For heavy particle production, the fragmentation function is replaced by $\delta(1-z)$.

The factorized formula in Eq. (1.4) illustrates the general leading power collinear factorization theorem [17]. It consistently separates perturbatively calculable short-distance physics into $\hat{\sigma}$, and isolates long-distance effects into universal nonperturbative matrix elements (or distributions), such as $f_{i/A}$ or $D_{h/k}$, associated with each observed hadron. Quantum interference between long- and short-distance physics is power-suppressed by the large energy exchange of the collisions. Predictions of pQCD follow when processes with different hard scatterings but the same set of parton distributions and/or fragmentation functions are compared [18].

With the vast data available, the parton distributions of a free nucleon are well determined by QCD global analyses [19, 20]. Thanks to recent efforts, sets of fragmentation functions for light hadrons are becoming available though the precision is not as good as the parton distributions due to the limited data [21, 22].

Studies of hard processes at the LHC will cover a very large range of longitudinal momentum fractions x of parton distributions: $x \geq x_T\, e^y/(2 - x_T e^{-y})$ with $x_T = 2p_T/\sqrt{s}$ for inclusive jet production in Eq. (1.4), where y and p_T are the rapidity and transverse momentum of the produced jets, respectively. For the most forward or backward jets, or low p_T Drell–Yan dileptons, x can be as small as 10^{-6} at $\sqrt{s}$ = 14 TeV. The number of gluons having such small x and transverse size $\Delta r_\perp \propto 1/p_T$ may be so large that gluons appear more like a collective wave than individual particles, and a new nonperturbative regime of QCD, such as gluon saturation or the colour glass condensate [23], might be reached.

The use of heavy-ion beams allows one to enhance the coherent effects because of the larger number of gluons. In the small x regime of hadron–nucleus collisions, a hard collision of a parton of the projectile nucleon with a parton of the nucleus occurs coherently with all the nucleons at a given impact parameter. The coherence length ($\sim 0.1/x$ fm) far exceeds the nuclear size. To distinguish parton–nucleus multiple scattering from partonic dynamics internal to the nucleus, we classify multiple scattering in the following three categories: (a) interactions internal to the nucleus, (b) initial-state parton–nucleus interactions (ISI), and (c) final-state parton–nucleus interactions (FSI), as shown in Fig. 1.5 [18].

Interactions internal to the nucleus change the parton distributions of the nucleus, as shown in Fig. 1.5a. As a result, the effective parton distributions of a large nucleus are different from a simple sum of individual nucleon parton distributions. Since only a single parton from the nucleus participates in the hard collision to leading power, the effect of the initial-state interactions internal to the nucleus does not change the hard collisions between two incoming partons. This preserves the factorized single scattering formula in Eq. (1.4) [24] except now the twist-2 parton distributions $f_{i/A}$ are replaced by the corresponding effective nuclear parton distributions, which are defined in terms of the same operators but on a nuclear state. Such effective nuclear parton distributions include the 'EMC' effect and other nuclear effects so that they differ from the parton distributions of a free nucleon. However, they are still twist-2 distribution functions by definition of the operators of the matrix elements and are still universal.

Because of the twist-2 nature of the nuclear parton distributions, their nuclear dependence can only come from the A-dependence of the nonperturbative input parton distributions at a low momentum

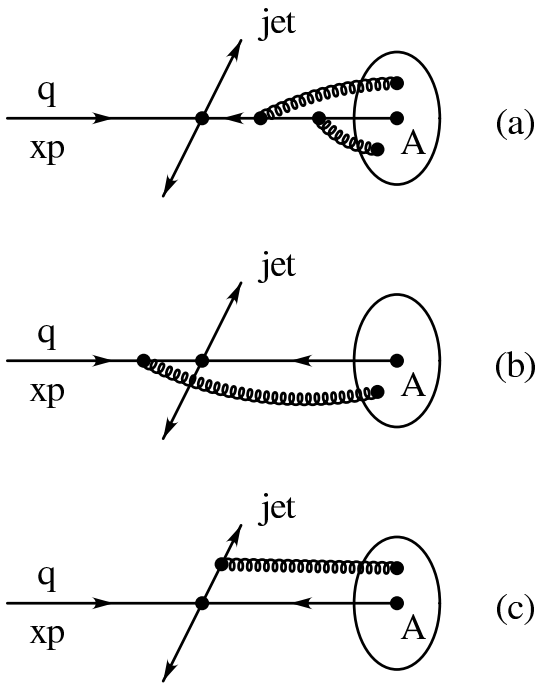

Fig. 1.5: Classification of parton multiple scattering in nuclear medium: (a) interactions internal to the nucleus, (b) initial-state interactions, and (c) final-state interactions

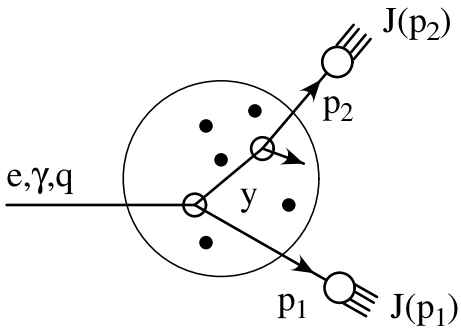

Fig. 1.6: Sketch for the scattering of an elementary particle or a parton of momentum xp in a large nucleus

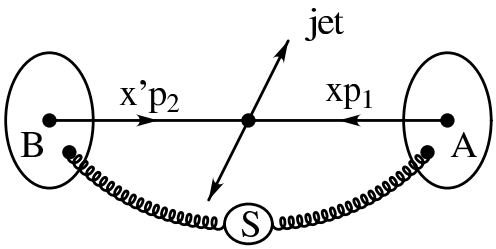

Fig. 1.7: Soft interactions of long-range fields that might enhance the gluon density in nuclear medium and affect the FSI

scale Q_0 and the A-dependent modifications to the DGLAP evolution equations from Q_0 to Q due to the interactions between partons from different nucleons in the nucleus [25, 26]. The nonperturbative nuclear dependence in the input distributions can be either parametrized with parameters fixed by fits to experimental data [27–29] or calculated with some theoretical inputs [30, 31].

Let hard probes be those whose cross sections are dominated by the leading power contributions in Eq. (1.4). That is, nuclear dependence of the hard probes comes entirely from that of nuclear parton distributions and is universal. Because of the wide range of x and Q covered, the hard probes in hadron–nucleus collisions at the LHC directly detect the partonic dynamics internal to the nucleus and provide excellent information on nuclear parton distributions. The knowledge of these distributions is very useful for understanding gluon saturation, a new nonperturbative regime of QCD [31, 32].

On the other hand, the hadronic cross sections receive power-suppressed corrections to Eq. (1.4) [33–35]. These corrections can come from several different sources, including the effect of partonic non-collinear momentum components and effects of non-vanishing invariant mass of the fragmenting parton k, as well as the effects of interactions involving more than one parton from each hadron, as shown in Fig. 1.5b and 1.5c. Although such multiple coherent scattering is formally a higher-twist effect and suppressed by powers of the large momentum scale of the hard collision, the corrections to the leading power factorized formula in Eq. (1.4) are proportional to the density of additional scattering centers and can be substantial due to a large density of soft gluons in the nucleus–nucleus collisions. For the ISI, the number of gluons available at the same impact parameter of the hard collision is enhanced due to the large nucleus, while the densities of soft partons available to the FSI can be even larger since they can come either from the initial wave functions of the colliding nuclei or be produced in the long-range soft parton interactions between different nucleons at the time when the hard collision took place.

Consider the scattering of an elementary particle or a parton (a quark or a physically polarized gluon) of momentum xp in nuclear matter, as shown in Fig. 1.6. A hard scattering with momentum transfer Q can resolve states whose lifetimes are as short as $1/Q$ [18]. The off-shellness of the scattered parton increases with the momentum transfer simply because the number of available states increases

with increasing momentum. Typically, the scattered parton (say, of momentum p_1) is off-shell by $m_J \leq Q$, where m_J is the invariant mass of the jet into which parton fragments. Further interactions of the off-shell parton are suppressed by an overall factor of $1/m_J^2 \sim 1/Q^2$, since the effective size of the scattered parton decreases with momentum transfer, and by the strong coupling evaluated at scale $m_J \sim Q$. Thus rescattering in nuclear collisions is suppressed by $\alpha_s(Q)/Q^2$ compared to single scattering.

Counting of available states ensures that $m_J \geq \sum_h \langle N_h \rangle m_h \gg \Lambda_{\rm QCD}$, where $\sum_h$ runs over all hadron types in the jet and $\langle N_h \rangle$ is the corresponding multiplicity. On the other hand, if we are to recognize the jet, we must have $m_J \ll E_J = p_1^0$, where E_J is the jet energy. In the rest frame of the nucleus, the scattered parton has a lifetime $\Delta t \sim (E_J/m_J)/m_J$. Thus, at high enough jet energy, $\Delta t > R_A$, the lifetime of the scattered parton will exceed the size of nuclear matter even though the parton itself is far off mass shell. Then the interactions of the scattered off-shell parton with nuclear matter may be treated by the formalism of pQCD [18].

In order to consistently treat the power-suppressed multiple scattering, we need a factorization theorem for higher-twist (i.e. power suppressed) contributions to hadronic hard scattering. It was shown in Ref. [33] that the first power-suppressed contribution to the hadronic cross section can be factorized into the form

$$
\begin{aligned}
E_h \frac{d\sigma^{(4)}_{AB\to h(p')}}{d^3p'} &= \sum_{(ii')jk} \int dx'\, f_{j/B}(x') \int dz\, D_{h/k}(z) \\
&\times \int dx_1 dx_2 dx_3\; T_{(ii')/A}(x_1,x_2,x_3)\, E_h \frac{d\hat{\sigma}^{(4)}_{(ii')j\to k}}{d^3p'}(x_i p_A, x' p_B, \frac{p'}{z})\,,
\end{aligned}
\tag{1.5}
$$

where the partonic hard part $\hat{\sigma}^{(4)}_{(ii')j\to k}$ is infrared safe and depends on the identities and momentum fractions of the incoming partons but is otherwise independent of the structure – in particular the size – of the hadron and/or heavy-ion beams. The superscript (4) on the partonic hard part indicates the dependence on twist-4 operators [33, 36]. The correlation functions $T_{(ii')/A}$ are defined in terms of matrix elements of twist-4 operators made of two pairs of parton fields of flavour i and i', respectively. For example, a correlation function between quark and gluon in a hadron h of momentum p can be expressed as

$$
\begin{aligned}
T_{(qG)/A}(x_1,x_2,x_3) &= \int \frac{dy_1^- dy_2^- dy_3^-}{(2\pi)^3}\, {\rm e}^{ip^+(x_1 y_1^- + x_2 y_2^- + x_3 y_3^-)} \\
&\times \langle p|\bar{\psi}(0)\frac{\gamma^+}{2} F^{+\alpha}(y_3^-) F_\alpha{}^+(y_2^-)\psi(y_1^-)|p\rangle\,,
\end{aligned}
\tag{1.6}
$$

with quark field ψ and gluon field strength $F^{+\alpha}$.

Demonstrating factorization at the next-to-leading power is a starting point for a unified discussion of the power-suppressed effects in a wide class of processes. A systematic treatment of double scattering in a nuclear medium is an immediate application of the generalized factorization theorem [18]. Because of the infrared safe nature of the partonic hard part $\hat{\sigma}^{(4)}_{(ii')j\to k}$ in Eq. (1.5), the nuclear dependence of the double scattering comes entirely from the correlation functions of two pairs of parton fields which can be linearly proportional to $A^{1/3}$ (or nuclear size) [36]. Therefore, if the scattered off-shell parton has a lifetime longer than the nuclear size, rescattering is enhanced by $A^{1/3}$ from the medium size and gets an overall suppression factor, $\alpha_s(Q)\, A^{1/3}\, \lambda^2/Q^2$, where λ has the dimension of mass and represents the nonperturbative scale of the twist-4 correlation functions in Eq. (1.6). A semiclassical estimate gives $\lambda^2 \sim \langle F^{+\alpha} F_\alpha{}^+ \rangle {\rm fm}^2/\pi$ [36].

For the ISI encountered by the incoming parton, λ^2 is proportional to the average squared transverse field strength, $\langle F^{+\alpha}F_{\alpha}^{\ +}\rangle$, inside the nucleus, which should be more or less universal. From the data on Drell–Yan transverse momentum broadening, it was found [37] that $\lambda^2_{\rm ISI} \approx \lambda^2_{\rm DY} \sim 0.01$ GeV^2. However, the numerical value of λ^2 for the FSI does not have to be equal to the $\lambda^2_{\rm ISI}$ due to extra soft gluons produced by the instantaneous soft interactions of long-range fields between the beams at the same time when the jets were produced by two hard partons, as shown in Fig. 1.7.

It was explicitly shown [38–40] that the corrections to hadronic Drell–Yan cross sections cannot be factorized beyond the next-to-leading power. However, it can be shown using the technique developed in Ref. [33] that the type of $A^{1/3}$-enhanced power corrections to hadronic cross sections in hadron–nucleus collisions can be factorized to all powers,

$$E_h \frac{d\sigma^{(2n)}_{AB\to h(p')}}{d^3p'} = \sum_{(i_n)jk} f_{j/B}(x') \otimes D_{h/k}(z) \otimes T^{(2n)}_{(i_n)/A}(x_i) \otimes E_h \frac{d\hat{\sigma}^{(2n)}_{(i_n)j\to k}}{d^3p'}(x_i p_A, x' p_B, \frac{p'}{z}) \,, \quad (1.7)$$

where $\otimes$ represents convolutions in fractional momenta carried by the partons and $T^{(2n)}(x_i)$ represent the correlation functions of n pairs of parton fields with flavours i_n = 1, 2,..., n. In Eq. (1.7), no power corrections are initiated by the higher-twist matrix elements of the incoming hadron B because such contributions do not have the $A^{1/3}$-type enhancement in hadron–nucleus collisions. For example, the recently proposed reaction operator approach to multiple scattering [41, 42] should fit into the type of factorization in Eq. (1.7) with the independent-scattering-centre approximation to the $T^{(2n)}(x_i)$ and keeping the lowest order in α_s to the partonic $\hat{\sigma}^{(2n)}$, which can be obtained using a recursive method. To the contrary, in nucleus–nucleus collisions, even the nuclear size enhanced power corrections cannot be formally factorized beyond the next-to-leading power.

Let semi-hard probes in hadronic collisions be those with a large momentum exchange as well as large power corrections. We expect that pQCD has good predictive power for semi-hard observables in hadron–nucleus collisions but the pQCD factorization approach does not work well for semi-hard observables in nucleus–nucleus collisions.

In conclusion, the factorized single scattering formula in Eq. (1.4) remains valid for hard probes in nuclear collisions, except that the parton distributions are replaced by corresponding effective nuclear parton distributions which are independent of the hard scattering and thus universal. Hard probes in nuclear collisions at the LHC can provide excellent information on nuclear parton distributions and detect the partonic dynamics internal to the nucleus.

However, the power-suppressed corrections to the single scattering formula can be substantial and come from several different sources. The effect of the off-shellness of the fragmenting parton k leads to a correction of the order $(m_J/p_T)^2$ with $m_J = \sum_h \langle N_h \rangle m_h$. Both the ISI and FSI double scatterings give power-suppressed corrections proportional to $\alpha_s A^{1/3}\lambda^2/p_T^2$, where $\lambda^2_{\rm ISI}$ is relatively small and almost universal and $\lambda^2_{\rm FSI}$ is sensitive to the number of soft partons produced by the instantaneous collisions of long-range fields between nucleons in the incoming beams.

Beyond double scattering (or next-to-leading power corrections), pQCD calculations might not be reliable due to the lack of factorization theorems at this level. However, pQCD factorization for the type of $A^{1/3}$-enhanced power corrections in hadron–nucleus collisions is likely to be valid to all powers.

4. NUCLEAR PARTON DISTRIBUTION FUNCTIONS (nPDFs)

4.1. Global DGLAP Fit Analyses of the nPDFs: EKS98 and HKM

K.J. Eskola, H. Honkanen, V.J. Kolhinen and C.A. Salgado

4.1.1. Introduction

Inclusive cross sections for hard processes $A+B \to c+X$ involving a sufficiently large scale $Q \gg \Lambda_{\rm QCD}$ are computable by using collinear factorization. In the leading-twist approximation power corrections $\sim 1/Q^2$ are neglected and

$$d\sigma(Q^2,\sqrt{s})_{AB\to c+X} = \sum_{i,j=q,\bar{q},g} \left[Z_A f_i^{p/A}(x_1,Q^2) + (A-Z_A) f_i^{n/A}(x_1,Q^2) \right] \otimes$$
$$\otimes \left[Z_B f_j^{p/B}(x_2,Q^2) + (B-Z_B) f_j^{n/B}(x_2,Q^2) \right] \otimes d\hat{\sigma}(Q^2,x_1,x_2)_{ij\to c+x}\,, \qquad (1.8)$$

where A, B are the colliding hadrons or nuclei containing Z_A and Z_B protons respectively, c is the produced parton, x and X are anything, $d\hat{\sigma}(Q^2,x_1,x_2)_{ij\to c+x}$ is the perturbatively calculable differential cross section for the production of c at the scale Q, and $x_{1,2} \sim Q/\sqrt{s}$ are the fractional momenta of the colliding partons i and j. The number distribution function of the parton flavour i of the protons (neutrons) in A is denoted as $f_i^{p/A}$ ($f_i^{n/A}$), and similarly for partons j in B.

In the leading-twist approximation, multiple scattering of the bound nucleons does occur but all collisions are independent, correlations between partons from the same object A are neglected, and only one-parton densities are needed. The parton distribution functions (PDFs) $f_i^{p/A}$ are universal quantities applicable in all collinearly factorizable processes. The PDFs cannot be computed by perturbative methods and, so far, it has not been possible to compute them from first principles, either. Thus, nonperturbative input from data on various hard processes is needed for the extraction of the PDFs. However, once the PDFs are known at some initial (lowest) scale $Q_0 \gg \Lambda_{\rm QCD}$, QCD perturbation theory predicts the scale evolution of the PDFs to other (higher) values of Q^2 in form of the Dokshitzer–Gribov–Lipatov–Altarelli–Parisi (DGLAP) equations [43].

The method of extracting the PDFs from experimental data is well established in the case of the free proton: the initial nonperturbative distributions are parametrized at some Q_0^2 and evolved to higher scales according to the DGLAP equations. Comparison with the data is made in various regions of the (x,Q^2)-plane. The parameters of the initial distributions, $f_i^p(x,Q_0^2)$, are fixed when the best global fit is found. The data from deeply inelastic lp scattering (DIS) are most important for these global DGLAP fits, especially the HERA data at small values of x and Q^2. The sum rules for momentum, charge and baryon number give further constraints. In this way, through the global DGLAP fits, groups like MRST [44], CTEQ [19] or GRV [45] obtain their well-known sets of the free proton PDFs.

The nuclear parton distribution functions (nPDFs) differ in magnitude from the PDFs of the free proton. In the measurements of the structure function, $F_2^A = Z_A F_2^{p/A} + (A-Z_A) F_2^{n/A}$, of nuclear targets in DIS (see e.g. Ref. [46] and references therein), and especially of the ratio

$$R_{F_2}^A(x,Q^2) \equiv \frac{\frac{1}{A} d\sigma^{lA}/dQ^2dx}{\frac{1}{2} d\sigma^{lD}/dQ^2dx} \approx \frac{\frac{1}{A} F_2^A(x,Q^2)}{\frac{1}{2} F_2^D(x,Q^2)}\,, \qquad (1.9)$$

the following nuclear effects have been discovered in different Bjorken-x regions:

- shadowing; a depletion, $R_{F_2}^A < 1$, at $x \lesssim 0.1$,
- antishadowing; an excess, $R_{F_2}^A > 1$, at $0.1 \lesssim x \lesssim 0.3$,
- EMC effect; a depletion at $0.3 \lesssim x \lesssim 0.7$, and
- Fermi motion; an excess towards $x \to 1$ and beyond.

The Q^2 dependence of $R^A_{F_2}$ is weaker and has thus been more difficult to measure. Data with high enough precision, however, exist. The NMC collaboration discovered a clear Q^2 dependence in the ratio $d\sigma^{\mu\mathrm{Sn}}/d\sigma^{\mu\mathrm{C}}$ [47], i.e. the scale dependence of the ratio $F_2^{\mathrm{Sn}}/F_2^{\mathrm{C}}$, at $x \gtrsim 0.01$. Since $F_2^{p(n)/A} = \sum_q e_q^2 x[f_q^{p(n)/A} + f_{\bar{q}}^{p(n)/A}] + \mathcal{O}(\alpha_s)$, the nuclear effects in the ratio $R^A_{F_2}$ directly translate into nuclear effects in the parton distributions: $f_i^{p/A} \neq f_i^p$.

The nPDFs, $f_i^{p/A}$, also obey the DGLAP equations in the large-Q^2 limit. They can be determined by using a global DGLAP fit procedure similar to the case of the free proton PDFs. Pioneering studies of the DGLAP evolution of the nPDFs are found in e.g. Ref. [48–51]. References for various other studies of perturbative evolution of the nPDFs and also to simpler Q^2-independent parametrizations of the nuclear effects in the PDFs can be found in Refs. [52, 53]. The nuclear case is, however, more complicated because of additional variables, the mass number A and the charge Z, and, because the number of data points available in the perturbative region is more limited than for the PDFs of the free proton. The DIS data play the dominant role in the nuclear case as well. However, as illustrated by Fig. 1.8, no data are available from nuclear DIS experiments below $x \lesssim 5 \times 10^{-3}$ at $Q^2 \gtrsim 1$ GeV^2. This makes the determination of the nuclear gluon distributions especially difficult. Further constraints on the global DGLAP fits of the nPDFs can be obtained from e.g. the Drell–Yan (DY) process measured in fixed-target pA collisions [54, 55]. Currently, there are two sets of nPDFs available which are based on the global DGLAP fits to the data: (i) EKS98 [27, 28] (the code in Refs. [56, 57]), and (ii) HKM [29] (the code in Ref. [58]). We shall compare the main features of these two analyses and comment on their differences below.

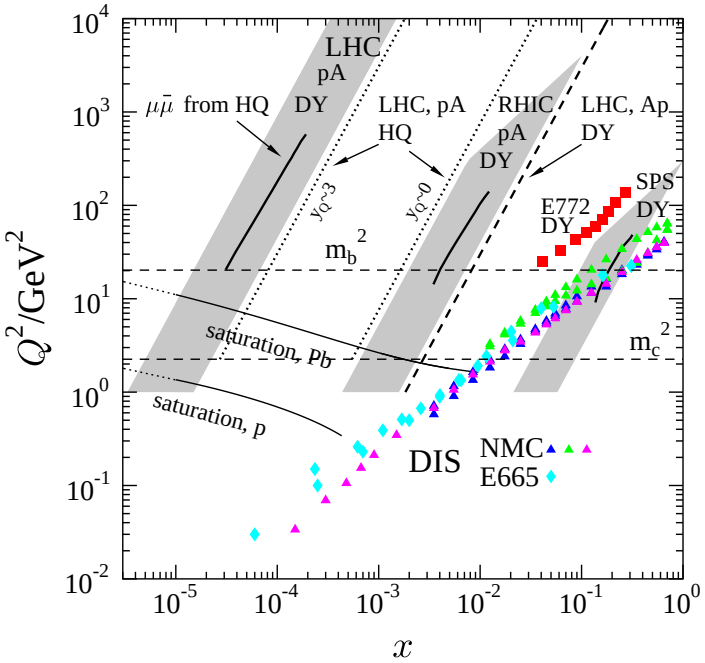

Fig. 1.8: The average values of x and Q^2 of the DIS data from NMC [59–61] (triangles) and E665 [62, 63] (diamonds) in lA, and of x_2 and M^2 of the DY dilepton data [54] (squares) in pA. The heavy quark mass scales are shown by the horizontal dashed lines. The initial scale Q_0^2 is m_c^2 in EKRS and 1 GeV^2 in HKM. For the rest of the figure, see the text in Section 4.1.3.

4.1.2. Comparison of EKS98 and HKM

EKS98 and overview of constraints available from data. The parametrization EKS98 [27] is based on the results of the DGLAP analysis [28] and its follow-up [27]. We refer to these together as EKRS here. In the EKRS approach, the nPDFs, the parton distributions of the bound protons, $f_i^{p/A}$, are defined through the modifications of the corresponding distributions in the free proton,

$$R_i^A(x,Q^2) \equiv \frac{f_i^{p/A}(x,Q^2)}{f_i^p(x,Q^2)}\,, \tag{1.10}$$

where the PDFs of the free proton are from a known set such as CTEQ, MRS or GRV. As in the case of the free nucleons, for isoscalar nuclei the parton distributions of bound neutrons are obtained through isospin symmetry, $f_{u(\bar{u})}^{n/A} = f_{d(\bar{d})}^{p/A}$ and $f_{d(\bar{d})}^{n/A} = f_{u(\bar{u})}^{p/A}$. Although exact only for isoscalar and mirror nuclei, this is expected to be a good first approximation for all nuclei.

To simplify the determination of the input nuclear effects for valence and sea quarks, the following flavour-independent *initial* modifications are assumed: $R_{u_V}^A(x,Q_0^2) \approx R_{d_V}^A(x,Q_0^2) \approx R_V^A(x,Q_0^2)$, and $R_{\bar{u}}^A(x,Q_0^2) \approx R_{\bar{d}}^A(x,Q_0^2) \approx R_s^A(x,Q_0^2) \approx R_S(x,Q_0^2)$. Thus only three independent initial ratios, R_V^A, R_S^A and R_G^A are to be determined at $Q_0^2 = m_c^2$ = 2.25 GeV^2. Note also that the approximations above are needed and used *only* at Q_0^2 in [28]. In the EKS98-parametrization [27] of the DGLAP-evolved results, it was observed that, to a good approximation, $R_{u_V}^A = R_{d_V}^A$ and $R_{\bar{u}}^A = R_{\bar{d}}^A$ for all Q^2. Further details of the EKRS analysis can be found in Ref. [28], here we summarize the constraints available in each x-region. Consider first quarks and antiquarks:

- At $x \gtrsim 0.3$ the DIS data constrains only the ratio R_V^A: valence quarks dominate F_2^A, so that $R_{F_2}^A \approx R_V^A$ but R_S^A and R_G^A are left practically unconstrained. An EMC effect is, however, assumed also for the initial R_S^A and R_G^A since in the scale evolution the EMC effect of valence quarks is transmitted to gluons and, further on, to sea quarks [50]. In this way the nuclear modifications R_i^A also remain stable against the evolution.
- At $0.04 \lesssim x \lesssim 0.3$ both the DIS and DY data constrain R_S^A and R_V^A but in different regions of Q^2, as shown in Fig. 1.8. In addition, conservation of baryon number restricts R_V^A. The use of DY data [54] is essential in order to fix the relative magnitude of R_V^A and R_S^A since the DIS data alone cannot distinguish between them. As a result, no antishadowing appears in $R_S^A(x,Q_0^2)$.
- At $5\times10^{-3} \lesssim x \lesssim 0.04$, only DIS data exist in the region $Q \gtrsim 1$ GeV where the DGLAP analysis can be expected to apply. Once R_V^A is fixed by the DIS and DY data at larger x, the magnitude of nuclear valence quark shadowing in the EKRS approach follows from the conservation of baryon number. As a result of these contraints, nuclear valence quarks in EKRS are less shadowed than the sea quarks, $R_V^A > R_S^A$.
- At $x \lesssim 5\times10^{-3}$, as shown by Fig. 1.8, the DIS data for the ratio $R_{F_2}^A$ lie in the region $Q \lesssim 1$ GeV where the DGLAP equations are unlikely to be applicable in the nuclear case. Indirect constraints, however, *can* be obtained by noting the following: (i) At the smallest values of x (where $Q \ll 1$ GeV), $R_{F_2}^A$ depends only very weakly, if at all, on x [60, 62]. (ii) $\partial(F_2^{\rm Sn}/F_2^{\rm C})/\partial\log Q^2 > 0$ at $x \sim 0.01$ [47], indicating that $\partial R_{F_2^A}/\partial\log Q^2 > 0$. (iii) Negative $\log Q^2$-slopes of $R_{F_2}^A$ at $x \lesssim 5\times10^{-3}$ have not been observed [60]. Based on these experimental facts, the EKRS approach assumes that the sign of the $\log Q^2$-slope of $R_{F_2}^A$ remains non-negative at $x < 0.01$ and therefore the DIS data [60, 62] in the nonperturbative region gives a *lower bound* on $R_{F_2}^A$ at Q_0^2 for very small x. The sea quarks dominate over the valence quarks at small values of x so that only R_S^A is constrained by the DIS data. R_V^A remains restricted by baryon number conservation.

Pinning down the nuclear gluon distributions is difficult in the absence of stringent direct constraints. What is available in different regions of x can be summarized as follows:

- At $x \gtrsim 0.2$, no experimental constraints are currently available on the gluons. Conservation of momentum is used as an overall constraint but this alone is not sufficient to determine whether

there is an EMC effect for gluons. Only about 30% of the gluon momentum comes from $x \gtrsim 0.2$ so that fairly sizeable changes in $R_G^A(x, Q_0^2)$ in this region can be compensated by smaller changes at $x < 0.2$ without violating the constraints discussed below. As mentioned above, in the EKRS approach an EMC effect is initially assumed for R_G. This guarantees a stable scale evolution and the EMC effect remains at larger Q^2.

- At $0.02 \lesssim x \lesssim 0.2$ the Q^2 dependence of the ratio $F_2^{\rm Sn}/F_2^{\rm C}$ measured by NMC [47] currently sets the most important constraint on R_G^A [64]. In the small-x region where gluons dominate the DGLAP evolution, the Q^2 dependence of $F_2(x, Q^2)$ is dictated by the gluon distribution as $\partial F_2(x, Q^2)/\partial \log Q^2 \sim \alpha_s x g(2x, Q^2)$ [65]. As discussed in Refs. [28, 52], this leads to $\partial R_{F_2}^A(x, Q^2)/\partial \log Q^2 \sim \alpha_s [R_G^A(2x, Q^2) - R_{F_2}^A(x, Q^2)] x g(2x, Q^2)/F_2^D(x, Q^2)$. The $\log Q^2$ slopes of $F_2^{\rm Sn}/F_2^{\rm C}$ measured by NMC [47] therefore constrain R_G^A. Especially, the positive $\log Q^2$-slope of $F_2^{\rm Sn}/F_2^{\rm C}$ measured by NMC indicates that $R_G^A(2x, Q_0^2) > R_{F_2}^A(x, Q_0^2)$ at $x \sim 0.01$ [28, 52]. Thus, within the DGLAP framework, much stronger gluon than antiquark shadowing at $x \sim 0.01$, as suggested e.g. in Ref. [66], is not supported by the NMC data. The antishadowing in the EKRS gluons follows from the constraint $R_G^A(0.03, Q_0^2) \approx 1$ imposed by the NMC data (see also Ref. [64]) combined with the requirement of momentum conservation. The EKRS antishadowing is consistent with the E789 data [67] on D-meson production in pA collisions (note, however, the large error bar on the data). It also seems to be supported by J/ψ production in DIS, measured by NMC [68].
- At $x \lesssim 0.02$, stringent experimental constraints do not yet exist for the nuclear gluons. It should be emphasized, however, that the initial R_G^A in this region is directly connected to the initial $R_{F_2}^A$. As discussed above, related to quarks at small x, taking the DIS data on $R_{F_2}^A$ in the non-perturbative region as a lower limit for $R_{F_2}^A$ at Q_0^2 corresponds to $\partial R_{F_2^A}/\partial \log Q^2 \geq 0$ so that $R_G^A(x < 0.02, Q_0^2) \geq R_{F_2}^A(x/2, Q_0^2) \geq R_{F_2}^A(x/2, Q^2 \ll 1\ {\rm GeV}^2)$. Reference [28] observed that setting $R_G^A(x, Q_0^2) \approx R_{F_2}^A(x, Q_0^2)$ at $x \lesssim 0.01$ fulfils this constraint. This approximation remains fairly good even after DGLAP evolution from $Q_0 \sim 1$ GeV to $Q \sim 100$ GeV, see Ref. [27].

As explained in detail in Ref. [28], in the EKRS approach the initial ratios $R_V^A(x, Q_0^2)$, $R_S^A(x, Q_0^2)$ and $R_G^A(x, Q_0^2)$ are constructed piecewise in different regions of x. Initial nPDFs are computed at Q_0^2. Leading order (LO) DGLAP evolution to higher scales is performed and comparisons with the DIS and DY data are made. The parameters in the input ratios are iteratively changed until the best global fit to the data is achieved. The determination of the input parameters in EKRS has so far been done only manually with the best overall fit determined by eye. For the quality of the fit, see the detailed comparison with the data in Figs. 4–10 of Ref. [28]. The parametrization EKS98 [27] of the nuclear modifications $R_i^A(x, Q^2)$ was prepared on the basis of the results from Ref. [28]. It was also shown that when the free proton PDFs were changed from GRVLO [69] to CTEQ4L [70] (differing from each other considerably), the changes induced in $R_i^A(x, Q^2)$ were within a few per cent [27]. Therefore, accepting this range of uncertainty, the EKS98 parametrization can be used together with any (LO) set of the free proton PDFs.

The HKM analysis. In principle, the definition of the nPDFs in the HKM analysis [29] differs slightly from that in EKRS: instead of the PDFs of the bound protons, HKM define the nPDFs as the *average* distributions of each flavour i in a nucleus A: $f_i^A(x, Q^2) = (Z/A) f_i^{p/A}(x, Q^2) + (1 - Z/A) f_i^{n/A}(x, Q^2)$. Correspondingly, the HKM nuclear modifications at the initial scale $Q_0^2 = 1\ {\rm GeV}^2$ are then defined through

$$f_i^A(x, Q_0^2) = w_i(x, A, Z)[(Z/A) f_i^p(x, Q_0^2) + (1 - Z/A) f_i^n(x, Q_0^2)]\,. \tag{1.11}$$

In practice, however, since in the EKS98 parametrization $R_{u_V}^A = R_{d_V}^A$ and $R_{\bar{u}}^A = R_{\bar{d}}^A$, the EKS98 modifications also represent average modifications. Flavour-symmetric sea quark distributions are assumed in HKM whereas the flavour asymmetry of the sea quarks in EKRS follows from that of the free proton.

An improvement relative to EKRS is that the HKM method to extract the initial modifications $w_i(x, A, Z)$ at Q_0^2 is more automatic and more quantitative in the statistical analysis since the HKM analysis is strictly a minimum-χ^2 fit. Also, with certain assumptions of a suitable form (see Ref. [29]) for the initial modifications w_i, the number of parameters has been conveniently reduced to seven. The form used in the fit is

$$w_i(x, A, Z) = 1 + \left(1 - \frac{1}{A^{1/3}}\right) \frac{a_i(A, Z) + H_i(x)}{(1-x)^{\beta_i}}, \tag{1.12}$$

where $H_i(x) = b_i x + c_i x^2$. An analysis with a cubic polynomial is also performed, with similar results. Due to the flavour symmetry, the sea quark parameters are identical for all flavours. For valence quarks, conservation of charge Z (not used in EKRS) and baryon number A are required, fixing a_{u_V} and a_{d_V}. In the case of non-isoscalar nuclei $w_{u_V} \neq w_{d_V}$. Also, momentum conservation is imposed fixing a_g. Taking β_V, b_V and c_V to be equal for u_V and d_V, and $\beta_{\bar{q}} = \beta_g = 1$, $b_g = -2c_g$, the remaining seven parameters b_V, c_V, β_V, $a_{\bar{q}}$ $b_{\bar{q}}$, $c_{\bar{q}}$ and c_g are determined by a global DGLAP fit which minimizes χ^2.

The comparison. Irrespective of whether the best fit is found automatically or by eye, the basic procedure to determine the nPDFs in the EKRS and HKM analyses is the same. The results obtained for the nuclear effects are, however, quite different, as can be seen in the comparison at $Q^2 = 2.25$ GeV^2 shown in Fig. 1.9. The main reason for this is that different data sets are used:

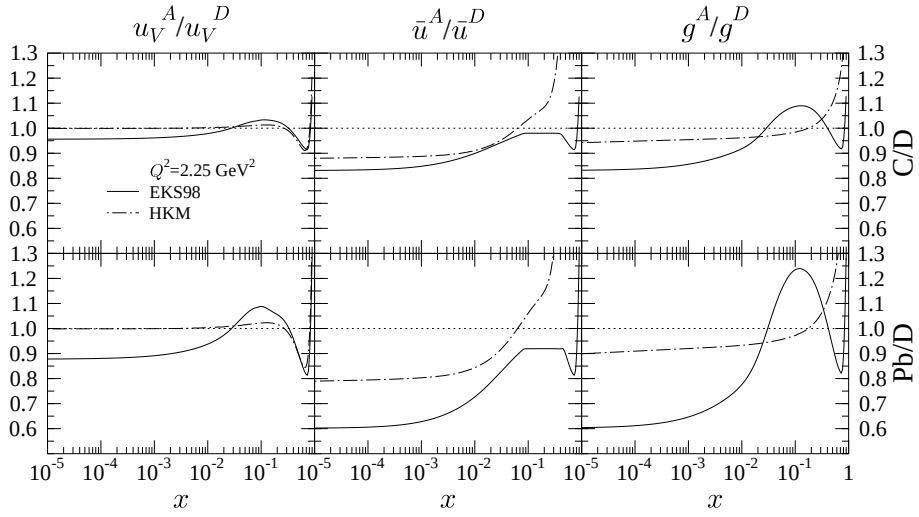

Fig. 1.9: The nuclear modifications for the u_V, $\bar{u}$ and gluon distributions in EKS98 (solid) and in HKM (dot-dashed) at $Q^2 = 2.25$ GeV^2. Upper panels: C/D. Lower panels: Pb/D with isoscalar Pb.

- The HKM analysis [29] uses only the DIS data whereas EKRS include also the DY data from pA collisions. As explained above, the DY data are very important in the EKRS analysis to fix the relative modifications of valence and sea quarks at intermediate x. Preliminary results reported in Ref. [71] show that, when the DY data are included in the HKM analysis, the antiquark modifications become more similar to those of EKRS.
- The NMC data on F_2^A/F_2^{C} [61], which imposes quite stringent constraints on the A-systematics in the EKRS analysis, is not used in HKM. As a result, $R_{F_2}^A$ has less shadowing in HKM than in EKRS (see also Fig. 1 of Ref. [52]), especially for heavy nuclei.

- In addition to the recent DIS data sets, some older ones are used in the HKM analysis. The older sets are not included in EKRS. This, however, presumably does not cause any major differences between EKRS and HKM since the older data sets have larger error bars and will therefore typically have less statistical weight in the χ^2 analysis.
- The HKM analysis does not make use of the NMC data [47] on the Q^2 dependence of $F_2^{\rm Sn}/F_2^{\rm C}$. As explained above, these data are the main experimental constraint on the nuclear gluons in the EKRS analysis. Figure 1.10 shows a comparison of the EKRS (solid) and the HKM (dot-dashed) results to the NMC data on $F_2^{\rm Sn}/F_2^{\rm C}$ as a function of Q^2. The HKM results do not reproduce the measured Q^2 dependence of $F_2^{\rm Sn}/F_2^{\rm C}$ at the smallest values of x. This figure demonstrates explicitly that the nuclear modifications of gluon distributions at $0.02 \lesssim x \lesssim 0.1$ *can* be pinned down with the help of these NMC data.

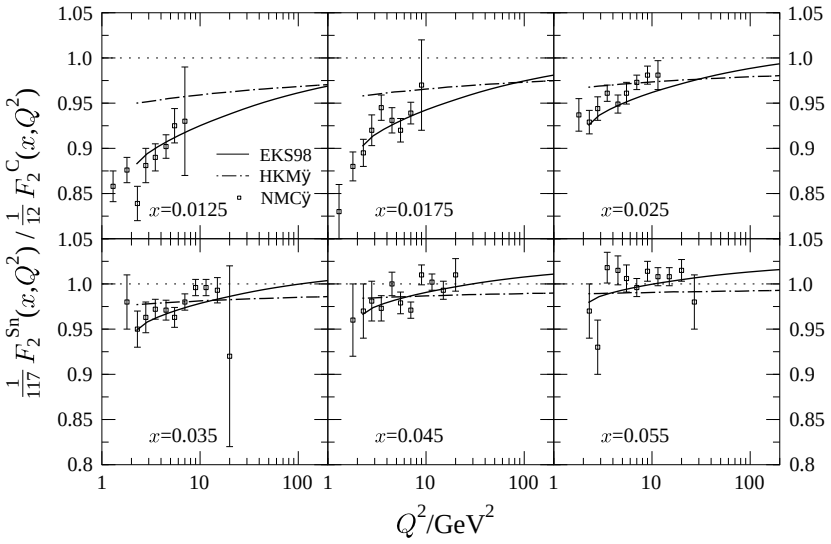

Fig. 1.10: The ratio $F_2^{\rm Sn}/F_2^{\rm C}$ as a function of Q^2 at different fi xed values of x. The data are from NMC [47] and the curves are EKS98 [27] (solid) and HKM [29] (dot-dashed).

4.1.3. Future prospects

Constraints from pA collisions at LHC, RHIC and SPS. The hard probes in pA collisions, especially those at the LHC, will play a major role in probing the nPDFs at regions not accessible before. Figure 1.8 shows the x and Q^2 regions of the phase space probed by certain hard processes at different centre-of-mass energies[1]. Let us consider the figure in more detail:

• The measurements of semileptonic decays of D and $\overline{D}$ mesons in pA will help to pin down the nuclear gluon distributions [72, 73]. Borrowed from an LO analysis [73], the thick solid lines in Fig. 1.8 show how the average scale $Q^2 = \langle m_T^2 \rangle$ of open charm production is correlated with the average fractional momentum $x = \langle x_2 \rangle$ of the incoming nuclear gluon in dimuon production in correlated $D\overline{D}$ decays at the LHC (computed for pPb at $\sqrt{s} = 5500$ GeV and single muon acceptance $2.5 \leq y_\mu \leq 4.0$, with no rapidity shifts), at RHIC (pAu at $\sqrt{s} = 200$ GeV, $1.15 \leq y_\mu \leq 2.44$) and at the SPS (pPb at $\sqrt{s} = 17.3$ GeV, $0 \leq y_\mu \leq 1$). For each solid curve, the smallest Q^2 shown corresponds to a dimuon invariant mass $M = 1.25$ GeV, and the the largest Q^2 to $M = 9.5$ GeV (LHC), 5.8 GeV (RHIC) and 4.75 GeV (SPS) (cf. Fig. 5 in Ref. [73]). We observe that data from the SPS, RHIC and the LHC will offer constraints in different regions of x. The data from NA60 at the SPS will probe the antishadowing

[1]No counting rates have been considered for the fi gure.

of nuclear gluons, while the RHIC data probe the onset of gluon shadowing, and the LHC data constrain the nuclear gluons at very small x, deep in the shadowing region.

• Similarly, provided that the DY dimuons can be distinguished from those coming from the D and B decays, the DY dimuon pA cross sections are expected to set further constraints on the nuclear effects on the sea quark distributions. In $2 \to 1$ kinematics, $x_2 = (M/\sqrt{s})e^{-y}$ where M and y are the invariant mass and rapidity of the lepton pair. The rapidity of the pair is always between those of the leptonic constituents of the pair. The shaded regions in Fig. 1.8 illustrate the regions in $x = x_2^A$ and $Q^2 = M^2$ probed by DY dimuons in pA collisions at the LHC, RHIC and SPS. The parameters used for the LHC are $\sqrt{s} = 5500$ GeV and $2.5 \leq y \leq 4.0$ with no rapidity shifts [74]. Note that from the (phase space) point of view of x_2^A (but *not* of x_1^p), PbPb collisions at $\sqrt{s}_{\rm PbPb} = 5500$ GeV at the LHC are equivalent to pPb collisions at $\sqrt{s}_{p\rm Pb} = 8800$ GeV: the decrease of x_2 due to the increase in $\sqrt{s}$ is compensated by the rapidity shift y_0 [74]: $x_2^{pA} = (M/\sqrt{s}_{pA})e^{-(y_{AA}+y_0)} = (M/\sqrt{s}_{AA})e^{-y_{AA}} = x_2^{AA}$. For RHIC, the shaded region corresponds to $\sqrt{s} = 200$ GeV and $1.2 \leq y \leq 2.2$, the rapidity acceptance of the PHENIX forward muon arm [75]. For the SPS, we have again used $\sqrt{s} = 17.3$ GeV and $0 \leq y \leq 1$. Single muon p_T-cuts (see Refs. [75, 76]) have not been applied and the shaded regions all correspond to $M^2 \geq 1$ GeV^2. At the highest scales shown, the dimuon regions probed at the SPS and RHIC are limited by the phase space. The SPS data may shed more light on the existence of an EMC effect for the sea quarks [77]. At the LHC the dimuons from decays of D and B mesons are expected to dominate the dilepton continuum up to the Z mass [78–80]. If, however, the DY contribution can be identified (see Section 6.1. for more discussion), DY dimuons at the LHC will probe the sea quark distributions deep in the shadowing region and also at high scales, up to $Q^2 = M_Z^2$. The RHIC region again lies conveniently between the SPS and the LHC, mainly probing the beginning of sea quark shadowing region. In pA collisions at the LHC, DY dimuons with $y = (y_{\rm min} + y_{\rm max})/2$ probe the regions indicated by the dashed line (the spread due to the y acceptance is not shown).

• The dotted line shows the kinematical region probed by open heavy flavour production in pA (and also in AA) collisions, when both heavy quarks are at $y = 0$ in the detector frame. In this case, again assuming $2 \to 2$ kinematics, $x_2^{pA} = x_2^{AA} = 2Q/\sqrt{s}_{AA}$ with $Q = m_T$. To illustrate the effect of moving towards forward rapidities, the case $y_Q = y_{\overline{Q}} = 3$ is also shown. Only the region where $Q^2 \gtrsim m_b^2$ (above the upper horizontal line) is probed by $b\bar{b}$ production. Due to the same kinematics (in x_2 and Q^2) as in open heavy quark production, the dotted lines also correspond to the regions probed by direct photon production (with $Q = p_T$).

• As demonstrated by Fig. 1.8, hard probes in pA collisions at RHIC and at the LHC in particular will provide us with very important constraints on the nPDFs at scales where the DGLAP evolution is expected to be applicable. Power corrections to the evolution [25, 26] can, however, be expected to play an increasingly important role towards small values of x and Q^2. The effects of the first of such corrections, the GLRMQ terms [25, 26] leading to non-linear DGLAP+GLRMQ evolution equations, have been studied recently in light of the HERA data [81]. From the point of view of the DGLAP evolution of the (n)PDFs, gluon saturation occurs when their evolution becomes dominated by power corrections [82]. Figure 1.8 shows the saturation limits obtained for the free proton and for Pb in the DGLAP+GLRMQ approach [32] (solid curves, the dotted curves are extrapolations to guide the eye). The saturation limit obtained for the free proton in the DGLAP+GLRMQ analysis should be taken as an upper limit in Q^2. It is constrained quite well by the HERA data (see Ref. [81]). The constraints from the Q^2 dependence of $F_2^{\rm Sn}/F_2^{\rm C}$, however, were not taken into account in obtaining the saturation limit shown for the Pb nucleus [32]. For a comparison of the saturation limits obtained in other models, see Ref. [32].

• Figure 1.8 also shows which hard probes of pA collisions can be expected to probe the nPDFs in the gluon saturation region. The probes directly sensitive to the gluon distributions are especially interesting from this point of view. Such probes include open $c\bar{c}$ production at small p_T and direct photon production at $p_T \sim$ few GeV, both as far forward in rapidity as possible (see the dotted lines). Note that

open $b\bar{b}$ production is already in the region where linear DGLAP evolution is applicable. In light of the saturation limits shown, the chances of measuring the effects of non-linearities in the evolution through open $c\bar{c}$ production in pA at RHIC would seem marginal. At the LHC, however, measuring saturation effects in the nuclear gluon distributions through open $c\bar{c}$ in pA could be possible.

Improvements of the DGLAP analyses. On the practical side, the global DGLAP fits of the nPDFs discussed above can be improved in obvious ways. The EKRS analysis should be made more automatic and a proper statistical treatment, such as in HKM, should be added. The automatization alone is, however, not expected to change the nuclear modifications of the PDFs significantly from EKS98 but more quantitative estimates of the uncertainties and of their propagation would be obtained. This work is in progress. As also discussed above, more contraints from data should be added to the HKM analysis. More generally, all presently available data from hard processes in DIS and pA collisions have not yet been exhausted: for instance, the recent CCFR DIS data for $F_2^{\nu\mathrm{Fe}}$ and $F_3^{\nu\mathrm{Fe}}$ from νFe and $\bar{\nu}$Fe collisions [83] (not used in EKRS or in HKM), could help to pin down the valence quark modifications [84]. In the future, hard probes of pA collisions at the LHC, RHIC and the SPS will offer very important constraints on the nPDFs, especially for gluons and sea quarks. Eventually, the nPDF DGLAP analyses should be extended to NLO perturbative QCD. As discussed above, the effects of power corrections [25, 26] to the DGLAP equations and also to the cross sections [85] should be analysed in detail in the context of global fits to the nuclear data.

4.2. Nonlinear Corrections to the DGLAP Equations; Looking for the Saturation Limits

K.J. Eskola, H. Honkanen, V.J. Kolhinen, J.W. Qiu and C.A. Salgado

Free proton PDFs, $f_i(x, Q^2)$, are needed for the calculation of hard process cross sections in hadronic collisions. Once they are determined at a certain initial scale Q_0^2, the DGLAP equations [43] well describe their evolution to large scales. Based on global fits to the available data, several different sets of PDFs have been obtained [19, 20, 44, 86]. The older PDFs do not adequately describe the recent HERA data [87] on the structure function F_2 at the perturbative scales Q^2 at small x. In the analysis of newer PDF sets, such as CTEQ6 [19] and MRST2001 [44], these data have been taken into account. However, difficulties arise when fitting both small and large-scale data simultaneously. In the new MRST set, the entire H1 data set [87] has been used in the analysis, leading to a good average fit at all scales but at the expense of a negative NLO gluon distribution at small x and $Q^2 \lesssim 1$ GeV^2. In the CTEQ6 set only the large scale ($Q^2 > 4$ GeV^2) data have been included, giving a good fit at large Q^2 but resulting in a poorer fit at small-x and small Q^2 ($Q^2 < 4$ GeV^2). Moreover, the gluon distribution at small x with $Q^2 \lesssim 1.69$ GeV^2 has been set to zero.

These problems are interesting since they could indicate a new QCD phenomenon. At small values of momentum fraction x and scales Q^2, gluon recombination terms, which lead to non-linear corrections to the evolution equations, can become significant. The first of these non-linear terms have been calculated by Gribov, Levin and Ryskin [25], and Mueller and Qiu [26]. In the following, these corrections shall be referred to as the GLRMQ terms for short. With these modifications, the evolution equations become [26]

$$\frac{\partial x g(x,Q^2)}{\partial \log Q^2} = \left.\frac{\partial x g(x,Q^2)}{\partial \log Q^2}\right|_{\mathrm{DGLAP}} - \frac{9\pi}{2}\frac{\alpha_s^2}{Q^2}\int_x^1 \frac{dy}{y} y^2 G^{(2)}(y,Q^2), \tag{1.13}$$

$$\frac{\partial x \bar{q}(x,Q^2)}{\partial \log Q^2} = \left.\frac{\partial x \bar{q}(x,Q^2)}{\partial \log Q^2}\right|_{\mathrm{DGLAP}} - \frac{3\pi}{20}\frac{\alpha_s^2}{Q^2} x^2 G^{(2)}(x,Q^2) + \ldots G_{\mathrm{HT}}\,, \tag{1.14}$$

where the two-gluon density can be modelled as $x^2 G^{(2)}(x,Q^2) = \frac{1}{\pi R^2}[x g(x,Q^2)]^2$, with proton radius $R = 1$ fm. The higher dimensional gluon term, G_{HT} [26], is here assumed to be zero. The effects of the non-linear corrections on the DGLAP evolution of the free proton PDFs were studied in Ref. [81] in view of the recent H1 data. The results are discussed below.

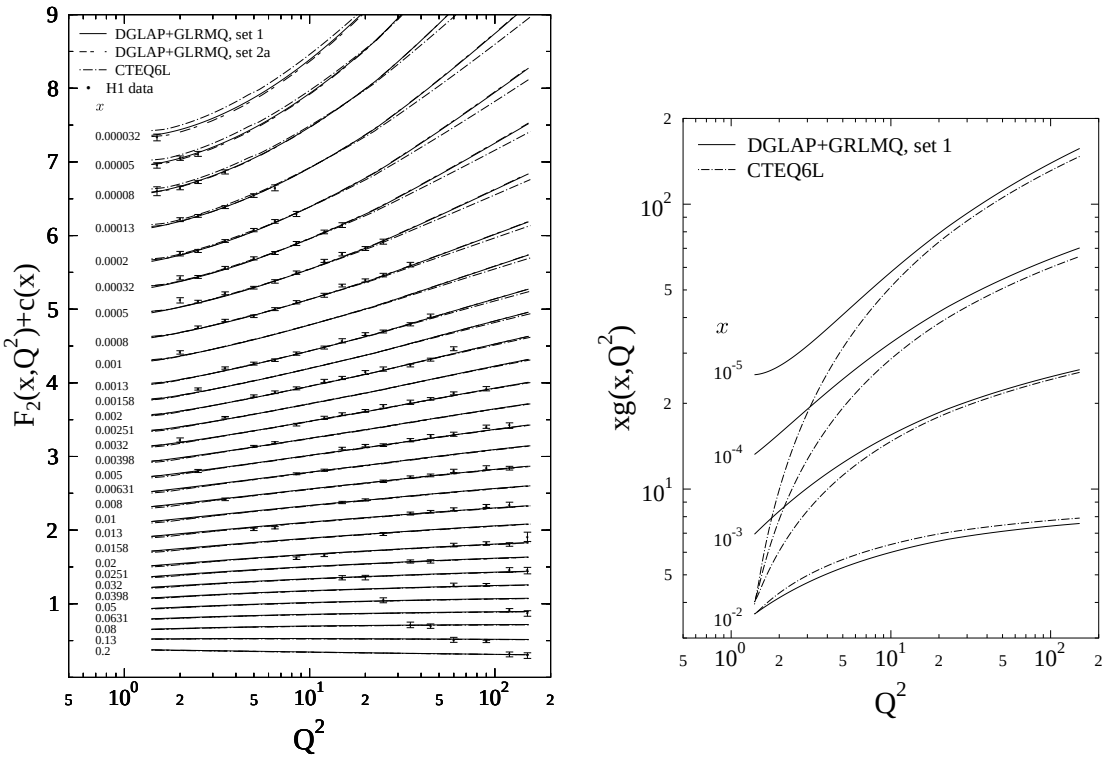

Fig. 1.11: Left: $F_2(x, Q^2)$ calculated using CTEQ6L [19] (dotted-dashed) and the DGLAP+GLRMQ results with set 1 (solid) and set 2a (double dashed) [81], compared with the H1 data [87]. Right: The Q^2 dependence of the gluon distribution function at fi xed x, from set 1 evolved with DGLAP+GLRMQ (solid) and directly from CTEQ6L (dotted-dashed).

4.2.1. Constraints from the HERA data

The goal of the analysis in Ref. [81] was (1) to possibly improve the (LO) fit of the calculated $F_2(x, Q^2)$ to the H1 data [87] at small Q^2 while (2) concurrently maintaining the good fit at large Q^2 and, finally, (3) to study the interdependence of the initial distributions and the evolution.

In CTEQ6L, a good fit to the H1 data is obtained (see Fig. 1.11) with a flat small-x gluon distribution at $Q^2 \sim 1.4$ GeV^2. As can be seen from Eqs. (1.13), (1.14), the GLRMQ corrections slow the scale evolution. Now one may ask whether the H1 data can be reproduced equally well with different initial conditions (i.e. assuming larger initial gluon distributions) and the GLRMQ corrections included in the evolution. This question was addressed in Ref. [81] by generating three new sets of initial distributions using DGLAP + GLRMQ evolved CTEQ5 [86] and CTEQ6 distributions as guidelines. The initial scale was chosen to be Q_0^2 = 1.4 GeV^2, slightly below the smallest scale of the data. The modified distributions at Q_0^2 were constructed piecewise from CTEQ5L and CTEQ6L distributions evolved down from Q^2 = 3 and 10 GeV^2 (CTEQ5L) and Q^2 = 5 GeV^2 (CTEQ6L). A power law form was used in the small-x region to tune the initial distributions until good agreement with the H1 data was found.

The difference between the three sets in Ref. [81] is that in set 1 there is still a nonzero charm distribution at Q_0^2 = 1.4 GeV^2, slightly below the charm mass threshold with m_c = 1.3 GeV in CTEQ6. In set 2a and set 2b the charm distribution has been removed at the initial scale and the resulting deficit in F_2 has been compensated by slightly increasing the other sea quarks at small x. Moreover, the effect of charm was studied by using different mass thresholds: m_c = 1.3 GeV in set 2a and $m_c = \sqrt{1.4}$ GeV in set 2b, i.e. charm begins to evolve immediately above the initial scale.

The results of the DGLAP+GLRMQ evolution with the new initial distributions are shown

in Fig. 1.11. The left panel shows the comparison between the H1 data and the (LO) structure function $F_2(x,Q^2) = \sum_i e_i^2 x[q_i(x,Q^2) + \bar{q}_i(x,Q^2)]$ calculated from set 1 (solid lines), set 2a (double dashed) and the CTEQ6L parametrization (dotted-dashed lines). As can be seen, the results are very similar, showing that with modified initial conditions and DGLAP+GLRMQ evolution, one obtains an as good or even a better fit to the HERA data ($\chi^2/N = 1.13$, 1.17, 0.88 for the sets 1, 2a, 2b, respectively) as with the CTEQ6L distributions ($\chi^2/N = 1.32$).

The evolution of the gluon distribution functions in the DGLAP+GLRMQ and DGLAP cases is illustrated more explicitly in the right panel of Fig. 1.11, where the absolute distributions for fixed x are plotted as a function of Q^2 for set 1 and for CTEQ6L. The figure shows how large differences at the initial scale vanish during the evolution due to the GLRMQ effects. At scales $Q^2 \gtrsim 4$ GeV^2, the GLRMQ corrections fade out rapidly and the DGLAP terms dominate the evolution.

4.2.2. Saturation limits: p and Pb

The DGLAP+GLRMQ approach also offers a way to study the gluon saturation limits. For each x in the small-x region, the saturation scale $Q^2_{\rm sat}$ can be defined as the value of the scale Q^2 where the DGLAP and GLRMQ terms in the non-linear evolution equation become equal, $\frac{\partial x g(x,Q^2)}{\partial \log Q^2}|_{Q^2=Q^2_{\rm sat}(x)} = 0$. The region of applicability of the DGLAP+GLRMQ is $Q^2 > Q^2_{\rm sat}(x)$ where the linear DGLAP part dominates the evolution. In the saturation region, at $Q^2 < Q^2_{\rm sat}(x)$, the GLRMQ terms dominate, and all non-linear terms become important.

In order to find the saturation scale $Q^2_{\rm sat}(x)$, for the free proton, the initial distributions (set 1) at Q_0^2 = 1.4 GeV^2 have to be evolved downwards in scale using the DGLAP+GLRMQ equations. As discussed in Ref. [81], since only the first correction term has been taken into account, the gluon distribution near the saturation region should be considered as an upper limit. Consequently, the saturation scale obtained is an upper limit as well. The result is shown by the asterisks in Fig. 1.12. The saturation line for the free proton from the geometric saturation model by Golec-Biernat and Wüsthoff (G-BW) [88] is also plotted (dashed line) for comparison. It is interesting to note that although the DGLAP+GLRMQ and G-BW approaches are very different, the slopes are very similar at the smallest values of x.

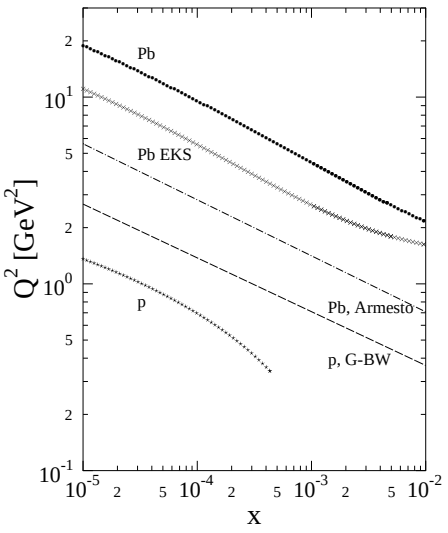

Fig. 1.12: The gluon saturation limits in the DGLAP+GLRMQ approach for proton (asterisks) and Pb (A = 208), with (crosses) and without (dots) nuclear modifi cations [81]. The saturation line for the proton from the geometric saturation model [88] (dashed line), and for Pb from [89] (dotted-dashed) are also plotted.

Saturation scales for nuclei can be determined similarly. For a nucleus A, the two-gluon density can be modelled as $x^2G^{(2)}(x,Q^2) = \frac{A}{\pi R_A^2}[xg_A(x,Q^2)]^2$, i.e. the effect of the correction is enhanced by a factor of $A^{1/3}$. An initial estimate of the saturation limit can be obtained by starting the downwards evolution at high enough scales, Q^2 = 100–200 GeV^2, for the GLRMQ terms to be negligible. Like in the proton case, the result is an upper limit. It is shown for Pb in Fig. 1.12 (dots). The effect of the nuclear modifications was also studied by applying the EKS98 [27] parametrization at the high starting scale. As a result, the saturation scales $Q^2_{\rm sat}(x)$ are somewhat reduced, as shown in Fig. 1.12 (crosses). The saturation limit obtained for a Pb nucleus by Armesto in a Glauberized geometric saturation model [89] is shown (dotted-dashed) for comparison. Again, despite the differences between the approaches, the slopes are strikingly similar.

For further studies and for more accurate estimates of $Q^2_{\rm sat}(x)$ in the DGLAP+GLRMQ approach, a full global analysis of the nuclear parton distribution functions should be performed, along the same lines as in EKRS [27, 28] and HKM [29].

4.3. Gluon Distributions in Nuclei at Small x: Guidance from Different Models

N. Armesto and C.A. Salgado

The difference between the structure functions measured in nucleons and nuclei [46] is a very important and well known feature of nuclear structure and nuclear collisions. At small values of x (< 0.01, shadowing region), the structure function F_2 per nucleon turns out to be smaller in nuclei than in a free nucleon. This corresponds to shadowing of parton densities in nuclei. While at small x valence quarks are of little importance and the behaviour of the sea is expected to follow that of F_2^A, the gluon distribution, which is not an observable quantity, is badly determined and represents one of the largest uncertainties for cross sections both at moderate and large Q^2 in collinear factorization [17]. For example, the uncertainty in the determination of the gluon distributions for Pb at $Q^2 \sim 5$ GeV^2 at LHC for $y = 0$, $x \sim m_T/\sqrt{s} \sim 10^{-4}$–$10^{-3}$, is a factor ~ 3 (see Fig. 1.13), which may result in an uncertainty of up to a factor of ~ 9 for the corresponding cross sections in PbPb collisions.

In this situation, while waiting for new data from lepton-ion [90–92] or pA colliders, guidance from different theoretical models is of utmost importance for controlled extrapolations from the region where experimental data exist to those interesting for the LHC. Two different approaches to the problem have been suggested: On one hand, some models try to explain the origin of shadowing, usually in terms of multiple scattering (in the frame where the nucleus is at rest) or parton interactions in the nuclear wave function (in the frame in which the nucleus is moving fast). On the other hand, other models parameterize parton densities inside the nucleus at some scale Q_0^2 large enough for perturbative QCD to be applied reliably and then evolve these parton densities using the DGLAP [43] evolution equations. Then, the origin of the differences between parton densities in nucleons and nuclei is not addressed, but contained in the parameterization at Q_0^2, obtained from a fit to data.

4.3.1. Multiple scattering and saturation models

The nature of shadowing is well understood qualitatively. In the rest frame of the nucleus, the incoming photon splits, at small enough x, into a $q\bar{q}$ pair long before reaching the nucleus, with a coherence length $l_c \propto 1/(m_N x)$ with m_N the nucleon mass. At small enough x, l_c becomes on the order of or greater than the nuclear size. Thus the $q\bar{q}$ pair interacts coherently with the nucleus with a typical hadronic cross section, resulting in absorption [93–100]. (See Ref. [101] for a simple geometrical approach in this framework.) In this way nuclear shadowing is a consequence of multiple scattering and is thus related to diffraction (see Refs. [102, 103]).

Multiple scattering is usually formulated in the dipole model [97, 104], equivalent to k_T-factorization [105] at leading order. In this framework, the γ^*-nucleus cross section is expressed as the convolution of the probability of the transverse or longitudinal γ^* to split into a $q\bar{q}$ pair of transverse

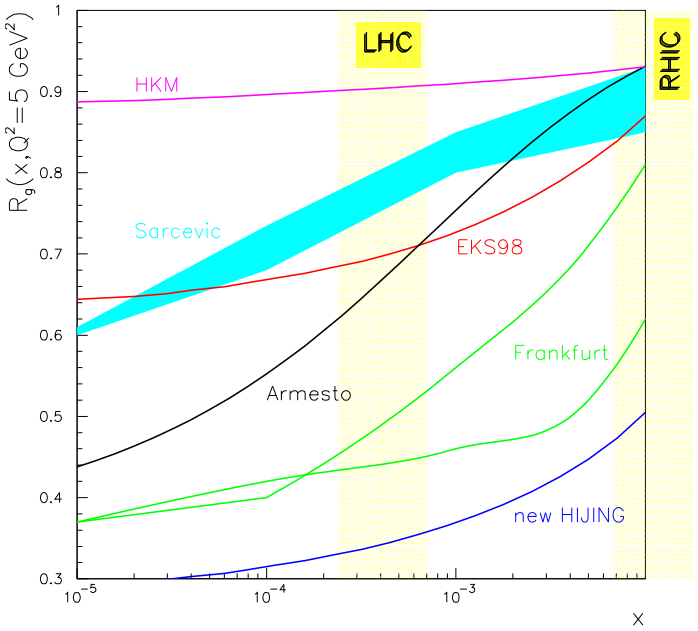

Fig. 1.13: Ratios of gluon distribution functions from different models at $Q^2 = 5$ GeV^2; HKM refers to the results from Ref. [29], Sarcevic, Ref. [107], EKS98, Refs. [27, 28], Frankfurt, Ref. [103], Armesto, Refs. [89, 106] and new HIJING, Ref. [66]. The bands represent the ranges of $x = (Q/\sqrt{s})e^y$ for processes with $|y| \leq 0.5$, Q^2 = 5 GeV^2 at RHIC ($\sqrt{s} = 200$ GeV) and LHC ($\sqrt{s}$ = 5.5 TeV).

dimension r times the cross section for dipole-nucleus scattering. It is this dipole-nucleus cross section at fixed impact parameter which saturates, i.e. reaches the maximum value allowed by unitarity. Most often this multiple scattering problem is modelled through the Glauber–Gribov approach [89, 103, 106, 107]. The dipole-target cross section is related through a Bessel–Fourier transform to the so-called unintegrated gluon distribution $\varphi_A(x, k_T)$ in k_T-factorization [89, 106, 108], which in turn can be related to the usual collinear gluon density by

$$xG_A(x, Q^2) = \int_{\Lambda^2}^{Q^2} dk_T^2 \, \varphi_A(x, k_T) \,, \tag{1.15}$$

where Λ^2 is some infrared cut-off, if required. This identification is only true for $Q^2 \gg Q^2_{\rm sat}$ [109, 110], where $Q^2_{\rm sat}$ corresponds to the transverse momentum scale at which the saturation of the dipole-target cross section occurs.

Other formulations of multiple scattering do not use the dipole formalism but relate shadowing to diffraction by Gribov theory. See recent applications in [102, 103] and the discussion in Section 4.4.

An explanation equivalent to multiple scattering, in the frame in which the nucleus is moving fast, is gluon recombination due to the overlap of the gluon clouds from different nucleons. This makes the gluon density in a nucleus with mass number A smaller than A times that of a free nucleon [25, 26]. At small x, the interaction develops over longitudinal distances $z \sim 1/(m_N x)$ which become of the order of or larger than the nuclear size, leading to the overlap of gluon clouds from different nucleons located in a transverse area $\sim 1/Q^2$. Much recent work in this field stems from the development of the semiclassical approximations in QCD and the appearance of nonlinear evolution equations in x (see Refs. [111, 112], the contributions by Mueller, Iancu *et al.*, Venugopalan, Kaidalov and Kharzeev in [113], and references therein), although saturation appears to be different from shadowing [109, 110] (i.e. the reduction in the number of gluons as defined in DIS is not apparent). In the semiclassical framework, the gluon field at saturation reaches a maximum value and becomes proportional to the inverse QCD coupling constant,

gluon correlations are absent and the dipole-target cross section has a form which leads to geometrical scaling of the γ^*-target cross section. Such scaling has been found in small x nucleon data [114] and also in analytical and numerical solutions of the nonlinear equations [115–118] but the data indicate that apparently the region where this scaling should be seen in lepton–nucleus collisions has not yet been reached [119]. Apart from proposed eA colliders [90–92], the LHC will be the place to look for nonlinear effects. However, the consequences of such high density configurations may be masked in AB collisions by other effects, such as final-state interactions. Thus pA collisions would be essential for these studies, see Ref. [120]. Moreover, they would be required to fix the baseline for other studies in AB collisions such as the search for and characterization of the QGP. As a final comment, we note that the nonlinear terms in Refs. [25, 26] are of a higher-twist nature. Then, in the low density limit, the DGLAP equations [43] are recovered. However, the nonlinear evolution equations in x [111–113] do not correspond to any definite twist. Their linear limit corresponds to the BFKL equation [121, 122].

We now comment further on the difference between gluon shadowing and saturation. In saturation models, see Refs. [111–113], saturation, defined as either a maximum value of the gluon field or by the scattering becoming black, and gluon shadowing, defined as $xG_A/(xG_N) < 1$, are apparently different phenomena, i.e. saturation does not necessarily lead to gluon shadowing [109, 110]. Indeed, in numerical studies of the nonlinear small x evolution equations, the unintegrated gluon distribution turns out to be a universal function of just one variable $\tau = k_T^2/Q_{\rm sat}^2$ [115–117], vanishing quickly for $k_T^2 > Q_{\rm sat}^2$. (In Ref. [118] this universality is analytically shown to be fulfiled up to k_T^2 much larger than $Q_{\rm sat}^2$). This scaling also arises in the analysis of DIS data on nucleons [114]. It has also been searched for in nuclear data [119]. In nuclei, $Q_{\rm sat}^2$ increases with increasing nuclear size, centrality and energy. Thus, through the relation to the collinear gluon density given in Eq. (1.15), this scaling implies that the integral gives the same value (up to logarithmic corrections if a perturbative tail $\propto 1/k_T^2$ exists for $k_T^2 \gg Q_{\rm sat}^2$), provided that the upper limit of the integration domain $Q^2 \gg Q_{\rm sat}^2$. Thus the ratio $xG_A/(xG_N)$ remains equal to 1 (or approaching 1 as a ratio of logs if the perturbative tail exists) for $Q^2 \gg Q_{\rm sat}^2$. So saturation or nonlinear evolution do not automatically guarantee the existence of gluon shadowing. Since shadowing is described in terms of multiple scattering in many models, this result [109, 110] seems somewhat surprising.

4.3.2. DGLAP evolution models

A different approach is taken in Refs. [27–29, 123]. Parton densities inside the nucleus are parameterized at some scale $Q_0^2 \sim 1 \ldots 5$ GeV^2 and then evolved using the DGLAP [43] equations. Now all nuclear effects on the parton densities are included in the parameterization at Q_0^2, obtained from a fit to experimental data. The differences between the approaches mainly come from the data used to constrain the parton distributions (e.g. including or excluding Drell–Yan data). In these calculations lack of data leaves the gluon badly constrained at very small x. Data on the Q^2-evolution of F_2^A give direct constraints [52] through DGLAP evolution but only for $x \geq 0.01$. See Section 4.1. for more discussion of this framework.

4.3.3. Comparison between different approaches

Model predictions usually depend on additional semi-phenomenological assumptions. Since these assumptions are typically different, the predictions often contradict each other. For example, in Refs. [93–97] it is argued that large size $q\bar{q}$ configurations give the dominant contribution to the absorption, which does not correspond to any definite twist but to an admixture of all twists, resulting in essentially Q^2-independent shadowing. On the other hand, in the gluon recombination approach [25, 26] the absorption is clearly a higher-twist effect dying out at large Q^2. Finally, in the DGLAP-based models [27–29, 123], all Q^2-dependence comes from QCD evolution and is thus of a logarithmic, leading-twist nature. Thus these approaches all lead to very different predictions at small x, particularly for the gluon density.

We now compare available numerical results from different approaches. Recall that in dipole approaches such as that of Ref. [89], there are difficulties in identifying the unintegrated gluon distribution with the ordinary gluon density at small and moderate Q^2, see the discussion of Eq. (1.15). A comparison at Q^2 = 5 GeV^2 for the Pb/p gluon ratio can be found in Fig. 1.13. In the RHIC region, $x \simeq 10^{-2}$, the results from Refs. [27–29, 89, 107] roughly coincide but lie above those from Refs. [66, 103]. At $x \simeq 10^{-4} \ldots 10^{-5}$ (accessible at the LHC) the results of Ref. [89] are smaller than those of Refs. [27–29, 107], approaching those of Ref. [103] but remaining larger than those of Ref. [66]. Apart from the loose small x gluon constraints from DIS data on nuclei, in Refs. [27–29] saturation is imposed on the initial conditions for DGLAP evolution, while Refs. [89, 103, 107] are multiple scattering models. In Ref. [66], the Q^2-independent gluon density is tuned at $x \sim 10^{-2}$ to reproduce charged particle multiplicities in AuAu collisions at RHIC. The strongest gluon shadowing is thus obtained. However, it seems to be in disagreement with existing DIS data [52]. Additional caution has to be taken when comparing results from multiple scattering models with those from DGLAP analysis [27–29]. The gluon ratios at some moderate, fixed Q^2 and very small x may become smaller (e.g. in Ref. [89]) than the F_2 ratios at the same x and Q^2, which might lead to problems with leading-twist DGLAP evolution [52].

4.4. Predictions for the Leading-twist Shadowing at the LHC

L. Frankfurt, V. Guzey, M. McDermott and M. Strikman

The basis of our present understanding of nuclear shadowing in high-energy scattering on nuclei was formulated in the seminal work by V. Gribov [124]. The key observation was that, within the approximation that the range of the strong interactions is much smaller than the average inter-nucleon distances in nuclei, there is a direct relationship between nuclear shadowing in the total hadron–nucleus cross section and the cross section for diffractive hadron–nucleon scattering. While the original derivation was presented for hadron–deuterium scattering, it can be straightforwardly generalized to lepton–nucleus DIS.

Reference [125] demonstrated how to use the Collins factorization theorem for hard diffraction in DIS [126] to generalize Gribov theory to calculate the leading-twist component of nuclear shadowing *separately* for each nuclear parton distribution. The correspondence between the two phenomena is illustrated in Fig. 1.14.

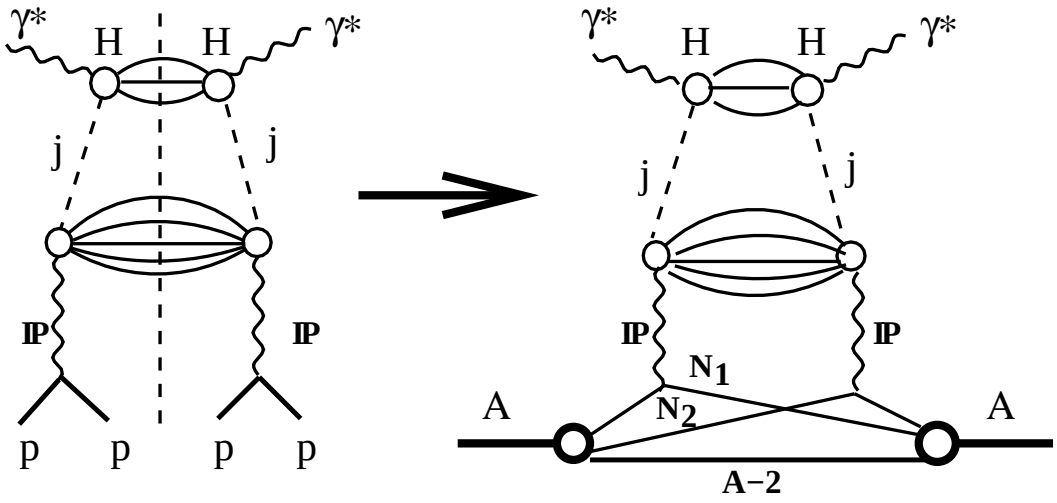

Fig. 1.14: Diagrams for hard diffraction in ep scattering and for the leading-twist nuclear shadowing

As a result, the double scattering term of the shadowing correction to the nuclear parton distributions, $\delta f_{j/A}^{(2)}(x,Q^2)$, takes the form

$$\delta f_{j/A}^{(2)}(x,Q^2) = \frac{A(A-1)}{2} 16\pi\,\mathrm{Re}\left[\frac{(1-i\eta)^2}{1+\eta^2}\int d^2b \int_{-\infty}^{\infty} dz_1 \int_{z_1}^{\infty} dz_2 \int_x^{x_{I\!P,0}} dx_{I\!P} \times \right.$$

$$\left. f_{j/N}^D(\beta,Q^2,x_{I\!P},0)\;\rho_A(b,z_1)\;\rho_A(b,z_2)\;e^{ix_{I\!P}m_N(z_1-z_2)}\right]. \qquad (1.16)$$

Here j is a generic parton label (i.e. a gluon or a quark of a particular flavour), $f_{j/N}^D$ is the diffractive parton distribution function (DPDF) of the nucleon for parton j, $\rho_A(b,z)$ is the nucleon density normalized to unity, η is the ratio of the real to imaginary parts of the nucleon diffractive amplitude, while $x_{I\!P,0}$ = 0.1 for quarks and $x_{I\!P,0}$ = 0.3 for gluons. Since $f_{j/N}^D$ obeys the leading-twist DGLAP evolution equation, the Q^2-evolution of $\delta f_{j/A}^{(2)}$ is also governed by DGLAP, i.e. it is *by definition* a leading-twist contribution. This explains why the approach of Ref. [125] can be legitimately called a leading-twist approach. However, in this approach, one can also take into account higher-twist effects in diffraction.

The HERA diffractive data are consistent with the dominance of leading-twist diffraction in the process $\gamma^* + p \to M_X + p$ for $Q^2 \geq 4$ GeV^2. These studies have determined NLO quark DPDFs directly and the gluon diffractive DPDF indirectly through scaling violations. More recent studies of charm production and diffractive dijet production in the direct photon kinematics measured the gluon DPDF directly. It was found to be consistent (within a 30% uncertainty primarily determined by the treatment of the NLO contribution to two-jet production) with the inclusive diffraction in DIS. As a result, we were able to determine the strength of interaction in the quark and gluon channels, $\sigma_{\rm eff}^j$. This strength turns out to be large at $Q_0^2 \sim 4$ GeV^2, where one can set up the boundary condition[2] for the subsequent QCD evolution. The interaction strength is typically of the order of 20 mb for the quark channel and 30–40 mb for the gluon channel at $Q^2 \sim 4$ GeV^2, $x \leq 10^{-3}$. Consequently, it is necessary to include the interactions with $N \geq 3$ nucleons in the calculations. These interactions were modelled using the quasi-eikonal approximation. Corrections due to fluctuations in the cross section were also analysed and found to be rather small for reasonable models of these effects [127]. Therefore, the master equation for the evaluation of nuclear shadowing takes the following form

$$\delta f_{j/A}(x,Q^2) = \frac{A(A-1)}{2} 16\pi\,\mathrm{Re}\left[\frac{(1-i\eta)^2}{1+\eta^2}\int d^2b \int_{-\infty}^{\infty} dz_1 \int_{z_1}^{\infty} dz_2 \int_x^{x_{I\!P,0}} dx_{I\!P} \times \right.$$

$$\left. f_{j/N}^D(\beta,Q^2,x_{I\!P},0)\;\rho_A(b,z_1)\;\rho_A(b,z_2)\;e^{ix_{I\!P}m_N(z_1-z_2)} e^{-(A/2)(1-i\eta)\sigma_{\rm eff}^j \int_{z_1}^{z_2} dz \rho_A(b,z)}\right]. \qquad (1.17)$$

It is important to note that Eq. (1.17) defines the input nuclear PDFs at the initial, low scale $Q = Q_0$ = 2 GeV for subsequent QCD evolution to higher scales Q^2. In order to have consistent results after evolution, Eq. (1.17), applicable for $10^{-5} \leq x \leq 0.05$, should be supplemented by a model of nuclear PDFs for larger x, $x > 0.05$. In our analysis, this is done by assuming no enhancement for quarks and some enhancement (antishadowing) for gluons (see Fig. 1.15).

We have recently performed a detailed analysis of nuclear shadowing within the leading-twist approach using the current HERA diffractive data [103]. We have analysed the uncertainties originating from the input diffractive parton distribution functions, related to the uncertainties in the data, and found that they are less than $\leq$ 20–30% for $x \leq 10^{-3}$. The biggest uncertainty in the gluon channel originates from the t-dependence of the gluon DPDF, not directly measured. An example of our calculations [128] is presented in Fig. 1.15.

[2]For $Q^2 \leq 4$ GeV^2, higher-twist effects in ep diffraction appear to be significant. This leads to 30–50% contributions of higher-twist effects in nuclear shadowing at $Q^2 \sim$ 1–2 GeV^2, which may make the use of the small-x NMC data for the extraction of nuclear PDFs problematic.

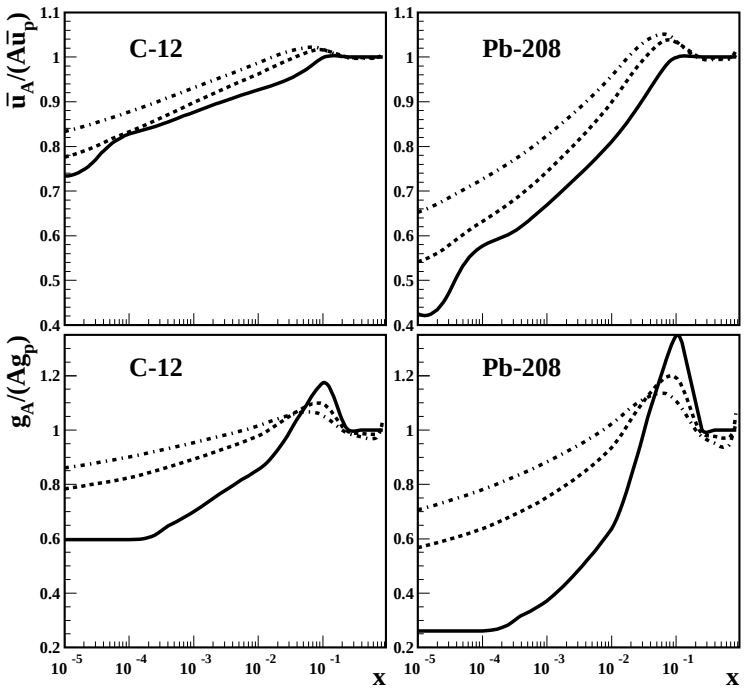

Fig. 1.15: Predictions of quark and gluon shadowing for Q = 2 GeV (solid curves), Q = 10 GeV (dashed curves) and Q = 100 GeV (dot-dashed curves)

We also calculated the higher-twist shadowing, which we estimated in the eikonal approximation, and demonstrated that the leading-twist contribution dominates down to very small x at $Q^2 \geq 4$ GeV^2. (Numerical results are available from V. Guzey upon request.) Also, we found large differences between the LO and NLO calculations of the nuclear structure function F_2^A.

One can see from Fig. 1.15 that the leading-twist shadowing effects are expected to be large for small x for both the quark and gluon channels at $Q \sim$ few GeV. These effects are expected to survive up to scales characteristic of Z and W production.

Our formalism can be readily applied to evaluate nuclear shadowing in nPDFs at all impact parameters. The nuclear shadowing correction to the impact-parameter-dependent nPDFs, $\delta f_{j/A}(x, Q^2, b)$, can be found from Eq. (1.17) by simply differentiating with respect to the impact parameter b [103]. The effect of nuclear shadowing increases with decreasing impact parameter. This is illustrated in Fig. 1.16, where we plot the ratios $f_{j/A}(x, Q^2, b)/(AT_A(b) f_{j/N}(x, Q^2))$, where $T_A(b) = \int dz \rho_A(b, z)$, for quarks and gluons at b = 0 (solid curves) and b = 6 fm (dashed curves). For comparison, the impact-parameter-averaged ratios $f_{j/A}(x, Q^2)/(A f_{j/N}(x, Q^2))$ are given by the dot-dashed curves. Figure 1.16 demonstrates that nuclear shadowing significantly depends on the impact parameter b. Hence, comparing peripheral and central pA collisions will provide an additional measure of the nuclear shadowing.

It is worth emphasizing that the diagrams corresponding to leading-twist shadowing are usually neglected in the BFKL-type approaches to nuclear scattering. For example, these diagrams are neglected in the model of Balitsky [129] and Kovchegov [130]. Note also that higher-twist effects become important at sufficiently small x and $Q \leq Q_{\min}(x)$. Rough estimates indicate that, in the gluon sector with $A \sim 200$, $Q_{\min}(10^{-3}) \sim$ 2–5 GeV, depending on how the NLO effects are handled. Also, $Q_{\min}(x)$ should increase with decreasing x.

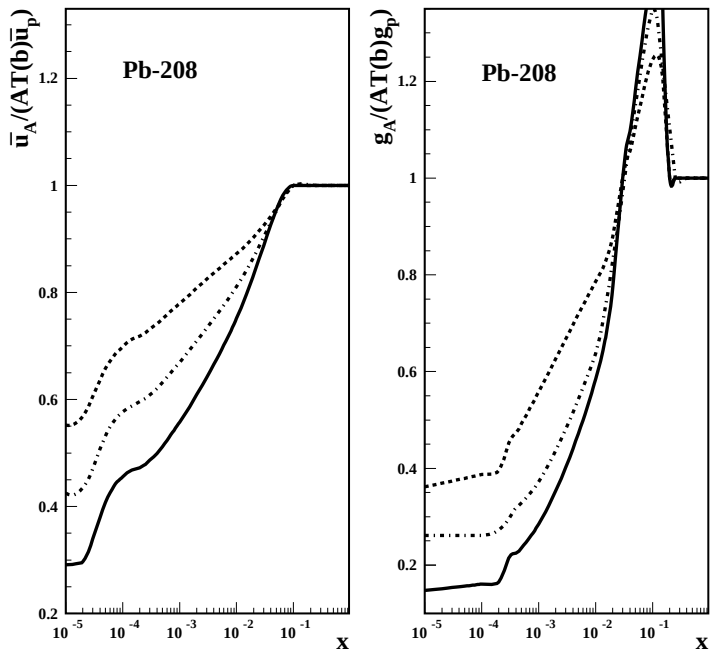

Fig. 1.16: Predictions of quark and gluon shadowing as a function of the impact parameter: b = 0 (solid curves); b = 6 rm (dashed curves); b-averaged ratios (dot-dashed curves). For all curves, Q = 2 GeV.

In conclusion, leading-twist shadowing effects are expected to lead to significant modifications of the hard process cross sections at the LHC in pA and AA collisions. Further progress in the diffraction studies at HERA will significantly reduce the uncertainties in the predictions.

4.5. Structure Functions are not Parton Distributions

S.J. Brodsky

Ever since the earliest days of the parton model, it has been assumed that the leading-twist structure functions $F_i(x, Q^2)$ measured in deep inelastic lepton scattering are determined by the *probability* distributions of quarks and gluons as determined by the light-cone (LC) wavefunctions of the target. For example, the quark distribution is

$$P_{q/N}(x_B, Q^2) = \sum_n \int^{k_{iT}^2 < Q^2} \left[\prod_i dx_i\, d^2k_{Ti}\right] |\psi_n(x_i, k_{Ti})|^2 \sum_{j=q} \delta(x_B - x_j)\,.$$

The identification of structure functions with the square of light-cone wavefunctions is usually made in the LC gauge, $n\cdot A = A^+ = 0$, where the path-ordered exponential in the operator product for the forward virtual Compton amplitude apparently reduces to unity. Thus the deep inelastic lepton scattering cross section (DIS) appears to be fully determined by the probability distribution of partons in the target. However, Paul Hoyer, Nils Marchal, Stephane Peigne, Francesco Sannino, and I have recently shown that the leading-twist contribution to DIS is affected by diffractive rescattering of a quark in the target, a coherent effect which is not included in the light-cone wavefunctions, even in light-cone gauge [131–133]. The distinction between structure functions and parton probabilities is already implied by the Glauber–Gribov picture of nuclear shadowing [134–137]. In this framework shadowing arises from interference between

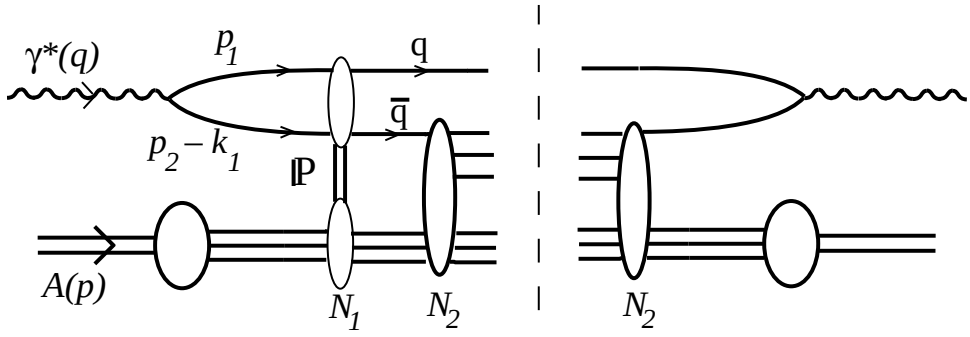

Fig. 1.17: Glauber–Gribov shadowing involves interference between rescattering amplitudes

complex rescattering amplitudes involving on-shell intermediate states, as in Fig.1.17. In contrast, the wavefunction of a stable target is strictly real since it does not have on energy-shell configurations. A probabilistic interpretation of the DIS cross section is thus precluded.

It is well-known that in the Feynman and other covariant gauges one has to evaluate the corrections to the 'handbag' diagram due to the final-state interactions of the struck quark (the line carrying momentum p_1 in Fig. 1.18) with the gauge field of the target. In light-cone gauge, this effect also involves rescattering of a spectator quark, the p_2 line in Fig. 1.18. The light-cone gauge is singular – in particular, the gluon propagator $d^{\mu\nu}_{LC}(k) = \frac{i}{k^2+i\varepsilon}\left[-g^{\mu\nu} + \frac{n^\mu k^\nu + k^\mu n^\nu}{n\cdot k}\right]$ has a pole at $k^+ = 0$ which requires an analytic prescription. In final-state scattering involving on-shell intermediate states, the exchanged momentum k^+ is of O($1/\nu$) in the target rest frame, which enhances the second term in the propagator. This enhancement allows rescattering to contribute at leading twist even in LC gauge.

The issues involving final-state interactions even occur in the simple framework of abelian gauge theory with scalar quarks. Consider a frame with $q^+ < 0$. We can then distinguish FSI from ISI using LC time-ordered perturbation theory, LCPTH [138]. Figure 1.18 illustrates two LCPTH diagrams which contribute to the forward $\gamma^* T \to \gamma^* T$ amplitude, where the target T is taken to be a single quark. In the aligned jet kinematics the virtual photon fluctuates into a $q\bar{q}$ pair with limited transverse momentum, and the (struck) quark takes nearly all the longitudinal momentum of the photon. The initial q and $\bar{q}$ momenta are denoted p_1 and $p_2 - k_1$, respectively.

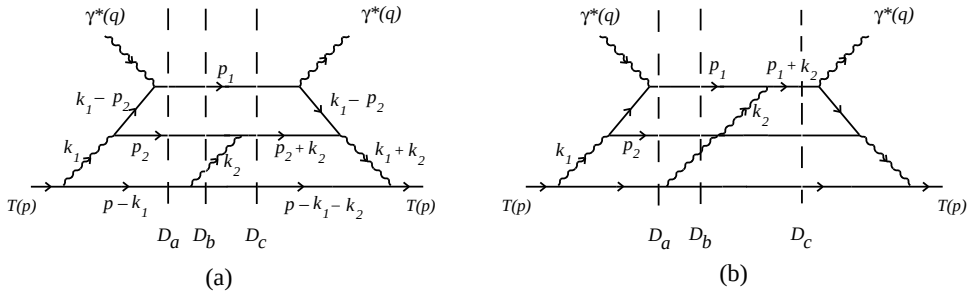

Fig. 1.18: Two types of final state interactions. (a) Scattering of the antiquark (p_2 line), which in the aligned jet kinematics is part of the target dynamics. (b) Scattering of the current quark (p_1 line). For each LC time-ordered diagram, the potentially on-shell intermediate states – corresponding to the zeros of the denominators D_a, D_b, D_c – are denoted by dashed lines.

The calculation of the rescattering effects on DIS in Feynman and light-cone gauge through three loops is given in detail in Ref. [131]. The result can be resummed and is most easily expressed in eikonal form in terms of transverse distances $r_\perp, R_\perp$ conjugate to $p_{2\perp}, k_\perp$. The DIS cross section can be

expressed as

$$Q^4 \frac{d\sigma}{dQ^2\, dx_B} = \frac{\alpha_{\rm em}}{16\pi^2} \frac{1-y}{y^2} \frac{1}{2M\nu} \int \frac{dp_2^-}{p_2^-}\, d^2\vec{r}_\perp\, d^2\vec{R}_\perp\, |\tilde{M}|^2\,, \tag{1.18}$$

where

$$|\tilde{M}(p_2^-, \vec{r}_\perp, \vec{R}_\perp)| = \left| \frac{\sin\left[g^2\, W(\vec{r}_\perp, \vec{R}_\perp)/2\right]}{g^2\, W(\vec{r}_\perp, \vec{R}_\perp)/2} \tilde{A}(p_2^-, \vec{r}_\perp, \vec{R}_\perp) \right| \tag{1.19}$$

is the resummed result. The Born amplitude is

$$\tilde{A}(p_2^-, \vec{r}_\perp, \vec{R}_\perp) = 2eg^2 MQ p_2^-\, V(m_{||} r_\perp) W(\vec{r}_\perp, \vec{R}_\perp)\,, \tag{1.20}$$

where $m_{||}^2 = p_2^- M x_B + m^2$ and

$$V(m\, r_\perp) \equiv \int \frac{d^2\vec{p}_\perp}{(2\pi)^2} \frac{e^{i\vec{r}_\perp \cdot \vec{p}_\perp}}{p_\perp^2 + m^2} = \frac{1}{2\pi} K_0(m\, r_\perp)\,. \tag{1.21}$$

The rescattering effect of the dipole of the $\mathrm{q\bar{q}}$ is controlled by

$$W(\vec{r}_\perp, \vec{R}_\perp) \equiv \int \frac{d^2\vec{k}_\perp}{(2\pi)^2} \frac{1 - e^{i\vec{r}_\perp \cdot \vec{k}_\perp}}{k_\perp^2} e^{i\vec{R}_\perp \cdot \vec{k}_\perp} = \frac{1}{2\pi} \log\left(\frac{|\vec{R}_\perp + \vec{r}_\perp|}{R_\perp} \right). \tag{1.22}$$

The fact that the coefficient of $\tilde{A}$ in Eq. 1.19 is less than unity for all $\vec{r}_\perp, \vec{R}_\perp$ shows that the rescattering corrections reduce the cross section. It is the analogue of nuclear shadowing in our model.

We have also found the same result for the DIS cross sections in light-cone gauge. Three prescriptions for defining the propagator pole at $k^+ = 0$ have been used in the literature:

$$\frac{1}{k_i^+} \to \left[\frac{1}{k_i^+}\right]_{\eta_i} = \begin{cases} k_i^+ \left[(k_i^+ - i\eta_i)(k_i^+ + i\eta_i)\right]^{-1} & \text{(PV)} \\ \left[k_i^+ - i\eta_i\right]^{-1} & \text{(K)} \\ \left[k_i^+ - i\eta_i \epsilon(k_i^-)\right]^{-1} & \text{(ML)} \end{cases} \tag{1.23}$$

the principal-value (PV), Kovchegov (K) [139], and Mandelstam–Leibbrandt (ML) [140] prescriptions. The 'sign function' is denoted $\epsilon(x) = \Theta(x) - \Theta(-x)$. With the PV prescription we have $I_\eta = \int dk_2^+ \left[k_2^+\right]_{\eta_2}^{-1} = 0$. Since an individual diagram may contain pole terms $\sim 1/k_i^+$, its value can depend on the prescription used for light-cone gauge. However, the $k_i^+ = 0$ poles cancel when all diagrams are added. The net is thus prescription-independent and agrees with the Feynman gauge result. It is interesting to note that the diagrams involving rescattering of the struck quark p_1 do not contribute to the leading-twist structure functions if we use the Kovchegov prescription to define the light-cone gauge. In other prescriptions for light-cone gauge the rescattering of the struck quark line p_1 leads to an infrared divergent phase factor $\exp(i\phi)$, where

$$\phi = g^2\, \frac{I_\eta - 1}{4\pi}\, K_0(\lambda R_\perp) + O(g^6)\,, \tag{1.24}$$

where λ is an infrared regulator, and $I_\eta = 1$ in the K prescription. The phase is exactly compensated by an equal and opposite phase from FSI of line p_2. This irrelevant change of phase can be understood by the fact that the different prescriptions are related by a residual gauge transformation proportional to $\delta(k^+)$ which leaves the light-cone gauge $A^+ = 0$ condition unaffected.

Diffractive contributions which leave the target intact thus contribute at leading twist to deep inelastic scattering. These contributions do not resolve the quark structure of the target, and thus they are contributions to structure functions which are not parton probabilities. More generally, the rescattering contributions shadow and modify the observed inelastic contributions to DIS.

Our analysis in the K prescription for light-cone gauge resembles the 'covariant parton model' of Landshoff, Polkinghorne and Short [141,142] when interpreted in the target rest frame. In this description of small x DIS, the virtual photon with positive q^+ first splits into the pair p_1 and p_2. The aligned quark p_1 has no final state interactions. However, the antiquark line p_2 can interact in the target with an effective energy $\hat{s} \propto k_\perp^2/x$ while staying close to mass shell. Thus at small x and large $\hat{s}$, the antiquark p_2 line can first multiply scatter in the target via pomeron and Reggeon exchange, and then it can finally scatter inelastically or be annihilated. The DIS cross section can thus be written as an integral of the $\sigma_{\bar{q}p\to X}$ cross section over the p_2 virtuality. In this way, the shadowing of the antiquark in the nucleus $\sigma_{\bar{q}A\to X}$ cross section yields the nuclear shadowing of DIS [136]. Our analysis, when interpreted in frames with $q^+ > 0$, also supports the colour dipole description of deep inelastic lepton scattering at small x. Even in the case of the aligned jet configurations, one can understand DIS as due to the coherent colour gauge interactions of the incoming quark-pair state of the photon interacting first coherently and finally incoherently in the target. For further discussion see Refs. [132, 143, 144]. The same final-state interactions that produce leading-twist diffraction and shadowing in DIS also lead to Bjorken-scaling single-spin asymmetries in semi-inclusive deep inelastic, see Refs. [145–147].

The analysis presented here has important implications for the interpretation of the nuclear structure functions measured in deep inelastic lepton scattering. Since leading-twist nuclear shadowing is due to the destructive interference of diffractive processes arising from final-state interactions (in the $q^+ \leq 0$ frame), the physics of shadowing is not contained in the wavefunctions of the target alone. For example, the light-front wavefunctions of stable states computed in light-cone gauge (PV prescription) are real, and they only sum the interactions within the bound-state which occur up to the light-front time $\tau = 0$ when the current interacts. Thus the shadowing of nuclear structure functions is due to the mutual interactions of the virtual photon and the target nucleon, not the nucleus in isolation [131].

4.6. Nuclear Parton Distribution Functions in the Saturation Regime

Yu.V. Kovchegov

4.6.1. Introduction

At the high collision energies reached at the LHC, parton densities in the nuclear wavefunctions will become very large, resulting in the onset of parton recombination and *saturation* of parton distribution functions [23, 25, 26]. In the saturation regime, the growth of partonic structure functions with energy is expected to slow down sufficiently to unitarize the total nuclear cross sections. Gluonic fields in the saturated nuclear wavefunction would become very strong, reaching the maximum possible magnitude in QCD of $A_\mu \sim 1/g$ [139, 148, 149]. The transition to the saturation region can be characterized by the *saturation scale* $Q_s^2(s, A)$, which is related to the typical two dimensional density of the parton colour charge in the infinite momentum frame of the hadronic or nuclear wavefunctions [23, 139, 148, 149]. The saturation scale is an increasing function of energy $\sqrt{s}$ and of the atomic number A [116, 118, 130, 150–154]. It is expected that it (roughly) scales as

$$Q_s^2(s, A) \sim A^\alpha s^\delta , \tag{1.25}$$

where $\delta \approx 0.2$–0.3 based on HERA data [88, 155] and $\alpha \geq 1/3$ [116, 118, 152–154]. Various estimates predict the saturation scale for lead nuclei at 14 TeV to be $Q_s^2 \approx 10$–20 GeV^2. This high value of the saturation scale would ensure that the strong coupling constant $\alpha_s(Q_s^2)$ is small, making the vast majority of partons in the nuclear wave functions at the LHC *perturbative* [109, 110, 149, 156, 157]! The presence of an intrinsic large momentum scale Q_s justifies the use of a perturbative QCD expansion even for such traditionally nonperturbative observables as total hadronic cross sections [23, 150].

Below we first discuss the predictions for gluon and quark distribution functions of a large nucleus, given by the quasi-classical model of McLerran and Venugopalan [23, 109, 139, 148, 150]. We then

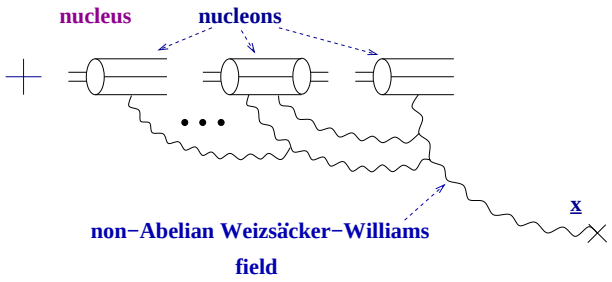

Fig. 1.19: The non-Abelian Weizs¨acker–Williams fi eld of a nucleus

discuss how quantum corrections should be included to obtain an equation for the realistic F_2 structure function of the nucleus [129, 130, 151, 158, 159]. We will conclude by deriving the gluon production cross section for pA scattering in the quasi-classical approximation [109] and generalizing it to include quantum corrections [160].

4.6.2. Structure functions in the quasi-classical approximation

The gluon distribution

As suggested originally by McLerran and Venugopalan [23], the gluon field of a large ultrarelativistic nucleus is classical and is given by the solution of the Yang–Mills equations of motion with the nucleus providing the source current. The classical solution in the light cone gauge of the nucleus, known as the non-Abelian Weizsäcker–Williams field (WW), has been found in Refs. [139, 148, 149]. It includes the effects of all multiple rescatterings of the small-x gluon on the nucleons in the nucleus located at the same impact parameter as the gluon. This resummation parametrically corresponds to resumming powers of Q_s^2/q^2 (higher twists), where q is the gluon transverse momentum. Diagrammatically, the field is shown in Fig. 1.19. The correlator of two WW fields gives rise to the unintegrated nuclear gluon distribution given by [109, 149]

$$\begin{aligned}\frac{dxG_A(x,\underline{q}^2)}{d\underline{q}^2} &= \frac{2}{(2\pi)^2}\int d^2\underline{z}\, e^{-i\underline{z}\cdot\underline{q}}\int d^2\underline{b}\,\mathrm{Tr}\,\langle \underline{A}^{WW}(\underline{0})\,\underline{A}^{WW}(\underline{z})\rangle \\ &= \frac{2}{\pi(2\pi)^2}\int d^2\underline{z}\, e^{-i\underline{z}\cdot\underline{q}}\,\frac{S_\perp C_F}{\alpha_s\,\underline{z}^2}\left(1-e^{-\frac{1}{4}\underline{z}^2Q_s^2}\right), \end{aligned} \tag{1.26}$$

where $\underline{b}$ is the gluon impact parameter and

$$Q_s^2(\underline{z}) \;=\; \frac{4\pi^2\,\alpha_s N_c}{N_c^2-1}\,\rho\, xG_N(x,1/\underline{z}^2)\,T_A(\underline{b}) \tag{1.27}$$

is the saturation scale with atomic number density $\rho = A/[(4/3)\pi R_A^3]$ and $T_A(\underline{b}) = 2\sqrt{R_A^2-b^2}$ for spherical nuclei A considered here. The gluon distribution in a single nucleon, $xG_N(x,Q^2)$, is assumed to be a slowly varying function of Q^2. In the two-gluon exchange approximation [109] $xG_N(x,Q^2) = (\alpha_s C_F)/\pi\,\ln Q^2/\Lambda^2$.

The gluon distribution function of Eq. (1.26) falls off perturbatively as $xG_A \sim Q_s^2/\underline{q}^2$ for large transverse momenta q, but is much less singular in the infrared region, scaling as $xG_A \sim \ln Q_s/q$ for small q [149]. We conclude that multiple rescattering softens the infrared singular behaviour of the traditional perturbative distribution. Note also that the number of gluons given by Eq. (1.26) is of the order of $1/\alpha_s$, corresponding to strong gluonic fields of the order of $A_\mu \sim 1/g$.

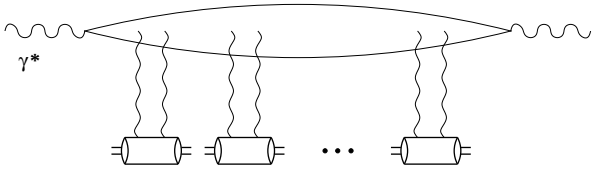

Fig. 1.20: DIS on a nucleus in the quasi-classical approximation

The quark distribution

To calculate the quark distribution function in the quasi-classical approximation, one has to consider deep inelastic scattering in the rest frame of the nucleus including all multiple rescatterings, as shown in Fig. 1.20. The F_2 structure function (and the quark distribution) was first calculated by Mueller [150] in this approximation, yielding

$$F_2(x,Q^2) = \sum_q e_q^2 [x q(x,Q^2) + x\overline{q}(x,Q^2)] = \frac{Q^2}{4\pi^2 \alpha_{\rm em}} \sum_q e_q^2 \int \frac{d^2 r dz}{2\pi}\, \Phi^{\gamma^* \to q\bar{q}}(\underline{r},z)\; d^2b\, N(\underline{r},\underline{b},Y)\,, \tag{1.28}$$

where $\Phi^{\gamma^* \to q\bar{q}}(\underline{r},z)$ is the wavefunction of a virtual photon in DIS, splitting into a $q\bar{q}$ pair with transverse separation $\underline{r}$. The fraction of photon longitudinal momentum carried by the quark is z. The quantity $N(\underline{r},\underline{b},Y)$ is the forward scattering amplitude of a dipole with transverse size $\underline{r}$ at impact parameter $\underline{b}$ with rapidity Y on a target nucleus. In the quasi-classical approximation of Refs. [23, 150], $N(\underline{r},\underline{b},\ Y = 0)$ is given by

$$N(\underline{r},\underline{b},Y=0) \;=\; 1 - e^{-r^2 Q^2_{s,\rm quark}/4}\,, \tag{1.29}$$

where $Q^2_{s,\rm quark}$ is the quark saturation scale which can be obtained from the gluon saturation scale in Eq. (1.27) by replacing N_c by C_F in the numerator [150, 160].

4.6.3. Inclusion of quantum corrections

At high energy, the quasi-classical approximation previously considered ceases to be valid. The energy dependence of the cross sections comes in through the quantum corrections which resum logarithms of energy [122, 161–165]. The evolution equation for N, resumming logarithms of energy, closes only in the large-N_c limit of QCD and reads [104, 129, 130, 151, 158, 159, 166–168]

$$N(\underline{x}_{01},\underline{b},Y) = N(\underline{x}_{01},\underline{b},0)\, e^{-\frac{4\alpha C_F}{\pi}\ln\left(\frac{x_{01}}{\rho}\right)Y} + \frac{\alpha C_F}{\pi^2}\int_0^Y dy\, e^{-\frac{4\alpha C_F}{\pi}\ln\left(\frac{x_{01}}{\rho}\right)(Y-y)}$$

$$\times \int_\rho d^2x_2 \frac{x_{01}^2}{x_{02}^2 x_{12}^2}\left[2\,N(\underline{x}_{02},\underline{b}+\frac{1}{2}\underline{x}_{12},y) - N(\underline{x}_{02},\underline{b}+\frac{1}{2}\underline{x}_{12},y)\,N(\underline{x}_{12},\underline{b}+\frac{1}{2}\underline{x}_{02},y)\right], \tag{1.30}$$

with initial condition in Eq. (1.29) and $\underline{x}_{ij} = \underline{x}_i - \underline{x}_j$. In the usual Feynman diagram formalism, it resums multiple pomeron exchanges (fan diagrams). Together with Eq. (1.28), it provides the quark distribution function in a nucleus at high energies. The equation has been solved both by approximate analytical methods and numerically in Refs. [116, 118, 152–154], providing unitarization of the total DIS cross section and saturation of the quark distribution functions in the nucleus.

Using Eq. (1.30) together with Eq. (1.26), one may conjecture the following expression for the unintegrated gluon distribution function including quantum corrections [160]

$$\frac{dxG_A(x,\underline{q}^2)}{d\underline{q}^2} \;=\; \frac{2}{\pi(2\pi)^2}\int d^2b\, d^2\underline{z}\, e^{-i\underline{z}\cdot\underline{q}}\,\frac{C_F}{\alpha_s\,\underline{z}^2}\,N_G(\underline{z},\underline{b},Y=\ln 1/x)\,, \tag{1.31}$$

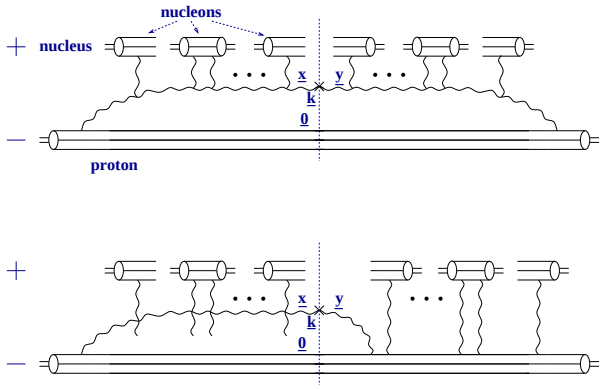

Fig. 1.21: Gluon production in pA collisions in the quasi-classical approximation.

with N_G the forward amplitude of a gluon dipole scattering on the nucleus which, in the large-N_c limit, is $N_G = 2N - N^2$ [160], where N is the forward amplitude of the $q\bar{q}$ dipole scattering on the nucleus used in Eq. (1.30). Equation (1.31) must still be proven.

4.6.4. Gluon production in pA collisions

The pA programme at the LHC will test the above predictions for parton distribution functions by measuring particle production cross sections which depend on these quantities. Below we discuss gluon production in pA.

Quasi-classical result

Gluon production in pA interactions has been calculated in the quasi-classical approximation in Ref. [109]. The relevant diagrams in the light cone gauge of the proton are shown in Fig. 8.8.. The cross section is [109]

$$\frac{d\sigma^{pA}}{d^2k\,dy} = \int d^2b\,d^2x\,d^2y\,\frac{\alpha_s C_F}{\pi^2\,(2\pi)^2}\,\frac{\underline{x}\cdot\underline{y}}{\underline{x}^2\underline{y}^2}\,e^{i\underline{k}\cdot(\underline{x}-\underline{y})}\,\left(1 - e^{-\underline{x}^2\,Q_s^2/4} - e^{-\underline{y}^2\,Q_s^2/4} + e^{-(\underline{x}-\underline{y})^2\,Q_s^2/4}\right). \tag{1.32}$$

Gluon production including quantum corrections

To include quantum corrections in Eq. (1.32), it must be rewritten in the factorized form [160] and generalized to include the linear evolution of the proton structure function and nonlinear evolution of the nuclear structure function. The result, see also Ref. [160], is

$$\frac{d\sigma^{pA}}{d^2k\,dy} = \frac{C_F}{\alpha_s\pi(2\pi)^3}\int d^2z\,n_G(\underline{z}, Y-y)\,\frac{\overleftarrow{\nabla}_z^2\;e^{i\underline{k}\cdot\underline{z}}\;\overrightarrow{\nabla}_z^2}{\underline{k}^2}\,N_G(\underline{z}, y)\,, \tag{1.33}$$

where Y is the total rapidity interval between the proton and the nucleus, $N_G(\underline{z}, y) = \int d^2b\,N_G(\underline{z}, \underline{b}, y)$ and $\overrightarrow{\nabla}_z^2$ is the transverse gradient squared. The function $n_G(\underline{z}, Y-y)$ in Eq. (1.33) is the solution of the linear part of Eq. (1.30) (BFKL) integrated over all b with the two-gluon exchange amplitude between the proton and a gluon dipole as initial conditions. In the no-evolution limit, Eq. (1.33) reduces to Eq. (1.32). Equation (1.33) gives the saturation physics prediction for particle production at midrapidity in pA collisions at the LHC.

5. THE BENCHMARK TESTS IN pA

5.1. W, Z, and Drell–Yan Cross Sections

R. Vogt

Studies of $W^\pm$ and Z^0 gauge bosons as well as high mass Drell–Yan production in pA interactions at the LHC will provide information on the nuclear parton densities at much higher Q^2 than previously available. The high Q^2 measurements will probe the x range around 0.015 at y = 0. This range of x has been probed before by fixed target nuclear deep-inelastic scattering so that a measurement at the LHC will constrain the evolution of the nuclear quark distributions over a large lever arm in Q^2. Knowledge of the nuclear quark distributions in this region will aid in studies of jet quenching with a Z^0 opposite a jet in AA collisions. At least one of the initial partons will be a quark or antiquark in the reactions $q\overline{q} \to Z^0 g$ and $q(\overline{q})g \to q(\overline{q})Z^0$.

Since the W and Z^0 studies will open a new window in the (x, Q^2) plane for nuclear parton distribution functions, these measurements are obvious benchmarks. The Z^0 measurement probes symmetric $q\overline{q}$ annihilation while measurements such as the W^+–W^- asymmetry via high p_T decay leptons are better probes of the nuclear valence quark distributions. Drell–Yan production at high Q^2 is a somewhat different story because, to be an effective benchmark, the Drell–Yan signal should dominate the dilepton mass spectrum. In AA collisions, the signal dilepton mass distribution is dominated by $b\overline{b}$ decays until $M > M_Z$ [169]. Thus only in this large mass region is Drell–Yan a useful benchmark.

We very briefly outline the next-to-leading order, NLO, calculation here. The NNLO cross sections are available [170] but are only a small addition (a few per cent) compared to the NLO correction. The NLO cross section for production of a vector boson, V, with mass M at scale Q in a pp interaction is

$$\begin{aligned}\frac{d\sigma^V_{pp}}{dy} &= H^V_{ij} \int dx_1\, dx_2\, dx\, \delta\left(\frac{M_V^2}{s} - x x_1 x_2\right)\delta\left(y - \frac{1}{2}\ln\left(\frac{x_1}{x_2}\right)\right) \\ &\times \left\{ \sum_{i,j\in Q,\overline{Q}} C^{\rm ii}(q_i, \overline{q}_j)\Delta_{q\overline{q}}(x,Q^2) f^p_{q_i}(x_1,Q^2) f^p_{\overline{q}_j}(x_2,Q^2) \right. \\ &+ \left. \sum_{i,k\in Q,\overline{Q}} C^{\rm if}(q_i,q_k)\Delta_{qg}(x,Q^2)\left[f^p_{q_i}(x_1,Q^2) f^p_g(x_2,Q^2) + f^p_g(x_1,Q^2) f^p_{q_j}(x_2,Q^2)\right]\right\}, \end{aligned} \tag{1.34}$$

where H^V_{ij} is proportional to the LO partonic cross section, $ij \to V$, and the sum over Q includes u, d, s and c. The matrices $C^{\rm ii}$ and $C^{\rm if}$ contain information on the coupling of the various quark flavours to boson V. The parton densities in the proton, f^p_i, are evaluated at momentum fraction x and scale Q^2. The convolutions of the parton densities, including the proton and neutron (isospin) content of the nucleus, with shadowing parametrizations formulated assuming $f^A_i(x,Q^2) = f^p_i(x,Q^2)R^A_i(x,Q^2)/A$ are given in the appendix of Ref. [171][3]. All the results are calculated with the MRST HO densities [172] at $Q = M_V$ and the EKS98 shadowing parametrization [27, 28]. In the Drell–Yan process, the mass distribution can also be calculated by adding a dM in the denominator of the left-hand side of Eq. (1.34) and the delta function $\delta(M - M_V)$ on the right-hand side. The prefactors H^V_{ij} are rather simple [170],

$$H^{Z^0}_{ij} = \frac{8\pi}{3}\frac{G_F}{\sqrt{2}}\left[(g^i_V)^2 + (g^i_A)^2\right]\frac{M_Z^2}{s}, \qquad H^{W^\pm}_{ij} = \frac{2\pi}{3}\frac{G_F}{\sqrt{2}}\frac{M_W^2}{s}, \tag{1.35}$$

where $G_F = 1.16639 \times 10^{-5}$ GeV^2, $M_Z = 91.187$ GeV, and $M_W = 80.41$ GeV. In the case of the Drell–Yan process, there are three contributions to H^V_{ij}: virtual photon exchange, Z^0 exchange, and

[3] In Ref. [171], $S^i(x,Q^2,A) \equiv R^A_i(x,Q^2)$.

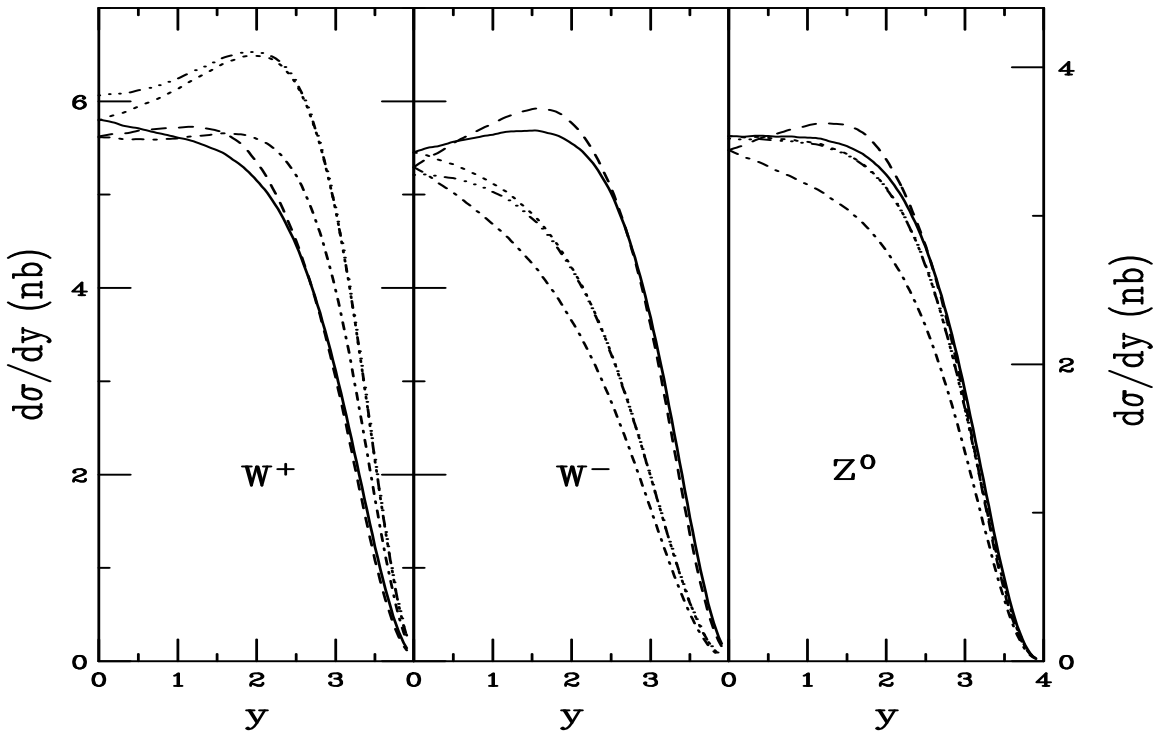

Fig. 1.22: The W^+, W^- and Z^0 rapidity distributions in pp, pPb and Pbp collisions at 5.5 TeV/nucleon evaluated at $Q = M_V$. The solid and dashed curves show the results without and with shadowing respectively in Pbp collisions while the dotted and dot-dashed curves give the results without and with shadowing for pPb collisions. The dot-dot-dot-dashed curve is the pp result.

$\gamma^* - Z^0$ interference so that

$$
\begin{aligned}
H_{ij}^{M} &= H_{ij}^{\gamma^*} + H_{ij}^{\gamma^*-Z^0} + H_{ij}^{Z^0}\,, \qquad (1.36)\\
H_{ij}^{\gamma^*} &= \frac{4\pi\alpha^2}{9M^2 s}|e_i|^2\,,\\
H_{ij}^{\gamma^*-Z^0} &= \frac{\alpha}{9}\frac{G_F}{\sqrt{2}}\frac{M_Z^2}{s}\frac{(1-4\sin^2\theta_W)(M^2-M_Z^2)}{(M^2-M_Z^2)^2+M_Z^2\Gamma_Z^2}|e_i|(1-4|e_i|\sin^2\theta_W)\,,\\
H_{ij}^{Z^0} &= \frac{1}{3}\frac{G_F}{\sqrt{2}}\frac{M^2}{s}\frac{M_Z\Gamma_{Z\to l^+l^-}}{(M^2-M_Z^2)^2+M_Z^2\Gamma_Z^2}(1+(1-4|e_i|\sin^2\theta_W)^2)\,,
\end{aligned}
$$

where $\sin^2\theta_W = 1 - M_W^2/M_Z^2$, Γ_Z = 2.495 GeV, and $\Gamma_{Z\to l^+l^-}$ = 3.367%. The functions $\Delta_{ij}(x,Q^2)$ in Eq. (1.34) are universal for gauge bosons and Drell–Yan production [170]. We work in the $\overline{\rm MS}$ scheme. The NLO correction to the $q\overline{q}$ channel includes contributions from soft and virtual gluons as well as hard gluons from the process $q\overline{q} \to Vg$. The quark–gluon contribution only appears at NLO through the real correction $qg \to qV$. At NLO, $\alpha_s(Q^2)$ is calculated to two loops with $n_f = 5$.

As we show in Fig. 1.22, the isospin of the nucleus is most important for $q\overline{q}$-dominated processes. Gauge boson and Drell–Yan production are the best examples of this domination in hadroproduction. We compare the pPb and Pbp W^+, W^- and Z^0 distributions per nucleon with and without the EKS98 shadowing parametrization to pp production at 5.5 TeV. The pp distributions closely follow the pPb distributions without shadowing except for $y < 2$. Since the W^+ distribution is most sensitive to the $f_u^p(x_1)f_{\overline{d}}^p(x_2)$ contribution, the pp and pPb distributions peak away from y = 0. The Pbp distribution, on the other hand, decreases with increasing y because the neutron content of lead washes out the peak. The opposite effect is seen for W^- production where, in Pbp, the neutrons produce a peak at forward rapidity since $f_d^n = f_u^p$. The Z^0 distribution is almost independent of isospin, as are the high mass

Table 1.5: Gauge boson cross sections per nucleon. No decay channel is specified

Δy	σ_{NS} (nb)	σ_{EKS98} (nb)	σ_{NS} (nb)	σ_{EKS98} (nb)	σ_{NS} (nb)	σ_{EKS98} (nb)
	Z^0		W^+		W^-	
			pp 5.5 TeV			
$0 < y < 2.4$	8.10	–	15.13	–	11.41	–
$0 < y < 1$	3.51	–	6.13	–	5.16	–
$2.4 < y < 4$	2.01	–	5.68	–	2.42	–
			Pbp 5.5 TeV			
$0 < y < 2.4$	8.23	8.37	13.12	13.34	13.37	13.63
$0 < y < 1$	3.53	3.53	5.71	5.67	5.56	5.54
$2.4 < y < 4$	2.14	2.06	3.72	3.62	4.36	4.24
			pPb 5.5 TeV			
$0 < y < 2.4$	8.12	7.39	14.87	13.43	11.62	10.57
$0 < y < 1$	3.52	3.33	5.95	5.60	5.31	5.01
$2.4 < y < 4$	2.01	1.68	5.67	4.69	2.43	2.02
			Pbp 8.8 TeV			
$0 < y < 2.4$	12.37	12.47	19.62	19.71	19.87	20.01
$0 < y < 1$	5.22	5.11	8.37	8.16	8.22	8.02
$2.4 < y < 4$	5.07	5.03	8.30	8.31	9.46	9.47
			pPb 8.8 TeV			
$0 < y < 2.4$	12.26	10.93	21.41	18.96	18.08	16.09
$0 < y < 1$	5.20	4.82	8.60	7.92	7.98	7.35
$2.4 < y < 4$	4.83	3.95	11.80	9.58	5.98	4.87

Drell–Yan distributions. We see antishadowing in Pbp interactions with large nuclear x_1 while we have small nuclear x_2 in the pPb calculations, reducing the y distributions. The W^+ pA distributions are all reduced compared to the pp distributions, the W^- pA results are typically enhanced relative to pp while the Z^0 pA/pp ratios do not change much with y.

The gauge boson cross sections in pp, Pbp, and pPb collisions at 5.5 TeV/nucleon as well as Pbp and pPb collisions at 8.8 TeV/nucleon are given in Table 1.5. The Drell–Yan cross sections in the mass bins $60 < M < 80$ GeV, $80 < M < 100$ GeV, and $100 < M < 120$ GeV are given in Table 1.6 for pp, Pbp, and pPb collisions at 5.5 TeV/nucleon. The cross sections are presented in three rapidity intervals, $0 < y < 2.4$, corresponding to the CMS barrel+endcaps, $0 < y < 1$, the central part of ALICE, and

Table 1.6: Drell–Yan cross sections in the indicated mass intervals at 5.5 TeV/nucleon in pp, Pbp and pPb collisions

Δy	σ (nb)	$\sigma_{\rm NS}$ (nb)	$\sigma_{\rm EKS98}$ (nb)	$\sigma_{\rm NS}$ (nb)	$\sigma_{\rm EKS98}$ (nb)
	pp	Pbp		pPb	
		$60 < M < 80$ GeV			
$0 < y < 2.4$	0.012	0.012	0.012	0.012	0.011
$0 < y < 1$	0.0048	0.0048	0.0047	0.0048	0.0044
$2.4 < y < 4$	0.0038	0.0036	0.0035	0.0038	0.0031
		$80 < M < 100$ GeV			
$0 < y < 2.4$	0.26	0.27	0.27	0.26	0.24
$0 < y < 1$	0.11	0.11	0.11	0.11	0.10
$2.4 < y < 4$	0.055	0.059	0.057	0.055	0.046
		$100 < M < 120$ GeV			
$0 < y < 2.4$	0.0088	0.0088	0.0090	0.0088	0.0080
$0 < y < 1$	0.0037	0.0037	0.0037	0.0037	0.0035
$2.4 < y < 4$	0.0015	0.0015	0.0014	0.0015	0.0012

$2.4 < y < 4$, the ALICE muon arm. The difference in the Pbp and pPb cross sections without shadowing is entirely due to isospin. Thus the pA cross section in $|y| < 2.4$ is not a simple factor of two larger than the $0 < y < 2.4$ cross section since the results are not symmetric around y = 0, as can be seen in Fig. 1.22.

We have checked the dependence of the gauge boson results on scale, parton density, and shadowing parametrization. The scale dependence enters in the PDFs, α_s, and the scale-dependent logarithms $\ln(Q^2/M_V^2)$ [170]. At these high Q^2 values, $M_V/2 < Q < 2M_V$, the change in α_s is $\approx \pm$ 10%, small compared to the variation at lower scales. When $Q^2 = M_V^2$, the scale dependent terms drop out. If $Q^2 > M_V^2$, the logs are positive, enhancing the $\mathcal{O}(\alpha_s)$ component, but if $Q^2 < M_V^2$, the scale-dependent logs change sign, reducing the NLO contribution. Evolution with Q^2 increases the low x density of the sea quarks and gluons while depleting the high x component and generally reducing the valence distributions. Since the x values do not change when Q^2 is varied, the higher scales also tend to enhance the cross sections. The gauge boson cross sections are decreased $\sim$ 30% when Q^2 is decreased and increased by 20% with increased Q^2. The scale change is even smaller for high mass Drell–Yan production, a few per cent in the 60–80 GeV bin and 1% or less for higher masses.

The variation with parton density can be as large as the scale dependence. The MRST and CTEQ [86] rapidity distributions are similar but the CTEQ cross sections are 7% higher. The GRV 98 [45] results are stronger functions of rapidity than the MRST. The total GRV 98 cross sections, however, are about 13% smaller.

We have also compared the pA/pp ratios to the HPC [173] and HKM [29] parametrizations. The HPC parametrization does not distinguish between the sea and valence effects and includes no Q^2 evo-

lution. HKM actually parameterizes the nuclear parton distributions themselves and focuses on the distinction between the up and down nuclear distributions. It is only useful to LO. However, shadowing at LO and NLO is nearly identical [174].

In Pbp collisions, the EKS98 and HKM ratios are similar for $y \leq 1.5$. At higher rapidities, the HKM ratio is larger because its sea distribution increases more with x_1 but its valence shadowing is weaker. The HPC ratio is lower than the EKS98 ratio at $y \sim 0$, ~ 0.8 relative to ~ 0.97. However the two ratios are very similar for $y > 2$. In pPb collisions, x_2 is in the shadowing region and all three ratios decrease with rapidity. Again, near $y \sim 0$, the HKM and EKS98 ratios are similar but the HKM sea quark shadowing is nearly independent of x_2 while the EKS98 ratio drops from 0.97 to 0.8 between y = 0 and 4. The HPC ratio is parallel to but lower than the EKS98 ratio.

Finally, we note that, without keeping the energy fixed, extracting the nuclear quark distributions from pp and pA and applying them to AA is difficult[4] since the isospin is an additional, nonnegligible uncertainty. Therefore, it is desirable to make pp and pPb runs at 5.5 TeV for a more precise correlation with the PbPb data at 5.5 TeV/nucleon. Indeed, for best results, both pPb and Pbp runs should be done since the ALICE muon detector is not symmetric around y = 0. Its large rapidity coverage would extend the nuclear x coverage to much higher (Pbp) and lower (pPb) values since $y \sim 4$ is the maximum rapidity for Z^0 production at 5.5 TeV/nucleon, the upper limit of the muon coverage, where $x_1 \sim 1$ and $x_2 \sim 0.0003$.

Systematic studies with nuclear beams could be very useful for fully mapping out the A dependence of the nuclear parton densities. The LHC Ar beam would link to the NMC Ca data while the LHC O beam could connect back to previous C data [59]. However, these A systematics are best tuned to the AA collision energies, different for O, Ar, and Pb. Comparing pA and pp at the same energies does not shift x while a comparison to pp at 14 TeV rather than 5.5 TeV would shift the x values by a factor of ~ 3 between PbPb and pp. Energy systematics of gauge boson production between RHIC and LHC are more difficult because W and Z^0 production in pA at RHIC is quite close to threshold. However, at RHIC, larger x values can be probed at $y \sim 0$, $x \sim 0.45$, where the cross sections are quite sensitive to the valence distributions. High mass Drell–Yan is likely to be beyond the reach of RHIC.

5.2. Z^0 and W Transverse Momentum Spectra

X.F. Zhang and G. Fai

At LHC energies, perturbative QCD (pQCD) provides a powerful calculational tool. For Z^0 and W transverse momentum spectra, pQCD theory agrees with the CDF [175] and D0 [176] data very well at Tevatron energies [177]. The LHC pp programme will test pQCD at an unprecedented energy. The heavy-ion programme at the LHC will make it possible for the first time to observe the full p_T spectra of heavy vector bosons in nuclear collisions and will provide a testing ground for pQCD resummation theory [178].

In nuclear collisions, power corrections will be enhanced by initial and final state multiple scattering. As we will show, higher-twist effects are small at the LHC for heavy boson production. The only important nuclear effect is the nuclear modification of the PDFs (shadowing). Because of their large masses, the W and Z^0 will tell us about the nPDFs at large scales. Since contributions from different scales need to be resummed, the p_T spectra of heavy vector bosons will provide information about the evolution of nPDFs from small scales to large scales. Since it is more difficult to detect $W^\pm$ than Z^0, we will concentrate on the Z^0 here (the results for $W^\pm$ production are very similar [179]).

Resummation of large logarithms in QCD can be carried out either directly in p_T-space, or in the so-called 'impact parameter', $\tilde{b}$-space, the Fourier conjugate of the p_T-space. Using the renormalization group equation technique, Collins, Soper, and Sterman (CSS) derived a formalism for the transverse

[4]For a discussion of shadowing effects on gauge boson production in PbPb collisions at 5.5 TeV/nucleon and the possible impact parameter dependence of the effect, see Ref. [171].

momentum distribution of vector boson production in hadronic collisions [178]. In the CSS formalism, nonperturbative input is needed for the large $\tilde{b}$ region. The dependence of the pQCD results on the nonperturbative input is not weak if the original extrapolation proposed by CSS is used. Recently, a new extrapolation scheme was introduced, based on solving the renormalization group equation including power corrections [177]. Using the new extrapolation formula, the dependence of the pQCD results on the nonperturbative input was significantly reduced.

For vector boson (V) production in a hadron collision, the CSS resummation formalism yields [178]

$$\frac{d\sigma(h_A + h_B \to V + X)}{dM^2\, dy\, dp_T^2} = \frac{1}{(2\pi)^2} \int d^2\tilde{b}\, e^{i\vec{p}_T\cdot\vec{\tilde{b}}}\, \tilde{W}(\tilde{b}, M, x_A, x_B) + Y(p_T, M, x_A, x_B)\,, \qquad (1.37)$$

where $x_A = e^y\, M/\sqrt{s}$ and $x_B = e^{-y}\, M/\sqrt{s}$, with rapidity y and collision energy $\sqrt{s}$. In Eq. (1.37), the $\tilde{W}$ term dominates the p_T distributions when $p_T \ll M$, and the Y term gives corrections that are negligible for small p_T but become important when $p_T \sim M$.

The function $\tilde{W}(\tilde{b}, M, x_A, x_B)$ can be calculated perturbatively for small $\tilde{b}$, but an extrapolation to the large $\tilde{b}$ region, requiring nonperturbative input, is necessary in order to complete the Fourier transform in Eq. (1.37). In order to improve the situation, a new form was proposed [177] by solving the renormalization equation including power corrections. In the new formalism, $\tilde{W}(\tilde{b}, M, x_A, x_B) = \tilde{W}^{\rm pert}(\tilde{b}, M, x_A, x_B)$, when $\tilde{b} \le \tilde{b}_{\rm max}$, with

$$\tilde{W}^{\rm pert}(\tilde{b}, M, x_A, x_B) = {\rm e}^{S(\tilde{b},M)}\, \tilde{W}(\tilde{b}, c/\tilde{b}, x_A, x_B)\,, \qquad (1.38)$$

where all large logarithms from $\ln(1/\tilde{b}^2)$ to $\ln(M^2)$ have been completely resummed into the exponential factor $S(\tilde{b}, M)$, and c is a constant of order unity [178]. For $\tilde{b} > \tilde{b}_{\rm max}$,

$$\tilde{W}(\tilde{b}, M, x_A, x_B) = \tilde{W}^{\rm pert}(\tilde{b}_{\rm max}, M, x_A, x_B) F^{\rm NP}(\tilde{b}; \tilde{b}_{\rm max})\,, \qquad (1.39)$$

where the nonperturbative function $F^{\rm NP}$ is given by

$$F^{\rm NP} = \exp\{-\ln(M^2\tilde{b}_{\rm max}^2/c^2)\, \left[g_1\left((\tilde{b}^2)^\alpha - (\tilde{b}_{\rm max}^2)^\alpha\right) + g_2\left(\tilde{b}^2 - \tilde{b}_{\rm max}^2\right)\right] - \bar{g}_2\left(\tilde{b}^2 - \tilde{b}_{\rm max}^2\right)\}. \qquad (1.40)$$

Here, $\tilde{b}_{\rm max}$ is a parameter that separates the perturbatively calculated part from the nonperturbative input. Unlike in the original CSS formalism, $\tilde{W}(\tilde{b}, M, x_A, x_B)$ is independent of the nonperturbative parameters when $\tilde{b} < \tilde{b}_{\rm max}$. In addition, the $\tilde{b}$-dependence in Eq. (1.40) is separated according to different physics origins. The $(\tilde{b}^2)^\alpha$-dependence mimics the summation of the perturbatively calculable leading-power contributions to the renormalization group equations to all orders in the running coupling constant $\alpha_s(\mu)$. The $\tilde{b}^2$-dependence of the g_2 term is a direct consequence of dynamical power corrections to the renormalization group equations and has an explicit dependence on M. The $\bar{g}_2$ term represents the effect of the non-vanishing intrinsic parton transverse momentum.

A remarkable feature of the $\tilde{b}$-space resummation formalism is that the resummed exponential factor $\exp[S(\tilde{b}, M)]$ suppresses the $\tilde{b}$-integral when $\tilde{b}$ is larger than $1/M$. It can be shown using the saddle point method that, for a large enough M, QCD perturbation theory is valid even at p_T = 0 [178]. As discussed in Refs. [177, 179], the value of the saddle point strongly depends on the collision energy $\sqrt{s}$, in addition to its well-known M^2 dependence. The predictive power of the $\tilde{b}$-space resummation formalism should be even better at the LHC than at the Tevatron.

In Z^0 production, since final-state interactions are negligible, power corrections can arise only from initial state multiple scattering. Equations (1.39) and (1.40) represent the most general form of $\tilde{W}$ and thus, apart from isospin and shadowing effects, which will be discussed later. The only way nuclear modifications associated with scale evolution enter the $\tilde{W}$ term is through the coefficient g_2.

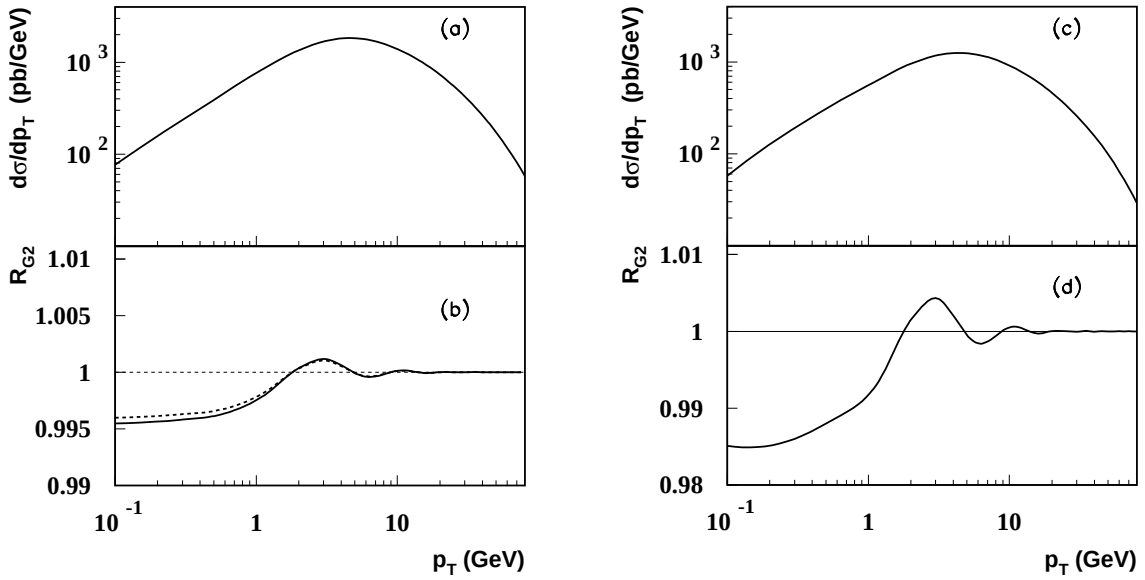

Fig. 1.23: (a) Cross section $d\sigma/dp_T$ for Z^0 production in pp collisions at the LHC with $\sqrt{s}$ = 14 TeV; (b) R_{G_2} defined in Eq. (1.41) with G_2 = 0.26 GeV^2 (dashed) and 0.40 GeV^2 (solid). (c) Cross section in pPb collisions at $\sqrt{s}$ = 8.8 TeV; (d) R_{G_2} in pPb with $G_2 = 0.8$GeV^2

The parameters g_1 and α of Eq. (1.40) are fixed by the requirement of continuity of the function $\tilde{W}(\tilde{b})$ and its derivative at $\tilde{b} = \tilde{b}_{\max}$. (The results are insensitive to changes of $\tilde{b}_{\max} \in [0.3\ \text{GeV}^{-1}, 0.7\ \text{GeV}^{-1}]$. We use $\tilde{b}_{\max} = 0.5\ \text{GeV}^{-1}$.) A fit to low energy Drell–Yan data gives $\bar{g}_2$ = 0.25 $\pm$ 0.05 GeV^2 and g_2 = 0.01 $\pm$ 0.005 GeV^2. As the $\tilde{b}$ dependence of the g_2 and $\bar{g}_2$ terms in Eq. (1.40) is identical, it is convenient to combine these terms and define $G_2 = \ln(M^2\tilde{b}^2_{\max}/c^2)g_2 + \bar{g}_2$. Using the values of the parameters listed above, we get G_2 = 0.33 $\pm$ 0.07 GeV^2 for Z^0 production in pp collisions. The parameter G_2 can be considered the only free parameter of the nonperturbative input in Eq. (1.40), arising from the power corrections in the renormalization group equations. An impression of the importance of the power corrections can be obtained by comparing results with the above value of G_2 to those with power corrections turned off (G_2 = 0). We therefore define the ratio

$$R_{G_2}(p_T) \equiv \frac{d\sigma^{(G_2)}(p_T)}{dp_T} \Big/ \frac{d\sigma(p_T)}{dp_T} \ . \tag{1.41}$$

The cross sections in the above equation and in the results presented here have been integrated over rapidity (–2.4 $\leq$ y $\leq$ 2.4) and M^2 in the narrow width approximation. For the PDFs, we use the CTEQ5M set [86].

Figure 1.23 displays the differential cross sections and the corresponding R_{G_2} ratio (with the limiting values of G_2 = 0.26 GeV^2 (dashed) and G_2 = 0.40 GeV^2 (solid)) for Z^0 production as functions of p_T in pp collisions at $\sqrt{s}$ = 14 TeV. The deviation of R_{G_2} from unity decreases rapidly as p_T increases. It is smaller than one per cent for both $\sqrt{s}$ = 5.5 TeV (not shown) and $\sqrt{s}$ = 14 TeV in pp collisions, even when p_T = 0. In other words, the effect of power corrections is very small at the LHC over the whole p_T region.

Without nuclear effects on the hard collision, the production of heavy vector bosons in nucleus–nucleus (AB) collisions should scale with the number of binary collisions, and $\sigma_{AB} \propto AB$. However, there are several additional nuclear effects on the hard collision in a heavy-ion reaction. First of all, the isospin effects, which come from the difference between the neutron PDFs and the proton PDFs, is about 2% at LHC. This is expected, since at the LHC $x \sim 0.02$ where the $u - d$ asymmetry is very small.

The dynamical power corrections entering the parameter g_2 should be enhanced by the nuclear size, i.e. proportional to $A^{1/3}$. Taking into account the A-dependence, we obtain G_2 = 1.15 $\pm$ 0.35 GeV^2

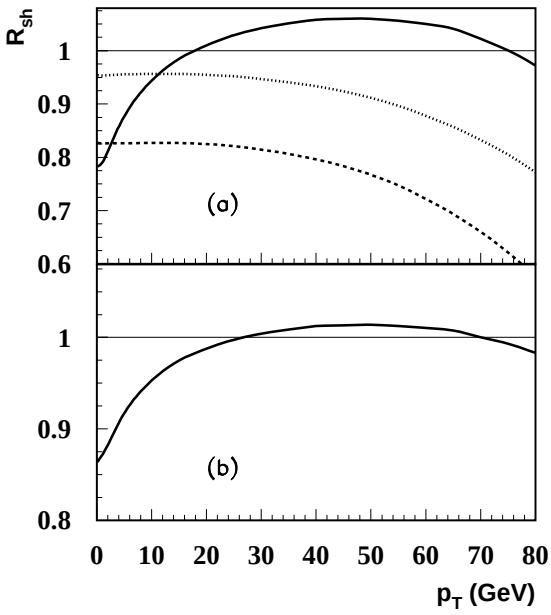

Fig. 1.24: (a) Cross section ratios for Z^0 production in PbPb collisions at $\sqrt{s}$ = 5.5 TeV: $R_{\rm sh}$ of Eq. (1.42) (solid line), and $R_{\rm sh}$ with the scale fixed at 5 GeV (dashed) and 90 GeV (dotted); (b) $R_{\rm sh}$ in pPb at $\sqrt{s}$ = 8.8 TeV

for PbPb reactions. We find that with this larger value of G_2, the effects of power corrections appear to be enhanced by a factor of about three from pp to PbPb collisions at the LHC. Thus, even the enhanced power corrections remain under 1% when 3 GeV $< p_T <$ 80 GeV. This small effect is taken into account in the following nuclear calculations.

Next we turn to the phenomenon of shadowing, expected to be a function of x, the scale μ, and of the position in the nucleus. The latter dependence means that in heavy-ion collisions, shadowing should be impact parameter (b) dependent. Here we concentrate on impact-parameter integrated results, where the effect of the b-dependence of shadowing is relatively unimportant [180], and focus on the scale dependence. We therefore use the EKS98 parametrization [27]. We define

$$R_{\rm sh}(p_T) \equiv \frac{d\sigma^{(\rm sh)}(p_T, Z_A/A, Z_B/B)}{dp_T} \Bigg/ \frac{d\sigma(p_T)}{dp_T}\,, \tag{1.42}$$

where Z_A and Z_B are the atomic numbers and A and B are the mass numbers of the colliding nuclei. The cross section $d\sigma^{(\rm sh)}(p_T, Z_A/A, Z_B/B)/dp_T$ has been averaged over AB, while $d\sigma(p_T)/dp_T$ is the pp cross section. We have seen above that shadowing remains the only significant effect responsible for nuclear modifications. Figure 1.23(c) shows $d\sigma^{(\rm sh)}/dp_T$ and (d) the corresponding R_{G_2} for pPb collisions at $\sqrt{s}$ = 8.8 TeV.

In Fig. 1.24(a), the result for $R_{\rm sh}$ (solid line) is surprising because even at p_T = 90 GeV, $x \sim 0.05$, and we are still in the 'strict shadowing' region. Therefore, the fact that $R_{\rm sh} > 1$ for 20 GeV $< p_T <$ 70 GeV is not 'anti-shadowing'. To better understand the shape of the ratio as a function of p_T, we also show $R_{\rm sh}$ with the scale fixed to 5 GeV (dashed line) and 90 GeV (dotted), respectively, in Fig. 1.24(a). The nuclear modification to the PDFs is only a function of x and flavour in the calculations represented by the dashed and dotted lines. These two curves are similar in shape, but rather different from the solid line. In $\tilde{b}$ space, $\tilde{W}(\tilde{b}, M, x_A, x_B)$ is almost equally suppressed in the whole $\tilde{b}$ region if the fixed scale shadowing is used. However, with scale-dependent shadowing, the suppression increases as $\tilde{b}$ increases since the scale $\mu \sim 1/\tilde{b}$ in the nPDFs. Thus the scale dependence redistributes the shadowing effect. Here the redistribution brings $R_{\rm sh}$ above unity for 20 GeV $< p_T <$ 70 GeV. When p_T increases further, the contribution from the Y term starts to be important and $R_{\rm sh}$ dips back below one to match the fixed order pQCD result. Figure 1.24(b) shows $R_{\rm sh}$ in pPb at $\sqrt{s}$ = 8.8 TeV.

We see from Fig. 1.24 that the shadowing effects on the p_T distribution of Z^0 bosons at the LHC are intimately related to the scale dependence of the nPDFs where the data are very limited [27]. Theoretical studies such as EKS98 are based on the assumption that the nPDFs differ from the parton distributions in the free proton but obey the same DGLAP evolution [27]. Therefore, the transverse momentum distribution of heavy bosons at the LHC in PbPb and pPb collisions can further test our understanding of the nPDFs.

In summary, higher-twist nuclear effects appear to be negligible in Z^0 production at LHC energies. We have demonstrated that the scale dependence of shadowing may lead to unexpected phenomenology of shadowing at these energies. Overall, the Z^0 transverse momentum distributions can be used as a precision test for leading-twist pQCD in the TeV energy region for both proton–proton and nuclear collisions. We propose that measurements of the Z^0 spectra be of very high priority at the LHC.

5.3. Jet and Dijet Rates in pA Collisions

A. Accardi and N. Armesto

The study of jet production has become one of the precision tests of QCD. Next-to-leading order (NLO) computations have been successfully confronted with experimental data. For example, jet production at the Tevatron [181] provides a very stringent test of available QCD Monte Carlo codes and gives very valuable information on the behaviour of the gluon distribution in the proton at large x.

On the other hand, few studies on jets in a nuclear environment have been performed in fixed target experiments [182, 183] and at colliders. There are prospects to measure high-p_T particles at RHIC but the opportunity of detecting and studying jets with $E_T \sim 100$ GeV, where E_T is the total transverse energy of all jets, will appear only at the LHC. Concretely, such measurements in pA collisions would settle some uncertainties such as the validity of collinear factorization [17, 184, 185], the modifications of nPDFs inside nuclei [46, 186], and the existence and amount of energy loss of fast partons inside cold nuclear matter [187]. Such issues have to be well understood before any claim, based on jet studies, of the existence of new physics in nucleus–nucleus collisions (hopefully QGP formation), can be considered conclusive. Furthermore, the study of high-p_T particles and jets can help not only to disentangle the existence of such new state of matter but also to characterize its properties, see Refs. [188–190].

For our computations we will use a NLO Monte Carlo code [191–193], adapted to include isospin effects and modifications of the PDFs inside nuclei. This code is based on the subtraction method to cancel the infrared singularities between real and virtual contributions. A full explanation, a list of available codes and detailed discussions on theoretical uncertainties in nucleon–nucleon collisions can be found in Ref. [194]. The accuracy of our computations, limited by CPU time, is estimated to be:

- 2% for the lowest and 15% for the highest E_T-bins of the transverse energy distributions.
- 3% for the pseudorapidity distributions.
- 20% for the least populated and 3% for the most populated bins of the dijet distributions of the angle between the two hardest jets.

The results will be presented in the LHC lab frame, so that for pPb collisions we have a 7 TeV proton beam on a 2.75 TeV Pb beam, see Section 2.1. on the experimental parameters in pA collisions. All the energies will be given per nucleon and, in order to compare with the pp case, all cross sections will be presented per nucleon–nucleon pair, i.e. divided by AB.

Unless explicitly stated, we will use the MRST98 central gluon distribution [172] with the EKS98 parametrization [27, 28] and identical factorization and renormalization scales $\mu = \mu_F = \mu_R = E_T/2$. We will employ the k_T-clustering algorithm for jet reconstruction [195, 196] with $D = 1$ which is more sound on theoretical grounds than the cone algorithm [197–199]. The kinematical regions we consider are:

- $|\eta_i| < 2.5$, where η_i is the pseudorapidity of the jet, corresponding to the acceptance of the central part of the CMS detector.
- $E_{Ti} < 20$ GeV for a single jet in the pseudorapidity distributions, to ensure the validity of perturbative QCD.
- $E_{T1} < 20$ GeV and $E_{T2} < 15$ GeV for the hardest and next-to-hardest jets entering the CMS acceptance in the ϕ-distributions, where ϕ is the angle between these two jets.

Please note that, even in the absence of nuclear effects, the η_i-distributions may be asymmetric with respect to η_i = 0 since we present our results in the lab frame, not the centre-of-mass frame.

Asymmetric E_{Ti}-cuts have been imposed on the ϕ distributions to avoid the generation of large logarithms at certain points in phase space, see Ref. [193]. Also, the results near $\phi = \pi$ are unreliable [193], because they require all-order resummation, not available in the code we are using.

We caution that a comparison of our results with data is not straightforward. Comparison with AB data will be even more problematic, see Chapter 2 for details. Several physical effects are not included in our computations. For example, the so-called underlying event (i.e. the soft particle production that coexists with the hard process) is not considered here. It may cause difficulties with jet reconstruction and increase the uncertainties in jet-definition algorithms. This effect has been considered in antiproton–proton collisions at the Tevatron [200, 201] but its estimate is model-dependent, relying on our limited knowledge of soft multiparticle production. In collisions involving nuclei, the situation is even worse since our knowledge is more limited. The only way to take this into account would be to use available Monte Carlo simulations for the full pA event [202, 203], modified to include the NLO contributions. Other processes which might need to be taken into account more carefully in our computations are multiple hard parton collisions [204–206]. They may be divided into two classes:

1) Disconnected collisions: more than one independent parton–parton collisions in the same event, each one producing a pair of high-p_T jets. This has been studied at the Tevatron [207, 208] for single $p\bar{p}$ collisions, but its quantitative explanation and the extension to nuclear collisions is model-dependent. Simple estimates of the influence of disconnected collisions on jet production in pA show it to be negligible[5]. This is not the case for AB collisions, see Chapter 2 of this report.
2) Rescatterings: a high-p_T parton may undergo several hard collisions before hadronizing into a jet, mimicking a single higher-order process. Quantitative descriptions of the modification of the jet E_{Ti} spectrum are model dependent. However, at the LHC the effect is expected to be very small, almost negligible at the transverse energies considered here (see Section 6.5. on the Cronin effect in pA collisions).

Finally, no centrality dependence has been studied. It is not clear how to implement such dependence in theoretical computations because both the number of nucleon–nucleon collisions and the modification of the nPDF may be centrality-dependent.

[5] We make a simple estimate of the average number of binary nucleon–nucleon collisions $\langle n \rangle$ associated with jet production for $E_{Ti} > E_{T0}$. In the Glauber model [209, 210], one obtains:

$$\langle n \rangle (b, E_{T0}) \, \frac{d\sigma_{pA}}{d^2b}(E_{T0}) = A T_A(b) \, \sigma_{pp}(E_{T0}) \, ,$$

where b is the impact parameter and the nuclear profi le function $T_A(b)$ is normalized to unity. The cross sections are $\sigma(E_{T0}) \equiv \sigma_{pp}(E_{T0}) = \int_{E_{T0}}^{\infty} dE_{Ti} \, d\sigma_{pp}(E_T)/dE_{Ti}$, the jet cross section for jets with $E_{Ti} > E_{T0}$ in pp collisions and $\sigma_{pA}(b, E_{T0}) \equiv d\sigma_{pA}(E_{T0})/d^2b = 1 - [1 - T_A(b)\sigma_{pp}(E_{T0})]^A$, the inelastic jet production cross section for $E_{Ti} > E_{T0}$ in pA collisions as a function of b. In both cases the cross sections are integrated over the pseudorapidity acceptance. Taking $\sigma(E_{T0})$ = 527, 1.13 and 0.046 μb as representative values in pPb collisions at 8.8 TeV for E_{T0} = 20, 100 and 200 GeV respectively, see Fig. 1.27, $\langle n \rangle$ = 1.0 for all E_{T0}, both for minimum bias collisions (i.e. integrating $T_A(b)$ and $d\sigma_{pA}(b, E_{T0})/d^2b$ over b between b = 0 and ∞) and for central collisions (e.g. integrating $0 < b < 1$ fm). Thus the contribution of multiple hard scattering coming from different nucleon–nucleon collisions seems to be negligible.

5.3.1. $d\sigma/dE_T$ and $d\sigma/d\eta$ for jets at large E_T

Uncertainties

A number of theoretical uncertainties in pp and pPb collisions are examined in Figs. 1.25 and 1.26.Varying the scale between $E_T/4$ and E_T gives differences of order $\pm$ 10%, the smaller scale giving the larger result. We have estimated the uncertainty due to the PDF by using CTEQ5M [86]. It gives a $\sim$ 5% larger results than the default MRST98 central gluon [172]. The effect of isospin alone (obtained from the comparison of pp and pPb without any modification of nPDF at the same energy per nucleon) is very small, as one would expect from gg dominance. The effect of nPDFs, estimated using EKS98 [27, 28], is also small. However it produces an extra asymmetry (an excess in the region $\eta_i < 0$) in pA collisions at reduced energy (e.g. pPb at 5.5 TeV), which disappears at maximum energy (e.g. pPb at 8.8 TeV), see Fig. 1.26 (bottom-left) and Fig. 1.27 (bottom-right), due to the asymmetry of the projectile and target momentum in the LHC lab frame. Finally, there is some uncertainty due to the choice of jet-finding algorithm. The cone algorithm [197–199] with $R = 0.7$ slightly reduces the cross section $\sim 1 \ldots$ 2% compared to the k_T-clustering algorithm [195, 196] with $D = 1$. The cone with $R = 1$ gives results $\sim$ 15% larger than our default choice.

Finally, we discuss the ratio of the NLO to LO cross sections, the K-factor. In Fig. 1.28 the K-factor is calculated for different collision systems and energies, varying the inputs. For our default options, the ratio is quite constant, $\sim$ 1.2, over all E_{Ti} and η_i for all energies. The μ-dependence results in $K \sim 1.35$ for $\mu = E_T$ and ~ 1.15 for $\mu = E_T/4$. The cone algorithm with $R = 0.7$ gives results very similar to those obtained with the k_T-clustering algorithm with $D = 1$, while a cone with $R = 1$ produces $K \sim 1.45$. (Note that at LO the choice of jet-finding algorithm has no influence on the results.) Finally, the choice of PDF, isospin and modifications of the nPDFs do not sizeably influence the K-factor.

Results

The expected LHC luminosities for different collisions are shown in Table 1.7, along with the one month (10^6 s) integrated luminosity expressed in units of $\mu\mathrm{b}/(AB)$. Using this table and the cross sections for inclusive single jet and dijet production in the figures, it is possible to extract the number of expected jets (Figs. 1.25, 1.26 and 1.27) or dijets (Figs. 1.29 and 1.30). For example, from the solid curve on the upper left-hand side of Fig. 1.27 and $\mathcal{L}$ = 10^{34} cm^{-2}s^{-1}, we expect 10^{10} jets with $E_{Ti} \sim 70$ GeV from a cross section of 1 μb/(AB), and 10^6 jets with $E_{Ti} \sim 380$ GeV from a cross section of 10^{-4} μb/(AB), in our η_i range.

Table 1.7: Luminosities $\mathcal{L}$ (cm^{-2}s^{-1}) and $\mathcal{L}\times$ 10^6 s ($\mu\mathrm{b}/AB$) for different collision systems at the LHC. The numbers of expected jets and dijets in a certain kinematical range are obtained by multiplying the last column by the cross sections given in Figs. 1.25, 1.26, 1.27 (jets) and 1.29, 1.30 (dijets).

System	$\sqrt{s_{NN}}$ **(TeV)**	$\mathcal{L}$ **(cm^{-2}s^{-1})**	$\mathcal{L}\times$ **10^6 s (μb/(AB))**
pp	14	10^{34}	10^{10}
pp	14	3×10^{30}	3×10^6
pAr	9.4	4×10^{30}	1.6×10^8
pAr	9.4	1.2×10^{29}	4.8×10^6
pPb	8.8	10^{29}	2.1×10^7

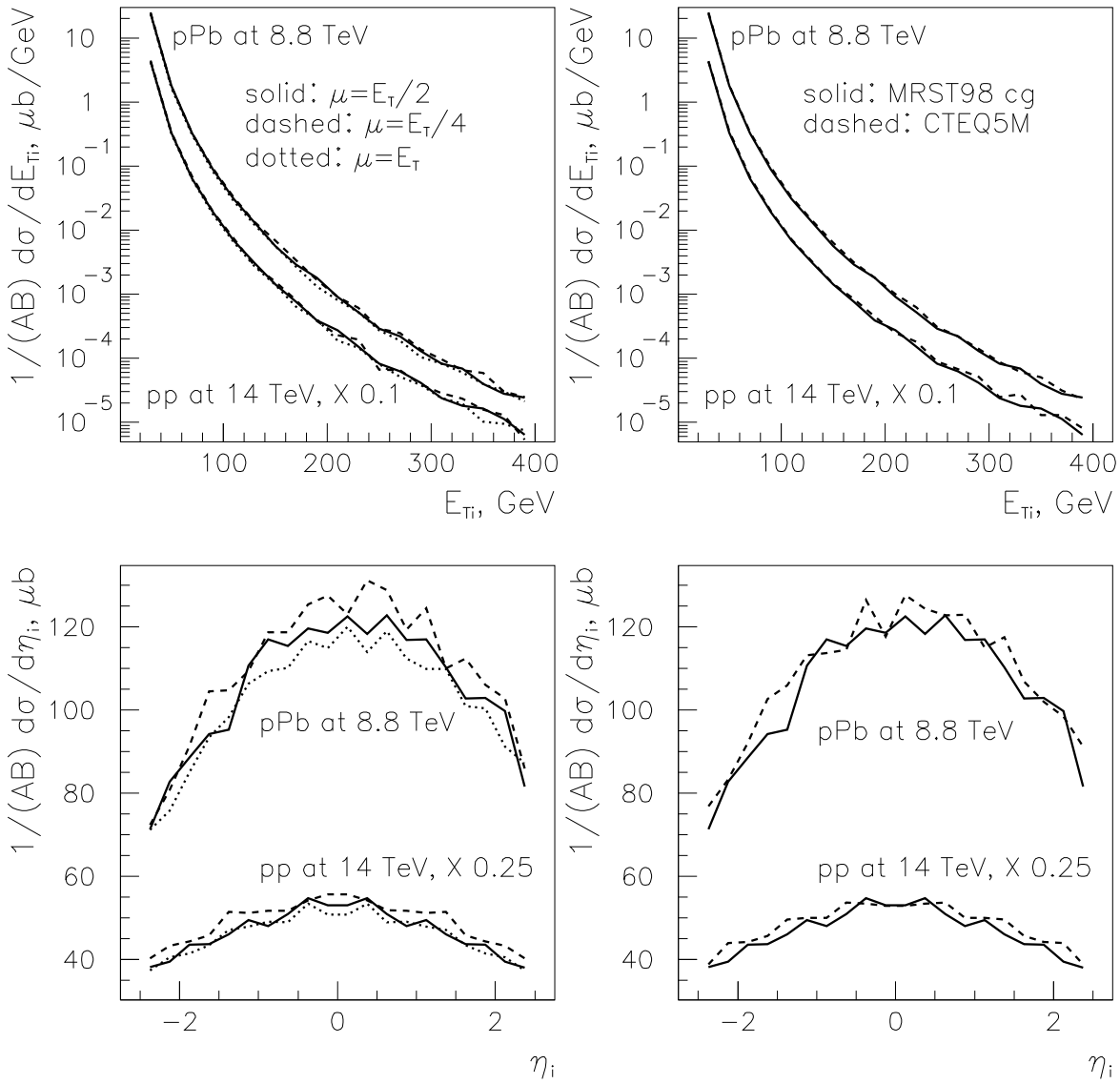

Fig. 1.25: Left: Scale dependence of jet cross sections [we use $\mu = E_T/2$ (solid), $\mu = E_T/4$ (dashed) and $\mu = E_T$ (dotted) lines] as a function of E_{Ti} for $|\eta_i| < 2.5$ (upper plot) and η_i for $E_{Ti} > 20$ GeV (lower plot). Right: PDF dependence of jet cross sections, MRST98 central gluon (solid) and CTEQ5M (dashed), as a function of E_{Ti} for $|\eta_i| < 2.5$ (upper plot) and η_i for $E_{Ti} > 20$ GeV (lower plot). In each plot, results for pPb at 8.8 TeV (upper lines) and pp at 14 TeV (lower lines, scaled by 0.1 in the upper plots and by 0.25 in the lower plots) are shown. Unless otherwise stated, default options are used, see text.

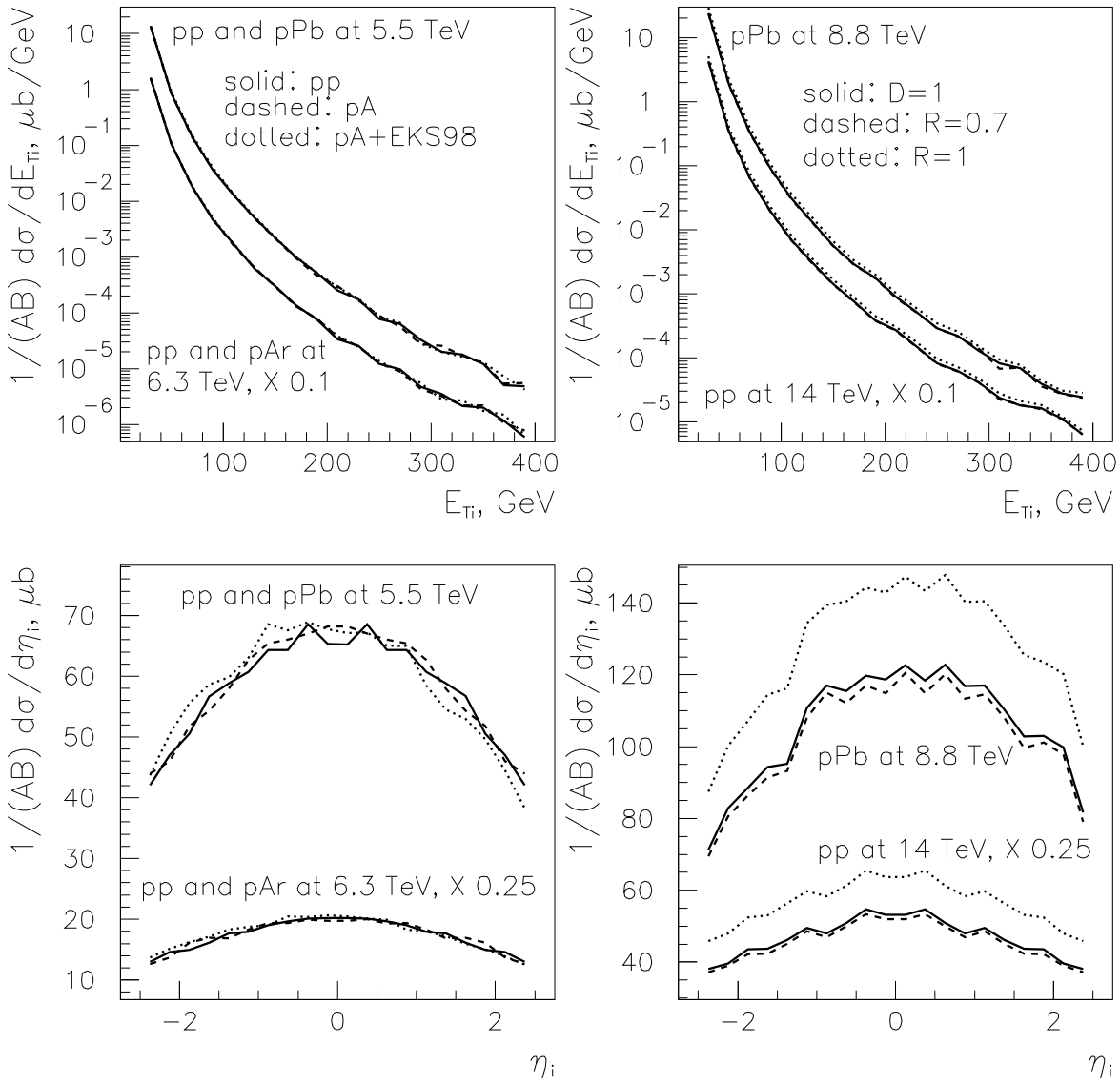

Fig. 1.26: Left: Isospin and nuclear PDF dependence of jet cross sections [we give the pp results (solid), pA results without (dashed) and pA results with EKS98 (dotted)] as a function of E_{Ti} for $|\eta_i| < 2.5$ (upper plot) and η_i for $E_{Ti} > 20$ GeV (lower plot). In each plot, results for pp and pPb at 5.5 TeV (upper lines) and pp and pAr at 6.3 TeV (lower lines, scaled by 0.1 in the upper plot and by 0.25 in the lower plot) are shown. Right: Dependence of jet cross sections on the jet reconstruction algorithm [we show the k_T-algorithm with $D = 1$ (solid), the cone algorithm with $R = 0.7$ (dashed) and the cone algorithm with $R = 1$ (dotted)] as a function of E_{Ti} for $|\eta_i| < 2.5$ (upper plot) and η_i for $E_{Ti} > 20$ GeV (lower plot). In each plot, results for pPb at 8.8 TeV (upper lines) and pp at 14 TeV (lower lines, scaled by 0.1 in the upper plot and by 0.25 in the lower plot) are shown. Unless otherwise stated, default options are used, see text.

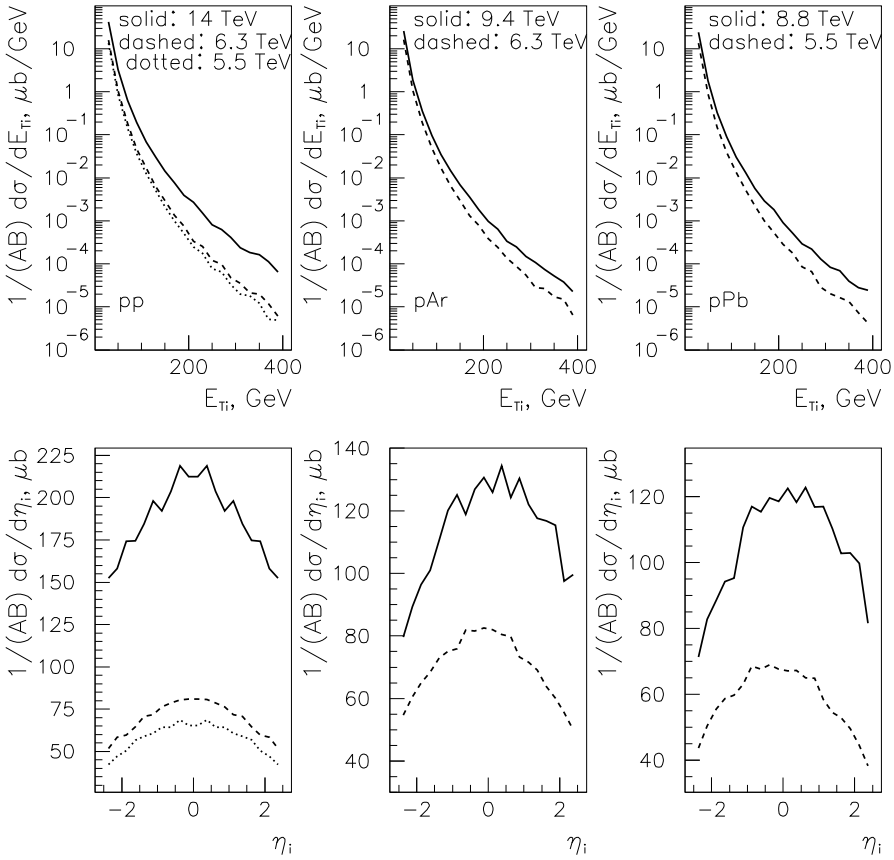

Fig. 1.27: Energy dependence of jet cross sections as a function of E_{Ti} for $|\eta_i| < 2.5$ (upper plots) and η_i for $E_{Ti} > 20$ GeV (lower plots). Left: pp collisions at 14 (solid), 6.3 (dashed) and 5.5 TeV (dotted). Centre: pAr collisions at 9.4 (solid) and 6.3 TeV (dashed). Right: pPb collisions at 8.8 (solid) and 5.5 TeV (dashed). Default options are used, see text.

Looking at the results of Fig. 1.27, it is evident that samples of $\sim 10^3$ jets are feasible, up to $E_{Ti} \sim 325$ GeV in a one-month run at the given luminosity. Indeed, from Table 1.7, 10^3 jets in pPb at 8.8 TeV would correspond to a cross section of 4.8×10^{-5} μb/(AB) which intersects the upper right solid curve in Fig. 1.27 at $E_{Ti} \sim 325$ GeV.

Some conclusions can now be drawn. First, since nuclear effects on the PDFs are not large (at most 10% at $E_T < 20$ GeV for Pb according to EKS98), an extensive systematic study of the A-dependence of the large-E_T jet cross sections does not seem to be the most urgent need. If, however, the nuclear effects in these cross sections turn out to be significant, the measurements of the A systematics, especially towards the smallest values of E_T, would be necessary in order to understand the new underlying QCD collision dynamics. Second, noting the asymmetry in the pseudorapidity distributions in pPb collisions at the reduced energy of 5.5 TeV, and to a lesser extent in pAr at 6.3 TeV, when EKS98 corrections are implemented, a pA run at reduced proton energies might test the nuclear PDF effects; a study of E_{Ti} distributions in different η_i slices going from the backward (A) to the forward (p) region would scan different regions in x of the ratio of the nuclear gluon distribution over that of a free nucleon, which is so far not well constrained. Nevertheless, this would require a detailed comparison with pp results at the same energy in order to disentangle possible biases (e.g. detector effects). If these pp results were not available experimentally, the uncertainty due to the scale dependence, which in our computations at reduced energies is as large as the asymmetry, in the extrapolation from 14 TeV to the pA energy should be reduced as much as possible for this study to be useful.

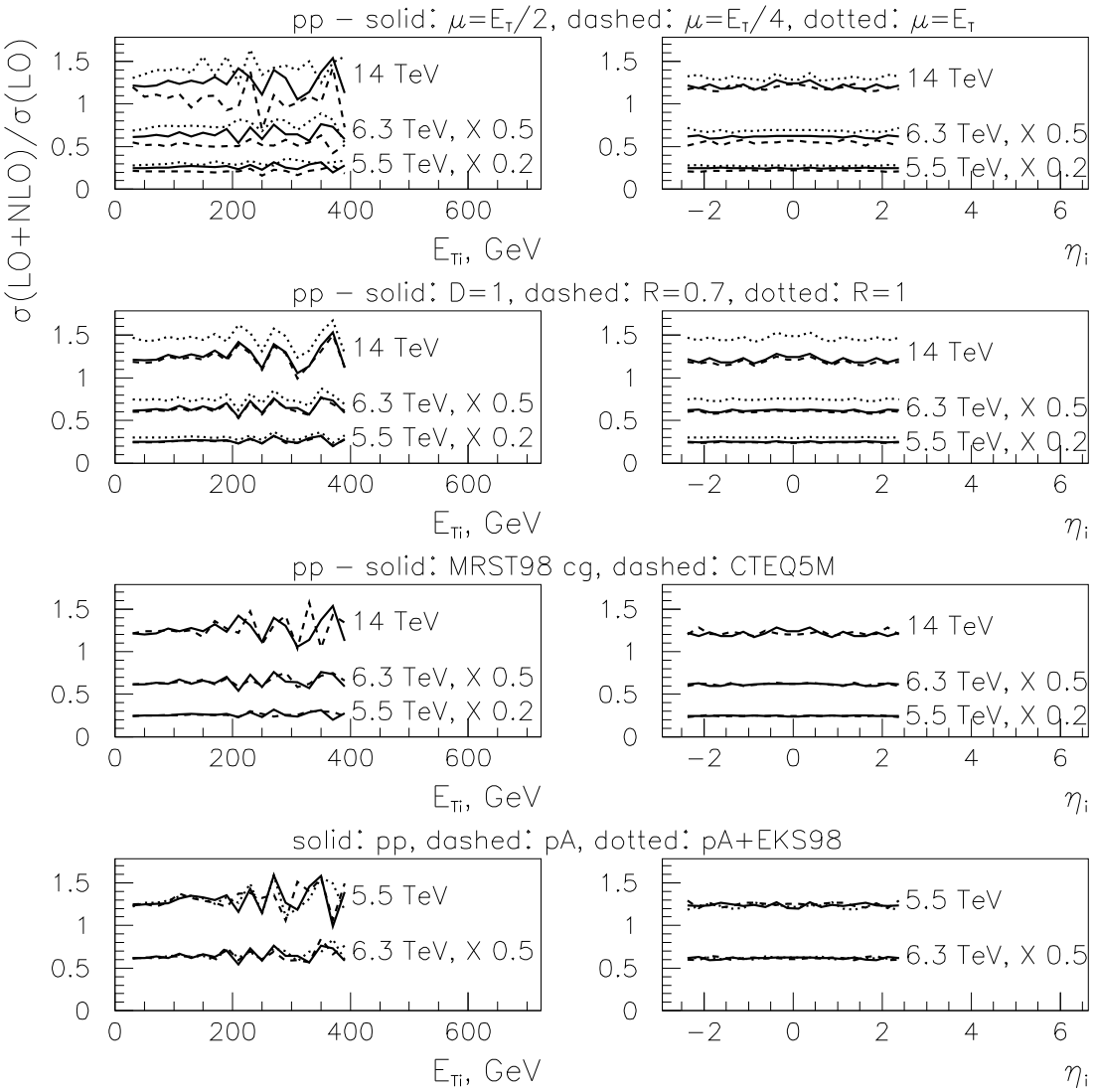

Fig. 1.28: The K-factors as a function of E_{Ti} for $|\eta_i| < 2.5$ (left) and η_i for $E_{Ti} > 20$ GeV (right). From top to bottom: scale dependence ($\mu = E_T/2$: solid; $\mu = E_T/4$: dashed; $\mu = E_T$: dotted); dependence on the jet reconstruction algorithm (k_T algorithm with $D = 1$: solid; cone algorithm with $R = 0.7$: dashed; cone algorithm with $R = 1$: dotted); nucleon PDF dependence (MRST98 central gluon: solid; CTEQ5M: dashed lines); and isospin and nuclear PDF dependence (pp: solid; pA without: dashed; pA with EKS98: dotted). Six upper plots: pp at 14, 6.3 (scaled by 0.5) and 5.5 (scaled by 0.2) TeV. Two bottom plots: pp and pAr at 6.3 TeV (scaled by 0.5), and pp and pPb at 5.5 TeV. Unless otherwise stated, default options are used, see text.

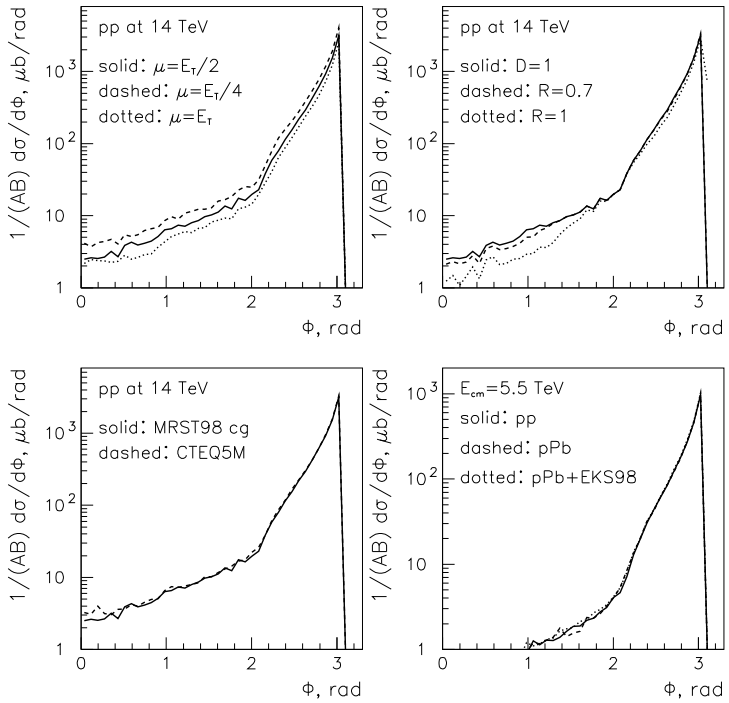

Fig. 1.29: Uncertainties in dijet cross sections as a function of ϕ for $E_{T1} < 20$ GeV, $E_{T2} < 15$ GeV and $|\eta_1|, |\eta_2| < 2.5$ in pp collisions at 14 TeV. Upper left: Scale dependence; Upper right: dependence on jet reconstruction algorithm; Lower left: PDF dependence in pp collisions at 14 TeV. Lower right plot shows the isospin and nuclear PDF dependence in pp and pPb collisions at 5.5 TeV. Unless otherwise stated, default options are used, see text.

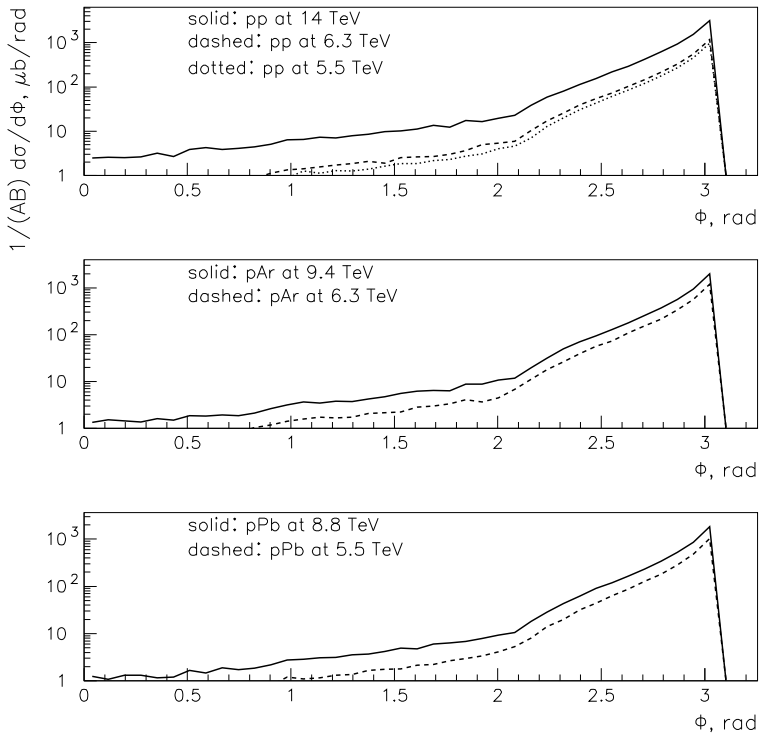

Fig. 1.30: Energy dependence of dijet cross sections as a function of ϕ for $E_{T1} < 20$ GeV, $E_{T2} < 15$ GeV and $|\eta_1|, |\eta_2| < 2.5$. Upper: pp collisions; Centre: pAr collision; Lower: pPb collisions. Default options are used, see text.

5.3.2. High-E_T dijet momentum imbalance

Dijet distributions as a function of ϕ, the angle between the two hardest jets, can test the perturbative QCD expansion. At LO in collinear factorization [17, 184, 185], the two jets are produced back-to-back, so that any deviation from a peak at $\phi = \pi$ is a signal of NLO corrections. However, recall that the results near $\phi = \pi$ are unreliable [193] since the NLO corrections become large and negative, requiring an all-order resummation in this region.

Uncertainties

In Fig. 1.29, the same uncertainties examined for E_{Ti} and η_i are studied in the dijet cross sections as a function of ϕ. First, the smaller the scale, the larger the results, so that the results for $\mu = E_T$ are up to $\sim$ 50% smaller than for $\mu = E_T/4$. Second, the PDF choice has less than a 10% effect when comparing CTEQ5M with the MRST98 central gluon. Third, the variation due to isospin, obtained from the comparison of pp and pPb without nuclear modifications of PDFs, is again negligible, and the effect of including EKS98 [27, 28] is also small, $\sim$ 3%. Finally, the jet-finding algorithm gives an uncertainty of order 20% for a cone with $R = 1$, $R = 0.7$ and the k_T-clustering algorithm with $D = 1$.

Results

Our results for pp and pA collisions at different energies are presented in Fig. 1.30. It is clear that the dijet momentum imbalance should be measurable provided jet reconstruction is possible in the nuclear environment and no other physics contribution, such as the underlying event or multiple hard parton scattering, interferes, spoiling the comparison with experimental data. Only extensive studies using Monte Carlo simulations including full event reconstruction will be able to clarify whether such measurements are feasible, see Chapter 2, Section 5.2.

5.4. Direct Photons

For direct photons, see Chapter 4, Sections 5–8.

5.5. Quarkonium Transverse Momentum Distributions

R. Vogt

Quarkonium suppression has already been an important plasma probe [211,212] at the SPS. It will be a major experimental focus at the LHC. These systematics are especially valuable for the Υ family where high statistics measurements of Υ production will be available in pp, pA, and AA interactions for the first time at the LHC.

Studies of quarkonium production in pA interactions are particularly relevant for LHC because the energy dependence of cold nuclear matter effects such as nucleon absorption are not fully understood and need to be checked with measurements. The existence of nuclear effects beyond the modifications of the parton densities in the nucleus argues that quarkonium production is not a good reaction by which to study the nuclear gluon distribution. However, the nuclear gluon distribution can be obtained through careful measurements of heavy-flavour production in pp and pA interactions and used as an input to quarkonium production. Thus quarkonium is still a benchmark process for testing cold matter effects in pA interactions at the LHC. It is important to study the shape of the quarkonium p_T distributions in pA interactions because plasma effects on the p_T distributions are expected to persist to high p_T [213, 214]. Detailed comparisons of the p_T dependencies of different quarkonium states in AA collisions will reveal whether or not the ratios of $\psi'/J/\psi$ and Υ'/Υ and Υ''/Υ, for example, are independent of p_T, as predicted by the colour evaporation model [215–217] or vary over the p_T range, as expected from nonrelativistic QCD [218]. Indeed quarkonium studies in pA may provide a crucial test of the

quarkonium production process because it is likely to be possible to separate the p and S states only in pA interactions where the accompanying decay photons can be found.

Two approaches have been successful in describing quarkonium production phenomenologically — the colour evaporation model (CEM) [215, 216] and nonrelativistic QCD (NRQCD) [218]. Both are briefly discussed.

In the CEM, any quarkonium production cross section is some fraction F_C of all $Q\overline{Q}$ pairs below the $H\overline{H}$ threshold where H is the lowest mass heavy hadron containing Q. Thus the CEM cross section is simply the $Q\overline{Q}$ production cross section with a mass cut imposed but without any contraints on the colour or spin of the final state. The produced $Q\overline{Q}$ pair then neutralizes its colour by interaction with the collision-induced colour field—"colour evaporation". The Q and the $\overline{Q}$ either combine with light quarks to produce heavy-flavoured hadrons or bind with each other in a quarkonium state. The additional energy needed to produce heavy-flavoured hadrons is obtained nonperturbatively from the colour field in the interaction region. The yield of all quarkonium states may be only a small fraction of the total $Q\overline{Q}$ cross section below the heavy hadron threshold, $2m_H$. At leading order, the production cross section of quarkonium state C is

$$\sigma_C^{\rm CEM} = F_C \sum_{i,j} \int_{4m_Q^2}^{4m_H^2} d\hat{s} \int dx_1 dx_2 \; f_i^p(x_1, Q^2) \; f_j^p(x_2, Q^2) \; \hat{\sigma}_{ij}(\hat{s}) \; \delta(\hat{s} - x_1 x_2 s) \, , \tag{1.43}$$

where $ij = q\overline{q}$ or gg and $\hat{\sigma}_{ij}(\hat{s})$ is the $ij \to Q\overline{Q}$ subprocess cross section. The fraction F_C must be universal so that, once it is fixed by data, the quarkonium production ratios should be constant as a function of $\sqrt{s}$, x_F and p_T. The actual value of F_C depends on the heavy quark mass, m_Q, the scale, Q^2, the parton densities and the order of the calculation.

Of course the leading order calculation in Eq. (3.3) is insufficient to describe high-p_T quarkonium production since the $Q\overline{Q}$ pair p_T is zero at LO. Therefore, the CEM was taken to NLO [217, 220] using the exclusive $Q\overline{Q}$ hadroproduction code of Ref. [219]. At NLO in the CEM, the process $gg \to gQ\overline{Q}$ is included, providing a good description of the quarkonium p_T distributions at the Tevatron [220]. The values of F_C for the individual charmonium and bottomonium states have been calculated from fits to the total J/ψ and inclusive Υ data combined with relative cross sections and branching ratios, see Refs. [213, 221] for details. The pp total cross sections at 5.5 TeV are shown in Tables 1.13 and 1.14 in Section 6.6., along with the fit parameters for the parton densities, quark masses and scales given for $Q\overline{Q}$ production in Table 1.9 in Section 6.4.

NRQCD was motivated by the success of potential models in determining the quarkonium mass spectra. It was first applied to high-p_T quarkonium production when it was clear that the leading colour singlet contribution severely underestimated direct J/ψ and ψ' production at the Tevatron [222, 223]. NRQCD describes quarkonium production as an expansion in powers of v, the relative Q-$\overline{Q}$ velocity. Thus NRQCD goes beyond the leading colour singlet state to include colour octet production. Now the initial $Q\overline{Q}$ quantum numbers do not have to be the same as in the final quarkonium state because an arbitrary number of soft gluons with $E < m_Q v$ can be emitted before bound state formation and change the colour and spin of the $Q\overline{Q}$. These soft gluon emissions are included in the hadronization process.

The cross section of quarkonium state C in NRQCD is

$$\sigma_C^{\rm NRQCD} = \sum_{i,j} \sum_n \int_0^1 dx_1 dx_2 f_i^p(x_1, Q^2) f_j^A(x_2, Q^2) C^{ij}_{Q\overline{Q}\,[n]}(Q^2) \langle \mathcal{O}_n^C \rangle \, , \tag{1.44}$$

where the partonic cross section is the product of perturbative expansion coefficients, $C^{ij}_{Q\overline{Q}\,[n]}(Q^2)$, and nonperturbative parameters describing the hadronization, $\langle \mathcal{O}_n^C \rangle$. The expansion coeffients can be factorized into the perturbative part and the nonperturbative parameters because the production time $\propto 1/m_Q$ is well separated from the timescale of the transition from the $Q\overline{Q}$ to the bound state $\propto 1/m_Q v$. If

$1/m_Q v \gg 1/m_Q$, the bound state formation is insensitive to the creation process. In principle, this argument should work even better for bottomonium because m_Q is larger. The colour singlet model result is recovered when $v \to 0$ [224]. The NRQCD parameters were obtained from comparison [225–228] to unpolarized high-p_T quarkonium production at the Tevatron [222, 223]. The calculations describe this data rather well but fail to explain the polarization data [229].

Both the CEM and NRQCD can explain the Tevatron quarkonium data because both are dominated by $gg \to gg^*$ and $gg \to gQ\overline{Q}$ at high-p_T. In the CEM $g^* \to Q\overline{Q}$ while in NRQCD, $g^* \to Q\overline{Q}[^3S_1^{(8)}]$ but $Q\overline{Q} \to Q\overline{Q}[^1S_0^{(8)}, ^3P_J^{(8)}]$ [224]. Direct J/ψ and ψ' production at the Tevatron are predominantly by $^3S_1^{(8)}$ states followed by $^1S_0^{(8)} + ^3P_J^{(8)}$ states and, while the χ_c singlet contribution does not underpredict the yield as badly, a $^3S_1^{(8)}$ component is needed for the calculations to agree with the data. The CEM includes the octet components automatically, but the relative strengths of the octet contributions are all determined perturbatively. The two approaches differ in their predictions of quarkonium polarization. NRQCD predicts transverse polarization at high-p_T [224] while the CEM predicts unpolarized quarkonium production. Neither approach can successfully explain the polarization data [229].

The bottomonium results at the Tevatron [230] extend to low p_T where the comparison to NRQCD is somewhat inconclusive. Some intrinsic k_T is needed to describe the data below $p_T \sim 5$ GeV.

In this Section, we present only the CEM p_T distributions. The NRQCD approach has not yet been fully calculated beyond LO [224]. We include intrinsic transverse momentum broadening, described further in Section 6.7., although it is a rather small effect at high-p_T. The direct J/ψ and Υ p_T distributions above 5 GeV in pp interactions at 5.5 TeV are shown in Fig. 1.31 for all the fits to the quarkonium data, described in Section 6.6. They all agree rather well with each other. However, the GRV98 result is slightly larger than the other J/ψ curves at high-p_T. Thus, changing the quark mass and scale does not have a large effect on the p_T dependence. In general, the J/ψ p_T distributions are more steeply falling than the Υ distributions.

Figure 1.32 shows the p_T distributions in pp and pPb interactions at 5.5 and 8.8 TeV along with pp interactions at 14 TeV. The shadowing effect is negligible at high-p_T so that the two distributions are indistinguishable.

6. PROCESSES WITH POTENTIALLY LARGE NUCLEAR EFFECTS

6.1. Drell–Yan Cross Sections at Low M^2: rapidity distributions

R. Vogt

Low-mass Drell–Yan production could provide important information on the quark and antiquark distributions at low x but still rather high Q^2 relative to the deep-inelastic scattering measurements. When M = 4, 11, 20 and 40 GeV, respectively, $x \sim$ 0.00073, 0.002, 0.0036 and 0.0073 at y = 0 and $\sqrt{s}$ = 5.5 TeV. Such low values of x have been measured before in nuclear deep-inelastic scattering but always at $Q^2 < 1$ GeV^2, out of reach of perturbative analyses. Thus, these measurements could be a benchmark for analysis of the nuclear quark and antiquark distributions.

As previously explained in Section 5.1., in AA collisions, the inclusive Drell–Yan contribution is unlikely to be extracted from the dilepton continuum which is dominated by correlated and uncorrelated $Q\overline{Q}$ ($D\overline{D}$, $B\overline{B}$) pair decays [79, 80]. However, in pA, the low-mass Drell–Yan may be competitive with the $Q\overline{Q}$ decay contributions to the dilepton spectra [79]. The number of uncorrelated $Q\overline{Q}$ pairs is also substantially reduced from the AA case [73]. Further calculations of the heavy quark contribution to dileptons are needed at higher masses to determine whether the Drell–Yan signal ever dominates the continuum or not. Perhaps the Drell–Yan and $Q\overline{Q}$ contributions can be separated using their different angular dependencies, isotropic for $Q\overline{Q}$ and $\propto (1 + \cos^2\theta)$ for Drell–Yan, as proposed by NA60 [231] and discussed in Section 6.2. When M is small and p_T is large relative to M, the $Q\overline{Q}$ background may be reduced and the Drell–Yan signal observable. This is discussed in the next Section.

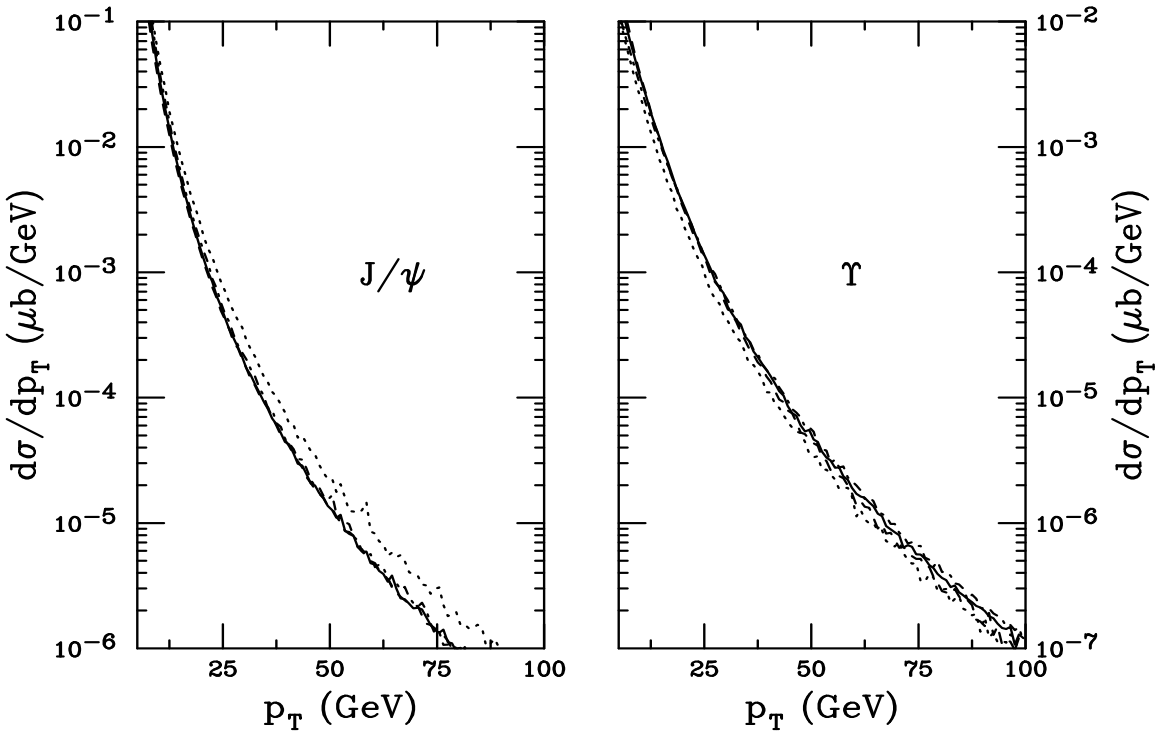

Fig. 1.31: The p_T distributions for J/ψ (left) and Υ (right) production assuming $\langle k_T^2 \rangle = 1$ GeV^2. On the left-hand side, the solid curve employs the MRST HO distributions with $m_c = Q/2 = 1.2$ GeV, the dashed, MRST HO with $m_c = Q = 1.4$ GeV, the dot–dashed, CTEQ 5M with $m_c = Q/2 = 1.2$ GeV, and the dotted, GRV 98 HO with $m_c = Q = 1.3$ GeV. On the right-hand side, the solid curve employs the MRST HO distributions with $m_b = Q = 4.75$ GeV, the dashed, $m_b = Q/2 = 4.5$ GeV, the dot–dashed, $m_b = 2Q = 5$ GeV, and the dotted, GRV 98 HO with $m_b = Q = 4.75$ GeV.

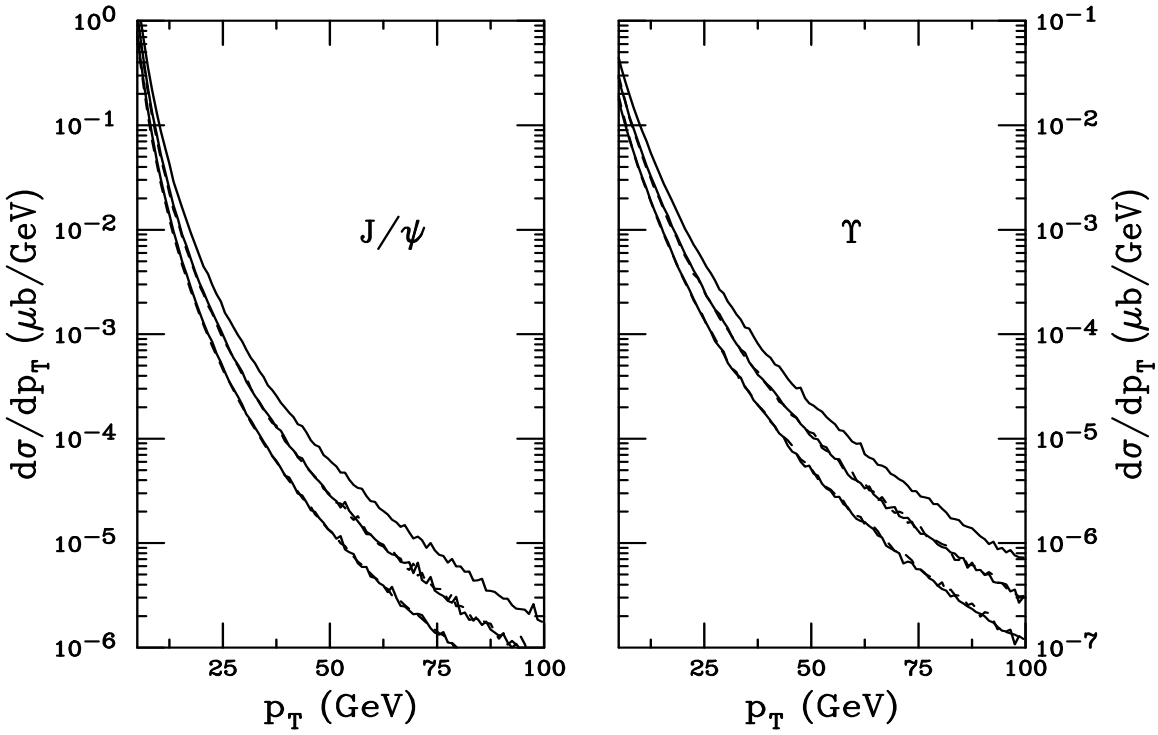

Fig. 1.32: The p_T distributions for J/ψ (left) and Υ (right) production assuming $\langle k_T^2 \rangle_{pp} = 1$ GeV^2 for pp interactions at 5.5 (lower), 8.8 (centre) and 14 (upper) TeV. On the left-hand side, we use the MRST HO distributions with $m_c = Q/2 = 1.2$ GeV while on the right-hand side, we use the MRST HO distributions with $m_b = Q = 4.75$ GeV.

The calculation of the Drell–Yan cross section is described in Section 5.1. Since the nuclear effects are larger at low Q^2, we will focus on the variation of the results with scale and shadowing parametrization. We again make our calculations with the MRST HO [172] parton densities with $Q^2 = M^2$ and the EKS98 parametrization [27,28] in the $\overline{\rm MS}$ scheme. The Drell–Yan convolutions with nuclear parton densities including isospin and shadowing effects are the same as for the Z^0 in the appendix of Ref. [171]. Only the prefactor changes from $H_{ij}^{Z^0}$ to H_{ij}^{M}. We present results for pp, Pbp and pPb collisions at 5.5 TeV/nucleon, the same energy as the PbPb centre of mass for better comparison without changing x. This is most desirable from the theoretical point of view because the nuclear parton densities are most easily extracted from the data. However, as was not touched upon in Section 5.1., the desirability of this approach ultimately depends upon the machine parameters. The highest pPb and Pbp luminosities can be achieved at 8.8 TeV/nucleon. Running the machine at lower energies will reduce the maximum luminosity, up to a factor of 20 if only injection optics are used [232], which could reduce the statistical significance of the measurement. This issue remains to be settled.

Figure 1.33 shows the rapidity distributions in pPb and Pbp collisions at 5.5 TeV/nucleon in four mass bins: $4 < M < 9$ GeV, $11 < M < 20$ GeV, $20 < M < 40$ GeV, and $40 < M < 60$ GeV. The shadowing effect decreases as the mass increases, from a $\sim$ 25% effect at y = 0 in the lowest mass bin to a $\sim$ 10% effect in the highest bin. Isospin is a smaller effect on low-mass Drell–Yan, as is clear from Fig. 1.34, where the pPb/pp and Pbp/pp ratios are given.

The pPb/pp ratio without shadowing is indistinguishable from unity over the whole rapidity range. The Pbp/pp ratio without shadowing differs from unity only for $y < 2$. The dashed curves in Fig. 1.34 represent the Pbp/pp ratios with EKS98 shadowing and show the pattern of increasing x_1 through the 'antishadowing' region into the EMC region. The ratio does not increase above unity because we present the Ap/pp ratio rather than a ratio of Ap with shadowing to Ap without shadowing. This difference can be easily seen by comparison to Fig. 1.33 where the dotted curves are equivalent to the pp distributions. The dashed curves in Fig. 1.34 are the ratios of the dashed to solid curves of Fig. 1.33. Clearly, at the peak of the rapidity distributions, the dashed curves are higher than the solid curves, signifying antishadowing, yet do not cross the dotted curves. The isospin of the Pb nucleus thus causes the Pbp/pp ratio to remain less than unity over all rapidity. Note also that the peaks of the ratios occur at smaller values of x_1, from $x_1 \sim 0.11$ in the lowest bin to ~ 0.062 in the highest. The evolution of the antishadowing region broadens and the average x decreases somewhat with increasing Q^2. On the other hand, the pPb/pp ratios are rather constant, decreasing only slowly with rapidity although the slope of the ratio increases with M. The pPb calculations are always at low x_2 where the shadowing parametrization does not change much with x_2. These results are reflected in the integrated cross sections in Table 1.8.

In Fig. 1.35 we show the effects of scale (upper two plots) and shadowing parametrization (lower two plots) on the results.

We choose the lowest mass bin to emphasize the overall effect. The scale variation, discussed in Section 5.1., shows that the cross sections are larger for scale $2M$ and smallest for scale $M/2$. This scale dependence is contrary to typical expectations since lower scales generally lead to larger cross sections. At lower energies and other processes this is true, but at high energies, the low-x evolution exceeds the effect of the scale-dependent logarithms [170]. The scale variation is a 50% effect in this bin, decreasing to 10% for $40 < M < 60$ GeV. The HPC [173] and HKM [29] shadowing calculations have the same general trends as the EKS98 parametrization. The HKM model has the weakest effect on sea quarks at low-x and produces the largest ratios for pPb/pp and in Pbp/pp for $y < 3$. The HPC parametrization has the strongest shadowing without evolution and is generally lower than the other two.

If the low Q^2 Drell–Yan cross section can be extracted from the other contributions to the continuum in pA, it could provide useful information on the low-x, moderate Q^2 regime not covered in previous experiments. Comparison could be made to the only previous available pA Drell–Yan measurements as a function of x_F by the E772 [54] and E866 [55] Collaborations at much higher x.

RHIC pA data should also be available by the time the LHC starts up. This could increase the $\sqrt{s}$

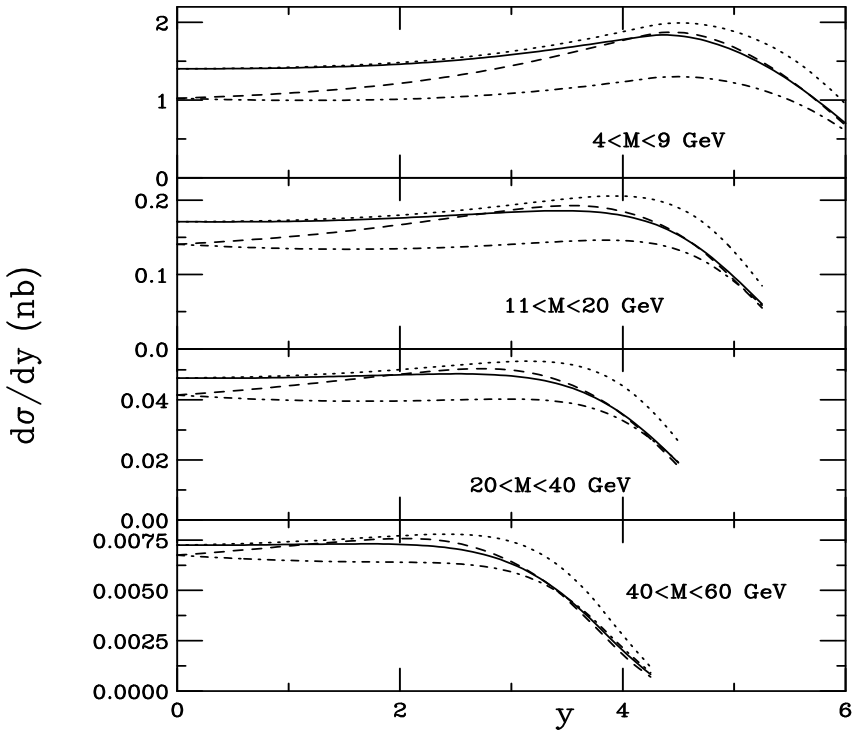

Fig. 1.33: The Drell–Yan rapidity distributions in pPb and Pbp collisions at 5.5 TeV evaluated at $Q = M$ for $4 < M < 9$ GeV, $11 < M < 20$ GeV, $20 < M < 40$ GeV and $40 < M < 60$ GeV. The solid and dashed curves show the results without and with shadowing, respectively, in Pbp collisions while the dotted and dot–dashed curves give the results without and with shadowing for pPb collisions.

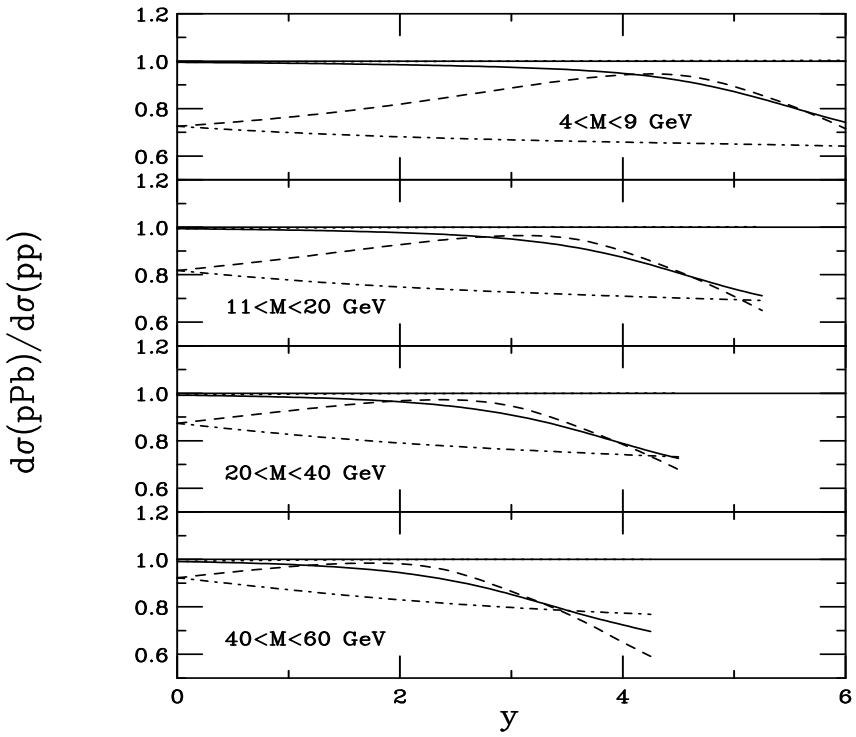

Fig. 1.34: The ratios of pPb and Pbp collisions to pp collisions at 5.5 TeV evaluated at $Q = M$ for $4 < M < 9$ GeV, $11 < M < 20$ GeV, $20 < M < 40$ GeV and $40 < M < 60$ GeV, as a function of rapidity. The solid and dashed curves show the Pbp/pp ratios without and with shadowing, respectively, while the dotted and dot–dashed curves are the pPb/pp ratios without and with shadowing.

Table 1.8: Rapidity-integrated Drell–Yan cross sections at 5.5 TeV/nucleon in the indicated mass intervals. The calculations are to NLO with the MRST HO parton densities and $Q^2 = M^2$.

Δy	σ (nb)	$\sigma_{\rm NS}$ (nb)	$\sigma_{\rm EKS98}$ (nb)	$\sigma_{\rm NS}$ (nb)	$\sigma_{\rm EKS98}$ (nb)
	pp	Pbp		pPb	
		$4 < M < 9$ GeV			
$0 < y < 2.4$	3.61	3.57	2.82	3.60	2.51
$0 < y < 1$	1.41	1.40	1.05	1.40	1.00
$2.4 < y < 4$	2.52	2.44	2.28	2.52	1.68
		$11 < M < 20$ GeV			
$0 < y < 2.4$	0.44	0.43	0.39	0.44	0.34
$0 < y < 1$	0.17	0.17	0.14	0.17	0.14
$2.4 < y < 4$	0.30	0.27	0.28	0.30	0.21
		$20 < M < 40$ GeV			
$0 < y < 2.4$	0.12	0.12	0.11	0.12	0.10
$0 < y < 1$	0.048	0.047	0.043	0.048	0.041
$2.4 < y < 4$	0.077	0.068	0.069	0.077	0.058
		$40 < M < 60$ GeV			
$0 < y < 2.4$	0.019	0.018	0.018	0.019	0.016
$0 < y < 1$	0.0074	0.0072	0.0070	0.0073	0.0066
$2.4 < y < 4$	0.0094	0.0078	0.0078	0.0094	0.007

systematics, providing, with both colliders, a collective measurement over a wide range of x values at similar Q^2.

6.2. Low-Mass Drell–Yan Production at LHC Energies

G. Fai, J.W. Qiu and X.F. Zhang

6.2.1. Introduction

Massive dilepton production in hadronic collisions is an excellent laboratory for theoretical and experimental investigations of strong interaction dynamics, and it is a channel for discovery of quarkonium states and a clean process for the study of the PDF. In the Drell–Yan process, the massive lepton pair is produced via the decay of an intermediate virtual photon γ^*. If both the physically measured dilepton mass M and the transverse momentum p_T are large, the cross section in a collision between hadrons (or nuclei) A and B, $A(P_A) + B(P_B) \to \gamma^*(\to l\bar{l}) + X$, can be factorized systematically in QCD

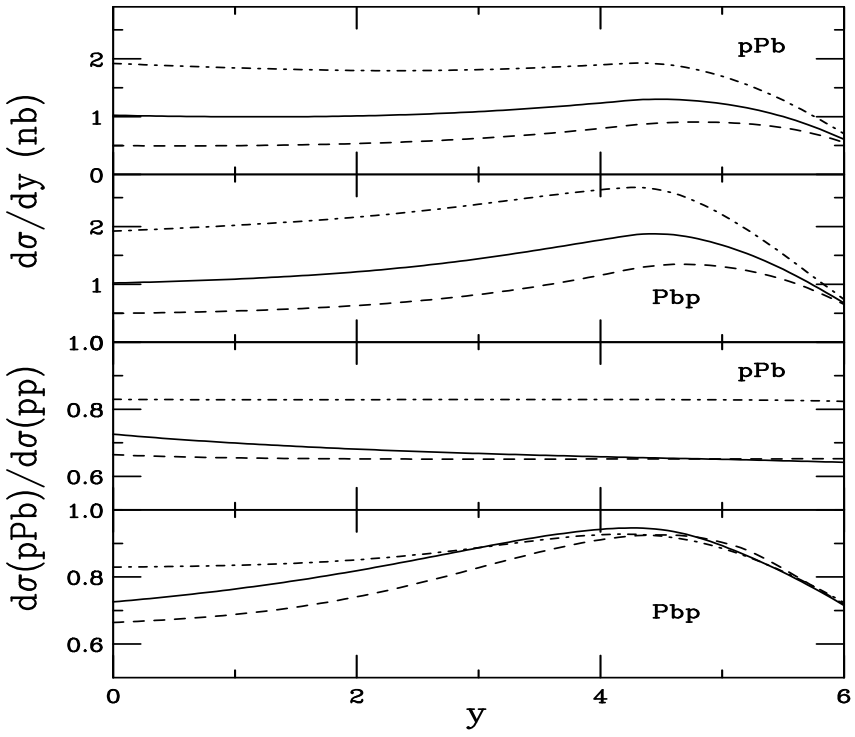

Fig. 1.35: The upper two plots present the scale dependence of the Drell–Yan cross section in the mass interval $4 < M < 9$ GeV in pPb and Pbp collisions at 5.5 TeV respectively. The EKS98 parametrization is used in all cases. The solid curve is calculated with $Q = M$, the dashed curve with $Q = M/2$ and the dot–dashed with $Q = 2M$. The lower plots present the dependence on the shadowing parametrization in the mass range $4 < M < 9$ GeV for the ratios pPb/pp and Pbp/pp at 5.5 TeV. The solid curve is the EKS98 parametrization, the dashed curve is the HPC parametrization and the dot–dashed curve is the HKM parametrization.

perturbation theory and expressed as [17]

$$\frac{d\sigma_{AB\to l\bar{l}(M)X}}{dM^2\,dy\,dp_T^2} = \left(\frac{\alpha_{\rm em}}{3\pi M^2}\right)\sum_{a,b}\int dx_1 f_{a/A}(x_1,\mu)\int dx_2 f_{b/B}(x_2,\mu)\,\frac{d\hat{\sigma}_{ab\to\gamma^*X}}{dp_T^2\,dy}(x_1,x_2,M,p_T,y;\mu). \tag{1.45}$$

The sum $\sum_{a,b}$ runs over all parton flavours, $f_{a/A}$ and $f_{b/B}$ are normal parton distributions and μ represents the renormalization and factorization scales. The partonic cross section $d\hat{\sigma}_{ab\to\gamma^*X}/dp_T^2dy$ in Eq. (1.45), the short-distance probability for partons of flavours a and b to produce a virtual photon of invariant mass M, is perturbatively calculable in terms of a power series in $\alpha_s(\mu)$. The scale μ is of the order of the energy exchange in the reaction, $\mu \sim \sqrt{M^2+p_T^2}$.

When $M \sim M_Z$, high-mass dilepton production in heavy-ion collisions at LHC energies is dominated by the Z^0 channel and is an excellent hard probe of QCD dynamics [233]. In this contribution, we demonstrate that the transverse-momentum distribution of low-mass ($\Lambda_{\rm QCD} \ll M \ll M_Z$) dilepton production at LHC energies is a reliable probe of both hard and semihard physics at LHC energies and is an advantageous source of constraints on gluon distributions in the proton and in nuclei [234]. In addition, it provides a significant contribution to the total dilepton spectra at the LHC, also an important channel for quarkonium and heavy-flavour decays.

The transverse-momentum (p_T) distribution of the dileptons can be divided into three regions: low p_T ($\ll M$), intermediate p_T ($\sim M$), and high-p_T ($\gg M$). When both the physically measured M and p_T are large and are of the same order, the short-distance partonic part $d\hat{\sigma}_{ab\to\gamma^*X}/dp_T^2dy$ in Eq. (1.45) can be calculated reliably in conventional fixed-order QCD perturbation theory in terms of a power series

in $\alpha_s(\mu)$. However, when p_T is very different from M, the calculation of Drell–Yan production in both low- and high-p_T regions becomes a two-scale problem in perturbative QCD and the calculated partonic parts include potentially large logarithmic terms proportional to a power of $\ln(M/p_T)$. As a result, the higher-order corrections in powers of α_s are not necessary small. The ratio $\sigma^{\rm NLO}/\sigma^{\rm LO} \propto \alpha_s \times$ (large logarithms) can be of order 1 and convergence of the conventional perturbative expansion in powers of α_s is possibly impaired.

In the low-p_T region, there are two powers of $\ln(M^2/p_T^2)$ for each additional power of α_s and the Drell–Yan p_T distribution calculated in fixed-order QCD perturbation theory is known to be unreliable. Only after all-order resummation of the large $\alpha_s^n \ln^{2n+1}(M^2/p_T^2)$ logarithms do predictions for the p_T distributions become consistent with data [177, 235]. We demonstrate in Section 6.2.2. that low-mass Drell–Yan production at p_T as low as $\Lambda_{\rm QCD}$ at LHC energies can be calculated reliably in perturbative QCD with all order resummation.

When $p_T \geq M/2$, the lowest-order virtual photon 'Compton' subprocess $g + q \to \gamma^* + q$ dominates the p_T distribution, and the high-order contributions including all-order resummation of $\alpha_s^n \ln^{n-1}(M^2/p_T^2)$ preserve the fact that the p_T distributions of low-mass Drell–Yan pairs are dominated by gluon-initiated partonic subprocesses [236]. We show in Section 6.2.3. that the p_T distribution of low-mass Drell–Yan pairs can be a good probe of the gluon distribution and its nuclear dependence. We give our conclusions in Section 6.2.4.

6.2.2. Low-mass Drell–Yan production at low transverse momentum

Resummation of large logarithmic terms at low-p_T can be carried out in either p_T or impact-parameter ($\tilde{b}$) space, the Fourier conjugate of p_T space. All else being equal, the $\tilde{b}$ space approach has the advantage of explicit transverse-momentum conservation. Using renormalization group techniques, Collins, Soper, and Sterman (CSS) [178] devised a $\tilde{b}$ space resummation formalism that resums all logarithmic terms as singular as $(1/p_T^2)\ln^m(M^2/p_T^2)$ when $p_T \to 0$. This formalism has been widely used for computations of vector boson p_T distributions in hadron reactions [237].

At low-mass M and p_T, Drell–Yan transverse-momentum distributions calculated in the CSS $\tilde{b}$-space resummation formalism strongly depend on the nonperturbative parameters determined at fixed target energies. However, it was pointed out recently that the predictive power of pQCD resummation improves with $\sqrt{s}$ and, when the energy is high enough, pQCD should have good predictive power even for low-mass Drell–Yan production [177]. The LHC will give us a chance to study low-mass Drell–Yan production at unprecedented energies.

In the CSS resummation formalism, the differential cross section for Drell–Yan production in Eq. (1.45) is reorganized as the sum

$$\frac{d\sigma_{AB\to l\bar{l}(M)X}}{dM^2\,dy\,dp_T^2} = \frac{d\sigma^{(\rm resum)}_{AB\to l\bar{l}(M)X}}{dM^2\,dy\,dp_T^2} + \frac{d\sigma^{(\rm Y)}_{AB\to l\bar{l}(M)X}}{dM^2\,dy\,dp_T^2}\,. \tag{1.46}$$

The all-orders resummed term is a Fourier transform from the $\tilde{b}$-space,

$$\frac{d\sigma^{(\rm resum)}_{AB\to l\bar{l}(M)X}}{dM^2\,dy\,dp_T^2} = \frac{1}{(2\pi)^2}\int d^2\tilde{b}\, e^{i\vec{p}_T\cdot\vec{\tilde{b}}}\, W(\tilde{b}, M, x_A, x_B) = \frac{1}{2\pi}\int d\tilde{b}\, J_0(p_T\tilde{b})\,\tilde{b}\, W(\tilde{b}, M, x_A, x_B)\ , \tag{1.47}$$

where J_0 is a Bessel function, $x_A = e^y\, M/\sqrt{s}$ and $x_B = e^{-y}\, M/\sqrt{s}$, with rapidity y and collision energy $\sqrt{s}$. In Eq. (1.46), the $\sigma^{(\rm resum)}$ term dominates the p_T distributions when $p_T \ll M$, while the $\sigma^{(Y)}$ term gives negligible corrections for small p_T but becomes important when $p_T \sim M$.

The function $W(\tilde{b}, M, x_A, x_B)$ resums to all orders in QCD perturbation theory the singular terms that would otherwise behave as $\delta^2(p_T)$ and $(1/p_T^2)\ln^m(M^2/p_T^2)$ in transverse-momentum space for all

$m \geq 0$. It can be calculated perturbatively for small $\tilde{b}$,

$$W(\tilde{b}, M, x_A, x_B) = \mathrm{e}^{-S(\tilde{b},M)}\, W(\tilde{b}, c/\tilde{b}, x_A, x_B) \equiv W^{\mathrm{pert}}(\tilde{b}, M, x_A, x_B)\,. \tag{1.48}$$

All large logarithms from $\ln(c^2/\tilde{b}^2)$ to $\ln(M^2)$ have been completely resummed into the exponential factor $S(\tilde{b}, M) = \int_{c^2/\tilde{b}^2}^{M^2} d\mu^2/\mu^2 \left[\ln(M^2/\mu^2)\mathcal{A}(\alpha_s(\mu)) + \mathcal{B}(\alpha_s(\mu))\right]$ where the functions $\mathcal{A}$ and $\mathcal{B}$ are given in Ref. [178] and $c = 2e^{-\gamma_E}$ with the Euler constant $\gamma_E \approx 0.577$. With only one large-momentum scale $1/\tilde{b}$, the function $W(\tilde{b}, c/\tilde{b}, x_A, x_B)$ in Eq. (1.48) is perturbatively calculable and is factorized as

$$W(\tilde{b}, c/\tilde{b}, x_A, x_B) = \sum_{a,b} \left[f_{a/A}(\xi_1, 1/\tilde{b}) \otimes \mathcal{C}_a(\frac{x_A}{\xi_1})\right] \left[f_{b/B}(\xi_2, 1/\tilde{b}) \otimes \mathcal{C}_b(\frac{x_B}{\xi_2})\right] \sigma_0\,, \tag{1.49}$$

where the sum $\sum_{a,b}$ runs over all parton flavours, the $\otimes$ represents the convolution over parton momentum fraction, and σ_0 is the lowest order partonic cross section for the Drell–Yan process [178]. The functions $\mathcal{C} = \sum_n \mathcal{C}^{(n)}(\alpha_s/\pi)^n$ in Eq. (1.49) are perturbatively calculable and given in Ref. [178]. Since the perturbatively resummed $W^{\mathrm{pert}}(\tilde{b}, M, x_A, x_B)$ in Eq. (1.48) is reliable only for the small $\tilde{b}$ region, an extrapolation to the nonperturbative large $\tilde{b}$ region is necessary in order to complete the Fourier transform in Eq. (1.47).

In the original CSS formalism, a variable $\tilde{b}_*$ and a nonperturbative function $F^{\mathrm{NP}}_{\mathrm{CSS}}(\tilde{b}, M, x_A, x_B)$ were introduced to extrapolate the perturbatively calculated W^{pert} into the large $\tilde{b}$ region. The full $\tilde{b}$-space distribution was of the form

$$W^{\mathrm{CSS}}(\tilde{b}, M, x_A, x_B) \equiv W^{\mathrm{pert}}(\tilde{b}_*, M, x_A, x_B)\, F^{\mathrm{NP}}_{\mathrm{CSS}}(\tilde{b}, M, x_A, x_B)\,, \tag{1.50}$$

where $\tilde{b}_* = \tilde{b}/\sqrt{1 + (\tilde{b}/\tilde{b}_{\mathrm{max}})^2}$, with $\tilde{b}_{\mathrm{max}} = 0.5\ \mathrm{GeV}^{-1}$. This construction ensures that $\tilde{b}_* \leq \tilde{b}_{\mathrm{max}}$ for all values of $\tilde{b}$.

In terms of the $\tilde{b}_*$ formalism, a number of functional forms for the $F^{\mathrm{NP}}_{\mathrm{CSS}}$ have been proposed. A simple Gaussian form in $\tilde{b}$ was first proposed by Davies, Webber and Stirling (DWS) [238],

$$F^{\mathrm{NP}}_{\mathrm{DWS}}(\tilde{b}, M, x_A, x_B) = \exp\left\{-(g_1 + g_2 \ln(M/2M_0))\tilde{b}^2\right\}, \tag{1.51}$$

with the parameters M_0 = 2 GeV, g_1 = 0.15 GeV^2, and g_2 = 0.4 GeV^2. In order to take into account the apparent dependence on collision energies, Ladinsky and Yuan (LY) introduced a new functional form [239],

$$F^{\mathrm{NP}}_{\mathrm{LY}}(\tilde{b}, M, x_A, x_B) = \exp\left\{-(g_1 + g_2 \ln(M/2M_0))\tilde{b}^2 - g_1\, g_3 \ln(100 x_A x_B)\tilde{b}\right\}, \tag{1.52}$$

with M_0 = 1.6 GeV, $g_1 = 0.11^{+0.04}_{-0.03}$ GeV^2, $g_2 = 0.58^{+0.1}_{-0.2}$ GeV^2, and $g_3 = -1.5^{+0.1}_{-0.1}$ GeV^{-1}. Recently, Brock, Landry, Nadolsky, and Yuan proposed a modified Gaussian form [240],

$$F^{\mathrm{NP}}_{\mathrm{BLNY}}(\tilde{b}, M, x_A, x_B) = \exp\left\{-\left[g_1 + g_2 \ln(M/2M_0) + g_1\, g_3 \ln(100 x_A x_B)\right]\tilde{b}^2\right\}, \tag{1.53}$$

with M_0 = 1.6 GeV, $g_1 = 0.21^{+0.01}_{-0.01}$ GeV^2, $g_2 = 0.68^{+0.01}_{-0.02}$ GeV^2, and $g_3 = -0.6^{+0.05}_{-0.04}$. All these parameters were obtained by fitting low-energy Drell–Yan and high-energy W and Z data. Note, however, that the $\tilde{b}_*$ formalism introduces a modification to the perturbative calculation. The size of the modifications strongly depends on the nonperturbative parameters in $F^{\mathrm{NP}}(\tilde{b}, M, x_A, x_B)$, M, and $\sqrt{s}$ [237].

A remarkable feature of the $\tilde{b}$-space resummation formalism is that the resummed exponential factor $\exp[-S(\tilde{b}, M)]$ suppresses the $\tilde{b}$-integral when $\tilde{b}$ is larger than $1/M$. It can be shown using the saddle point method that, for a large enough M, QCD perturbation theory is valid even at p_T = 0 [178]. For high-energy heavy boson (W, Z, and Higgs) production, the integrand of $\tilde{b}$-integration in Eq. (1.47) at

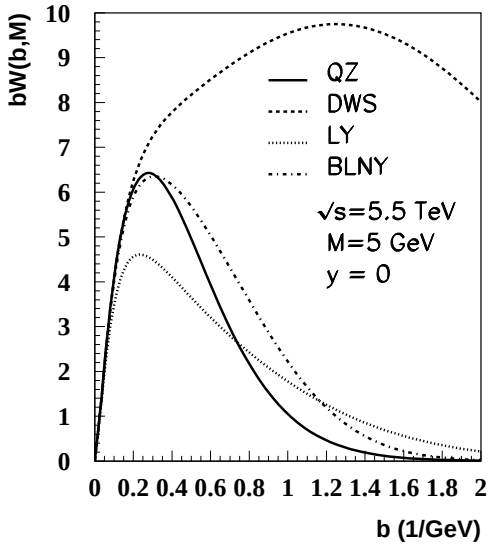

Fig. 1.36: The $\tilde{b}$-space resummed functions $\tilde{b}W(\tilde{b})$ in Eq. (1.47) for Drell–Yan production of dilepton mass M = 5 GeV at $\sqrt{s}$ = 5.5 TeV with the QZ (solid), DWS (dashed), LY (dotted), and BNLY (dot–dashed) formalism of nonperturbative extrapolation

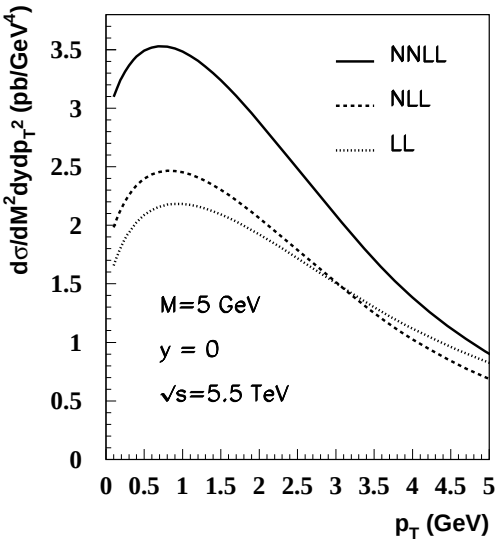

Fig. 1.37: Differential cross section $d\sigma/dM^2dydp_T^2$ for production of Drell–Yan pairs of M = 5 GeV in pp collisions at the LHC with y = 0, and $\sqrt{s}$ = 5.5 TeV with the NNLL (solid), NLL (dashed), and LL (dotted) accuracy

p_T = 0 is proportional to $\tilde{b}W(\tilde{b}, Q, x_A, x_B)$, with a saddle point $\tilde{b}_{\rm sp}$ well within the perturbative region ($\tilde{b}_{\rm sp} < \tilde{b}_{\rm max}$). Therefore, the $\tilde{b}$-integration in Eq. (1.47) is dominated by the perturbatively resummed calculation. The uncertainties from the large-$\tilde{b}$ region have very little effect on the calculated p_T distributions and the resummation formalism has good predictive power.

On the other hand, in low-energy Drell–Yan production, there is no saddle point in the perturbative region for the integrand in Eq. (1.47). Therefore the dependence of the final result on the nonperturbative input is strong [177, 235]. However, as discussed in Refs. [177, 179, 237], the value of the saddle point strongly depends on $\sqrt{s}$ in addition to its well-known M^2 dependence.

Figure 1.36 shows the integrand of the $\tilde{b}$-integration in Eq. (1.47) at p_T = 0 for production of Drell–Yan pairs of mass M = 5 GeV in pp collisions at $\sqrt{s}$ = 5.5 TeV and $b_{\rm max}$ = 0.5 GeV^{-1}. The curves represent different extrapolations to the large-$\tilde{b}$ region. The three curves (dashed, dotted, and dot–dashed) are evaluated using the $\tilde{b}_*$ formalism with the DWS, LY, and BLNY nonperturbative functions, respectively. Although these three nonperturbative functions give similar $\tilde{b}$-space distributions for heavy-boson production at Tevatron energies, they predict very different $\tilde{b}$-space distributions for low-mass Drell–Yan production at LHC energies even within the perturbative small-$\tilde{b}$ region. Since the $\tilde{b}$-distribution in Fig. 1.36 completely determines the resummed p_T distribution through the $\tilde{b}$-integration weighted by the Bessel function $J_0(p_T\tilde{b})$, we need to worry about the uncertainties of the resummed low-mass p_T distributions calculated with different nonperturbative functions.

In order to improve the situation, a new formalism of extrapolation (QZ) was proposed [177],

$$W(\tilde{b}, M, x_A, x_B) = \begin{cases} W^{\rm pert}(\tilde{b}, M, x_A, x_B) & \tilde{b} \le \tilde{b}_{\rm max} \\ W^{\rm pert}(\tilde{b}_{\rm max}, M, x_A, x_B)\, F^{\rm NP}(\tilde{b}, M, x_A, x_B; \tilde{b}_{\rm max}, \alpha) & \tilde{b} > \tilde{b}_{\rm max} \end{cases} , \quad (1.54)$$

where the nonperturbative function $F^{\rm NP}$ is given by

$$F^{\rm NP} = \exp\left\{ -\ln(M^2\tilde{b}_{\rm max}^2/c^2) \left[g_1 \left((\tilde{b}^2)^\alpha - (\tilde{b}_{\rm max}^2)^\alpha \right) + g_2 \left(\tilde{b}^2 - \tilde{b}_{\rm max}^2 \right) \right] - \bar{g}_2 \left(\tilde{b}^2 - \tilde{b}_{\rm max}^2 \right) \right\} . \quad (1.55)$$

Here, $\tilde{b}_{\rm max}$ is a parameter to separate the perturbatively calculated part from the nonperturbative input, and its role is similar to the $\tilde{b}_{\rm max}$ in the $\tilde{b}_*$ formalism. The term proportional to g_1 in Eq. (1.55) represents

a direct extrapolation of the resummed leading power contribution to the large-$\tilde{b}$ region. The parameters g_1 and α are determined by the continuity of the function $W(\tilde{b}, M, x_A, x_B)$ at $\tilde{b}_{\rm max}$. On the other hand, the values of g_2 and $\bar{g}_2$ represent the size of nonperturbative power corrections. Therefore, sensitivity to g_2 and $\bar{g}_2$ in this formalism clearly indicates the precision of the calculated p_T distributions.

The solid line in Fig. 1.36 is the result of the QZ parametrization with $\tilde{b}_{\rm max}$ = 0.5 GeV^{-1} and $g_2 = \bar{g}_2$ = 0. Unlike in the $\tilde{b}_*$ formalism, the solid line represents the full perturbative calculation and is independent of the nonperturbative parameters for $\tilde{b} < \tilde{b}_{\rm max}$. The difference between the solid line and the other curves in the small-$\tilde{b}$ region, which can be as large as 40%, indicates the uncertainties introduced by the $\tilde{b}_*$ formalism.

It is clear from the solid line in Fig. 1.36 that there is a saddle point in the perturbative region even for dilepton masses as low as M = 5 GeV in Drell–Yan production at $\sqrt{s}$ = 5.5 TeV. At that energy, $x_A, x_B \sim 0.0045$. For such small values of x, the PDFs have very strong scaling violations, leading to large parton showers. It is the large parton shower at the small x that strongly suppresses the function $W(\tilde{b}, c/\tilde{b}, x_A, x_B)$ in Eq. (1.48) as $\tilde{b}$ increases. Therefore, for $\tilde{b}_{\rm max}$ $\sim$(a few GeV)$^{-1}$, the predictive power of the $\tilde{b}$-space resummation formalism depends on the relative size of contributions from the small-$\tilde{b}$ ($\tilde{b} < \tilde{b}_{\rm max}$) and large-$\tilde{b}$ ($\tilde{b} > \tilde{b}_{\rm max}$) regions of the $\tilde{b}$-integration in Eq. (1.47). With a narrow $\tilde{b}$ distribution peaked within the perturbative region for the integrand, the $\tilde{b}$-integration in Eq. (1.48) is dominated by the small-$\tilde{b}$ region and, therefore, we expect pQCD to have good predictive power even for low-M Drell–Yan production at LHC energies.

Figure 1.37 presents our prediction of the fully differential cross section $d\sigma/dM^2 dy dp_T^2$ for Drell–Yan production in pp collisions at $\sqrt{s}$ = 5.5 TeV and y = 0 [234]. Three curves represent the different order of contributions in α_s to the perturbatively calculated functions $\mathcal{A}(\alpha_s)$, $\mathcal{B}(\alpha_s)$, and $\mathcal{C}(\alpha_s)$ in the resummation formalism [241]. The solid line represents a next-to-next-to-leading-logarithmic (NNLL) accuracy corresponding to keeping the functions, $\mathcal{A}(\alpha_s)$, $\mathcal{B}(\alpha_s)$, and $\mathcal{C}(\alpha_s)$ to order α_s^3, α_s^2, and α_s^1, respectively. The dashed line has next-to-leading-logarithmic (NLL) accuracy with the functions, $\mathcal{A}(\alpha_s)$, $\mathcal{B}(\alpha_s)$, and $\mathcal{C}(\alpha_s)$ at α_s^2, α_s, and α_s^0, respectively, while the dotted line has the lowest leading-logarithmic (LL) accuracy with the functions, $\mathcal{A}(\alpha_s)$, $\mathcal{B}(\alpha_s)$, and $\mathcal{C}(\alpha_s)$ at the α_s, α_s^0, and α_s^0, respectively. Similar to what was seen in the fixed-order calculation, the resummed p_T distribution has a K-factor about 1.4–1.6 around the peak due to the inclusion of the coefficient $\mathcal{C}^{(1)}$.

In Eq. (1.55), in addition to the g_1 term from the leading power contribution of soft gluon showers, the g_2 term corresponds to the first power correction from soft gluon showers and the $\bar{g}_2$ term is from the intrinsic transverse momentun of the incident parton. The numerical values of g_2 and $\bar{g}_2$ have to be obtained from fits to the data. From fits of low-energy Drell–Yan data and heavy gauge boson data at the Tevatron, we found that the intrinsic transverse-momentum term dominates the power corrections. It has a weak energy dependence. For convenience, we combine the parameters of the $\tilde{b}^2$ term as $G_2 = g_2 \ln(M^2 \tilde{b}_{\rm max}^2/c^2) + \bar{g}_2$. For M = 5 GeV and y = 0, we use $G_2 \sim 0.25$ in the discussion here [177]. To test the G_2 dependence of our calculation, we define

$$R_{G_2}(p_T) \equiv \frac{d\sigma^{(G_2)}_{AB\to l\bar{l}(M)X}(p_T)}{dM^2\, dy\, dp_T^2} \Bigg/ \frac{d\sigma_{AB\to l\bar{l}(M)X}(p_T)}{dM^2\, dy\, dp_T^2}\,, \tag{1.56}$$

where the numerator represents the result with finite G_2, and the denominator contains no power corrections, G_2 = 0.

The result for R_{G_2} is shown in Fig. 1.38. It deviates from unity by less than 1%. The dependence of our result on the nonperturbative input is indeed very weak.

Since the G_2 terms represent the power corrections from soft gluon showers and parton intrinsic transverse momenta, the smallness of the deviation of R_{G_2} from unity also means that leading power contributions from gluon showers dominate the dynamics of low-mass Drell–Yan production at LHC energies. Even though the power corrections will be enhanced in nuclear collisions, we expect them

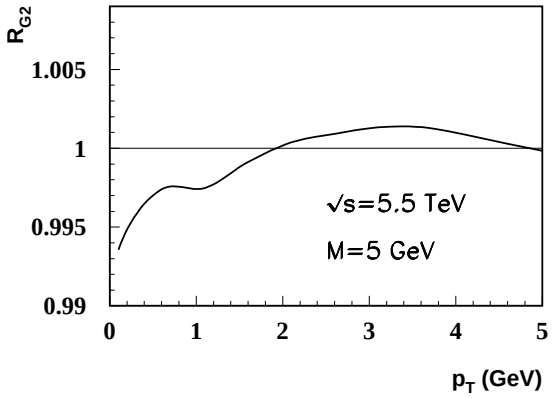

Fig. 1.38: The ratio R_{G_2} defined in Eq. (1.56) with G_2 = 0.25 GeV^2 for the differential cross section shown in Fig. 1.37

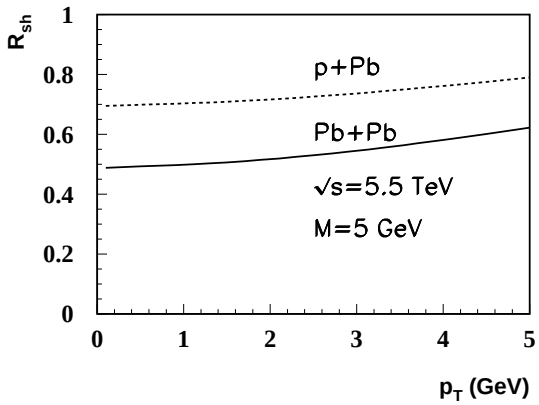

Fig. 1.39: $R_{\rm sh}$ as a function of p_T using EKS shadowing in pPb and PbPb collisions at $\sqrt{s}$ = 5.5 TeV

to be still less than several per cent [179]. The isospin effects are also small here because x_A and x_B are small.

Since the leading power contributions from initial-state parton showers dominate the production dynamics, the important nuclear effect is the modification of the parton distributions. Because x_A and x_B are small for low-mass Drell–Yan production at LHC energies, shadowing is the only dominant nuclear effect. In order to study the shadowing effects, we define [179]

$$R_{\rm sh}(p_T) \equiv \frac{d\sigma^{(\rm sh)}_{AB\to l\bar{l}(M)X}(p_T, Z_A/A, Z_B/B)}{dM^2\, dy\, dp_T^2} \Bigg/ \frac{d\sigma_{AB\to l\bar{l}(M)X}(p_T)}{dM^2\, dy\, dp_T^2}\,. \tag{1.57}$$

We plot the ratio $R_{\rm sh}$ as a function of p_T in PbPb collisions at $\sqrt{s}$ = 5.5 TeV for M = 5 GeV and y = 0 in Fig. 1.39. The EKS parametrization of nuclear parton distributions [27, 28] was used to evaluate the cross sections in Eq. (1.57). It is clear from Fig. 1.39 that low-mass Drell–Yan production can be a good probe of nuclear shadowing [234], both in PbPb and in pPb collisions at the LHC.

6.2.3. Low-mass Drell–Yan production at high transverse momentum

The gluon distribution plays a central role in calculating many important signatures at hadron colliders because of the dominance of gluon-initiated subprocesses. A precise knowledge of the gluon distribution as well as its nuclear dependence is absolutely vital for understanding both hard and semihard probes at LHC energies.

It was pointed out recently that the transverse-momentum distribution of massive lepton pairs produced in hadronic collisions is an advantageous source of constraints on the gluon distribution [242], free from the experimental and theoretical complications of photon isolation that beset studies of prompt photon production [243, 244]. Other than the difference between a virtual and a real photon, the Drell–Yan process and prompt photon production share the same partonic subprocesses. Similar to prompt photon production, the lowest-order virtual photon 'Compton' subprocess $g + q \to \gamma^* + q$ dominates the p_T distribution when $p_T > M/2$. The next-to-leading order contributions preserve the fact that the p_T distributions are dominated by gluon-initiated partonic subprocesses [242].

There is a phase space penalty associated with the finite mass of the virtual photon, and the Drell–Yan factor $\alpha_{\rm em}/(3\pi M^2) < 10^{-3}/M^2$ in Eq. (1.45) renders the production rates for massive lepton pairs

small at large values of M and p_T. In order to enhance the Drell–Yan cross section while keeping the dominance of the gluon-initiated subprocesses, it is useful to study lepton pairs with low invariant mass and relatively large transverse momenta [236]. With the large p_T setting the hard scale of the collision, the invariant mass of the virtual photon M can be small, as long as the process can be identified experimentally and $M \gg \Lambda_{\rm QCD}$. For example, the cross section for Drell–Yan production was measured by the CERN UA1 Collaboration [245] for virtual photon mass $M \in [2m_\mu, 2.5]$ GeV.

When $p_T^2 \gg M^2$, the perturbatively calculated short-distance partonic parts, $d\hat{\sigma}_{ab\to\gamma^* X}/dp_T^2 dy$ in Eq. (1.45), receive one power of the logarithm $\ln(p_T^2/M^2)$ at every order of α_s beyond leading order. At sufficiently large p_T, the coefficients of the perturbative expansion in α_s will have large logarithmic terms, so that these higher-order corrections may not be small. In order to derive reliable QCD predictions, resummation of the logarithmic terms $\ln^m(p_T^2/M^2)$ must be considered. It was recently shown [236] that the large $\ln^m(p_T^2/M^2)$ terms in the low-mass Drell–Yan cross sections can be systematically resummed into a set of perturbatively calculable virtual-photon fragmentation functions [246]. Similar to Eq. (1.46), the differential cross section for low-mass Drell–Yan production at large p_T can be reorganized as

$$\frac{d\sigma_{AB\to l\bar{l}(M)X}}{dM^2\,dy\,dp_T^2} = \frac{d\sigma^{(\rm resum)}_{AB\to l\bar{l}(M)X}}{dM^2\,dy\,dp_T^2} + \frac{d\sigma^{(\rm Dir)}_{AB\to l\bar{l}(M)X}}{dM^2\,dy\,dp_T^2}\,, \tag{1.58}$$

where $\sigma^{(\rm resum)}$ includes the large logarithms and can be factorized as [236]

$$\begin{aligned}\frac{d\sigma^{(\rm resum)}_{AB\to l\bar{l}(M)X}}{dM^2\,dy\,dp_T^2} &= \Big(\frac{\alpha_{\rm em}}{3\pi M^2}\Big)\sum_{a,b,c}\int dx_1 f_{a/A}(x_1,\mu)\int dx_2 f_{b/B}(x_2,\mu) \\ &\quad\times\int\frac{dz}{z^2}\,\frac{d\hat{\sigma}_{ab\to cX}}{dp_{c_T}^2\,dy}(p_{c_T}=p_T/z)\;D_{c\to\gamma^* X}(z,\mu_F^2;M^2)\;,\end{aligned} \tag{1.59}$$

with the factorization scale μ and fragmentation scale μ_F, and virtual photon fragmentation functions $D_{c\to\gamma^*}(z,\mu_F^2;Q^2)$. The $\sigma^{(\rm Dir)}$ term plays the same role as $\sigma^{(\rm Y)}$ term in Eq. (1.46), dominating the cross section when $p_T \to M$.

Figure 1.40 presents the fully resummed transverse-momentum spectra of low-mass Drell–Yan production in pp collisions with M = 5 GeV at y = 0 and $\sqrt{s}$ = 5.5 TeV (solid). For comparison, we also plot the leading order spectra calculated in conventional fixed-order pQCD. The fully resummed distribution is larger in the large-p_T region and smoothly convergent as $p_T \to 0$. In addition, as discussed in Ref. [236], the resummed differential cross section is much less sensitive to the changes of renormalization, factorization, and fragmentation scales and should thus be more reliable than the fixed-order calculations.

To demonstrate the relative size of gluon-initiated contributions, we define the ratio

$$R_g = \frac{d\sigma_{AB\to\gamma^*(M)X}(\text{gluon-initiated})}{dp_T^2\,dy}\Bigg/\frac{d\sigma_{AB\to\gamma^*(M)X}}{dp_T^2\,dy}\,. \tag{1.60}$$

The numerator includes the contributions from all partonic subprocesses with at least one initial-state gluon while the denominator includes all subprocesses.

In Fig. 1.41, we show R_g as a function of p_T in pp collisions at y = 0 and $\sqrt{s}$ = 5.5 TeV with M = 5 GeV. It is clear from Fig. 1.41 that gluon-initiated subprocesses dominate the low-mass Drell–Yan cross section and that low-mass Drell–Yan lepton-pair production at large transverse-momentum is an excellent source of information about the gluon distribution [236]. The slow falloff of R_g at large-p_T is related to the reduction of phase space and the fact that cross sections are evaluated at larger values of x.

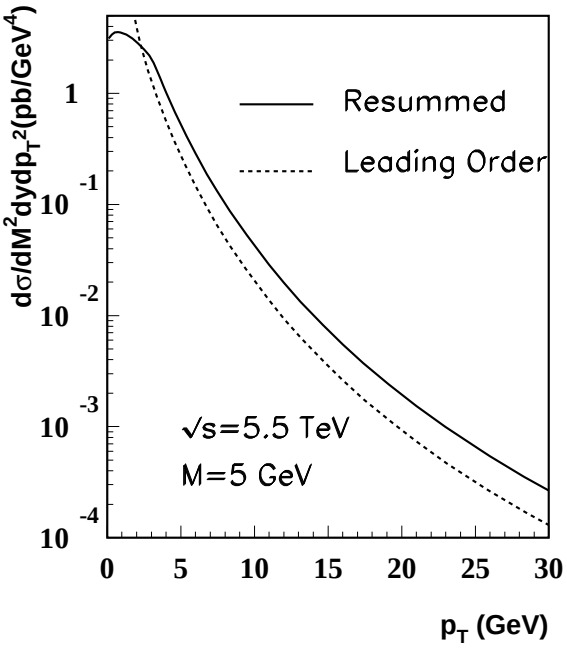

Fig. 1.40: Differential cross section $d\sigma/dM^2dydp_T^2$ for production of Drell–Yan pairs of M = 5 GeV in pp collisions at $\sqrt{s}$ = 5.5 TeV with low- and high-p_T resummation (solid), in comparison to conventional lowest result (dashed)

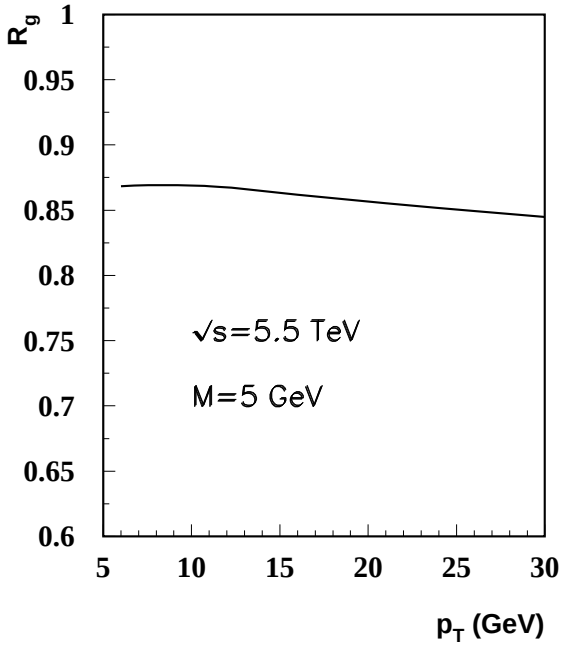

Fig. 1.41: Ratio of gluonic over total contributions to Drell–Yan production at the LHC, R_g, defined in Eq. (1.60) with M = 5 GeV at $\sqrt{s}$ = 5.5 TeV

6.2.4. Conclusions

In summary, we present the fully differential cross section of low-mass Drell–Yan production calculated in QCD perturbation theory with all-order resummation. For $p_T \ll M$, we use CSS $\tilde{b}$-space resummation formalism to resum large logarithmic contributions as singular as $(1/p_T^2)\ln^m(M^2/p_T^2)$ to all orders in α_s. We show that the resummed p_T distribution of low-mass Drell–Yan pairs at LHC energies is dominated by the perturbatively calculable small $\tilde{b}$-region and thus reliable for p_T as small as $\Lambda_{\rm QCD}$. Because of the dominance of small x PDFs, the low-mass Drell–Yan cross section is a good probe of the nuclear dependence of parton distributions. For $p_T \gg M$, we use a newly derived QCD factorization formalism [236] to resum all orders of $\ln^m(p_T^2/M^2)$ type logarithms. We show that almost 90% of the low-mass Drell–Yan cross sections at LHC energies is from gluon initiated partonic subprocesses. Therefore, the low-mass Drell–Yan cross section at $p_T > M$ is an advantageous source of information on the gluon distribution and its nuclear dependence — shadowing. Unlike other probes of gluon distributions, low-mass Drell–Yan does not have the problem of isolation cuts associated with direct photon production at collider energies and does not have the hadronization uncertainties of J/ψ and charm production. Moreover, the precise information on dilepton production in the Drell–Yan channel is critical for studying charm production at LHC energies.

6.3. Angular Distribution of Drell–Yan Pairs in pA at the LHC

R.J. Fries

6.3.1. Introduction

The Drell–Yan cross section can be described by a contraction of the lepton and hadron tensors

$$\frac{d\sigma}{dM^2\,dp_T^2\,dy\,d\Omega} = \frac{\alpha_{\rm em}^2}{64\pi^3 s M^4} L_{\mu\nu} W^{\mu\nu}\,. \tag{1.61}$$

Here we parametrize the lepton pair by the invariant mass M of the virtual photon and its transverse-momentum p_T and rapidity y in the centre-of-mass frame of the colliding hadrons. In addition we give the direction of one of the leptons, say the positively charged one, in the photon rest frame using polar and azimuthal angles ϕ and θ: $d\Omega = d\phi\, d\cos\theta$. Now the cross section can be understood in terms of four helicity amplitudes [247–249]

$$\begin{aligned}\frac{d\sigma}{dM^2\,dp_T^2\,dy\,d\Omega} = \frac{\alpha_{\rm em}^2}{64\pi^3 s M^2}\Big[&W_{\rm TL}\,(1+\cos^2\theta) + W_{\rm L}\,(1/2 - 3/2\cos^2\theta)\\ &+ W_\Delta\,\sin 2\theta\cos\phi + W_{\Delta\Delta}\,\sin^2\theta\cos 2\phi\Big]\,.\end{aligned} \tag{1.62}$$

These are defined as contractions $W_{\sigma,\sigma'} = \epsilon_\mu(\sigma) W^{\mu\nu} \epsilon_\nu^*(\sigma')$ of the hadron tensor with polarization vectors of the virtual photon for polarizations σ = 0, ± 1. Only four out of all possible contractions are independent, the others can be related by symmetries of the hadron tensor. The usual choice is to pick the longitudinal $W_{\rm L} = W_{0,0}$, the helicity flip $W_\Delta = (W_{1,0} + W_{0,1})/\sqrt{2}$ and the double helicity-flip amplitude $W_{\Delta\Delta} = W_{1,-1}$ together with the trace $W_{\rm TL} = W_{\rm T} + W_{\rm L}/2 = -W_\mu^\mu/2$ as a basis. Note that integration over the angles θ and ϕ leaves only contributions from the trace

$$\frac{d\sigma}{dM^2\,dp_T^2\,dy} = \frac{\alpha_{\rm em}^2}{64\pi^3 s M^2}\,\frac{16\pi}{3}\,W_{\rm TL} = \frac{\alpha_{\rm em}^2}{24\pi^2 s M^2}\,(-g_{\mu\nu})\,W^{\mu\nu}\,. \tag{1.63}$$

On the other hand, if we are only interested in relative angular distributions, i.e. in the ratio

$$\frac{16\pi}{3}\,\frac{d\sigma}{dM^2\,dp_T^2\,dy\,d\Omega}\Big/\,\frac{d\sigma}{dM^2\,dp_T^2\,dy}\,, \tag{1.64}$$

we can make use of angular coefficients. Two different sets can be found in the literature [250]. One set consists of the coefficients

$$A_0 = \frac{W_{\rm L}}{W_{\rm TL}}\,, \qquad A_1 = \frac{W_\Delta}{W_{\rm TL}}\,, \qquad A_2 = \frac{2W_{\Delta\Delta}}{W_{\rm TL}}\,, \tag{1.65}$$

the other one is defined by

$$\lambda = \frac{2-3A_0}{2+A_0}\,, \qquad \mu = \frac{2A_1}{2+A_0}\,, \qquad \nu = \frac{2A_2}{2+A_0}\,. \tag{1.66}$$

The helicity amplitudes are frame-dependent. In principle we allow all frames where the photon is at rest, i.e. $q^\mu = (M,0,0,0)$. However, there are some frames with particular properties studied in Ref. [248]. Here we use only the Collins–Soper (CS) frame. It is characterized by two properties. First, the y-axis is perpendicular to the plane spanned by the two hadron momenta $\mathbf{P}_1$ and $\mathbf{P}_2$ (which are no longer collinear in the photon rest frame as long as $p_T \neq 0$, as in our kinematic domain) and second, the z-axis cuts the angle between $\mathbf{P}_1$ and $-\mathbf{P}_2$ into two equal halves, see Fig. 1.42.

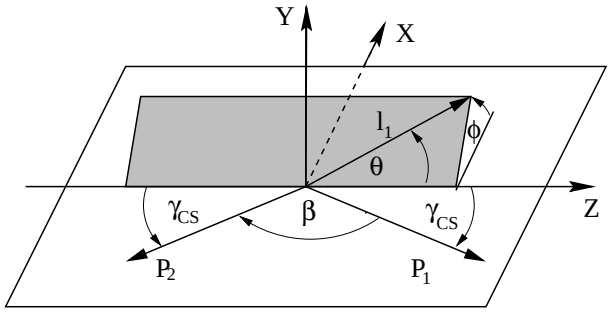

Fig. 1.42: The Collins–Soper frame: the z-axis cuts the angle between $\mathbf{P}_1$ and $-\mathbf{P}_2$ into halves (the half angle is called the Collins–Soper angle $\gamma_{\rm CS}$) while the x-axis is perpendicular to $\mathbf{P}_1$ and $\mathbf{P}_2$. The direction of one lepton momentum $\mathbf{l}_1$ can then be given by the angles θ and ϕ.

6.3.2. Leading twist

The hadron tensor for the Drell–Yan process in a leading-twist (twist-2) calculation is given by the well-known factorization formula as a convolution of two parton distributions with a perturbative parton cross section. We are interested here in the kinematic region characterized by intermediate photon mass M of a few GeV and intermediate transverse-momentum $p_T \sim M$. For these values, the dominant contribution to twist-2 is given by the NLO perturbative diagrams like the one in Fig. 1.43 (left) and we can safely omit logarithmic corrections of type $\ln^2(M^2/p_T^2)$. It has been shown that a leading-twist calculation up to NLO respects the so-called Lam–Tung sum rule, $W_{\rm L} = 2W_{\Delta\Delta}$ [251]. In terms of angular coefficients this can be rewritten as $A_0 = A_2$ or $2\nu = 1 - \lambda$. Furthermore, the spin-flip amplitude W_Δ has to vanish for a symmetric colliding system like pp. For pA we expect small contributions for W_Δ due to lost isospin symmetry and nuclear corrections to the parton distributions. Results for pp at $\sqrt{s}$ = 5.5 TeV have already been presented elsewhere [252].

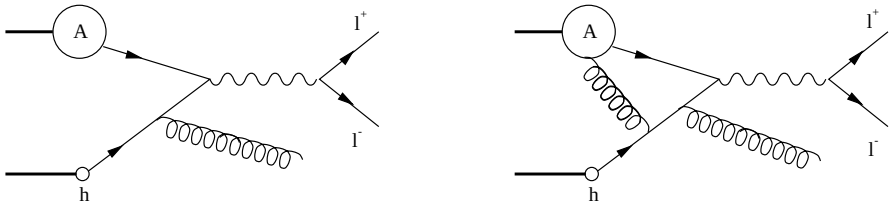

Fig. 1.43: Examples for diagrams contributing to the dilepton production in hadron (h) nucleus (A) scattering at twist-2 (left) and twist-4 (right) level

6.3.3. Nuclear-enhanced twist-4

For large nuclei, corrections to the leading-twist calculation, induced by multiple scattering, play an important role. The formalism for including these nuclear-enhanced higher-twist contributions was worked out by Luo, Qiu and Sterman [36, 253, 254]. The leading nuclear corrections (twist-4 or double scattering) have already been calculated for some observables. For Drell–Yan this was first done by Guo [37] and later generalized to the Drell–Yan angular distribution [250, 255].

Figure 1.43 (right) shows an example for a diagram contributing at twist-4 level. Now two partons a, b from the nucleus and one (c) from the single hadron are involved. As long as $p_T \sim M$, twist-4 is dominated by two different contributions. The double-hard (DH) process where each parton from the nucleus has a finite momentum fraction and the soft-hard (SH) process where one parton has vanishing

momentum fraction. The factorization formulas are given by

$$W^{\mu\nu} = \sum_{a,b,c} \int \frac{dx_c}{x_c}\, T_{ab}^{\mathrm{DH}}(x_a, x_b)\, H_{ab+c}^{\mu\nu}(q, x_a, x_b, x_c)\, f_c(x_c)\,, \tag{1.67}$$

$$W^{\mu\nu} = \sum_{a,b,c} \int \frac{dx_c}{x_c}\, D_{x_a,x_b}(q, x_c) T_{ab}^{\mathrm{SH}}(x_a)\, H_{ab+c}^{\mu\nu}(q, x_a, x_b = 0, x_c)\, f_c(x_c) \tag{1.68}$$

for double-hard and soft-hard scattering, respectively [37, 250, 255]. The function $D_{x_a,x_b}(q, x_c)$ is a second-order differential operator in x_a and x_b while T_{ab}^{DH} and T_{ab}^{SH} are new twist-4 matrix elements which encode nonperturbative correlations between the partons a and b. Since we are still missing solid experimental information about these new quantities, they are usually modelled in a simple way through parton distributions. We use $T_{ab}^{\mathrm{DH}}(x_a, x_b) = CA^{4/3} f_a(x_a) f_b(x_b)$ and $T_{ab}^{\mathrm{SH}}(x_a) = \lambda^2 A^{4/3} f_a(x_a)$ where C and λ^2 are normalization constants. The key feature, the nuclear enhancement, is their scaling with the nuclear size.

It has been shown in Refs. [250, 255] that the DH process shows a trivial angular pattern in the sense that it is similar to the LO annihilation of on-shell quarks. The only difference is that one of the quarks now carries finite p_T. In this spirit, it is no surprise that the DH contribution respects the Lam–Tung relation. On the other hand, SH scattering is more complicated and violates the Lam–Tung sum rule. We also expect that the spin-flip amplitude W_Δ can receive large contributions from the twist-4 calculation.

6.3.4. Numerical results

In this section, we present some numerical results obtained for pPb collisions at the LHC energy $\sqrt{s}$ = 8.8 TeV. Results for RHIC energies can be found elsewhere [250]. We use the CTEQ5L parton distributions [86] combined with EKS98 [27] nuclear modifications both for the nuclear parton distributions and for the models of the twist-4 matrix elements. In some plots we also give results for double-hard contributions without nuclear modification. Since we do not know anything about the correct x-dependence of the higher-twist matrix elements, this gives an impression of the theoretical uncertainty we may assume for the higher-twist calculation. The normalization constants for the twist-4 matrix elements are chosen to be $\lambda^2 = 0.01$ GeV^2 and C = 0.005 GeV^2. In order to enable convenient comparison with cross sections, we show all helicity amplitudes multiplied by the prefactor $N_\sigma = \alpha_{\mathrm{em}}^2/(64\pi^3 s M^2)$ of Eq. (1.62).

In Fig. 1.44 we give results for the helicity amplitudes W_{TL} and W_Δ as functions of rapidity. We observe that DH scattering gives a large contribution at negative rapidities (the direction of the proton) which can easily balance the suppression of the twist-2 contribution by shadowing. Soft-hard scattering is strongly suppressed at these energies. W_{L} (not shown) has qualitatively the same behaviour as W_{TL}. The helicity-flip amplitude W_Δ picks up only a small contribution from twist-2 and is entirely dominated by double-hard scattering, as already expected. This would be a good observable to pin down nuclear effects in pA collisions. Figure 1.45 gives the full set of angular coefficients λ, μ and ν as functions of y and p_T. Both the twist-2 results and the modifications by twist-4 are given. The violation of the Lam–Tung sum rule is numerically almost negligible since the soft-hard contribution is so small. Note here that earlier experiments have discovered a large violation of the Lam–Tung relation in πA collisions [256]. This issue is still not fully resolved.

Thus pA collisions offer the unique opportunity to study nuclear effects directly via the rapidity dependence of observables. Helicity amplitudes and angular coefficients can help to pin down the role of nuclear-enhanced higher twist. The helicity-flip amplitude W_Δ and the coefficient μ, which both vanish for pp, are particularly promising. Several different species of nuclei are advisable to address the important question of A scaling.

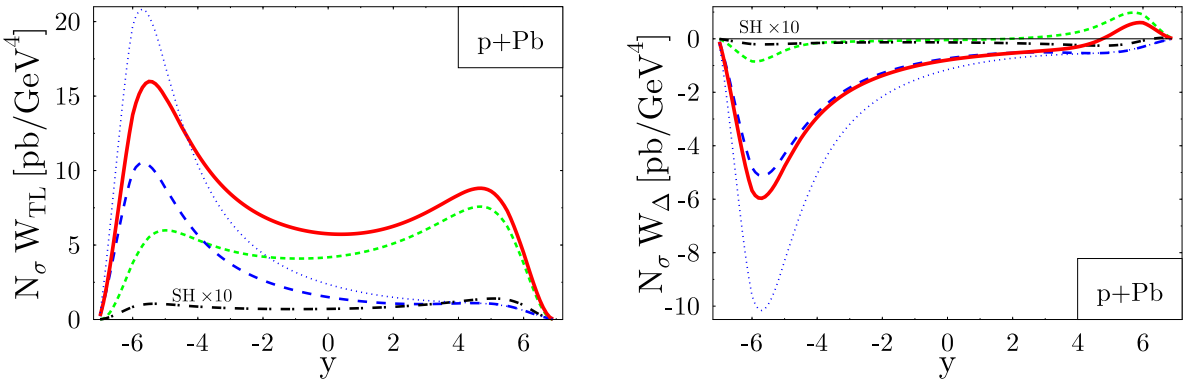

Fig. 1.44: Rapidity dependence of $N_\sigma W_{\rm TL}$ (left) and $N_\sigma W_\Delta$ (right) for pPb at $\sqrt{s}$ = 8.8 TeV, M = 5 GeV and p_T = 4 GeV: twist-2 NLO (short dashed), double-hard with EKS98 modifi cations (long dashed), soft hard (dot–dashed, scaled up by a factor of 10) and the sum of all contributions (bold solid line). The double hard contribution calculated without EKS98 modifi cations is also shown (dotted line). Note that the incoming nucleus has positive rapidity.

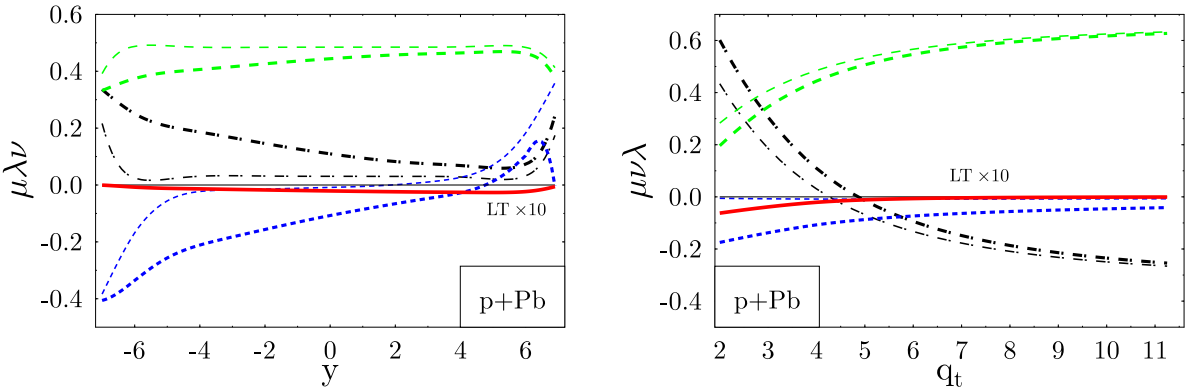

Fig. 1.45: The angular coeffi cients λ (long dashed), μ (short dashed) and ν (dot dashed) for pPb at $\sqrt{s}$ = 8.8 TeV and M = 5 GeV as functions of rapidity (left, at p_T = 4 GeV) and transverse-momentum (right, at y = 0). Thin lines represent pure twist-2 calculations, thick lines show the results including twist-4. The solid line gives the violation of the Lam–Tung relation $2\nu - (1 - \lambda)$ scaled up by a factor of 10.

In addition, the angular distribution of Drell–Yan lepton pairs might play a crucial role in the extraction of the Drell–Yan process from dilepton data. Dilepton spectra at the LHC have a large contribution from the decay of correlated and uncorrelated heavy quark pairs [79, 80]. However, the angular pattern of these dileptons is isotropic rather than modulated as in the Drell–Yan case. This provides additional means to discriminate between Drell–Yan dileptons and those from heavy quark decays.

6.4. Heavy Flavour Total Cross Sections

R. Vogt

Heavy quark production will be an important part of the LHC programme, with both open heavy flavours and quarkonium studied extensively. Heavy quark production will probe the small-x region of the gluon distribution in the proton and in the nucleus: at y = 0, $x \sim 4 \times 10^{-4}$ for charm and $x \sim 0.0011$ for bottom. Direct information on the gluon distribution in the proton is still lacking, let alone the nucleus. Open heavy-flavour production is a better direct test of the nuclear gluon distribution than quarkonium which is subject to other cold matter effects such as nuclear absorption.

Heavy quark studies in pA interactions provide important benchmarks for further measurements in AA. More than one $Q\overline{Q}$ pair (bottom as well as charm) will be produced in each central AA collision. Therefore heavy quark decays will dominate the lepton-pair continuum between the J/ψ and Z^0 peaks [169]. Although heavy quark energy loss in the medium is currently expected to be small [257], the shape of the dilepton continuum could be significantly altered due to modifications of the heavy quark distributions by energy loss [80, 258]. An understanding of heavy quark production in pA is also a necessity for the study of quarkonium production in AA collisions. Models predicting a quarkonium enhancement relative to heavy flavour production in nuclear collisions require a reliable measure of the heavy flavour production rates in AA collisions with shadowing included to either verify or disprove these predictions.

In this section, we first discuss our estimates of the $Q\overline{Q}$ total cross sections and some of their associated uncertainties. We then describe a more detailed measurement of the nuclear gluon distribution using dileptons from heavy quark decays.

At LO heavy quarks are produced by gg fusion and $q\overline{q}$ annihilation while at NLO qg and $\overline{q}g$ scattering is also included. To any order, the partonic cross section may be expressed in terms of dimensionless scaling functions $f_{ij}^{(k,l)}$ that depend only on the variable η [259],

$$\hat{\sigma}_{ij}(\hat{s}, m_Q^2, Q^2) = \frac{\alpha_s^2(Q^2)}{m^2} \sum_{k=0}^{\infty} \left(4\pi\alpha_s(Q^2)\right)^k \sum_{l=0}^{k} f_{ij}^{(k,l)}(\eta) \ \ln^l\left(\frac{Q^2}{m_Q^2}\right) , \tag{1.69}$$

where $\hat{s}$ is the partonic centre-of-mass energy squared, m_Q is the heavy quark mass, Q is the scale and $\eta = \hat{s}/4m_Q^2 - 1$. The cross section is calculated as an expansion in powers of α_s with k = 0 corresponding to the Born cross section at order $\mathcal{O}(\alpha_s^2)$. The first correction, $k = 1$, corresponds to the NLO cross section at $\mathcal{O}(\alpha_s^3)$. It is only at this order and above that the dependence on renormalization scale Q_R enters the calculation since when $k = 1$ and $l = 1$ the logarithm $\ln(Q^2/m_Q^2)$ appears, as in gauge boson and Drell–Yan production at $\mathcal{O}(\alpha_s)$, described in Section 5.1. The dependence on the factorization scale Q_F in the argument of α_s, appears already at LO. We assume that $Q_R = Q_F = Q$. The next-to-next-to-leading order (NNLO) corrections to next-to-next-to-leading logarithm (NNLL) have been calculated near threshold [259] but the complete calculation only exists to NLO.

The total hadronic cross section is obtained by convoluting the total partonic cross section with the parton distribution functions (PDFs) of the initial hadrons,

$$\sigma_{pp}(s, m_Q^2) = \sum_{i,j=q,\overline{q},g} \int_{\frac{4m_Q^2}{s}}^{1} \frac{d\tau}{\tau} \, \delta(x_1 x_2 - \tau) \, \frac{f_i^p(x_1, Q^2)}{x_1} \, \frac{f_j^p(x_2, Q^2)}{x_2} \, \hat{\sigma}_{ij}(\tau, m_Q^2, Q^2) \, , \tag{1.70}$$

where the sum i is over all massless partons and x_1 and x_2 are fractional momenta. The parton densities are evaluated at scale Q. All our calculations are fully NLO, applying NLO parton distribution functions and the two-loop α_s to both the $\mathcal{O}(\alpha_s^2)$ and $\mathcal{O}(\alpha_s^3)$ contributions, as is typically done [219, 259].

To obtain the pp cross sections at the LHC, we compare the NLO cross sections to the available $c\overline{c}$ and $b\overline{b}$ production data by varying the mass, m_Q, and scale, Q, to obtain the 'best' agreement with the data for several combinations of m_Q, Q, and PDF. We use the recent MRST HO central gluon [172], CTEQ 5M [86], and GRV 98 HO [45] distributions. The charm mass is varied between 1.2 and 1.8 GeV with scales between m_c and $2m_c$. The bottom mass is varied over 4.25–5 GeV with $m_b/2 \leq Q \leq 2m_b$. The best agreement for $Q = m_c$ is with m_c = 1.4 GeV, and m_c = 1.2 GeV is the best choice using $Q = 2m_c$ for the MRST HO and CTEQ 5M distributions. The best agreement with GRV 98 HO is $Q = m_c$ = 1.3 GeV while the results with $Q = 2m_c$ lie below the data for all m_c. All five results agree very well with each other for $pp \to c\overline{c}$. We find reasonable agreement with all three PDFs for $m_b = Q$ = 4.75 GeV, $m_b = Q/2$ = 4.5 GeV, and $m_b = 2Q$ = 5 GeV.

Before calculating the $Q\overline{Q}$ cross sections at nuclear colliders, some comments need to be made about the validity of the procedure. Since the $c\overline{c}$ calculations can only be made to agree with the data

when somewhat lower than average quark masses are used and the $pp \to b\bar{b}$ data also need smaller m_b to agree at NLO, it is reasonable to expect that corrections beyond NLO could be large. Indeed, the preliminary HERA-B cross section agrees with the NNLO–NNLL cross section in Ref. [259], suggesting that the next-order correction could be nearly a factor of two. Thus the NNLO correction could be nearly as large as the NLO cross section.

Unfortunately, the NNLO–NNLL calculation is not a full result and is valid only near threshold. The $p\bar{p}$ data at higher energies, while not total cross sections, also show a large discrepancy between the perturbative NLO result and the data, nearly a factor of three [260]. This difference could be accounted for using unintegrated parton densities [261] although the unintegrated distributions vary widely. The problem remains how to connect the regimes where near-threshold corrections are applicable and where high-energy, small-x physics dominates. The problem is increased for charm where, even at low energies, we are far away from threshold.

We take the most straightforward approach — comparing the NLO calculations to the pp and π^-p data without higher-order corrections. The $c\bar{c}$ data are extensive while the $b\bar{b}$ data are sparse. The $c\bar{c}$ data tend to favor lighter charm masses but the $b\bar{b}$ data are less clear. A value of m_b = 4.75 GeV underpredicts the Tevatron results [260] at NLO but agrees reasonably with the average of the π^-p data. However, for the HERA-B measurement [262] to be compatible with a NLO evaluation, the b quark mass would have to be reduced to 4.25 GeV, perhaps more compatible with the Tevatron results. Therefore, if the NNLO cross section could be calculated fully, it would likely be more compatible with a larger quark mass. A quantitative statement is not possible, particularly for charm which is far enough above threshold at fixed-target energies for the approximation to be questionable [263], see however Ref. [264].

If we assume that the energy dependence of the NNLO and higher order cross sections is not substantially different from that at LO and NLO, then we should be in the right range for collider energies. The theoretical K factors have a relatively weak $\sqrt{s}$ dependence, $\leq$ 50% for 20 GeV $\leq \sqrt{s} \leq$ 14 TeV [265]. The heavy quark distributions might be slightly affected since the shapes are somewhat sensitive to the quark mass but the LHC energy is far enough above threshold for the effect to be small.

The total pp and pA cross sections at 5.5, 8.8 and 14 TeV, calculated with a code originally from J. Smith, are given in Table 1.9. Shadowing is the only nuclear effect included in the calculation. The cross sections do not reflect any possible difference between the pA and Ap rates because they are integrated over all x_1 and x_2. However, the different x regions probed by flipping the beams could be effectively studied through the dilepton decay channel. Thus we now turn to a calculation of the nuclear gluon distribution in pA interactions [73]. We show that the dilepton continuum can be used to study nuclear shadowing and reproduces the input shadowing function well, in this case, the EKS98 parametrization [27, 28]. To simplify notation, we refer to generic heavy quarks, Q, and heavy-flavoured mesons, H. The lepton-pair production cross section in pA interactions is

$$\begin{aligned}
\frac{d\sigma^{pA\to l\bar{l}+X}}{dM_{l\bar{l}}dy_{l\bar{l}}} &= \int d^3\vec{p}_l d^3\vec{p}_{\bar{l}} \int d^3\vec{p}_H d^3\vec{p}_{\overline{H}}\, \delta(M_{l\bar{l}} - M(p_l, p_{\bar{l}}))\, \delta(y_{l\bar{l}} - y(p_l, p_{\bar{l}})) \\
&\times \frac{d\Gamma^{H\to l+X}(\vec{p}_H)}{d^3\vec{p}_l}\, \frac{d\Gamma^{\overline{H}\to \bar{l}+X}(\vec{p}_{\overline{H}})}{d^3\vec{p}_{\bar{l}}}\, \frac{d\sigma^{\mathrm{p}A\to H\overline{H}+X}}{d^3\vec{p}_H d^3\vec{p}_{\overline{H}}} \\
&\times \theta(y_{\min} < y_l, y_{\bar{l}} < y_{\max})\theta(\phi_{\min} < \phi_l, \phi_{\bar{l}} < \phi_{\max})\,, \qquad (1.71)
\end{aligned}$$

where $M(p_l, p_{\bar{l}})$ and $y(p_l, p_{\bar{l}})$ are the invariant mass and rapidity of the lepton pair. The decay rate, $d\Gamma^{H\to l+X}(\vec{p}_H)/d^3\vec{p}_l$, is the probability that meson H with momentum $\vec{p}_H$ decays to a lepton l with momentum $\vec{p}_l$. The θ functions define single lepton rapidity and azimuthal angle cuts used to simulate detector acceptances.

Using a fragmentation function D_Q^H to describe quark fragmentation to mesons, the $H\overline{H}$ produc-

Table 1.9: Charm and bottom total cross sections per nucleon at 5.5, 8.8 and 14 TeV

			5.5 TeV		**8.8 TeV**		**14 TeV**
			pp	**pPb**	**pp**	**pPb**	**pp**
				$c\bar{c}$			
PDF	m_c (GeV)	Q/m_c	σ (mb)	σ (mb)	σ (mb)	σ (mb)	σ (mb)
MRST HO	1.4	1	3.54	3.00	4.54	3.76	5.71
MRST HO	1.2	2	6.26	5.14	8.39	6.76	11.0
CTEQ 5M	1.4	1	4.52	3.73	5.72	4.61	7.04
CTEQ 5M	1.2	2	7.39	5.98	9.57	7.56	12.0
GRV 98 HO	1.3	1	4.59	3.70	6.20	4.89	8.21
				$b\bar{b}$			
PDF	m_b (GeV)	Q/m_b	σ (μb)	σ (μb)	σ (μb)	σ (μb)	σ (μb)
MRST HO	4.75	1	195.4	180.1	309.8	279.7	475.8
MRST HO	4.5	2	201.5	186.6	326.1	296.0	510.2
MRST HO	5.0	0.5	199.0	183.9	302.2	272.6	445.1
GRV 98 HO	4.75	1	177.6	162.7	289.7	259.7	458.3
GRV 98 HO	4.5	2	199.0	183.9	329.9	298.7	530.7
GRV 98 HO	5.0	0.5	166.0	151.2	262.8	233.6	403.2

tion cross section can be written as

$$\begin{aligned}\frac{d\sigma^{pA\to H\overline{H}+X}}{d^3\vec{p}_H d^3\vec{p}_{\overline{H}}} &= \int \frac{d^3\vec{p}_Q}{E_Q}\frac{d^3\vec{p}_{\overline{Q}}}{E_{\overline{Q}}}\,E_Q E_{\overline{Q}}\frac{d\sigma^{pA\to Q\overline{Q}+X}}{d^3\vec{p}_Q d^3\vec{p}_{\overline{Q}}}\int dz_1 dz_2 D_Q^H(z_1) D_{\overline{Q}}^{\overline{H}}(z_2)\\ &\times\ \delta^{(3)}(\vec{p}_H - z_1\vec{p}_Q)\,\delta^{(3)}(\vec{p}_{\overline{H}} - z_2\vec{p}_{\overline{Q}})\,. \end{aligned} \tag{1.72}$$

Our calculations proved to be independent of D_Q^H. The hadronic heavy-quark-production cross section per nucleon in Eq. (1.72) is

$$\frac{1}{A}\,E_Q E_{\overline{Q}}\frac{d\sigma^{pA\to Q\overline{Q}+X}}{d^3\vec{p}_Q d^3\vec{p}_{\overline{Q}}} = \sum_{i,j}\int dx_1 dx_2\, f_i^p(x_1,Q^2) f_j^A(x_2,Q^2)\,E_Q E_{\overline{Q}}\frac{d\hat{\sigma}^{ij\to Q\overline{Q}}}{d^3\vec{p}_Q d^3\vec{p}_{\overline{Q}}}\,, \tag{1.73}$$

where the parton densities in the nucleus are related to those in the proton by $f_i^A = f_i^p R_i^A$ where R_i^A is the EKS98 parametrization [27, 28]. The partonic cross section in Eq. (1.73) is the differential of Eq. (1.69) at k = 0. Note that the total lepton-pair production cross section is equal to the total $Q\overline{Q}$ cross section multiplied by the square of the lepton branching ratio.

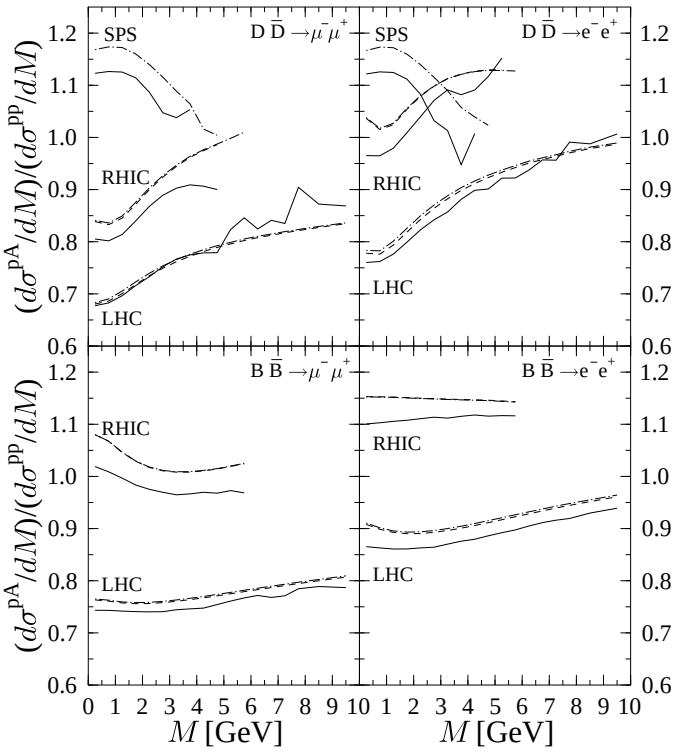

Fig. 1.46: The ratios of lepton pairs from correlated $D\overline{D}$ and $B\overline{B}$ decays in pA to pp collisions at the same energies (solid curves) compared to the input R_g^A at the average x_2 and Q (dashed)/$\sqrt{\langle Q^2\rangle}$ (dot–dashed) of each M bin. From Ref. [73].

We compare the ratios of lepton-pair cross sections with the input R_g^A in Fig. 1.46. The RHIC and LHC results are integrated over the rapidity intervals appropriate to the PHENIX and ALICE dilepton coverages. The ratio is similar to but smaller than R_g^A at all energies. The higher the energy, the better the agreement. The ratio always lies below R_g^A because we include $q\overline{q}$ annihilation, which decreases with energy, but quark and gluon shadowing are different and the phase space integration smears the shadowing effect relative to $R_g^A(\langle x_2\rangle, \langle Q\rangle)$. The calculated ratio deviates slightly more from $R_g^A(\langle x_2\rangle, \langle Q\rangle)$ for e^+e^- than for $\mu^+\mu^-$ because the curvature of R_g^A with x is stronger at larger x and, due to the differences in rapidity coverage, the average values of x_2 are larger for e^+e^-.

The average Q^2 increases with energy and quark mass while the average x_2 decreases with energy. At the SPS, $0.14 \leq \langle x_2\rangle \leq 0.32$, R_g^A is decreasing. At RHIC, $0.003 \leq \langle x_2\rangle \leq 0.012$, R_g^A is increasing quite rapidly. Finally, at the LHC, $3 \times 10^{-5} \leq \langle x_2\rangle \leq 2 \times 10^{-4}$, R_g^A is almost independent of x. The values of $\langle x_2\rangle$ are typically larger for electron pairs at collider energies because the electron coverage is more central than the muon coverage. We have only considered pPb collisions but in Pbp collisions x_1 is an order of magnitude or more greater than x_2 at forward rapidities such as in the ALICE muon spectrometer. Thus doing both pA and Ap collisions would greatly increase the x range over which the nuclear gluon distribution could be determined. By assessing $c\overline{c}$ and $b\overline{b}$ pairs together, it is possible to investigate the evolution of the nuclear gluon distribution with Q^2, albeit with slightly shifted values of x due to the mass difference.

The importance of such a study as a function of A and $\sqrt{s}$ is clear, especially when there is currently little direct information on the nuclear gluon distribution. It is desirable for the pp, pPb, and Pbp measurements to be performed at the same energy as the PbPb collisions at 5.5 TeV even though the relative proton/neutron number is negligible in gluon-dominated processes. The effect of shadowing is easier

to determine if the x value does not shift with energy, particularly because the dilepton measurement does not provide a precise determination of the heavy quark momenta, only an average.

As shown in Fig. 1.46, energy systematics would provide a much clearer picture of the nuclear gluon distribution over the entire x range. The PHENIX Collaboration has already demonstrated that charm can be measured using single leptons [266]. Perhaps it might be possible to obtain the bottom cross section the same way as well at higher p_T. Another handle on the $Q\overline{Q}$ cross sections may be obtained by $e\mu$ correlations, since the Drell–Yan and quarkonium decays will not contribute. At the LHC, uncorrelated $Q\overline{Q}$ pairs can make a large contribution to the continuum. These pairs, with a larger rapidity gap between the leptons, are usually of higher mass than the correlated pairs. However, the larger rapidity gap reduces their acceptance in a finite detector. Like-sign subtraction also reduces the uncorrelated background. For further discussion, see Refs. [72, 73, 79].

6.5. Cronin Effect in Proton–Nucleus Collisions: a Survey of Theoretical Models

A. Accardi

6.5.1. Introduction

In this short note I shall compare available theoretical models for the description of the so-called Cronin effect [267] in inclusive hadron spectra in pA collisions. The analysis will be limited to references containing quantitative predictions for pA collisions [180, 205, 268–270]. The observable we study is the *Cronin ratio*, R, of the inclusive differential cross sections for proton scattering on two different targets, normalized to the respective atomic numbers A and B:

$$R(p_T) = \frac{B}{A}\,\frac{d\sigma_{pA}/d^2p_T}{d\sigma_{pB}/d^2p_T}\,.$$

In absence of nuclear effects one would expect $R(p_T) = 1$, but for $A > B$ a suppression is measured at small p_T, and an enhancement at moderate p_T with $R(p_T) \to 1$ as $p_T \to \infty$. This behaviour may be characterized by the value of three parameters: the transverse-momentum $p_\times$ at which R crosses unity and the transverse-momentum p_M at which R reaches its maximum value $R_M = R(p_M)$, see Fig. 1.47. These *Cronin parameters* will be studied in Section 6.5.3.

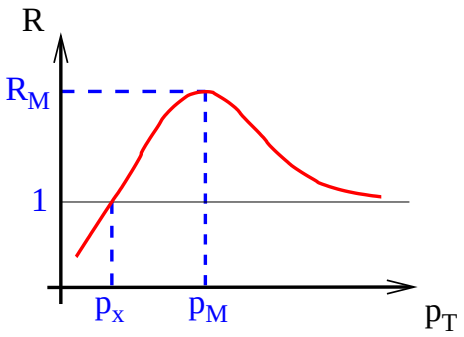

Fig. 1.47: Definition of $p_\times$, p_M, R_M

The Cronin effect has received renewed interest after the experimental discovery at RHIC of an unexpectedly small $R < 1$ in AuAu collisions at $\sqrt{s} = 130$ GeV compared to pp collisions at the same energy [271, 272]. This fact has been proposed as an experimental signature of large jet quenching, suggesting that a Quark–Gluon Plasma was created during the collision [273, 274]. However, the extrapolation to RHIC and LHC energies of the known Cronin effect at lower energies is haunted by large theoretical uncertainties which may make the interpretation of such signals unreliable. More light has recently been shed on this problem by the RHIC data on dA collisions at $\sqrt{s}$ = 200 GeV [6–8, 275].

Since no hot and dense medium is expected to be created in pA collisions, a pA run at the same nucleon–nucleon energy as in AA collisions would be of major importance to test the theoretical models and to have reliable baseline spectra for the extraction of novel physical effects. This has been the key in establishing the relevance of final-state effects (jet quenching) as the the cause of the suppression of the Cronin ratio R in AuAu collision at RHIC [275, 276]. This measurement will also be essential at LHC, where at the accessible Bjorken $x \lesssim 10^{-3}$ new physics such as gluon saturation may (or may not) come into play.

A further advantage of pA collisions is the relatively small multiplicity compared to AA collisions. For this reason, at ALICE, minijets may be observed at $p_T > 5$ GeV, see Section 2. As I shall discuss in Section 6.5.3., the Cronin effect on minijet production may then be a further check of the models.

6.5.2. The models

Soon after the discovery of the Cronin effect [267], it was realized that the observed nuclear enhancement of the p_T spectra could be explained in terms of multiple interactions [277, 278]. The models may be classified according to the physical object which is rescattering (the projectile hadron or its partons), and to the 'hardness' of the rescattering processes taken into account. Note that a parton is commonly said to undergo a hard scattering if the exchanged momentum is of the order of or greater than approximately 1 GeV. However, physically there is no sharp distinction between soft and hard momentum transfer. Therefore, I prefer to refer to the so-called two-component models of hadron transverse spectra, and call a scattering which is described by a power-law differential cross section at large-p_T hard, and a scattering whose cross section is decreasing faster than any inverse power of the transverse-momentum at large-p_T soft. In Tables 1.10 and 1.11, I provide a quick comparison of the hadronic and partonic rescattering models.

Soft hadronic rescattering models [180, 268]

These models are based on the pQCD collinearly factorized cross section for inclusive particle production in pp collisions. In order to better describe the hadron transverse-momentum spectra at $\sqrt{s} \sim 20$ GeV, and in the semi-hard region $p_T \sim 1 \times 5$ GeV at higher cms energies, one has to also include an intrinsic transverse-momentum [279, 280] for the colliding parton. The p_T spectrum in a pA collision is obtained from a Glauber-type model[6]:

$$\frac{d\sigma^h_{pA}}{d^2p_T} = K \sum_{i,j,k,l} F_{i/p} \otimes F_{j/A} \otimes \frac{d\hat{\sigma}}{d\hat{t}}(ij \to kl) \otimes D^h_k \,, \tag{1.74}$$

where the proton and nucleus parton distribution functions are, respectively,

$$F_{i/p} = f_{i/p}(x_i, Q^2)\, \frac{e^{-k^2_{iT}/\langle k^2_T\rangle_{pA}(b)}}{\pi \langle k^2_T\rangle_{pA}} \quad \text{and} \quad F_{j/A} = T_A(b)\, f_{j/A}(x_j, Q^2)\, \frac{e^{-k^2_{jT}/\langle k^2_T\rangle_{Ap}(b)}}{\pi \langle k^2_T\rangle_{Ap}} \,. \tag{1.75}$$

In Eq. (1.74), $d\hat{\sigma}/d\hat{t}(ij \to kl)$ is the pQCD parton–parton cross section, the variables with a hat are the partonic Mandelstam variables, and a sum over incoming and outgoing parton flavours is performed. The proton is considered point-like compared to the target nucleus, and the scattering occurs at impact parameter b. The nucleus is described by the Woods–Saxon nuclear thickness function $T_A(b)$. In Eq. (1.75), $f_{i/p(A)}(x, Q^2)$ are the PDFs of the proton (nucleus). Isospin imbalance is taken into account and nuclear shadowing is included by the HIJING parametrization [281]. Partons are assumed to have an intrinsic transverse-momentum with average squared value $\langle k^2_T\rangle_{pA(Ap)}$ and a Gaussian distribution. Due to the k_i and k_j integrations a regulator mass m = 0.8 GeV has been used in the pQCD cross section.

[6] Integrations are schematically indicated with crossed circle symbols. For details see the original references.

Table 1.10: Parameters of the soft hadronic rescattering models [180]

Model	**Hard scales (GeV)**	**K**	**Regul.**	**Proton intrinsic k_T (GeV^2)**	**n**	**Average k_T kick (GeV^2)**	**nPDF**
Soft	$Q = Q' = p_T$	2	0.8 GeV	$\langle k_T^2 \rangle_{pp}$ = 1.2 + 0.2 $\alpha_s(q^2) q^2$ [a)]	∞	$\delta(Q)$ = 0.255 $\frac{\ln^2(Q/\mathrm{GeV})}{1+\ln(Q/\mathrm{GeV})}$	HIJING
Soft-sat.	$Q = \frac{p_T}{2z_c}$; $Q' = \frac{p_T}{2}$ [b)]	1	0.8 GeV	$\langle k_T^2 \rangle_{pp} = F(\sqrt{s})$ [c)]	4	δ = 0.4	HIJING

[a)] $q^2 = 2\hat{s}\hat{t}\hat{u}/(\hat{s}+\hat{t}+\hat{u})^2$. Parametrization chosen to best reproduce pp data.

[b)] These scales used in the computations of Table 1.12. In Ref. [180] $Q = p_T/2$ and $Q' = p_T/2z_c$.

[c)] No explicit parametrization is given. Values of $\langle k_T^2 \rangle_{pp}$ extracted from a "best fit" to pp data, see Fig.15 of Ref. [180].

Table 1.11: Parameters of the soft partonic rescattering model (at short-l_c) and of the hard partonic rescattering models

Model	**Hard scales**	**K**	**Regulators (GeV)**	**Intr. k_T**	**dE/dz**	**Dipole cross-section**	**nPDF**
Col. dip.	$Q = Q' = p_T$	[a]	m_g = 0.8, m_q = 0.2	as Soft mod.	−2.5 GeV/fm	σ_0 = 23 mb, λ = 0.288, $x_0 = 3 \times 10^{-4}$	EKS98 [b]
Hard AT	$Q = Q' = p_T$ [c]	2	μ free param.	no	no	computed from pQCD	no
Hard GV	$Q = Q' = p_T$	[a]	μ = 0.42 [d]	as Soft mod.	no	—	EKS98

[a] Factors out in the Cronin ratio.

[b] Only at large x_j (EMC effect).

[c] $Q = \mu$ in Ref. [205].

[d] μ determines only the typical momentum transfer in elastic rescatterings.

Finally, $D_k^h(z, Q'^2)$ are the fragmentation functions of a parton k into a hadron h with a fraction z of the parton momentum.

Soft proton–nucleon interactions are assumed to excite the projectile proton wavefunction, so that when the proton interacts with the next target nucleon its partons have a broadened intrinsic momentum. Each proton rescattering is assumed to contribute to the intrinsic momentum broadening in the same way so that:

$$\langle k_T^2 \rangle_{pA}(b, \sqrt{s}) = \langle k_T^2 \rangle_{pp} + \delta \, h_A(b, \sqrt{s}) \, , \tag{1.76}$$

where $\langle k_T^2 \rangle_{pp}$ is the parton intrinsic momentum needed to describe hadron transverse spectra in pp collisions, δ is the average momentum squared acquired in each rescattering, and

$$h_A(b, \sqrt{s}) = \begin{cases} \nu_A(b, \sqrt{s}) - 1 & \text{if} \quad \nu_A - 1 \leq n \\ n & \text{if} \quad \nu_A - 1 > n \end{cases} \tag{1.77}$$

represent the average number of collisions which are effective in broadening the intrinsic momentum. Both models assume h_A to be a function of the number of proton–nucleon collisions $\nu_a(b, \sqrt{s}) = \sigma_{pp}(\sqrt{s}) T_A(b)$, with σ_{pp} the nucleon–nucleon inelastic cross section. However, Ref. [268] takes $n = \infty$, while Ref. [180] assumes an upper limit n = 4 justified in terms of a proton dissociation mechanism: after a given number of interactions, the proton is so excited that it can no longer interact as a whole with the next nucleon. I shall call the first model simply *soft* and the second *soft-saturated*. In both models, target nucleons do not rescatter, so that

$$\langle k_T^2 \rangle_{Ap}(b, \sqrt{s}) = \langle k_T^2 \rangle_{pp} \, .$$

Further differences between the models are related to the choices of the hard scales, of the K-factor which simulates NLO contributions to the parton cross section, and to the parametrizations of $\langle k_T^2 \rangle_{pp}$ and δ (see Table 1.10).

Soft partonic rescatterings: the colour dipole model [269]

In this model, the particle production mechanism is controlled by the *coherence length* $l_c = \sqrt{s}/(m_N k_T)$, where m_N is the nucleon mass and k_T the transverse-momentum of the parton which fragments in the observed hadron. Depending on the value of l_c, three different calculational schemes are considered. *(a)* In fixed-target experiments at low energy (e.g., at the SPS), where $l_c \ll R_A$, the projectile partons interact incoherently with target nucleons. High-p_T hadrons are assumed to originate mainly from a projectile parton which experienced a hard interaction and whose transverse-momentum was broadened by soft parton rescatterings. The parton is then put on-shell by a single semihard scattering computed in factorized pQCD. This scheme will be discussed in detail below. *(b)* At LHC, where the c.m. energy is very large and $l_c \gg R_A$, the partons interact coherently with the target nucleons and high-p_T hadrons are assumed to originate from radiated gluons. Parton scatterings and gluon radiation are computed in the light-cone dipole formalism in the target rest frame. *(c)* At intermediate energies, like RHIC, an interpolation is made between the results of the low- and high-energy regimes discussed above. All the phenomenological parameters needed in this model are fixed in reactions other than from pA collisions, and in this sense the model is said to be parameter-free.

In the short coherence length scheme, pQCD factorization is assumed to be valid and Eq. (1.74) is used with parton masses $m_g = 0.8$ GeV and $m_q = 0.2$ GeV for, viz., gluons and quarks. Moreover,

$$F_{i/p} = f_{i/p}\big(x_i + \tfrac{\Delta E}{x_a E_p}, Q^2\big) \, \frac{dN_i}{d^2 k_{iT}}(x, b) \quad \text{and} \quad F_{j/A} = T_A(b) \, f_{j/A}\big(x_j, Q^2\big) \, \frac{dN_j^{(0)}}{d^2 k_{jT}}(x, b) \, .$$

Parton rescatterings are computed in terms of the propagation of a $q\bar{q}$ pair through the target nucleus. The final parton transverse-momentum distribution dN_i/d^2k_{iT} is written as:

$$\frac{dN_i}{d^2k_{iT}} = \int d^2r_1 d^2r_2\, e^{i\,\vec{k}_T\,(\vec{r}_1-\vec{r}_2)} \left[\frac{\langle k_0^2\rangle}{\pi}\, e^{-\frac{1}{2}(r_1^2+r_2^2)\langle k_0^2\rangle}\right] \left[e^{-\frac{1}{2}\,\sigma_{\bar{q}q}^N(\vec{r}_1-\vec{r}_2,x)\,T_A(b)}\right] = \frac{dN^{(0)}}{d^2k_T} + O\big(\sigma_{\bar{q}q}^N T_A\big)\,. \tag{1.78}$$

The first bracket in Eq. (1.78) represents the contribution of the proton intrinsic momentum. The second bracket is the contribution of soft parton rescatterings on target nucleons, expressed through the phenomenological dipole cross section. For a quark, $\sigma_{\bar{q}q}^N(r_T,x) = \sigma_0\,\left[1-\exp\left(-\frac{1}{4}\,r_T^2\,Q_s^2(x)\right)\right]$ with $Q_s = 1\ \mathrm{GeV}(x/x_0)^{\lambda/2}$ (the parameters ar given in Table 1.11). For a gluon, σ_{gg}^N = 9/4 $\sigma_{\bar{q}q}^N$ is used. The expansion of Eq. (1.78) to zeroth order in $\sigma_{\bar{q}q}^N$ gives the intrinsic k_T distribution, $dN^{(0)}/d^2k_T$, of the nucleon partons. The first-order term represents the contribution of one-rescattering processes, and so on. Partons from the target nucleus are assumed not to rescatter because of the small size of the projectile. Energy loss of the projectile partons is taken into account by a shift of their fractional momentum proportional to the energy of the radiated gluons, given by the product of the average mean path length ΔL and the energy loss per unit length dE/dz [282,283]. Since nuclear shadowing effects are computed in the dipole formalism, see Eq. (1.78), parton distribution functions in the target are modified only to take into account antishadowing at large x according to the EKS98 parametrization [27].

By Fourier-transforming the dipole cross section we find that the transverse-momentum distribution of single parton–nucleon scattering is Gaussian, which justifies the classification of this model as 'soft'. However, the single distributions are not just convoluted to obtain a broadening proportional to the average number of rescatterings. Indeed, in the second bracket, the rescattering processes have a Poisson probability distribution. As a result, the nuclear broadening of the intrinsic momentum is smaller than the product of the average number of rescatterings and the single scattering broadening; perhaps a dynamical explanation of the assumption that $n \lesseqgtr \infty$ in Eq. (1.77), used in the soft-saturated model [180].

Hard partonic rescattering model [205,270]

The model of Ref. [205], hereafter labeled 'hard AT', assumes that parton rescatterings are responsible for the Cronin enhancement. Up to now, it includes only semihard scatterings, i.e. scatterings described by the pQCD parton–parton cross section. It is the generalization to an arbitrary number of hard parton rescatterings of the early models of Refs. [277,278,284] and of the more recent Refs. [285,286], which are limited to a single hard rescattering. As shown in Ref. [278], considering only one rescattering may be a reasonable assumption at low energy to describe the gross features of the Cronin effect, but already at RHIC energies this might be insufficient to determine the Cronin peak R_M [205]. The AT model assumes that the S-matrix for a collision of n partons from the projectile on m partons from the target is factorizable in terms of S-matrices of parton–parton elastic-scattering. It also assumes generalized pQCD factorization [18,287]. The result is a unitarized cross section, as discussed in Refs. [205,288]:

$$\frac{d\sigma_{pA}^h}{d^2p_T} = \sum_i f_{i/p} \otimes \frac{dN_{i/A}}{d^2k_T} \otimes D_i^h + \sum_j f_{j/A}\,T_A \otimes \frac{dN_{j/p}}{d^2k_T} \otimes D_j^h\,. \tag{1.79}$$

The first term accounts for multiple semihard scatterings of partons in the proton on the nucleus. In the second term, partons of the nucleus are assumed to undergo a single scattering, with $dN_{j/p}/d^2k_T = \sum_i f_{i/p} \otimes \sigma_{i/N}^{\mathrm{hard}}$. Nuclear effects are included in $dN_{i/A}/d^2k_T$, the average transverse-momentum distribution of a proton parton that suffered *at least* one semihard scattering. In impact parameter space it reads

$$\frac{dN_{i/A}}{d^2k_T}(b) = \int \frac{d^2r}{4\pi} e^{-i\vec{k}_T\cdot\vec{r}} \left[e^{-\sigma_{i/N}^{\mathrm{hard}}(r)T_A(b)} - e^{-\sigma_{i/N}^{\mathrm{hard}}T_A(b)}\right]\,, \tag{1.80}$$

where unitarity is explicitly implemented at the nuclear level, as discussed in Ref. [288]. In Eq. (1.80), $\sigma_{i/N}^{\rm hard}(r) = K \sum_j \int d^2p \left[1 - e^{-i\vec{p}\cdot\vec{r}}\right] \frac{d\hat{\sigma}}{d\hat{t}}(ij \to ij) \otimes f_{j/p}$. Moreover, $\omega_i \equiv \sigma_{i/N}^{\rm hard} T_A(b)$ is identified with the target opacity to the parton propagation. Note that $\sigma_{i/N}^{\rm hard}(r) \propto r^2$ as $r \to 0$ and $\sigma_{i/N}^{\rm hard}(r) \to \sigma_{i/N}^{\rm hard}$ as $r \to \infty$. This, together with the similarity of Eqs. (1.78) and (1.80), suggests the interpretation of $\sigma_{i/N}^{\rm hard}(r)$ as a *hard dipole cross section*, accounting for hard parton rescatterings on target nucleons analogous to what $\sigma_{q\bar{q}}^N$ does for soft parton rescatterings. Note that no nuclear effects on PDFs are included. However, shadowing is partly taken into account by the multiple scattering processes.

To regularize the IR divergences of the pQCD cross section, a small mass regulator μ is introduced in the parton propagators. It is considered a free parameter of the model that sets the scale at which pQCD computations break down. As a consequence of the unitarization of the interaction, due to the inclusion of rescatterings, both $p_\times$ and p_M are almost insensitive to μ [205]. Therefore, these two quantities are considered reliable predictions of the model[7]. Note, however, that they both depend on the c.m. energy $\sqrt{s}$ and on the pseudorapidity η. On the other hand, R_M is quite sensitive to the IR regulator. This sensitivity may be traced back to the inverse-power dependence of the target opacity ω_i on μ, $\omega_i \propto 1/\mu^a$, where $a > 2$ is energy- and rapidity-dependent. The divergence of ω_i as $\mu \to 0$ indicates the need for unitarization of the parton–nucleon cross section and deserves further study. Therefore, μ can here be considered only as an effective scale which simulates nonperturbative physics [289, 290], the nonlinear evolution of target PDFs [81] and physical effects so far neglected, e.g., collisional and radiative energy losses [291].

Another model which implements hard partonic rescatterings, labeled 'hard GV', is found in Ref. [270]. This model is discussed in more detail in Chapter 2, see also Ref. [292]. In the hard GV model, the transverse-momentum broadening of a parton which experiences semihard rescatterings is evaluated, using Eq. (1.80), to be

$$\langle k_T^2 \rangle_{\rm hard} = \omega \mu^2 \ln\left(1 + c\frac{p_T^2}{\mu^2}\right) . \tag{1.81}$$

The IR regulator is fixed to μ = 0.42 GeV and identified with the medium screening mass. It represents the typical momentum kick in each elastic rescattering of a hard parton. The factor c and the constant term 1 are introduced in order to obtain no broadening for $p_T \approx 0$, as required by kinematic considerations. The average value of the opacity in the transverse plane, $\omega \approx (0.4/\text{fm}) R_A$ (where R_A is the nuclear radius), and the factor c/μ^2 = 0.18 are fixed in order to reproduce the experimental data at $\sqrt{s}$ = 27.4 GeV and $\sqrt{s}$ = 38.8 GeV [293]. With these values the logarithmic enhancement in Eq. (1.81) is of order 1 for $p_T \approx 3$ GeV. Note that ω and c are assumed to be independent of $\sqrt{s}$ and η. Finally, the transverse spectrum is computed by using Eq. (1.74) and adding to the semihard broadening of Eq. (1.81) the intrinsic momentum of the projectile partons, $\langle k_0^2 \rangle$ = 1.8 GeV^2:

$$\langle k_T^2 \rangle_{pA} = \langle k_T^2 \rangle_{pp} + \langle k_T^2 \rangle_{\rm hard} ,$$

with shadowing and antishadowing corrections to target partons from the EKS98 parametrization [27].

6.5.3. Predictions and conclusions

Table 1.12 shows the values of the Cronin parameters p_M and R_M computed in various models of pA collisions at $\sqrt{s}$ = 27.4 GeV (for low-energy experiments), 200 GeV (RHIC) and 5.5 TeV (LHC). The targets considered in the Cronin ratio are also listed. I do not include $p_\times$ in the tables since in almost all models $p_\times \sim 1$ GeV, independent of energy, which lies at the border of validity of the models. Uncertainties in the model calculations are included when discussed in the original references, see the table footnotes. In the case of the soft-saturated model, the uncertainty due to the choice of shadowing

[7] This result is very different from the conclusion that $p_\times \propto p_0$, Ref. [286], based on a single-rescattering approximation. Hence $p_\times$ cannot be used to 'measure' the onset of hard dynamics as proposed in that paper.

parametrization is illustrated by giving the results obtained with no shadowing, and with the HIJING parametrization [281]. Using the 'new' HIJING parametrization [66] would change the mid-rapidity results only at LHC energies, where a 15% smaller Cronin peak would be predicted [294][8]. In the case of 'hard AT' rescattering, the major theoretical uncertainty is in the choice of μ, as discussed at the end of Section 6.5.2. In the table, two choices are presented: *(a)* an energy-independent value μ = 1.5 GeV, which leads to an increasing Cronin effect with energy; *(b)* μ is identified with the IR cutoff p_0 discussed in Ref. [295], in the context of a leading-order pQCD analysis of pp collisions. That analysis found p_0 to be an increasing function of $\sqrt{s}$. By performing a simple logarithmic fit to the values extracted from data in Ref. [295], we find $\mu = p_0(\sqrt{s})$ = 0.060 + 0.283 $\log(\sqrt{s})$, which decreases the Cronin effect with energy. Note that a scale increasing with $\sqrt{s}$ also appears naturally in the so-called 'saturation models' for hadron production in AA collisions [289,296,297]. In the 'hard GV' model at the LHC, the remnants of the Cronin effect at $p_T \sim 3$ GeV are overwhelmed by shadowing and the calculation is not considered reliable in this region. The value R_M = 1.05 at $p_T \simeq 40$ in Ref. [270] is a result of antishadowing in the EKS98 parametrization and is not related to multiple initial state scatterings.

As discussed in the introduction, experimental reconstruction of minijets with ALICE may be possible in pA collisions for minijet transverse momenta $p_T \gtrsim 5$ GeV. The p_T spectrum of the partons which hadronize into the observed minijet may be obtained by setting $D_i^h = \delta(z-1)$ in Eqs. (1.74) and (1.79). Minijet reconstruction may be very interesting because pQCD computations suffer from large uncertainties in the determination of the large-z fragmentation functions, where they are only loosely constrained by existing data [298]. For this reason I also listed the Cronin parameters for parton production in Table 1.12. However, jet reconstruction efficiency should be accurately evaluated to assess the usefulness of this observable.

Table 1.12 shows that there are large theoretical uncertainties in the extrapolation of the Cronin effect from lower energies to the LHC. A major source of uncertainty for most of the models is nuclear shadowing and antishadowing at small x, see Refs. [52, 53] and Section 4. for a detailed discussion and comparison of the existing parametrizations. For example, the HIJING parametrizations [66, 281] suggest more gluon shadowing than EKS98 [27] at small $x \lesssim 10^{-2}$. At the LHC the small-x region is dominant at midrapidity and small to medium p_T. On the other hand, the HIJING parametrizations give less antishadowing than EKS98 at $x \gtrsim 10^{-1}$, which is the dominant region at large-p_T for all energies. At the LHC, all these effects may lead to up to a factor of 2 uncertainty in the height of the Cronin peak R_M.

In conclusion, a pA run at the LHC is necessary both to test theoretical models of particle production in a cleaner experimental environment than AA collisions, and to make reliable extrapolations to AA collisions, which are the key to disentangling known effects from new physics. Since, as we have seen, the nuclear effects are potentially large, it would even be preferable to have a pA run at the same energy as AA. In addition, the study of the A dependence, or collision centrality, would be interesting since it would change the opacity of the target — thus the size of the Cronin effect — in a controllable way. Finally, note that the η systematics of the Cronin effect has so far been considered only in Ref. [205]. However, as also discussed in Ref. [292], given the large pseudorapidity coverage of CMS, the η dependence might be a very powerful tool for understanding the effect. It would systematically scan nuclear targets in the low-x region and would help test proposed models where the rapidity influences the Cronin effect in different ways.

[8] Note, however, that the new parametrization [66], which predicts a much larger gluon shadowing at $x \lesssim 10^{-2}$ than the 'old' one [281], seems ruled out by data on the Sn/Ca F_2 ratio [52, 53].

Table 1.12: Comparison of models of the Cronin effect at η = 0

$\sqrt{s}$	Model	Charged pions			Partons		
		p_M (GeV)	R_M	Ref.	p_M (GeV)	R_M	Ref.
27.4 GeV pW/pBe data [293]	Soft	4.0	1.55[a]	[268]			
	Soft-saturated	4.5[a]; 4.4[b]	1.46[a]; 1.46[b]	[294]	5.1[a]; 5.1[b]	1.50[a]; 1.51[b]	[294]
	Colour dipole	4.5	1.43 ± 0.08[c]	[269]			
	Hard AT				6 ± 0.8 [d]	1.1[e]; 1.4[f]	
	Hard GV	4	1.4	[270]			
200 GeV pAu/pp	Soft	3.5	1.35 ± 0.2[g]	[268]			
	Soft-saturated	2.9[a]; 2.7[b]	1.15[a]; 1.47[b]	[294]	4.4[a]; 4.2[b]	1.29[a]; 1.70[b]	[294]
	Colour dipole	2.7	1.1	[269]			
	Hard AT				7 ± 1 [d]	1.25[e]; 1.2[f]	
	Hard GV	3.0	1.3	[270]			
5500 GeV pPb/pp	Soft	3.5	1.08 ± 0.02[g]	[299]			
	Soft-saturated	2.4[a]; 2.2[b]	0.78[a]; 1.36[b]	[294]	4.2[a]; 4.2[b]	0.91[a]; 1.60[b]	[294]
	Colour dipole	2.5	1.06	[269]			
	Hard AT				11 ± 1.3 [d]	2.1[e]; 1.2[f]	
	Hard GV	≈ 40[h]	1.05[h]	[270]			

[a] With HIJING shadowing [281].
[b] Without shadowing.
[c] Error estimated by varying dE/dz within error bars [300].
[d] Numerical errors mainly.
[e] Using μ = 1.5 GeV.
[f] Using $\mu = 0.060 + 0.283 \log(\sqrt{s})$, see text.
[g] Central value with multiple scattering effects only; the error estimated by using different shadowing parametrizations.
[h] Very sensitive to the shadowing parametrization, see text.

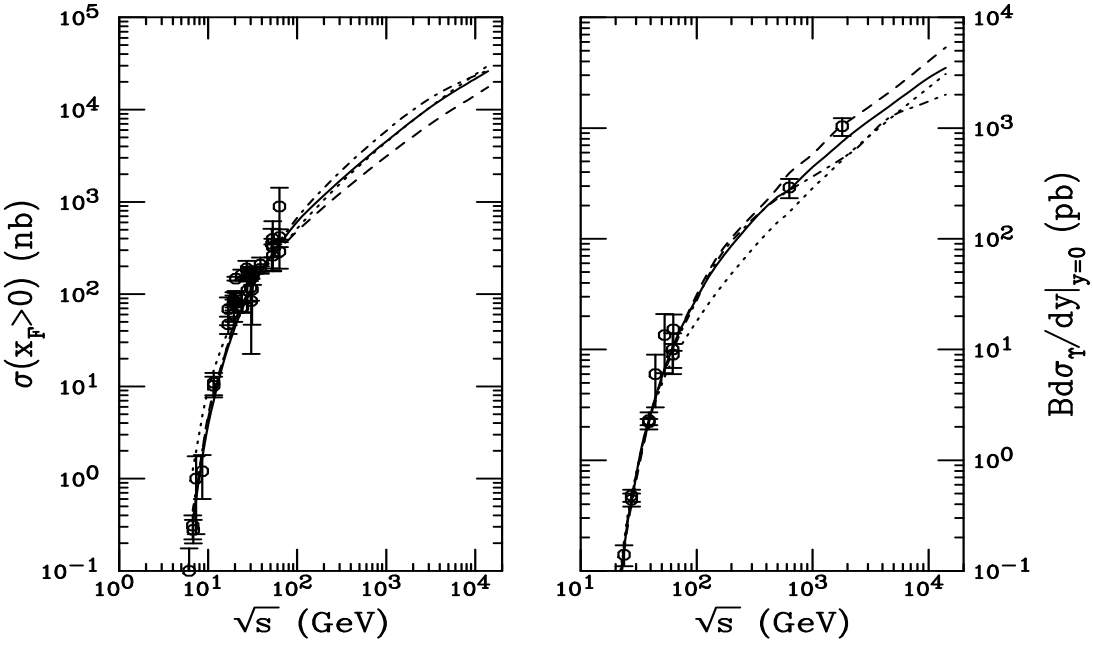

Fig. 1.48: Forward J/ψ (left) and combined $\Upsilon + \Upsilon' + \Upsilon''$ inclusive (right) cross sections calculated to NLO in the CEM. On the left-hand side, the solid curve employs the MRST HO distributions with $m_c = Q/2 = 1.2$ GeV; the dashed, MRST HO with $m_c = Q = 1.4$ GeV; the dot–dashed, CTEQ 5M with $m_c = Q/2 = 1.2$ GeV; and the dotted, GRV 98 HO with $m_c = Q = 1.3$ GeV. On the right-hand side, the solid curve employs the MRST HO distributions with $m_b = Q = 4.75$ GeV; the dashed, $m_b = Q/2 = 4.5$ GeV; the dot-dashed, $m_b = 2Q = 5$ GeV; and the dotted, GRV 98 HO with $m_b = Q = 4.75$ GeV.

6.6. Quarkonium Total Cross Sections

R. Vogt

To better understand quarkonium suppression, it is necessary to have a good estimate of the expected yields. However, there are still a number of unknowns about quarkonium production in the primary nucleon–nucleon interactions. In this section, we report the quarkonium total cross sections in the CEM [215, 216] and NRQCD [218], both briefly described in Section 5.5. We also discuss shadowing effects on the p_T-integrated rapidity distributions.

Recall that at leading order, the production cross section of quarkonium state C in the CEM is

$$\sigma_C^{\rm CEM} = F_C \sum_{i,j} \int_{4m_Q^2}^{4m_H^2} d\hat{s} \int dx_1 dx_2 \; f_i^p(x_1, Q^2) \; f_j^p(x_2, Q^2) \; \hat{\sigma}_{ij}(\hat{s}) \; \delta(\hat{s} - x_1 x_2 s) \; . \qquad (1.82)$$

In a pA collision, one of the proton parton densities is replaced by that of the nucleus. Since quarkonium production in the CEM is gluon dominated, isospin is a negligible effect. However, since shadowing effects on the gluon distribution are large, it could strongly influence the total cross sections. We shall use the same parton densities and parameters that fit the $Q\overline{Q}$ cross section data, given in Table 1.9 in Section 6.4., to determine F_C for J/ψ and Υ production.

In the left-hand side of Fig. 1.48, we show the resulting fits to the forward $(x_F > 0)$ J/ψ total cross sections. These data also include feeddown from χ_c and ψ' decays. The right-hand plot is the sum of all three Υ S states, including the branching ratios to lepton pairs.

All the fits are equivalent for $\sqrt{s} = 100$ GeV but differ by up to a factor of two at 5.5 TeV. The high-energy Υ results seem to agree best with the energy dependence of the MRST calculations with m_b = 4.75 GeV and 4.5 GeV.

Table 1.13: The production fractions obtained from fitting the CEM cross section to the J/ψ forward cross sections ($x_F > 0$) and y = 0 cross sections as a function of energy. The parton distribution function (PDF), charm quark mass (in GeV), and scales used are the same as those obtained by comparison of the $c\overline{c}$ cross section to the pp data. The charmonium cross sections (in μb) obtained from the CEM fits for NN collisions at 5.5 TeV are also given. The production fractions are then multiplied by the appropriate charmonium ratios determined from data. Note that the χ_c cross section includes the branching ratios to J/ψ. The last row gives the NRQCD cross sections with the parameters from Ref. [301].

PDF	m_c	Q/m_c	F_ψ	$\sigma^{\rm tot}_{J/\psi}$	$\sigma^{\rm dir}_{J/\psi}$	$\sigma_{\chi_c \to J/\psi}$	$\sigma^{\rm dir}_{\psi'}$
MRST HO	1.2	2	0.0144	30.6	19.0	9.2	4.3
MRST HO	1.4	1	0.0248	20.0	12.4	6.0	2.8
CTEQ 5M	1.2	2	0.0155	36.0	22.2	10.8	5.0
GRV 98 HO	1.3	1	0.0229	32.1	19.8	9.6	4.5
CTEQ 3L	1.5	2	–	83.1	48.1	27.6	13.6

Table 1.14: The production fractions obtained from fitting the CEM cross section to the combined Υ cross sections to muon pairs at y = 0 as a function of energy. The PDF, bottom quark mass (in GeV), and scales used are the same as those obtained by comparison of the $b\overline{b}$ cross section to the $\pi^- p$ data. The direct bottomonium cross sections (in nb) obtained from the CEM fits for NN collisions at 5.5 TeV in each case above. The production fractions for the total Υ are multiplied by the appropriate ratios determined from data. In this case, the χ_b cross sections do not include any branching ratios to lower S states. The last row gives the NRQCD cross sections with the parameters from Ref. [301].

PDF	m_b	Q/m_b	$F_{\sum\Upsilon}$	F_Υ	σ_Υ	$\sigma_{\Upsilon'}$	$\sigma_{\Upsilon''}$	$\sigma_{\chi_b(1P)}$	$\sigma_{\chi_b(2P)}$
MRST HO	4.75	1	0.000963	0.0276	188	119	72	390	304
MRST HO	4.50	2	0.000701	0.0201	256	163	99	532	414
MRST HO	5.00	0.5	0.001766	0.0508	128	82	49	267	208
GRV 98 HO	4.75	1	0.000787	0.0225	145	92	56	302	235
CTEQ 3L	4.9	2	–	–	280	155	119	1350	1440

The pp cross sections obtained for the individual states are shown in Tables 1.13 and 1.14 along with the values of F_C determined from the fits. Two values are given for the Υ family.

The first is obtained from the combined S state fits shown in the right-hand side of Fig. 1.48, including the branching ratios to lepton pairs, and the second is that of the total Υ $1S$ state after the branching ratios have been extracted. The cross sections given in the tables are, with the exception of the total J/ψ cross section including feeddown, all for direct production. To obtain these direct cross sections, we use the production ratios given by data and branching ratios to determine the relative cross sections, as in Refs. [213, 221].

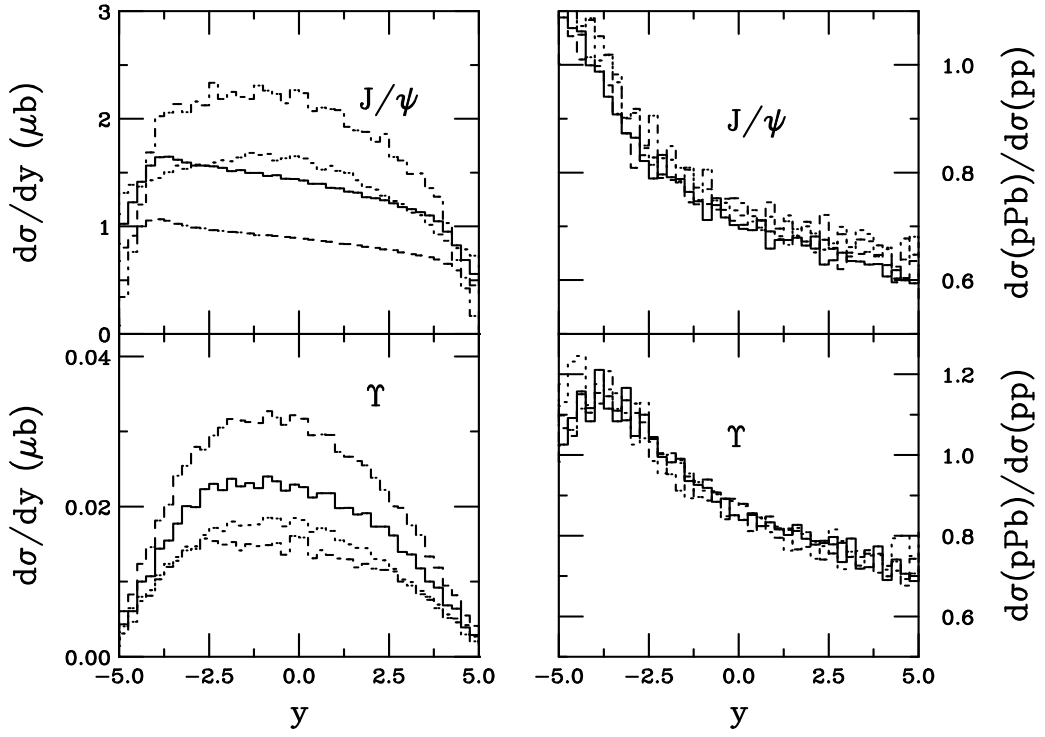

Fig. 1.49: The J/ψ and Υ rapidity distributions in pPb collisions (left) and the pPb/pp ratios (right). The J/ψ calculations employ the MRST HO distributions with $m_c = Q/2 = 1.2$ GeV (solid), MRST HO with $m_c = Q = 1.4$ GeV (dashed), CTEQ 5M with $m_c = Q/2 = 1.2$ GeV (dot-dashed), and GRV 98 HO with $m_c = Q = 1.3$ GeV (dotted). The Υ calculations employ the MRST HO distributions with $m_b = Q = 4.75$ GeV (solid), $m_b = Q/2 = 4.5$ GeV (dashed), $m_b = 2Q = 5$ GeV (dot–dashed), and GRV 98 HO with $m_b = Q = 4.75$ GeV (dotted).

The direct J/ψ and Υ rapidity distributions in pPb interactions at 5.5 TeV/nucleon are shown in Fig. 1.49 for all the fits along with the pPb/pp ratios at the same energy. Note how the average rapidity in the pPb distributions is shifted to negative rapidities due to the low-x shadowing at positive rapidity. The 'corners' in the J/ψ rapidity distributions at $|y| \sim 4$ are equivalent to $x \sim 10^{-5}$, the lowest x for which the MRST and CTEQ5 densities are valid. The pPb/pp ratios show antishadowing at large negative rapidities, large x_2, and 30–40% shadowing at large positive rapidities for the Υ and J/ψ respectively (small x_2). At $y \sim 0$, the effect is $\sim 30\%$ for J/ψ and $\sim 20\%$ for Υ. We plot pPb/pp here but the Pbp/pp ratio would simply be these results reflected around $y = 0$.

The NRQCD total cross sections, calculated with the CTEQ3L densities [302], are also shown in Tables 1.13 and 1.14. The parameters used for the NRQCD calculations were determined for fixed-target hadroproduction in Ref. [301] with m_c = 1.5 GeV, m_b = 4.9 GeV, and $Q = 2m_Q$. Calculations of shadowing effects predicted for NRQCD can be found in Ref. [174]. The dependence on the shadowing parametrization is also discussed. It was found that the EKS98 parametrization [27, 28] predicted weaker shadowing than the HPC parametrization [173], mainly because of the larger gluon antishadowing in the EKS98 parametrization [174]. The predicted shadowing effects were similar for the CEM and NRQCD approaches.

Another approach to quarkonium production has been presented recently. Reference [303] argues that the existing quarkonium data suggest the presence of a strong colour field, Γ, surrounding the hard $Q\overline{Q}$ production vertex in hadroproduction. This field is assumed to arise from the DGLAP evolution of the initial colliding partons. The effect of rescatterings between the quark pair and this comoving field was shown to be in qualitative agreement with the main features of the pp and pA data [303].

Quantitative predictions within this model are difficult because the form of the field Γ is unknown but some predictions assuming an isotropic and transversely polarized field were given in Ref. [304][9].

So far we have not discussed nuclear absorption in cold matter. The A dependence of J/ψ, ψ' and the Υ S states have all been measured in pA interactions. (See Ref. [214] for a compilation of the data.) However, there is still no measurement of the p state A dependence. The CEM makes no distinction between singlet and octet $Q\overline{Q}$ production so that the J/ψ, ψ' and χ_c A dependencies should all be the same. The NRQCD approach, on the other hand, predicts that direct ψ' and J/ψ are 60–80% octet but the χ_c states are 95% singlet [306]. If octets and singlets are absorbed differently, the χ_c A dependence should be quantitatively different than the quarkonium S states; see Ref. [306] for a detailed discussion at fixed-target energies. In addition, the hard rescattering approach leads to a larger χ_{c1} A dependence at high x_F than for the χ_{c2} [307]. Thus, measuring the χ_c A dependencies could help distinguish the underlying quarkonium production mechanism.

Experiments NA60 [231] and HERA-B [308] will measure the χ_c A dependence for the first time at $\sqrt{s}$ = 29.1 and 41.6 GeV, respectively. At the LHC, it may also be possible to extract the χ_b A dependence in pA interactions as well. Comparing the A dependence of all quarkonium states at the LHC with earlier results will also provide a test of the energy dependence of the absorption mechanism, suggested to be independent of energy [309]. Since the absorption mechanism depends on impact parameter, centrality measurements of the A dependence could also be useful in the comparison to AA interactions.

6.7. p_T Broadening in Quarkonium Production

R. Vogt

The broadening of the quarkonium transverse-momentum distribution was first observed by NA3 [310]. Additional data at similar energies showed that the change in the J/ψ p_T slope with A was larger than for the Drell–Yan slope [311]. The Υ p_T distribution was shown to broaden still more than the J/ψ [312].

The p_T broadening effect was explained as multiple elastic scattering of the initial parton before the hard collision [313–315]. The difference between the J/ψ and Drell–Yan broadening can be attributed to the larger colour factor for gluons (J/ψ) than for quarks (Drell–Yan). The difference between Υ and J/ψ broadening was more difficult to explain. The hard rescattering model of quarkonium production [303, 304] is able to describe the effect [316]. By Coulomb rescattering in the nucleus, the $Q\overline{Q}$ pair acquires additional transverse-momentum k_T with an upper limit given by m_Q. Indeed, for $k_T > m_Q$ the colour octet $Q\overline{Q}$ pair can be 'probed' and cannot rescatter as a gluon any longer. Since $m_b > m_c$, the Υ transverse-momentum broadening should be larger than that of the J/ψ [316][10].

In this Section, we investigate the combined effect of shadowing and transverse-momentum broadening on J/ψ and Υ production. The double differential distribution for $Q\overline{Q}$ pair production in pp collisions is

$$s^2\,\frac{d^2\sigma_{pp}(s)}{dtdu} = \sum_{i,j}\int \frac{dx_1}{x_1}\frac{dx_2}{x_2} d^2k_{T1} d^2k_{T2}\, g_p(k_{T1}^2) g_p(k_{T2}^2) f_i^p(x_1,Q^2) f_j^p(x_2,Q^2) \mathcal{J}_K(\hat{s})\hat{s}^2\,\frac{d^2\hat{\sigma}_{ij}(\hat{s})}{d\hat{t}d\hat{u}}\,, \tag{1.83}$$

where $\mathcal{J}_K$ is a kinematics-dependent Jacobian and $\hat{s}^2 d^2\hat{\sigma}_{ij}(\hat{s})/d\hat{t}d\hat{u}$ is the partonic cross section. These partonic cross sections are difficult to calculate analytically beyond LO and expressions only exist near threshold for $\hat{s}^2 d^2\hat{\sigma}_{ij}(\hat{s},\hat{t},\hat{u})/d\hat{t}d\hat{u}$, see, for example, Ref. [259]. However, the exclusive $Q\overline{Q}$ pair NLO [219] code calculates double differential distributions numerically.

[9] Thanks to P. Hoyer and S. Peigne for comments on their work. See also Ref. [305].

[10] Thanks to P. Hoyer and S. Peigne for comments on their work. See also Ref. [305].

The bare quark p_T distributions have often been sufficient to describe inclusive D meson production. However, the $Q\overline{Q}$ pair distributions, particularly the pair p_T and the azimuthal angle distributions at fixed target energies, are broader than can be accounted for by the bare quark distributions without fragmentation and intrinsic transverse-momentum k_T. Heavy quark fragmentation, parameterized from $e^+e^- \to HX$, which reduced the average momentum of the heavy quark in the final-state hadron, is included. This effect, along with momentum broadening with $\langle k_T^2 \rangle = 1$ GeV^2, can describe the $Q\overline{Q}$ measurements [317]. We include the broadening here but not fragmentation since, in the CEM, both the Q and $\overline{Q}$ hadronize together to make the quarkonium state, inconsistent with independent fragmentation.

The intrinsic k_T of the initial partons has been used successfully to describe the p_T distributions of other processes such as Drell–Yan [279] and hard photon production [280]. Some of the low-p_T Drell–Yan data have subsequently been described by resummation to all orders but the inclusion of higher orders has not eliminated the need for this intrinsic k_T.

The implementation of intrinsic k_T in the $Q\overline{Q}$ code in Ref. [219] is not the same as in other processes because divergences are cancelled numerically. Since including additional numerical integrations would slow this process, the k_T kick is added in the final, rather than the initial, state. In Eq. (1.83), the Gaussian $g_p(k_T^2)$,

$$g_p(k_T^2) = \frac{1}{\pi \langle k_T^2 \rangle_{pp}} \exp(-k_T^2/\langle k_T^2 \rangle_{pp}) \,, \tag{1.84}$$

with $\langle k_T^2 \rangle_{pp} = 1$ GeV^2 [317], assumes that the x and k_T dependencies completely factorize. If this is true, it does not matter whether the k_T dependence appears in the initial or final state, modulo some caveats. In the code, the $Q\overline{Q}$ system is boosted to rest from its longitudinal centre-of-mass frame. Intrinsic transverse momenta of the incoming partons, $\vec{k}_{T1}$ and $\vec{k}_{T2}$, are chosen at random with k_{T1}^2 and k_{T2}^2 distributed according to Eq. (1.84). A second transverse boost out of the pair rest frame changes the initial transverse-momentum of the $Q\overline{Q}$ pair, $\vec{p}_T$ to $\vec{p}_T + \vec{k}_{T1} + \vec{k}_{T2}$. The initial k_T of the partons could have alternatively been given to the entire final-state system, as is essentially done if applied in the initial state, instead of to the $Q\overline{Q}$ pair. There is no difference if the calculation is only to LO but at NLO a light parton may also appear in the final state. In Ref. [318], it is claimed that the difference between adding the k_T to the initial or final state is rather small if $k_T^2 \leq 2$ GeV^2. However, this may not turn out to be the case for nuclei [319].

The average intrinsic k_T is expected to increase in pA interactions. This broadening is observed in Drell–Yan [311, 312], J/ψ [310], and Υ [312] production and has been used to explain high-p_T pion production in nuclear interactions [320]. We follow the formulation of Ref. [320], similar to Refs. [313–315] for J/ψ and Drell–Yan production, where the k_T broadening in pA interactions is

$$\langle k_T^2 \rangle_{pA} = \langle k_T^2 \rangle_{pp} + (\langle \nu \rangle - 1)\Delta^2(Q) \tag{1.85}$$

with $\langle k_T^2 \rangle_{pp} = 1$ GeV^2. The number of collisions in a pA interaction, ν, averaged over impact parameter, is [321, 322]

$$\langle \nu \rangle = \sigma_{NN} \frac{\int d^2b\, T_A^2(b)}{\int d^2b\, T_A(b)} = \frac{3}{2}\, \sigma_{NN} \rho_0\, R_A \,, \tag{1.86}$$

where $T_A(b) = \int dz \rho_A(b,z)$ is the nuclear profile function, σ_{NN} is the inelastic nucleon–nucleon scattering cross section, ρ_0 is the central nuclear density, and R_A is the nuclear radius. Our calculations assume R_A = 1.2 $A^{1/3}$ and ρ_0 = 0.16/fm^3. The strength of the nuclear broadening, Δ^2, depends on Q, the scale of the interaction [320]

$$\Delta^2(Q) = 0.225\, \frac{\ln^2(Q/\text{ GeV})}{1 + \ln(Q/\text{ GeV})}\, \text{GeV}^2 \,. \tag{1.87}$$

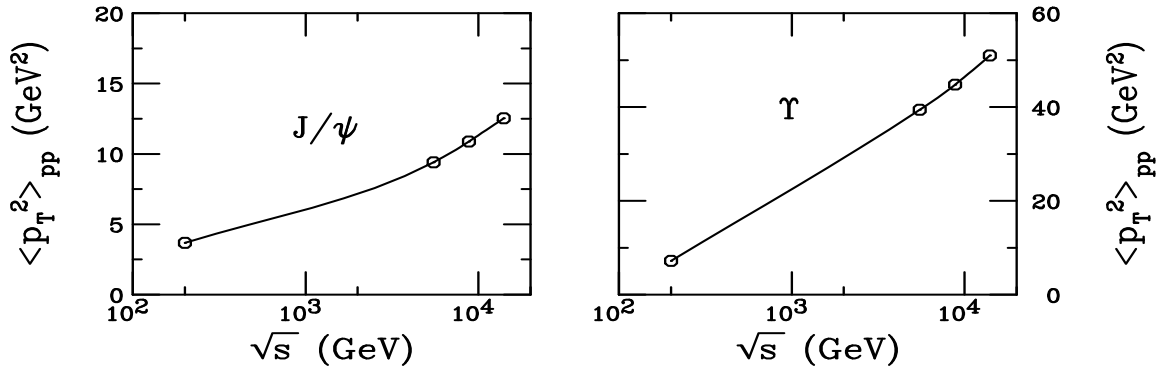

Fig. 1.50: The energy dependence of $\langle p_T^2 \rangle_{pp}$ for J/ψ (left) and Υ (right) production assuming $\langle k_T^2 \rangle_{pp}$ = 1 GeV^2. The open circles are the calculated energies at $\sqrt{s}$ = 0.2, 5.5, 8.8, and 14 TeV.

Thus Δ^2 is larger for $b\overline{b}$ production than $c\overline{c}$ production. This empirically reflects the larger k_T broadening of the Υ [312] relative to the J/ψ [310]. We evaluate $\Delta^2(Q)$ at $Q = 2m_Q$ for both charm and bottom production. We find $(\langle\nu\rangle - 1)\Delta^2(Q)$ = 0.35 GeV^2 for $c\overline{c}$ and 1.57 GeV^2 for $b\overline{b}$ production in pA collisions at b = 0 and A = 200. We can change the centrality by changing $\langle\nu\rangle - 1$.

In Fig. 1.50, we show the increase in $\langle p_T^2 \rangle$ for pp collisions at heavy-ion collider energies using the MRST parton densities with $m_c = 1.2$ GeV and m_b = 4.75 GeV from Table 1.9. The average p_T^2 is obtained by integrating over all p_T and rapidity. Increasing m_Q increases $\langle p_T^2 \rangle_{pp}$. At these energies, the difference between $\langle p_T^2 \rangle_{pp}$ with and without $\langle k_T^2 \rangle_{pp} = 1$ GeV^2 is small, a factor of ~ 1.3 for J/ψ and ~ 1.05 for Υ at 5.5 TeV.

Figure 1.51 compares the bare distributions, $\langle k_T^2 \rangle_{pp} = 1$ GeV^2, and $\langle k_T^2 \rangle_{pPb}$ calculated using Eq. (1.85), integrated over all rapidity. Without intrinsic transverse-momentum, the value of the cross

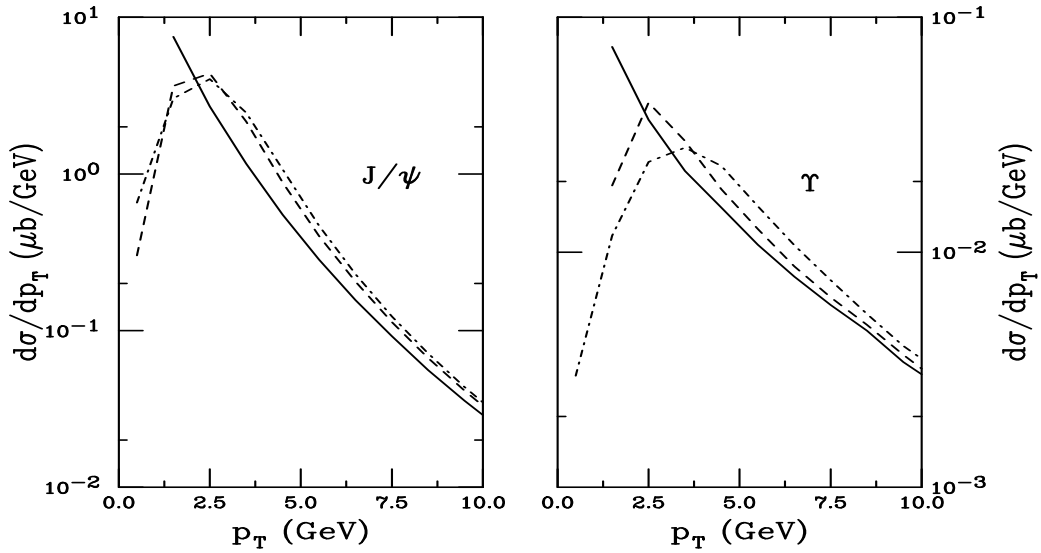

Fig. 1.51: The p_T distributions with $x_F > 0$ for J/ψ (left) and Υ (right) production in pA interactions at 5.5 TeV/nucleon. The solid curve is the bare distribution, the dashed curve employs $\langle k_T^2 \rangle_{pp} = 1$ GeV^2, and the dot–dashed curve uses a $\langle k_T^2 \rangle_{pA}$ appropriate for Pb.

section in the lowest p_T bin is less than zero due to incomplete cancellation of divergences, as discussed in Ref. [323]. This point is left out of the plots. It is interesting to note that, while shadowing is a small effect at large-p_T, the average p_T^2 increases with A, even without any broadening included. This arises because shadowing is a 25–50% effect on J/ψ production at low-p_T, increasing with A, and a 10–20%

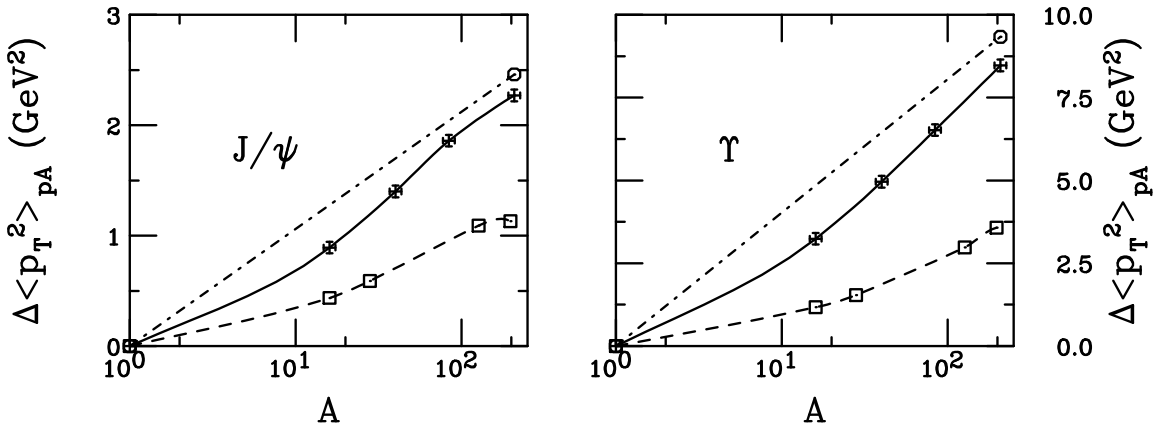

Fig. 1.52: The $\sqrt{s}$ and A dependencies of $\Delta\langle p_T^2\rangle_{\rm pA}$ for J/ψ (left) and Υ (right) production in pA interactions. The dashed curve is at $\sqrt{s} = 200$ GeV/nucleon, the solid at 5.5 TeV/nucleon and the dot–dashed at 8.8 TeV/nucleon. We use A = O, Si, I and Au at 200 GeV/nucleon, A = O, Ar, Kr, and Pb at 5.5 TeV/nucleon and A = Pb at 8.8 TeV/nucleon.

effect on the Υ. The resulting increase in $\langle p_T^2\rangle$ from pp to pPb is $\sim$ 1.2 for J/ψ and $\sim$ 1.13 for Υ. Including $\langle k_T^2\rangle_{\rm pp}$ = 1 GeV^2 increases $\langle p_T^2\rangle$ over all p_T as well, but only by $\sim$ 1.15 for both J/ψ and Υ. Including the A dependence of the broadening as in Eq. (1.85) gives about the same increase in $\langle p_T^2\rangle$ as the bare distributions.

Note that if a p_T cut was imposed, e.g. $p_T > 5$ GeV, $\langle p_T^2\rangle$ increases significantly but the effect of broadening is greatly reduced. In fact, $\langle p_T^2\rangle$ actually decreases with increasing $\langle k_T^2\rangle_{\rm pA}$ when such a cut is imposed. This feature is clear from an inspection of Fig. 1.51.

The energy and A dependence of $\Delta\langle p_T^2\rangle_{\rm pA} = \langle p_T^2\rangle_{\rm pA} - \langle p_T^2\rangle_{\rm pp}$ is given in Fig. 1.52 for $\sqrt{s} = 200$ GeV/nucleon at RHIC as well as 5.5 and 8.8 TeV/nucleon at the LHC. We find that $\Delta\langle p_T^2\rangle_{\rm pA}$ for J/ψ and Υ increase by factors of $\sim$ 3 and $\sim$ 5.3 over $\sqrt{s}$ = 19.4 GeV [310] and 38.8 GeV [312] respectively. Thus, in this calculation, the increase in $\Delta\langle p_T^2\rangle_{\rm pA}$ with $\sqrt{s}$ is stronger for Υ than J/ψ. Such a phenomenological parametrization should soon be tested at RHIC for the J/ψ.

7. NOVEL QCD PHENOMENA IN pA COLLISIONS AT THE LHC

L. Frankfurt and M. Strikman

7.1. Physics Motivations

An extensive discussion of the novel pA physics at the LHC was presented in Ref. [324]. Here we summarize a few key points of this analysis and extend it to consider effects of the small-x high-field regime.

The proton–ion collisions at the LHC will be qualitatively different from those at fixed-target energies. In soft interactions two prime effects are a strong increase of the mean number of 'wounded' nucleons — from $\sim$ 6 to $\sim$ 20 in pA central collisions (due to increase of $\sigma_{\rm inel}(NN)$) and a 50% increase of the average impact parameters in pp collisions (as manifested in the shrinkage of the diffractive peak in the elastic pp collisions with increasing energy) making it possible for a proton to interact, often simultaneously, with nucleons at the same longitudinal coordinate but different impact parameters. At the same time, the geometry of pA collisions at the LHC should be closer to that in classical mechanics due to a strong increase of the pp total cross section and smaller fluctuations of the interaction strength in the value of the effective NN cross section. (The dispersion of the fluctuations of the cross section is given by the ratio of the inelastic and elastic diffractive cross sections at t = 0, which is expected to be a factor of 3 $\times$ 4 smaller at the LHC relative to RHIC.) Among other things this will lead to a much weaker increase of the inelastic coherent diffractive cross section with A relative to fixed-target

energies [325]. In hard interactions, the prime effect is a strong increase of the gluon densities at small-x in both projectile and ion. Gluon densities can be measured at the LHC down to $x \propto 10^{-6} \times 10^{-7}$ where pQCD will be probed in a new domain [324]. As a consequence of blackening of the interaction of partons from the proton with nuclear partons at small $x_{\rm A}$, one should expect a disappearance of low-p_T hadrons in the proton fragmentation region and, hence, a strong suppression of nonperturbative QCD effects[11]. Thus the high-p_T proton fragmentation region is a natural place to search for unusual QCD states of quark–gluon matter which should be long lived due to the Lorentz time dilation. In spite of a small coupling constant, gluon densities of heavy-ions become larger over a wide range of x and Q^2 and impact parameters than that permitted by the conservation of probability within the leading-twist approximation [157,290,324,326,327]. Thus a decrease of α_s with Q^2 is insufficient for the applicability of leading-twist pQCD to hard processes in the small-x regime where gluon fields may be strong enough for the nonperturbative QCD vacuum to become unstable and to require modification of QCD dynamics including modification of the QCD evolution equations. The possibility for a novel QCD regime and therefore new phenomena is maximized in this QCD regime. [12] At the same time interpretation of these novel effects would be much more definitive in pA collisions than in heavy-ion collisions.

New classes of strong-interaction phenomena in the short-distance regime, near the light cone, which could be associated with perturbative QCD or with the interface of the perturbative and nonperturbative QCD regions, are much more probable in pA than pp collisions. The parton and energy densities may be high enough to 'burn away' the nonperturbative QCD vacuum structure in a cylinder of radius $\sim$ 1.2 fm and length $\sim 2\ R_{\rm A}$, leaving behind only a dense partonic fluid governed by new QCD dynamics with small α_s but large effective short-distance couplings. If there is a large enhancement of hard-collision, gluon-induced processes, then there should be an enhancement of hard multi-parton collisions, like production of several pairs of heavy-flavour particles [324]. The study of the x, p_T^2 and A-dependence of multi-parton interactions, and of forward charm and bottom production (in the proton fragmentation region) should be especially useful for addressing these questions.

We estimate the boundary of the kinematical regime for the new QCD dynamics to set in in pA collisions based on the LO formulae for the dipole cross section and the probability conservation. For central impact parameters with $A \sim 200$ and $Q^2 \sim 25$ GeV^2, we find $x_{\rm A} \leq 5 \times 10^{-5}$ for quarks and $x_{\rm A} \leq 10^{-3}$ for gluons [326].

7.2. Measurements of Nuclear Parton Densities at Ultra Small x

One of the fundamental issues in high-energy QCD is the dynamics of hard interactions at small-x. Depending on the Q^2, one investigates either leading-twist effects or strong colour fields. Since the cross sections for hard processes increase roughly linearly with A (except at very small-x and relatively small Q^2 where the counting rates are high anyway), even short runs with nuclear beams will produce data samples sufficient to measure parton distributions with *statistical* accuracy better than 1% practically down to the smallest kinematically allowed x: $x \sim 10^{-7}$ for quarks and $x \sim 10^{-6}$ for gluons [329]. The systematic errors on the ratios of nuclear and nucleon structure functions are also expected to be small since most of these errors cancel in the ratios of the cross sections, cf. Ref. [90]. The main limitations on such studies are the forward acceptance and the transverse-momentum resolution of the LHC detectors.

There are several processes which could be used to probe the small-x dynamics in pA collisions. They include the Drell–Yan pairs, dijets, jet + photon, charm production, diffractive exclusive 3-jet production, and multijet events. It is worth emphasizing that, for these measurements, it is necessary to detect jets, leptons, and photons at rapidities which are close to the nucleon rapidity. In this y-range,

[11] A similar phenomenon of the low-p_T suppression of another quantity, the nuclear light cone wave function at small-x, is discussed in the saturation models [157, 290].

[12] It is important to distinguish between parton densities that are defi ned within the leading-twist approximation only [328] and may increase with energy forever and physical quantities – cross sections/structure functions – whose increase with energy at a given impact parameter is restricted by probability conservation.

the accompanying soft hadron multiplicities are relatively small, leading to a soft particle background comparable to that in pp scattering. In fact, for $|y_{\max} - y| \leq$ 2–4, the background level is likely to be significantly smaller than in pp collisions due to suppression of the leading particle production in pA scattering, see Ref. [324].

Measurements of dimuon production appear to be more feasible at forward angles than hadron production due to small muon energy losses. In the kinematics where the leading-twist dominates, one can study both the small-x quark distributions at relatively small p_T, $p_T(\mu^+\mu^-) \ll M(\mu^+\mu^-)$, and the gluon distribution at $p_T(\mu^+\mu^-) \sim M(\mu^+\mu^-)$ [194]. Note also that in the forward region, the dimuon background from charm production is likely to be rather small since, on average, muons carry only 1/3 of the charm decay momentum.

7.3. Signals for Onset of the Black-Body Limit

A fast increase of nPDFs for heavy nuclei with energy contradicts probability conservation for a wide range of parton momenta and virtualities for the LHC energy range. On the contrary, the rapid, power-like growth of the nucleon structure function observed at HERA may continue forever because of the diffuse edge of a nucleon [330]. At present, new QCD dynamics in the regime of high parton densities where multi-parton interactions are inhibited remains a subject of lively debate. Possibilities include a pre-QCD black-body regime for the structure functions of heavy nuclei [331], a QCD black-body regime for hard processes with heavy nuclei [330], saturation of parton densities at a given impact parameter [157], a colour glass condensate [290], turbulence and related scaling laws. To estimate the pattern of the novel phenomena we shall use the formulae of the black-body regime because they are generic enough to illustrate the expectations of the onset of new QCD dynamics within the existing theoretical approaches [13].

High parton density effects can be enhanced in nuclei because of their uniform density and because it is possibile to select scattering at central impact parameters. Indeed, in the small-x regime, a hard collision of a parton of the projectile nucleon with a parton of the nucleus occurs coherently with all the nucleons at a given impact parameter. The coherence length $l_{\rm C} \approx 1/2m_N x$ by far exceeds the nuclear size. In the kinematic regime accessible at the LHC, $l_{\rm C}$ can be up to 10^5 fm in the nuclear rest frame. Here the large coherence length regime can be visualized in terms of the propagation of a parton through high-density gluon fields over much larger distances than is possible with free nucleons. In the Breit frame, this corresponds to the fact that small-x partons cannot be localized longitudinally within the Lorentz-contracted thickness of the nucleus. Thus low-x partons from different nucleons overlap spatially, creating much larger parton densities than in the free nucleon case. This leads to a large amplification of multi-parton hard collisions, expected at small x in QCD, see, for example, Refs [90, 324]. The eikonal approximation [26, 150] and constraints from the probability conservation [327, 332] indicate that new QCD dynamics should be revealed at significantly larger x in nuclei than in the proton and with more striking effects. Recently, extensive studies of hard diffraction were performed at HERA. For a review see Ref. [333]. Information obtained in these studies allows one to evaluate the leading-twist nuclear shadowing which turns out to be large both in the gluon and quark channels and significant up to very large Q^2. For a recent discussion see Ref. [326]. This leading-twist shadowing tames the growth of the nPDFs at small-x. However, even such large shadowing is still insufficient to restore probability conservation, leaving room for violation of the leading-twist approximation. This violation may be more serious than merely an enhancement of higher twist effects since the entire interaction picture can qualitatively change. The common wisdom that a small α_s guarantees asymptotic freedom, confirmed experimentally in many hard processes, is violated at small-x. This phenomenon can be considered in

[13] In the black-body regime, a highly virtual probe interacts at the same time with several high-k_T partons from the wave function of a hadron [330]. This is qualitatively different from the asymptotic freedom limit where interactions with only one highly virtual parton are important. Hence the interacting parton is far from being free when probed by an object with a large coherence length, $l_c = 1/2m_N x$.

terms of effective violation of asymptotic freedom in this limit. This regime is expected to be reached in heavy nuclei at x values at least an order of magnitude larger than in the proton. Hence in the LHC kinematics, the region where novel QCD phenomena are important will extend at least two orders of magnitude in $x_{\rm A}$ over a large range of virtualities.

The space–time picture of the black-body limit in pA collisions can be seen best in the rest frame of the nucleus. A parton belonging to the proton emits a hard gluon (virtual photon) long before the target and interacts with the target in a black regime releasing the fluctuation, a jet/$q\bar{q}$ (a Drell–Yan pair). This leads to a qualitative change in the picture of pA interactions for the partons with x_p and p_T satisfying the condition that

$$x_{\rm A} = \frac{4p_T^2}{x_p s_{NN}}\,, \tag{1.88}$$

is in the black-body kinematics for the resolution scale $p_T \leq p_T^{\rm bbl}(x_{\rm A})$. Here $p_T^{\rm bbl}(x_{\rm A})$ is the maximum p_T at which the black-body approximation is applicable. Hence by varying $x_{\rm A}$ for fixed x_p and looking for the the maximum value of $p_T^{\rm bbl}$ we can determine $p_T^{\rm bbl}(x_p)$. In the kinematics of the LHC, $Q^2 \approx 4\ (p_T^{\rm bbl})^2$ can be estimated by using formulae derived in Ref. [327]. At $x_p \sim 0.3$ Q^2 may be as large as $(p_T^{\rm bbl}(x_p))^2$ = 15 GeV^2. All the partons with such x_p will obtain $p_T({\rm jet}) \sim p_T^{\rm bbl}(x_p)$, leading to multi-jet production. The black-body regime will extend down in x_p with increasing $\sqrt{s_{NN}}$. For the LHC with $p_T \leq 3$ GeV/c, this regime may cover the whole region $x_p \geq 0.01$ where of the order 10 partons reside. Hence, in this limit, most of the final states will correspond to multi-parton collisions. For $p_T \leq 2$ GeV/c the region extends to $x_p \geq 0.001$. At the LHC, collisions of such partons correspond to central rapidities. Dynamics of the conversion of high-p_T partons with similar rapidities to hadrons is a collective effect requiring special consideration.

Inclusive observables. For the total cross sections, logic similar to that employed in γ^*–nucleus scattering [330] should be applicable. In particular, for the dimuon total cross section,

$$\frac{d\sigma(pA \to \mu^+\mu^- + X)}{dx_A dx_p} = \frac{4\pi\alpha_{\rm em}^2}{9}\frac{K(x_A, x_p, M^2)}{M^2}F_{2p}(x_p, Q^2)\frac{M^2}{6\pi^2}2\pi R_A^2 \ln\left(\frac{x_0}{x_A}\right), \tag{1.89}$$

for large but not too large dimuon masses, M. In particular we estimate $M^2({\rm bbl})$ ($x_{\rm A} = 10^{-7}$) $\approx$ 60 GeV^2. Here the K-factor has the same origin as in the leading-twist case but it should be smaller since it originates from gluon emissions only from the parton belonging to the proton. We define x_0 as the maximum x for which the black body limit is valid at the resolution scale M. Hence the expected M^2 dependence of dimuon production is qualitatively different than in pp scattering where scattering at large impact parameters may mask the contribution from the black-body limit. In this limit, the $x_{\rm A}$ dependence of the cross section becomes weak.

The study of the dimuon p_T distribution may also signal the onset of the black-body regime. As in the case of leading partons in deep inelastic scattering [330], a broadening of the dimuon p_T distribution is expected in the black-body limit compared to the DGLAP expectations. See Ref. [334] for a calculation of this effect in the colour glass condensate model.

At still lower $x_{\rm A}$, the black-body formalism will probably overestimate the cross section because the interaction the sea quarks and gluons in the proton will also be in the black-body limit.

The onset of the black-body regime will also lead to important changes in hadron production such as a much stronger drop of the x_F spectrum in the proton fragmentation region accompanied by p_T broadening and enhancement of hadron production at smaller rapidities, see the discussion in Section 7.4.3.

It is worth emphasizing that onset of the black-body limit for ultra small $x_{\rm A}$ will place limits on using forward kinematics for PDF measurements at larger $x_{\rm A}$. At the very least it would be necessary to satisfy the condition $p_T({\rm jet}) \gg p_T^{\rm bbl}(x_p)$. Indeed, as soon as large enough x_p are used for the nPDF measurements one would have to take into account that such collisions with nuclear partons are always

accompanied by significant p_T broadening, due to the interaction with the 'black component' of the nuclear wave function. At a minimum, this would lead to significant broadening of the p_T distribution of the produced hard system. One can also question the validity of the leading-twist expansion for the p_T-integrated cross sections. To investigate these phenomena, the ability to make measurements at fixed $x_{\rm A}$ and different x_p would be very important.

7.4. Mapping the Three-Dimensional Nucleon Parton Structure

Systematic studies of hard inclusive processes during the last two decades have led to a reasonably good understanding of the single parton densities in nucleons. However, very little is known about multiparton correlations in nucleons. These correlations can provide critical new insights into strong interaction dynamics, as well as discriminate between models of the nucleon. Such correlations may be generated, for example, by fluctuations in the transverse size of the colour field in the nucleon leading, via colour screening, to correlated fluctuations of the gluon and quark densities.

QCD evolution is a related source of correlations since selection of a parton with a given x and Q^2 may lead to a local enhancement of the parton density in the transverse plane at different x values. Also, practically nothing is known about possible correlations between the transverse size of a particular configuration in the nucleon and the longitudinal distribution of partons in this configuration.

7.4.1. Multi-jet production and double parton distributions

It was recognized already more than two decades ago [335] that the increase of parton densities at small x leads to a strong increase in the probability of NN collisions where two or more partons from each nucleon undergo pairwise independent hard interactions. Although multijet production through double-parton scattering was investigated in several experiments [207, 208, 336] at pp and p$\bar{\rm p}$ colliders, the interpretation of the data was hampered by the need to model both the longitudinal and the transverse partonic correlations simultaneously. Studies of pA collisions at the LHC will provide a feasible opportunity to study the longitudinal and transverse partonic correlations in the nucleon separately as well as to check the validity of the underlying picture of multiple collisions.

The simplest case of a multi-parton process is double-parton collisions. Since the momentum scale p_T of a hard interaction corresponds to much smaller transverse distances, $\sim 1/p_T$, in coordinate space than the hadronic radius, in a double-parton collision the two interaction regions are well separated in transverse space. Also, in the centre-of-mass frame, pairs of partons from the colliding hadrons are located in pancakes of thickness less than $(1/x_1 + 1/x_2)/p_{\rm cm}$. Thus two hard collisions occur almost simultaneously as soon as x_1 and x_2 are not too small. Hence there is no cross talk between two hard collisions. A consequence is that the different parton processes add incoherently in the cross section. The double-parton scattering cross section, proportional to the square of the elementary parton–parton cross section, is therefore characterized by a scale factor with dimension of inverse length squared. The dimensional quantity is provided by nonperturbative input, namely by the multi-parton distributions. In fact, because of the localization of the interactions in transverse space, the two pairs of colliding partons are aligned in such a way that the transverse distance between the interacting target partons is practically the same as the transverse distance between the projectile partons. The double-parton distribution, $\Gamma(x, x', b)$, is therefore a function of two momentum fractions and of the transverse distance, b. Although Γ also depends on the virtualities of the partons, Q^2 and Q'^2, to make the expressions more compact, this Q^2 dependence is not explicitly expressed. Hence the double-parton scattering cross section for the two '$2 \to 2$' parton processes α and β in an inelastic interaction between hadrons (or nuclei) a and b can be written as:

$$\sigma_D(\alpha,\beta) \;=\; \frac{m}{2}\int \Gamma_a(x_1,x_2;b)\hat{\sigma}_\alpha(x_1,x_1')\hat{\sigma}_\beta(x_2,x_2')\Gamma_b(x_1',x_2';b)dx_1dx_1'dx_2dx_2'd^2b\,, \quad (1.90)$$

where $m = 1$ for indistinguishable and m = 2 for distinguishable parton processes. Note that though the

factorization approximation of Eq. (1.90) is generally accepted in the analyses of the multijet processes and appears natural based on the geometry of the process, no formal proof exists. As we shall show below, the study of the A-dependence of this process will be a stringent test of this approximation.

To simplify the discussion, we neglect small non-additive effects in the parton densities, a reasonable approximation for $0.02 \leq x \leq 0.5$. In this case, we have to take into account only b-space correlations of partons in individual nucleons.

There are thus two different contributions to the double-parton scattering cross section ($A \equiv a, p \equiv b$): $\sigma_D = \sigma_D^1 + \sigma_D^2$. The first one, σ_1^D, the interaction of two partons from the same nucleon, is the same for nucleons and nuclei except for the enhancement of the parton flux. The corresponding cross section is

$$\sigma_D^1 = \sigma_D \int d^2B T_A(B) = A\sigma_D^{NN}\,, \tag{1.91}$$

where

$$T_A(B) = \int_{-\infty}^{\infty} dz \rho_A(r), \text{and} \int T_A(B) d^2B = A \tag{1.92}$$

is the nuclear thickness as a function of the impact parameter B of the hadron–nucleus collision.

The contribution to $\Gamma_A(x_1', x_2', b)$ from partons in different target nucleons, σ_D^2, can be calculated *solely* from the geometry of the process by observing that the nuclear density does not change within the transverse scale $\langle b \rangle \ll R_A$. It rapidly increases with A as $\int T_A^2(B) d^2B$. Using information from the CDF double scattering analysis [207, 208] on the mean transverse separation of partons in a nucleon, one finds that the contribution of the second term should dominate in pA collisions: $\sigma_D^2/\sigma_D^1 \approx 0.68\ (\mathrm{A}/12)^{0.39}$ for $A \geq 40$ [337]. Hence one expects a stronger than $\propto A$ increase of multijet production in pA collisions at the LHC. Measurements with a range of nuclei would probe the double-parton distributions in nucleons and also check the validity of QCD factorization for such processes. Factorization appears natural but is so far not derived in pQCD. An important application of this process would be the investigation of transverse correlations between the nuclear partons in the shadowing region. A study of these correlations would require selection of both nuclear partons in the shadowing region, $x_{\mathrm{A}} \leq x_{\mathrm{sh}} \sim 10^{-2}$ [14].

As discussed in Section 7.3., partons with sufficiently large x_p, satisfying Eq. (1.88), are expected to interact with small-x partons in the nucleus with a probability of order one. As a result, a hard collision of partons with sufficiently large x_p and $x_{\mathrm{A}} \geq 0.01$ will be accompanied by production of one or more minijets in the black-body regime with $p_T \sim p_T^{\mathrm{bbl}}(x_{\mathrm{A}})$. Most sufficiently fast partons from the proton will generate minijets, leading to a strong suppression of the cross section of events with only two jets.

Detectors with sufficiently forward rapidity acceptance could detect events originating from triple-parton collisions at $x_{\mathrm{A}} \geq x_{\mathrm{sh}}$ and large enough p_T where p_T broadening related to the black-body limit effects are sufficiently small. These triple-parton collisions provide stringent tests of the hard interaction dynamics as well as providing additional information on two-parton correlations and unique information on triple-parton correlations.

Other opportunities with multi-jets include:

- Probing correlations between partons in the nucleus at high densities, i.e. for $x_{1A}, x_{2A} \ll 10^{-3}$, which would provide qualitatively new information about the dynamics of nuclear shadowing and the presence of possible new parton condensates.
- Studying the accompanying soft hadron production (cf. the discussion in Section 7.4.2.), which would measure the transverse size of a proton configuration containing partons x_1 and x_2. In particular, the production of four jets with two of the jets at large x_p, $x_1 + x_2 \geq 0.5$, may provide

[14] The A-dependence of the ratio of σ_D^2/σ_D^1 in the kinematics where only one of the nuclear partons has $x_{\mathrm{A}} \leq x_{\mathrm{sh}}$ is practically the same as for the case when both nuclear partons have $x \geq x_{\mathrm{sh}}$.

another way to look for point-like configurations in nucleons, see Section 7.5. and Ref. [324] for discussion of other possibilities.

7.4.2. Proton–ion collisions probe transverse nucleon structure

As we discuss in Section 7.5., in some subclass of events the distribution of constituents in the initial proton may be unusually local in the transverse (impact parameter) plane when the proton collides with the ion. If this is so, its effective cross section per nucleon will be greatly reduced, perhaps all the way to the perturbative-QCD level. If the effective cross section of such a point-like configuration goes below 20 mb, there will be an appreciable probability that it can penetrate through the centre of a lead ion and survive, leading to a strongly enhanced diffractive yield of the products of the point-like configuration in collisions with heavy-ions.

Not only might the properties of the final-state collision products depend upon the nature of the transverse structure of the proton primary on arrival at the collision point, but even the conventional parton distributions could be affected. For example, let us consider a nucleon as a quark and small diquark connected by a narrow QCD flux-tube. It should be clear that if the flux-tube is at right angles to the collision axis at arrival, then the valence partons will have comparable longitudinal momentum or x. On the other hand, if the flux tube is parallel to the direction of motion, then one of the valence systems will have very large x and the other very small. This happens because in this case, the internal longitudinal momenta of the valence systems, in the rest frame of the projectile proton, are in opposite directions. Therefore the smallness of the configuration is correlated with the joint x-distribution of its constituents. This kind of nonfactorization may be determined by the study of perturbative QCD processes such as dilepton, direct-photon, or dijet production as a function of the centrality[15], soft hadron multiplicity, and A. Naturally such studies would also require investigation of soft hadron production as a function of impact parameter. At LHC energies it may differ quite strongly from fixed-target energies.

One possible kinematics where a strong correlation is expected is when a parton with large $x \geq 0.6$, is selected in the proton. The presence of such a parton requires three quarks to exchange rather large momenta. Hence one may expect that these configurations have a smaller transverse size and therefore interact with the target with a smaller effective cross section, $\sigma_{\rm eff}(x)$. Suggestions for such x dependence on the size are widely discussed in the literature. Using a geometric (eikonal type) picture of pA interactions as a guide and neglecting (for simplicity) shadowing effects on nPDFs, one can estimate the number of wounded nucleons, $\nu(x, A)$, in events with a hard trigger (Drell–Yan pair, γ-jet, dijet...) as a function of $\sigma_{\rm eff}$ [338]:

$$\nu(x, A) = 1 + \sigma_{\rm eff}(x)\frac{A-1}{A^2}\int T_A^2(B)\, d^2B\,, \tag{1.93}$$

where the nuclear density per unit area $T_A(B)$ is defined in Eq. (1.92). At the LHC, for average inelastic pPb collisions and $\sigma_{\rm eff} \sim \sigma_{\rm inel}(pp)$, Eq. (1.93) leads to $\nu \approx 10$, somewhat larger than the average number of wounded nucleons in pA collisions due to the selection of more central impact parameters in events with a hard trigger.

A decrease of the effective cross section for large x, say, by a factor of 2, would result in a comparable drop of the number of particles produced at central rapidities as well as in a smaller number of nucleons produced in the nuclear fragmentation region.

7.4.3. A-dependence of the particle production

Proton fragmentation region. The A-dependence of hadron production in the proton fragmentation region remains one of the least understood aspects of hadron–nucleus interactions. Practically all available data are inclusive and correspond to energies where the inelastic NN cross section is about three

[15]The impact parameter dependence is accessible in the pA collisions via a study of nuclear fragmentation into various channels. For an extensive discussion see Ref. [324].

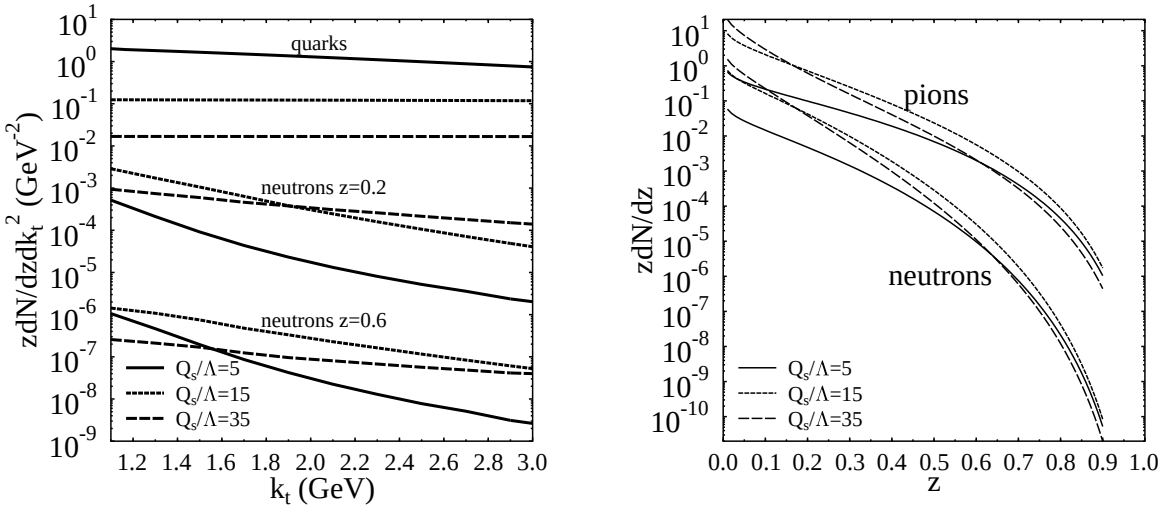

Fig. 1.53: Left: transverse-momentum distribution of neutrons (in fact, $n/2 + \bar{n}/2$) from the breakup of an incident proton at various longitudinal momentum fractions z and target saturation momenta Q_s (bottom six curves). The top three curves depict the underlying quark distributions. Right: Longitudinal distributions of $n/2+\bar{n}/2$ and π^0, integrated over k_T. From Ref. [341].

times smaller than at the LHC. They indicate that the cross section is dominated by the production of leading particles at large impact parameters where the projectile interacts with only one or two nucleons of the nucleus. As a result, very little information is available about hadron production at the central impact parameters most crucial for the study of AA collisions. Theoretical predictions for this region are also rather uncertain.

In eikonal-type models, where the energy is split between several soft interactions, one may expect a very strong decrease of the leading particle yield. The dependence is expected to be exponential with path length through the nucleus: the mean energy is attenuated exponentially. On the other hand, if the valence partons of the projectile do not lose a significant amount of their initial momentum, as suggested by pQCD motivated models, see the review in Ref. [187], the spectrum of leading particles may approach a finite limit for large A and central impact parameters [339]. Indeed, in this case, the leading partons will acquire significant transverse momenta and will not be able to coalescence back into leading baryons and mesons, as seemingly happens in nucleon–nucleon collisions. As a result, they will fragment practically independently, leading to much softer longitudinal momentum distributions for mesons and especially for baryons [339].

We discussed previously that the interaction strength of fast partons in the nucleon ($x_p \geq 10^{-2}$ for LHC) with heavy nuclei at central impact parameters might approach the black-body limit. In this scenario, all these partons will acquire large transverse momenta $\sim p_T^{\rm bbl}(x_{\rm A})$ [16], leading to a very significant p_T broadening of the leading hadron spectrum [120]. Probably the most feasible way to study this effect is measurement of the p_T distribution of leading hadrons (neutrons, K_L, π^0) in central collisions. These hadrons will closely follow the p_T of the leading quarks [341]. The results of the calculation [341] using the colour glass condensate model for modeling p_T broadening are shown in Fig. 1.53 for different values of the saturation parameter Q_s. It is worth emphasizing that strong p_T broadening, increasing with x_F, clearly distinguishes this mechanism of leading hadron suppression from the soft physics effect of increasing the total pp cross section by nearly a factor of three over fixed-target energies.

Central region. The Gribov–Glauber model, including inelastic screening effects but neglecting the final-state interactions between the hadrons produced in different Pomeron exchanges, as well as ne-

[16] Hence in the black-body limit, p_T broadening of the partons should be much larger than at low energies where it is consistent with QCD multiple rescattering model [187]. See Ref. [340] for a discussion of matching these two regimes.

glecting the interactions of these hadrons with the nuclear target, predicts that, at high energies and rapidities y such that $|y_p - y| \gg 1$, the inclusive pA spectrum should be proportional to that of pN scattering:

$$\frac{d\sigma^{p+A\to h+X}(y,p_T)}{dy\ d^2p_T} = A\frac{d\sigma^{p+N\to h+X}(y,p_T)}{dy\ d^2p_T}\,. \tag{1.94}$$

Since $\sigma_{\rm inel}(pA)/\sigma_{\rm inel}(pN) \propto A^{2/3}$, Eq. (1.94) implies that the multiplicity of particles produced in the inelastic pA collisions should increase as $\propto A^{1/3}$. Data at fixed-target energies do not contradict this relation but the energy is too low for an unambiguous interpretation. Effects of splitting the energy between multiple soft NN interactions are much larger in AA collisions than in pA collisions so checking whether a similar formula is valid for AA collisions would require energies much higher than those available at RHIC.

The opposite extreme is to assume that parton interactions in the black-body regime become important in a large range of $x_p \geq 10^{-2}$. In this case, multiple scatterings between the partons, their independent fragmentation together with associated QCD radiation (gluon bremsstrahlung), may produce most of the total entropy and transverse energy and will enhance hadron production at central rapidities relative to the Gribov–Glauber model.

Nuclear fragmentation region. For the rapidities close to that of the nucleus, there are indications of slow hadron rescatterings, leading to increased nucleon multiplicity for $1.0 \geq p_N \geq 0.3$ GeV compared to no final-state reinteractions, a factor of ~ 2 for heavy nuclei [342]. As discussed above, it is doubtful that the Gribov–Glauber picture is correct at LHC energies, so that significant deviations from Eq. (1.94) may be expected. It is likely that a coloured quark–gluon system with rapidities close to y_A will be excited along a cylinder of radius ~ 1 fm and length $2R_A$, resulting in unusual properties of hadron production in the nuclear fragmentation region, including production of exotic multi-quark, multi-gluon states.

We emphasize that a quantitative understanding of particle production in pA collisions in this phase-space region is a prerequisite for understanding the corresponding phenomenology in AA collisions.

7.5. A New Hard QCD Phenomenon: Proton Diffraction into Three Jets

7.5.1. Introduction

During the last ten years, a number of new, hard, small-x phenomena have been observed and calculated in QCD based on the QCD factorization theorems for inclusive DIS and hard exclusive processes. These phenomena include (i) observation of a fast increase of the PDFs with energy at HERA, reasonably described within the QCD evolution equation approximation[17]; (ii) discovery of colour transparency in pion coherent dissociation into two high-p_T jets [343], consistent with the predictions of Refs. [344,345]; (iii) observation of various regularities in exclusive vector-meson electroproduction at HERA induced by longitudinally polarized photons and photoproduction of mesons with hidden heavy flavour consistent with the predictions of Ref. [346]. These processes, in a wide kinematic range of small-x, have provided effective ways to study the interaction of small colourless dipoles with hadrons at high energies and to study the hadron wave functions in their minimal Fock space configurations. Here we outline new QCD phenomena [324] which may become important at the LHC because their cross sections are rapidly increasing with energy.

A fast increase of hard diffractive cross sections with energy, predicted within the leading-twist (LT) approximation, would be at variance with unitarity of the S-matrix for the interaction of spatially small wave packets of quarks and gluons with a hadron target at a given impact parameter. This new

[17] For a comprehensive review of the HERA data on inclusive and exclusive processes and the relevant theory, see Ref. [333].

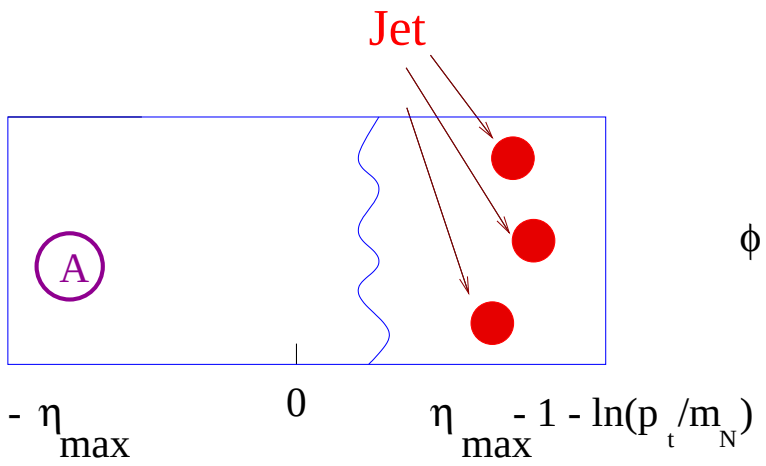

Fig. 1.54: LEGO plot for diffraction of proton into three jets

phenomenon may reveal itself at sufficiently small-x and/or sufficiently heavy nuclei. In the proton structure functions, this physics is masked by a significant contribution to the hard collisions of the nucleon periphery. Thus, unitarity of the S-matrix does not preclude an increase of nucleon structure functions as fast as $\propto \ln(1/x)^3$ [330]. Hence no dramatic signals for the breakdown of the DGLAP regime are expected in this case. On the contrary, a breakdown of the LT approximation in hard diffractive processes off nuclei leads to drastic changes in the cross section dependence on A, incident energy and jet p_T.

7.5.2. Three-jet exclusive diffraction

A nucleon (meson) has a significant amplitude to be in a configuration where the valence partons are localized in a small transverse area together with the rest of the partons. These configurations are usually referred to as *minimal* Fock space configurations – $|3q\rangle$. Experimental evidence for a significant probability for these configurations in mesons includes the significant decay amplitude for $\pi \to \text{leptons}$ as well as the significant observed diffractive vector meson electroproduction cross sections and the process $\pi + A \to 2\,\text{jets} + A$ [343]. In the proton case, the amplitude of the three-quark configuration can be estimated within QCD-inspired models and, eventually calculated in lattice QCD. Note that knowledge of this amplitude is important for the unambiguous calculation of proton decay within Grand Unification models.

Hadrons, in small size configurations with transverse size d, interact with a small cross section $\propto d^2 x G_N(x, Q^2)$, where $Q^2 \sim 10/d^2$. The factor $xG_N(x, Q^2)$ leads to a fast increase of the *small* cross section with energy. In the case of 'elastic scattering' of such a proton configuration off another proton, this three-quark system with large relative momenta should preferentially dissociate diffractively into a system of three jets with large transverse momenta $p_{Ti} \sim \pi/d$, where d is the transverse size of the minimal configuration. The kinematics of this process is presented in the LEGO plot of Fig. 1.54 for the case of coherent scattering off a nucleus.

The 3-jet production cross section can be evaluated based on the kind of QCD factorization theorem deduced in Ref. [345]. The cross section is proportional to the square of the gluon density in the nucleon at $x \approx M^2_{3\,\text{jets}}/s$ and virtuality $\sim (1-2)\, p_T^2$ [347]. The distribution over the fractions of the longitudinal momentum carried by the jets is proportional to the square of the light cone wave function of the $|3q\rangle$ configuration, $\psi(z_1, z_2, z_3, p_{T1}, p_{T2}, p_{T3})$ and large transverse momenta where

$$\psi(z_1, z_2, z_3, p_{T1}, p_{T2}, p_{T3}) \propto z_1 z_2 z_3 \sum_{i \neq j} \frac{1}{p^2_{Ti}} \frac{1}{p^2_{Tj}}\,. \tag{1.95}$$

The proper renormalization procedure accounting for cancellation of infrared divergences is implied. Otherwise the light cone gauge $p_{N,\mu}A_\mu$ = 0, should be used to describe the diffractive fragmentation region where there are no infrared divergences. Here p_N is the momentum of the diffracted proton. The summation over collinear radiation is included in the definition of the jets.

Naively, one can hardly expect that exclusive jet production would be a leading-twist effect at high energies since high-energy hadrons contain a very large number of soft partons in addition to three valence quarks. However, application of the QCD factorization theorem demonstrates that in high-energy exclusive processes these partons are hidden in the structure function of the target. Hence proton diffraction into three jets provides important information about the short-distance quark structure of the proton and also provides unique information about the longitudinal momentum distribution in the $|3q\rangle$ configuration at high-p_T. The amplitude of the process can be written as

$$A = \left[-\vec{\Delta}\psi(z_1, z_2, z_3, p_{T1}, p_{T2}, p_{T3})\right] \left[\frac{2\pi^2}{3}\alpha_s(xG(x, Q^2, t))\right]. \tag{1.96}$$

Here $\vec{\Delta} = \sum_{i=1}^{3} \frac{\partial^2}{\partial p_i^2}$. In Eq. (1.96) we simplify the expression by substituting a skewed gluon density reflecting the difference in the light-cone fractions of the gluons attached to the nucleon by the gluon density which is numerically a reasonable approximation for rough estimates. An additional factor of 2 in the numerator relative to the pion allows two gluons to be attached to different pairs of quarks. The p_T and longitudinal momentum fraction, z_i, dependence of the cross section is given by

$$\frac{d\sigma}{dz_1 dz_2 dz_3 d^2p_{T1} d^2p_{T2} d^2p_{T3}} = c_N \left|\alpha_s xG(x, Q^2)\right|^2 \frac{|\phi_N(z_1, z_2, z_3)|^2}{|p_{T1}|^4 |p_{T2}|^4 |p_{T3}|^4} F_{2g}^2(t) \\ \delta(\sum p_{Ti} - \sqrt{-t})\, \delta(\sum z_i - 1)\,. \tag{1.97}$$

The coefficient c_N is calculable in QCD and $\phi_N(z_1, z_2, z_3) = z_1 z_2 z_3$. The two-gluon form factor of a nucleon is known to some extent from hard diffractive processes [348]. A numerical estimate of the three-jet production cross section with p_T of one of the jet greater than a given value and integrated over all other variables gives, for $p_T \geq 10$ GeV/c,

$$\sigma(pp \to 3\,\text{jets} + p) \propto \frac{|\alpha_s xG(x, Q^2)|^2}{p_T^8} \propto 10^{-6} \ldots 10^{-7} \left(\frac{10\,\text{GeV}}{p_T}\right)^8 \text{mb} \tag{1.98}$$

for LHC energies. An urgent question is whether this cross section will continue to grow up to LHC energies, as assumed here based on extrapolations of $G_N(x, Q^2)$ to $x \sim 10^{-5}$. The probability of the $|3q\rangle$ configuration is estimated using a phenomenological fit to the probability of configurations of different interaction strengths in a nucleon, cf. Refs. [347, 349].

A study of the same process in pA collisions would provide an unambiguous test of the dominance of hard physics in this process. The cross section should grow with A as $\frac{A^2}{R_A^2} G_A^2(x, Q^2)/A^2 G_N^2(x, Q^2)$. Accounting for the skewness of the gluon distribution will lead to some enhancement in the absolute value of the cross section but will not strongly influence the A-dependence.

Our estimates indicate that for the relevant LHC kinematics, $x \sim 10^{-5}$ and $Q^2_{\text{eff}} \sim p_T^2$, nuclear shadowing in the gluon channel is a rather small correction, reducing the A-dependence of the cross section by $A^{0.1}$, leading to $\sigma(pA \to 3\,\text{jets} + A) \propto A^{1.25}$. The A-dependence of total inelastic cross section is $\propto A^{0.7}$. Hence we expect that the counting rate per inelastic interaction will be enhanced in pA collisions for a heavy nuclear target by a factor $\propto A^{0.55}$. At the same time, the background from soft diffraction should be strongly reduced. Indeed, if we estimate the A-dependence of soft diffraction based on the picture of colour fluctuations, which provides a good description of total cross section of the inelastic diffraction off nuclei at fixed-target energies [325], we find $\sigma_{pA}^{\text{inel. diff.}} \propto A^{0.25}$. Scattering off nuclei also has an obvious advantage in terms of selecting coherent processes since practically all inelastic interactions with nuclei would lead to the emission of neutrons at 0°.

A competing process is proton diffraction into 3 jets off the nuclear Coulomb field. It follows from the theorem proved in Refs. [345, 350] that to leading order in α_s the dominant contribution is given in the Weizsäcker–Williams representation by transverse photon interactions with external quark lines. The amplitude of the process is [350]:

$$\frac{-e^2\psi_N(z_i,p_{Ti})}{q^2-t_{\min}}ZF_A(t)\frac{2s}{M^2(3\text{jet})}\sum_i\frac{e_i(\vec{p}_{Ti}\cdot\vec{q_T})}{z_i}D^{-3/2}(p_{Ti})\,, \tag{1.99}$$

where e_i is the electric charge of the quark in the units of the electron charge, q^2 is the virtuality of the exchanged photon and $D(p_T^2)$ is the renormalization factor for the quark Green's function.

In the kinematics where LT dominates the QCD mechanism for 3-jet production, the electromagnetic process is a small correction. However, if the screening effects (approach to the black-body limit) occur in the relevant p_T range, the electromagnetic process may compete with the QCD contribution. In the case of nuclear breakup, the electromagnetic contribution remains a relatively modest correction, even in the black-body limit. This is primarily because the cross section for electromagnetic nuclear breakup does not have a singularity at $q^2 = 0$. Note also that, in the case of QCD interactions, one can consider processes with a large rapidity gap which have the same z_i and p_{Ti} dependence as the coherent process but with a significantly larger cross section.

Another interesting group of hard processes is proton diffraction into two high-p_T jets and one collinear jet. These processes are, in general, dominated at high energies by collisions of two nucleons at large impact parameters (otherwise multiple soft interactions would destroy the coherence). Hence the A-dependence of the dominant term should be similar to that of $\sigma_{pA}^{\text{inel. diff.}}$. However, fluctuations with cross sections of ~ 40 mb would have a much stronger A-dependence, $\sim A^{0.7}$. Thus the study of the A-dependence of coherent diffraction can filter out the smaller than average components in the nucleons at LHC energies.

7.5.3. Violation of the LT approximation and new QCD strong interactions

The energy dependence of cross section in the LT approximation follows from the properties of the target gluon distribution. Hence for the virtualities probed in 3-jet production, the energy dependence is $\propto x^2G^2(x,Q^2_{\text{eff}}) \propto s^{0.8}$ for $Q^2_{\text{eff}} \sim 100$ – 1000 GeV^2 and $10^{-5} \leq x \leq 10^{-2}$. In the black-body limit, the inelastic diffractive processes are strongly suppressed and hence the energy dependence of the 3-jet production cross section integrated over $p_T \geq p_{T\min} \sim$ a few GeV should slow down since only scattering off the grey edge of the nucleus (nucleon) will effectively survive. For Q^2 relevant to this process, the black-body limit may only be an interesting hypothesis for scattering off heavy nuclei. It would manifest itself in a strong decrease of the A-dependence of 3-jet production at the p_T corresponding to the black-body limit. At sufficiently small-x for a heavy nuclear target, $d\sigma(pA \to 3\text{jets} + A)/dp_T^2 \propto A^{1/3}$, in striking contrast with the LT expectations, $\propto A^{1.2}$.

7.6. Conclusions

In conclusion, studies of pA collisions at the LHC will reveal strong interactions in the high-field domain over an extended rapidity region. New phenomena will be especially prominent in the proton fragmentation region but will extend to the central region and the nuclear fragmentation region as well.

Acknowledgements

The convenors (K.J. Eskola, J.W. Qiu and W. Geist) thank the contributing authors for fruitful collaboration.

The editor (K.J. Eskola) is grateful to R. Vogt for many useful remarks in finalizing the manuscript.

The following sources of funding are acknowledged:

Academy of Finland,

Project 50338: K.J. Eskola, H. Honkanen, V.J. Kolhinen;

Project 80385: V.J. Kolhinen;

Alexander von Humboldt Foundation: R. Fries;

CICYT of Spain under contract AEN99-0589-C02: N. Armesto;

European Commission IHP programme, Contract HPRN-CT-2000-00130: A. Accardi;

German Israeli Foundation: L. Frankfurt;

Israeli Science Foundation, BSF grant # 9800276: Yu.V. Kovchegov;

Marie Curie Fellowship of the European Community programme TMR,

Contract HPMF-CT-2000-01025: C.A. Salgado;

United States Department of Energy,

Contract No. DE-AC03-76SF00515: S.J. Brodsky;

Grant No. DE-FG02-86ER-40251: G. Fai, X.F. Zhang;

Grant No. DE-FG02-96ER40945: R. Fries;

Grant No. DE-FG03-97ER41014: Yu.V. Kovchegov;

Grant No. DE-FG02-87ER40371: J.W. Qiu;

Contract No. DE-FG02-93ER40771: M. Strikman;

Contract No. DE-AC03-76SF00098: R. Vogt;

Universidad de Córdoba: N. Armesto.

References

[1] H. Satz and X.N. Wang, *Int. J. Mod. Phys.* **A10** (1995) 2881.

[2] H. Satz and X.N. Wang, *Int. J. Mod. Phys.* **E12** (2003) 147.

[3] S.S. Adler *et al.* (PHENIX Collaboration), nucl-ex/0304022.

[4] J. Adams *et al.* (STAR Collaboration), nucl-ex/0305015.

[5] B.B. Back *et al.* (PHOBOS Collaboration), nucl-ex/0302015.

[6] S.S. Adler (PHENIX Collaboration), nucl-ex/0306021.

[7] J. Adams (STAR Collaboration), nucl-ex/0306024.

[8] B.B. Back (PHOBOS Collaboration), nucl-ex/0306025.

[9] D. Brandt, *Review of the LHC Ion Programme*, LHC Project Report 450 (2000).

[10] A. Morsch, *Luminosity Considerations for pA Collisions at the LHC*, ALICE Internal Note, ALICE-INT-97-13.

[11] A. Morsch, *ALICE Luminosity and Beam Requirements*, ALICE Internal Note, ALICE-INT-2001-10 (Version 2).

[12] ALICE Collaboration, Technical Proposal, CERN/LHCC-95-71 (1995).

[13] P. Giubellino (ALICE Collaboration), *Eur. Phys. J. directC* **4S1** (2002) 05.

[14] I. Chemakin *et al.* (E910 Collaboration), *Phys. Rev.* **C60** (1999) 024902, nucl-ex/9902003.

[15] W. Geist, *Options for pA physics at the CMS site*, preprint IReS 00-04.

[16] ATLAS: Technical Proposal, CERN/LHCC/94-3.

[17] J.C. Collins, D.E. Soper and G. Sterman, *Adv. Ser. Direct. High Energy Phys.* **5** (1988) 1.

[18] J.W. Qiu and G. Sterman, *Int. J. Mod. Phys.* **E12** (2003) 149, hep-ph/0111002, and references therein.

[19] J. Pumplin *et al.*, *JHEP* **0207** (2002) 012, hep-ph/0201195.

[20] A.D. Martin, R.G. Roberts, W.J. Stirling and R.S. Thorne, *Phys. Lett.* **B531** (2002) 216, hep-ph/0201127.

[21] B.A. Kniehl, G. Kramer and B. Potter, *Nucl. Phys.* **B597** (2001) 337, hep-ph/0011155; *Nucl. Phys.* **B582** (2000) 514, hep-ph/0010289.

[22] S. Kretzer, E. Leader and E. Christova, *Eur. Phys. J.* **C22** (2001) 269, hep-ph/0108055.

[23] L.D. McLerran and R. Venugopalan, *Phys. Rev.* **D49** (1994) 2233, hep-ph/9309289; *Phys. Rev.* **D49** (1994) 3352, hep-ph/9311205; *Phys. Rev.* **D50** (1994) 2225, hep-ph/9402335.

[24] J.W. Qiu, *Nucl. Phys.* **A715** (2003) 309c, nucl-th/0211086.

[25] L.V. Gribov, E.M. Levin and M.G. Ryskin, *Phys. Rep.* **100** (1983) 1.

[26] A.H. Mueller and J.W. Qiu, *Nucl. Phys.* **B268** (1986) 427.

[27] K.J. Eskola, V.J. Kolhinen and C.A. Salgado, *Eur. Phys. J.* **C9** (1999) 61, hep-ph/9807297.

[28] K.J. Eskola, V.J. Kolhinen and P.V. Ruuskanen, *Nucl. Phys.* **B535** (1998) 351, hep-ph/9802350.

[29] M. Hirai, S. Kumano and M. Miyama, *Phys. Rev.* **D64** (2001) 034003, hep-ph/0103208.

[30] L. Frankfurt *et al.*, Chapter 1, Section 4.4, in *'Hard Probes in Heavy-Ion Collisions at the LHC'*, CERN-2004-009 (2004).

[31] Y.V. Kovchegov, Chapter 1, Section 4.6, in *'Hard Probes in Heavy-Ion Collisions at the LHC'*, CERN-2004-009 (2004).

[32] K.J. Eskola *et al.*, hep-ph/0302185, Chapter 1, Section 4.2, in *'Hard Probes in Heavy-Ion Collisions at the LHC'*, CERN-2004-009 (2004).

[33] J.W. Qiu and G. Sterman, *Nucl. Phys.* **B353** (1991) 105, **B353** (1991) 137.

[34] S.J. Brodsky, Chapter 1, Section 4.5, in *'Hard Probes in Heavy-Ion Collisions at the LHC'*, CERN-2004-009 (2004).

[35] J.W. Qiu and X.F. Zhang, *Phys. Lett.* **B525** (2002) 265, hep-ph/0109210.

[36] M. Luo, J.W. Qiu and G. Sterman, *Phys. Rev.* **D49** (1994) 4493.

[37] X.F. Guo, *Phys. Rev.* **D58** (1998) 114033, hep-ph/9804234.

[38] R. Doria, J. Frenkel and J.C. Taylor, *Nucl. Phys.* **B168** (1980) 93; C. Di'Lieto, S. Gendron, I.G. Halliday and C.T. Sachrajda, *Nucl. Phys.* **B183** (1981) 223.

[39] F.T. Brandt, J. Frenkel and J.C. Taylor, *Nucl. Phys.* **B312** (1989) 589.

[40] R. Basu, A.J. Ramalho and G. Sterman, *Nucl. Phys.* **B244** (1984) 221.

[41] M. Gyulassy, P. Levai and I. Vitev, *Phys. Rev.* **D66** (2002) 014005, nucl-th/0201078.

[42] M. Gyulassy, P. Levai and I. Vitev, *Nucl. Phys.* **B594** (2001) 371, nucl-th/0006010.

[43] Y.L. Dokshitzer, *JETP* **46** (1977) 641 [*Zh. Eksp. Teor. Fiz.* **73** (1977) 1216]; V.N. Gribov and L.N. Lipatov, *Sov. J. Nucl. Phys.* **15** (1972) 438, 675 [*Yad. Fiz.* **15** (1972) 781, 1218]; G. Altarelli and G. Parisi, *Nucl. Phys.* **B126** (1977) 298.

[44] A.D. Martin, R.G. Roberts, W.J. Stirling and R.S. Thorne, *Eur. Phys. J.* **C23** (2002) 73, hep-ph/0110215.

[45] M. Gluck, E. Reya and A. Vogt, *Eur. Phys. J.* **C5** (1998) 461, hep-ph/9806404.

[46] M. Arneodo, *Phys. Rep.* **240** (1994) 301.

[47] M. Arneodo *et al.* (New Muon Collaboration), *Nucl. Phys.* **B481** (1996) 23.

[48] J.W. Qiu, *Nucl. Phys.* **B291** (1987) 746.

[49] L.L. Frankfurt, M.I. Strikman and S. Liuti, *Phys. Rev. Lett.* **65** (1990) 1725.

[50] K.J. Eskola, *Nucl. Phys.* **B400** (1993) 240.

[51] S. Kumano, *Phys. Rev.* **C50** (1994) 1247, hep-ph/9402321;
S. Kumano and M. Miyama, *Phys. Lett.* **B378** (1996) 267, hep-ph/9512244.

[52] K.J. Eskola, H. Honkanen, V.J. Kolhinen and C.A. Salgado, *Phys. Lett.* **B532** (2002) 222, hep-ph/0201256.

[53] K.J. Eskola, H. Honkanen, V.J. Kolhinen, P.V. Ruuskanen and C.A. Salgado, hep-ph/0110348.

[54] D.M. Alde *et al.*, *Phys. Rev. Lett.* **64** (1990) 2479.

[55] M.A. Vasilev *et al.* (FNAL E866 Collaboration), *Phys. Rev. Lett.* **83** (1999) 2304, hep-ex/9906010.

[56] *http://urhic.phys.jyu.fi/*; *http://www-fp.usc.es/phenom/*.

[57] H. Plothow-Besch, *Comput. Phys. Commun.* **75** (1993) 396;
H. Plothow-Besch, *Int. J. Mod. Phys.* **A10** (1995) 2901; *'PDFLIB: Proton, Pion and Photon Parton Density Functions, Parton Density Functions of the Nucleus, and α_s'*, Users's Manual – Version 8.04, W5051 PDFLIB 2000.04.17 CERN-ETT/TT.

[58] *http://www-hs.phys.saga-u.ac.jp.*

[59] P. Amaudruz *et al.* (New Muon Collaboration), *Nucl. Phys.* **B441** (1995) 3, hep-ph/9503291.

[60] M. Arneodo *et al.* (New Muon Collaboration), *Nucl. Phys.* **B441** (1995) 12, hep-ex/9504002.

[61] M. Arneodo *et al.* (New Muon Collaboration), *Nucl. Phys.* **B481** (1996) 3.

[62] M.R. Adams *et al.* (E665 Collaboration), *Phys. Rev. Lett.* **68** (1992) 3266.

[63] M.R. Adams *et al.* (E665 Collaboration), *Z. Phys.* **C67** (1995) 403, hep-ex/9505006.

[64] T. Gousset and H.J. Pirner, *Phys. Lett.* **B375** (1996) 349, hep-ph/9601242.

[65] K. Prytz, *Phys. Lett.* **B311** (1993) 286.

[66] S.Y. Li and X.N. Wang, *Phys. Lett.* **B527** (2002) 85, nucl-th/0110075.

[67] M.J. Leitch *et al.* (E789 Collaboration), *Phys. Rev. Lett.* **72** (1994) 2542.

[68] P. Amaudruz *et al.* (New Muon Collaboration), *Nucl. Phys.* **B371** (1992) 553.

[69] M. Gluck, E. Reya and A. Vogt, *Z. Phys.* **C53** (1992) 127.

[70] H.L. Lai *et al.*, *Phys. Rev.* **D55** (1997) 1280, hep-ph/9606399.

[71] S. Kumano, *Nucl. Phys. Proc. Suppl.* **112** (2002) 42, hep-ph/0204242.

[72] Z.W. Lin and M. Gyulassy, *Phys. Rev. Lett.* **77** (1996) 1222 [*Heavy Ion Phys.* **4** (1996) 123], nucl-th/9510041.

[73] K.J. Eskola, V.J. Kolhinen and R. Vogt, *Nucl. Phys.* **A696** (2001) 729, hep-ph/0104124.

[74] A. Morsch, Chapter 1, Section 2.1, in *'Hard Probes in Heavy-Ion Collisions at the LHC'*, CERN-2004-009 (2004).

[75] J.L. Nagle (PHENIX Collaboration), nucl-ex/0209015.

[76] M. Botje, Chapter 1, Section 2.2, in *'Hard Probes in Heavy-Ion Collisions at the LHC'*, CERN-2004-009 (2004).

[77] K.J. Eskola, V.J. Kolhinen, C.A. Salgado and R.L. Thews, *Eur. Phys. J.* **C21** (2001) 613, hep-ph/0009251.

[78] B. Alessandro *et al.*, CERN-ALICE-INTERNAL-NOTE-2002-025.

[79] S. Gavin, P.L. McGaughey, P.V. Ruuskanen and R. Vogt, *Phys. Rev.* **C54** (1996) 2606.

[80] I.P. Lokhtin and A.M. Snigirev, *Eur. Phys. J.* **C21** (2001) 155, hep-ph/0105244.

[81] K.J. Eskola *et al.*, *Nucl. Phys.* **B660** (2003) 211, hep-ph/0211239.

[82] J.W. Qiu, Chapter 1, Section 3, in *'Hard Probes in Heavy-Ion Collisions at the LHC'*, CERN-2004-009 (2004).

[83] W.G. Seligman *et al.*, *Phys. Rev. Lett.* **79** (1997) 1213.

[84] M. Botje, *Eur. Phys. J.* **C14** (2000) 285, hep-ph/9912439.

[85] X.F. Guo, J.W. Qiu and W. Zhu, *Phys. Lett.* **B523** (2001) 88, hep-ph/0110038.

[86] H.L. Lai *et al.* (CTEQ Collaboration), *Eur. Phys. J.* **C12** (2000) 375, hep-ph/9903282.

[87] C. Adloff *et al.* (H1 Collaboration), *Eur. Phys. J.* **C21** (2001) 33, hep-ex/0012053.

[88] K. Golec-Biernat and M. Wusthoff, *Phys. Rev.* **D59** (1999) 014017, hep-ph/9807513.

[89] N. Armesto, *Eur. Phys. J.* **C26** (2002) 35, hep-ph/0206017.

[90] M. Arneodo *et al.*, *'Nuclear beams in HERA'*, in Proc. *Hamburg 1995/96, Future Physics at HERA*, 887–926, hep-ph/9610423.

[91] H. Abramowicz *et al.* (TESLA-N Study Group Collaboration), DESY-01-011.

[92] A. Deshpande, R. Milner and R. Venugopala (eds.), *EIC White Paper*, preprint BNL-68933.

[93] S.J. Brodsky and H.J. Lu, *Phys. Rev. Lett.* **64** (1990) 1342.

[94] V. Barone, *Z. Phys.* **C58** (1993) 541.

[95] B. Kopeliovich and B. Povh, *Phys. Lett.* **B367** (1996) 329, hep-ph/9509362.

[96] N. Armesto and M.A. Braun, *Z. Phys.* **C76** (1997) 81, hep-ph/9603360.

[97] N.N. Nikolaev and B.G. Zakharov, *Z. Phys.* **C49** (1991) 607.

[98] L.L. Frankfurt and M.I. Strikman, *Phys. Rept.* **160** (1988) 235.

[99] L.L. Frankfurt and M.I. Strikman, *Nucl. Phys.* **B316** (1989) 340.

[100] B.Z. Kopeliovich, J. Raufeisen and A.V. Tarasov, *Phys. Rev.* **C62** (2000) 035204, hep-ph/0003136.

[101] N. Armesto and C.A. Salgado, *Phys. Lett.* **B520** (2001) 124, hep-ph/0011352.

[102] N. Armesto *et al.*, hep-ph/0304119.

[103] L. Frankfurt, V. Guzey, M. McDermott and M. Strikman, *JHEP* **0202** (2002) 027, hep-ph/0201230.

[104] A.H. Mueller and B. Patel, *Nucl. Phys.* **B425** (1994) 471, hep-ph/9403256.

[105] S. Catani, M. Ciafaloni and F. Hautmann, *Nucl. Phys.* **B366** (1991) 135.

[106] N. Armesto and M.A. Braun, *Eur. Phys. J.* **C22** (2001) 351, hep-ph/0107114.

[107] Z. Huang, H.J. Lu and I. Sarcevic, *Nucl. Phys.* **A637** (1998) 79, hep-ph/9705250.

[108] B. Andersson *et al.* (Small x Collaboration), *Eur. Phys. J.* **C25** (2002) 77, hep-ph/0204115.

[109] Y.V. Kovchegov and A.H. Mueller, *Nucl. Phys.* **B529** (1998) 451, hep-ph/9802440.

[110] A.H. Mueller, *Nucl. Phys.* **B558** (1999) 285, hep-ph/9904404.

[111] A.H. Mueller, hep-ph/0208278.

[112] R. Venugopalan, *Acta Phys. Polon.* **B30** (1999) 3731, hep-ph/9911371.

[113] NATO Advanced Study Institue, J.-P. Blaizot and E. Iancu (eds.), *'QCD Perspectives on Hot and Dense Matter'*, Corsica, 6–18 Aug. 2001, NATO Science Series, (Kluwer, Dordrecht, 2002).

[114] A.M. Stasto, K. Golec-Biernat and J. Kwiecinski, *Phys. Rev. Lett.* **86** (2001) 596, hep-ph/0007192.

[115] M. Lublinsky, *Eur. Phys. J.* **C21** (2001) 513, hep-ph/0106112.

[116] K. Golec-Biernat, L. Motyka and A.M. Stasto, *Phys. Rev.* **D65** (2002) 074037, hep-ph/0110325.

[117] N. Armesto and M.A. Braun, *Eur. Phys. J.* **C20** (2001) 517, hep-ph/0104038.

[118] E. Iancu, K. Itakura and L. McLerran, *Nucl. Phys.* **A708** (2002) 327, hep-ph/0203137.

[119] A. Freund, K. Rummukainen, H. Weigert and A. Schafer, hep-ph/0210139.

[120] A. Dumitru and J. Jalilian-Marian, *Phys. Rev. Lett.* **89** (2002) 022301, hep-ph/0204028.

[121] V.S. Fadin, E.A. Kuraev and L.N. Lipatov, *Phys. Lett.* **B60** (1975) 50.

[122] I.I. Balitsky and L.N. Lipatov, *Sov. J. Nucl. Phys.* **28** (1978) 822 [*Yad. Fiz.* **28** (1978) 1597].

[123] D. Indumathi and W. Zhu, *Z. Phys.* **C74** (1997) 119, hep-ph/9605417.

[124] V.N. Gribov, *Sov. J. Nucl. Phys.* **9** (1969) 369 [*Yad. Fiz.* **9** (1969) 640];
Sov. Phys. JETP **30** (1970) 709 [*Zh. Eksp. Teor. Fiz.* **57** (1969) 1306].

[125] L. Frankfurt and M. Strikman, *Eur. Phys. J.* **A5** (1999) 293, hep-ph/9812322.

[126] J.C. Collins, *Phys. Rev.* **D57** (1998) 3051, Erratum **D61** (2000) 019902, hep-ph/9709499.

[127] L. Alvero, L.L. Frankfurt and M.I. Strikman, *Eur. Phys. J.* **A5** (1999) 97, hep-ph/9810331.

[128] L. Frankfurt, V. Guzey and M. Strikman, hep-ph/0303022.

[129] I. Balitsky, *Nucl. Phys.* **B463** (1996) 99, hep-ph/9509348.

[130] Y.V. Kovchegov, *Phys. Rev.* **D61** (2000) 074018, hep-ph/9905214.

[131] S.J. Brodsky *et al.*, *Phys. Rev.* **D65** (2002) 114025, hep-ph/0104291.

[132] A.V. Belitsky, X. Ji and F. Yuan, *Nucl. Phys.* **B656**, 165 (2003), hep-ph/0208038.

[133] J.C. Collins, hep-ph/0304122.

[134] V.N. Gribov, *Sov. Phys. JETP* **29** (1969) 483 [*Zh. Eksp. Teor. Fiz.* **56** (1969) 892].

[135] S.J. Brodsky and J. Pumplin, *Phys. Rev.* **182** (1969) 1794.

[136] S.J. Brodsky and H.J. Lu, *Phys. Rev. Lett.* **64** (1990) 1342.

[137] G. Piller and W. Weise, *Phys. Rep.* **330** (2000) 1, hep-ph/9908230.

[138] G.P. Lepage and S.J. Brodsky, *Phys. Rev.* **D22** (1980) 2157.

[139] Y.V. Kovchegov, *Phys. Rev.* **D55** (1997) 5445, hep-ph/9701229.

[140] G. Leibbrandt, *Rev. Mod. Phys.* **59** (1987) 1067.

[141] P.V. Landshoff, J.C. Polkinghorne and R.D. Short, *Nucl. Phys.* **B28** (1971) 225.

[142] S.J. Brodsky, F.E. Close and J.F. Gunion, *Phys. Rev.* **D8** (1973) 3678.

[143] S.J. Brodsky, hep-ph/0109205.

[144] P. Hoyer, hep-ph/0209317.

[145] S.J. Brodsky, D.S. Hwang and I. Schmidt, *Phys. Lett.* **B530** (2002) 99, hep-ph/0201296.

[146] J.C. Collins, *Phys. Lett.* **B536** (2002) 43, hep-ph/0204004.

[147] A.V. Efremov, K. Goeke and P. Schweitzer, hep-ph/0303062.

[148] Y.V. Kovchegov, *Phys. Rev.* **D54** (1996) 5463, hep-ph/9605446.

[149] J. Jalilian-Marian, A. Kovner, L.D. McLerran and H. Weigert, *Phys. Rev.* **D55** (1997) 5414, hep-ph/9606337.

[150] A.H. Mueller, *Nucl. Phys.* **B335** (1990) 115.

[151] Y.V. Kovchegov, *Phys. Rev.* **D60** (1999) 034008, hep-ph/9901281.

[152] E. Levin and K. Tuchin, *Nucl. Phys.* **B573** (2000) 833, hep-ph/9908317;
Nucl. Phys. **A691** (2001) 779, hep-ph/0012167;
Nucl. Phys. **A693** (2001) 787, hep-ph/0101275.

[153] M. Braun, *Eur. Phys. J.* **C16** (2000) 337, hep-ph/0001268; hep-ph/0010041; hep-ph/0101070.

[154] A.H. Mueller and D.N. Triantafyllopoulos, *Nucl. Phys.* **B640** (2002) 331, hep-ph/0205167.

[155] K. Golec-Biernat and M. Wusthoff, *Phys. Rev.* **D60** (1999) 114023, hep-ph/9903358.

[156] A.H. Mueller, *Nucl. Phys.* **B572** (2000) 227, hep-ph/9906322.

[157] A.H. Mueller, hep-ph/0111244.

[158] I. Balitsky, hep-ph/9706411.

[159] I. Balitsky, *Phys. Rev.* **D60** (1999) 014020, hep-ph/9812311.

[160] Y.V. Kovchegov and K. Tuchin, *Phys. Rev.* **D65** (2002) 074026, hep-ph/0111362.

[161] E.A. Kuraev.L.N. Lipatov and V.S. Fadin, *JETP* **45** (1977) 199 [*Zh. Eksp. Teor. Fiz.* **72** (1977) 377].

[162] J. Jalilian-Marian, A. Kovner, A. Leonidov and H. Weigert, *Phys. Rev.* **D59** (1999) 034007, and references therein; Erratum **D59** (1999) 099903, hep-ph/9807462.

[163] A. Kovner, J.G. Milhano and H. Weigert, *Phys. Rev.* **D62** (2000) 114005, hep-ph/0004014.

[164] H. Weigert, *Nucl. Phys.* **A703** (2002) 823, hep-ph/0004044.

[165] E. Ferreiro, E. Iancu, A. Leonidov and L. McLerran, *Nucl. Phys.* **A703** (2002) 489, hep-ph/0109115.

[166] A.H. Mueller, *Nucl. Phys.* **B415** (1994) 373.

[167] A.H. Mueller, *Nucl. Phys.* **B437** (1995) 107, hep-ph/9408245.

[168] Z. Chen and A.H. Mueller, *Nucl. Phys.* **B451** (1995) 579.

[169] G. Baur *et al.*, CMS Note-2000/060, available at *http://cmsdoc.cern.ch/documents/00/* .

[170] R. Hamberg, W.L. van Neerven and T. Matsuura, *Nucl. Phys.* **B359** (1991) 343.

[171] R. Vogt, *Phys. Rev.* **C64** (2001) 044901, hep-ph/0011242.

[172] A.D. Martin, R.G. Roberts, W.J. Stirling and R.S. Thorne, *Eur. Phys. J.* **C4** (1998) 463, hep-ph/9803445.

[173] J. Czyzewski, K.J. Eskola, and J. Qiu, in Proc. *III International Workshop on Hard Probes of Dense Matter*, ECT*, Trento, June 1995.

[174] V. Emel'yanov, A. Khodinov, S.R. Klein and R. Vogt, *Phys. Rev.* **C61** (2000) 044904, hep-ph/9909427.

[175] T. Affolder *et al.* (CDF Collaboration), *Phys. Rev. Lett.* **84** (2000) 845, hep-ex/0001021.

[176] B. Abbott *et al.* (D0 Collaboration), *Phys. Lett.* **B513** (2001) 292, hep-ex/0010026.

[177] J.W. Qiu and X.F. Zhang, *Phys. Rev. Lett.* **86** (2001) 2724, hep-ph/0012058; *Phys. Rev.* **D63** (2001) 114011, hep-ph/0012348.

[178] J.C. Collins, D.E. Soper and G. Sterman, *Nucl. Phys.* **B250** (1985) 199.

[179] X.F. Zhang and G. Fai, *Phys. Rev.* **C65** (2002) 064901, hep-ph/0202029.

[180] Y. Zhang, G. Fai, G. Papp, G.G. Barnafoldi and P. Levai, *Phys. Rev.* **C65** (2002) 034903, hep-ph/0109233.

[181] T. Affolder *et al.* (CDF Collaboration), *Phys. Rev.* **D64** (2001) 032001, Erratum: **D65** (2002) 039903, hep-ph/0102074.

[182] C. Bromberg *et al.*, *Nucl. Phys.* **B171** (1980) 38.

[183] C. Stewart *et al.*, *Phys. Rev.* **D42** (1990) 1385.

[184] J.C. Collins, D.E. Soper and G. Sterman, *Nucl. Phys.* **B261** (1985) 104.

[185] J.C. Collins, D.E. Soper and G. Sterman, *Nucl. Phys.* **B308** (1988) 833.

[186] D.F. Geesaman, K. Saito and A.W. Thomas, *Annu. Rev. Nucl. Part. Sci.* **45** (1995) 337.

[187] R. Baier, D. Schiff and B.G. Zakharov, *Annu. Rev. Nucl. Part. Sci.* **50** (2000) 37, hep-ph/0002198, and references therein.

[188] M. Gyulassy, P. Levai and I. Vitev, *Phys. Lett.* **B538** (2002) 282, nucl-th/0112071.

[189] E. Wang and X.N. Wang, *Phys. Rev. Lett.* **89** (2002) 162301, hep-ph/0202105.

[190] C.A. Salgado and U.A. Wiedemann, *Phys. Rev. Lett.* **89** (2002) 092303, hep-ph/0204221.

[191] S. Frixione, Z. Kunszt and A. Signer, *Nucl. Phys.* **B467** (1996) 399, hep-ph/9512328.

[192] S. Frixione, *Nucl. Phys.* **B507** (1997) 295, hep-ph/9706545.

[193] S. Frixione and G. Ridolfi, *Nucl. Phys.* **B507** (1997) 315, hep-ph/9707345.

[194] S. Catani *et al.*, hep-ph/0005025.

[195] S. Catani, Y.L. Dokshitzer, M.H. Seymour and B.R. Webber, *Nucl. Phys.* **B406** (1993) 187.

[196] S.D. Ellis and D.E. Soper, *Phys. Rev.* **D48** (1993) 3160, hep-ph/9305266.

[197] S.D. Ellis, DOE-ER-40423-27, presented at *1990 DPF Summer Inst. Study on High-Energy Physics Research: Directions for the Decade*, Snowmass, CO, Jun 25 – Jul 13, 1990.

[198] G. Sterman and S. Weinberg, *Phys. Rev. Lett.* **39** (1977) 1436.

[199] S. Bethke *et al.* (JADE Collaboration), *Phys. Lett.* **B213** (1988) 235.

[200] J. Huston (CDF Collaboration), *Int. J. Mod. Phys.* **A16S1A** (2001) 219.

[201] R. Field (CDF Collaboration), *Int. J. Mod. Phys.* **A16S1A** (2001) 250.

[202] N. Armesto and C. Pajares, *Int. J. Mod. Phys.* **A15** (2000) 2019, hep-ph/0002163.

[203] ALICE Physics Performance Report, Chapter IV: *'Monte Carlo generators and simulations'*, Eds. F. Carminati, Y. Foka, P. Giubellino, G. Paic, J.-P. Revol, K. Šafařik and U. A. Wiedemann, ALICE Internal Note 2002-033 (2002).

[204] A. Accardi and D. Treleani, *Nucl. Phys.* **A699** (2002) 82.

[205] A. Accardi and D. Treleani, *Phys. Rev.* **D64** (2001) 116004, hep-ph/0106306.

[206] L. Ametller, N. Paver and D. Treleani, *Phys. Lett.* **B169** (1986) 289.

[207] F. Abe *et al.* (CDF Collaboration), *Phys. Rev.* **D56** (1997) 3811.

[208] F. Abe *et al.* (CDF Collaboration), *Phys. Rev. Lett.* **79** (1997) 584.

[209] A. Capella *et al.*, *Phys. Lett.* **B107** (1981) 106, Erratum: **B109** (1982) 510.

[210] M. Braun and C. Pajares, *Nucl. Phys.* **A532** (1991) 678.

[211] T. Matsui and H. Satz, *Phys. Lett.* **B178** (1986) 416.

[212] M.C. Abreu *et al.* (NA50 Collaboration), *Phys. Lett.* **B410** (1997) 337.

[213] J.F. Gunion and R. Vogt, *Nucl. Phys.* **B492** (1997) 301, hep-ph/9610420.

[214] R. Vogt, *Phys. Rep* . **310** (1999) 197.

[215] V.D. Barger, W.Y. Keung and R.J. Phillips, *Phys. Lett.* **B91** (1980) 253.

[216] V.D. Barger, W.Y. Keung and R.J. Phillips, *Z. Phys.* **C6** (1980) 169.

[217] R. Gavai, *Int. J. Mod. Phys.* **A10** (1995) 3043, hep-ph/9502270.

[218] G.T. Bodwin, E. Braaten and G.P. Lepage, *Phys. Rev.* **D51** (1995) 1125, Erratum: **D55** (1997) 5853, hep-ph/9407339.

[219] M.L. Mangano, P. Nason and G. Ridolfi, *Nucl. Phys.* **B373** (1992) 295.

[220] G.A. Schuler and R. Vogt, *Phys. Lett.* **B387** (1996) 181, hep-ph/9606410.

[221] S. Digal, P. Petreczky and H. Satz, *Phys. Rev.* **D64** (2001) 094015, hep-ph/0106017.

[222] F. Abe *et al.* (CDF Collaboration), *Phys. Rev. Lett.* **79** (1997) 572.

[223] F. Abe *et al.* (CDF Collaboration), *Phys. Rev. Lett.* **79** (1997) 578.

[224] M. Kramer, *Prog. Part. Nucl. Phys.* **47** (2001) 141, hep-ph/0106120.

[225] P.L. Cho and A.K. Leibovich, *Phys. Rev.* **D53** (1996) 6203, hep-ph/9511315.

[226] M. Beneke and M. Kramer, *Phys. Rev.* **D55** (1997) 5269, hep-ph/9611218.

[227] B.A. Kniehl and G. Kramer, *Eur. Phys. J.* **C6** (1999) 493, hep-ph/9803256.

[228] E. Braaten, B.A. Kniehl and J. Lee, *Phys. Rev.* **D62** (2000) 094005, hep-ph/9911436.

[229] T. Affolder *et al.* (CDF Collaboration), *Phys. Rev. Lett.* **85** (2000) 2886, hep-ex/0004027.

[230] F. Abe *et al.* (CDF Collaboration), *Phys. Rev. Lett.* **75** (1995) 4358.

[231] A. Baldit *et al.* (NA60 Collaboration), Proposal SPSC/P316, March 2000; *http://na60.web.cern.ch/NA60* .

[232] D. Brandt, private communication.

[233] X.F. Zhang and G. Fai, *Phys. Lett.* **B545** (2002) 91, hep-ph/0205155.

[234] G. Fai, J.W. Qiu, and X.F. Zhang, in preparation.

[235] F. Landry, R. Brock, G. Ladinsky and C.P. Yuan, *Phys. Rev.* **D63** (2001) 013004, hep-ph/9905391, and references therein.

[236] E.L. Berger, J.W. Qiu and X.F. Zhang, *Phys. Rev.* **D65** (2002) 034006, hep-ph/0107309.

[237] E.L. Berger and J.W. Qiu, hep-ph/0210135.

[238] C.T. Davies, B.R. Webber and W.J. Stirling, *Nucl. Phys.* **B256** (1985) 413.

[239] G.A. Ladinsky and C.P. Yuan, *Phys. Rev.* **D50** (1994) 4239, hep-ph/9311341.

[240] F. Landry, R. Brock, P.M. Nadolsky and C.P. Yuan, hep-ph/0212159.

[241] W. Giele *et al.*, hep-ph/0204316.

[242] E.L. Berger, L.E. Gordon and M. Klasen, *Phys. Rev.* **D58** (1998) 074012, hep-ph/9803387.

[243] E.L. Berger and J.W. Qiu, *Phys. Lett.* **B248** (1990) 371; *Phys. Rev.* **D44** (1991) 2002.

[244] E.L. Berger, X.F. Guo and J.W. Qiu, *Phys. Rev. Lett.* **76** (1996) 2234; *Phys. Rev.* **D54** (1996) 5470.

[245] C. Albajar *et al.* (UA1 Collaboration), *Phys. Lett.* **B209** (1988) 397.

[246] J.W. Qiu and X.F. Zhang, *Phys. Rev.* **D64** (2001) 074007, hep-ph/0101004.

[247] J.C. Collins and D.E. Soper, *Phys. Rev.* **D16** (1977) 2219.

[248] C.S. Lam and W.K. Tung, *Phys. Rev.* **D18** (1978) 2447.

[249] E. Mirkes, *Nucl. Phys.* **B387** (1992) 3.

[250] R.J. Fries, A. Schafer, E. Stein and B. Muller, *Nucl. Phys.* **B582** (2000) 537, hep-ph/0002074.

[251] C.S. Lam and W.K. Tung, *Phys. Rev.* **D21** (1980) 2712.

[252] S. Gavin *et al.*, *Int. J. Mod. Phys.* **A10** (1995) 2961, hep-ph/9502372.

[253] M. Luo, J. Qiu and G. Sterman, *Phys. Lett.* **B279** (1992) 377.

[254] M. Luo, J.W. Qiu and G. Sterman, *Phys. Rev.* **D50** (1994) 1951.

[255] R.J. Fries, B. Muller, A. Schafer and E. Stein, *Phys. Rev. Lett.* **83** (1999) 4261, hep-ph/9907567.

[256] J.S. Conway *et al.*, *Phys. Rev.* **D39** (1989) 92.

[257] Y.L. Dokshitzer and D.E. Kharzeev, *Phys. Lett.* **B519** (2001) 199, hep-ph/0106202.

[258] Z.W. Lin and R. Vogt, *Nucl. Phys.* **B544** (1999) 339, hep-ph/9808214.

[259] N. Kidonakis, E. Laenen, S. Moch and R. Vogt, *Phys. Rev.* **D64** (2001) 114001, hep-ph/0105041.

[260] T. Affolder *et al.* (CDF Collaboration), *Phys. Rev. Lett.* **84** (2000) 232.

[261] A.V. Lipatov, V.A. Saleev and N.P. Zotov, hep-ph/0112114.

[262] I. Abt *et al.* (HERA-B Collaboration), hep-ex/0205106.

[263] J. Smith and R. Vogt, *Z. Phys.* **C75** (1997) 271, hep-ph/9609388.

[264] N. Kidonakis, E. Laenen, S. Moch and R. Vogt, *Phys. Rev.* **D67** (2003) 074037, hep-ph/0212173.

[265] R. Vogt, *Heavy Ion Phys.* **17** (2003) 75, hep-ph/0207359.

[266] K. Adcox *et al.* (PHENIX Collaboration), *Phys. Rev. Lett.* **88** (2002) 192303, nucl-ex/0202002.

[267] J.W. Cronin, *Phys. Rev.* **D11** (1975) 3105.

[268] X.N. Wang, *Phys. Rev.* **C61** (2000) 064910.

[269] B.Z. Kopeliovich, J. Nemchik, A. Schaefer and A.V. Tarasov, *Phys. Rev. Lett.* **88** (2002) 232303, hep-ph/0201010.

[270] I. Vitev and M. Gyulassy, *Phys. Rev. Lett.* **89** (2002) 252301, hep-ph/0209161;
I. Vitev, private communication.

[271] K. Adcox *et al.* (PHENIX Collaboration), *Phys. Rev. Lett.* **88** (2002) 022301, nucl-ex/0109003.

[272] K. Reygers (WA98 collaboration), nucl-ex/0202018.

[273] P. Levai *et al.*, *Nucl. Phys.* **A698** (2002) 631, nucl-th/0104035.

[274] I. Vitev, M. Gyulassy and P. Levai, nucl-th/0204019.

[275] PHENIX, PHOBOS and STAR Collaborations, results presented at *'RHIC & AGS Annual Users' Meeting'*, May 15–16 2003, Brookhaven National Laboratories, Upton, NY; and 'CIPANP 2003' May 19–24 2003, New York City.

[276] I. Vitev, talk at the *'RHIC & AGS Annual Users' Meeting'*, May 15–16 2003, Brookhaven National Laboratories, Upton, NY,
http://nt3.phys.columbia.edu/Vis03/Seminars/Vitev-AGS-RHIC-2003.htm .

[277] J. Kuhn, *Phys. Rev.* **D13** (1976) 2948;
A. Krzywicki, J. Engels, B. Petersson and U. Sukhatme, *Phys. Lett.* **B85** (1979) 407.

[278] M. Lev and B. Petersson, *Z. Phys.* **C21** (1983) 155.

[279] R.D. Field, *Applications of Perturbative QCD*, Frontiers in Physics, **77** (Addison-Wesley, Redwood City, 1989).

[280] J.F. Owens, *Rev. Mod. Phys.* **59** (1987) 465.

[281] X.N. Wang and M. Gyulassy, *Phys. Rev.* **D44** (1991) 3501; *Comput. Phys. Commun.* **83** (1994) 307, nucl-th/9502021.

[282] M.B. Johnson *et al.*, *Phys. Rev. Lett.* **86** (2001) 4483, hep-ex/0010051.

[283] M.B. Johnson *et al.*, *Phys. Rev.* **C65** (2002) 025203, hep-ph/0105195.

[284] K. Kastella, *Phys. Rev.* **D36** (1987) 2734.

[285] X.N. Wang, *Phys. Rept.* **280** (1997) 287, hep-ph/9605214.

[286] E. Wang and X.N. Wang, *Phys. Rev.* **C64** (2001) 034901, nucl-th/0104031.

[287] R.J. Fries, hep-ph/0201311.

[288] M.A. Braun, E.G. Ferreiro, C. Pajares, D. Treleani, hep-ph/0207303.

[289] K. Eskola, K. Kajantie, P.V. Ruuskanen, K. Tuominen, *Nucl. Phys.* **B570** (2000) 379, hep-ph/9909456.

[290] E. Iancu, A. Leonidov and L. McLerran, hep-ph/0202270; Contribution of nonlinear terms in DGLAP evolution in Chapter 1, Section 4.2, in *'Hard Probes in Heavy-Ion Collisions at the LHC'*, CERN-2004-009 (2004).

[291] For a summary of recent results on non-Abelian energy loss, see R. Baier, P. Levai, I. Vitev, U. Wiedemann, D. Schiff and B.G. Zakharov, 'Chapter 2 in 'Hard Probes in Heavy-Ion Collisions at the LHC', CERN–2004–009 (2004)' and references therein.

[292] I. Vitev, hep-ph/0212109.

[293] D. Antreasyan *et al.*, *Phys. Rev.* **D19** (1979) 764;
D.E. Jaffe *et al.*, *Phys. Rev.* **D40** (1989) 2777;
P.B. Straub *et al.*, *Phys. Rev. Lett.* **68** (1992) 452.

[294] P. Levai, private communication.

[295] K.J. Eskola and H. Honkanen, *Nucl. Phys.* **A713** (2003) 167, hep-ph/0205048.

[296] D. Kharzeev and M. Nardi, *Phys. Lett.* **B507** (2001) 121, nucl-th/0012025.

[297] A. Accardi, *Phys. Rev.* **C64** (2001) 064905, hep-ph/0107301.

[298] X.F. Zhang, G. Fai and P. Levai, *Phys. Rev. Lett.* **89** (2002) 272301, hep-ph/0205008.

[299] X.N. Wang, private communication.

[300] B. Kopeliovich, private communication.

[301] M. Beneke and I.Z. Rothstein, *Phys. Rev.* **D54** (1996) 2005, Erratum: **D54** (1996) 7082, hep-ph/9603400.

[302] H.L. Lai *et al.*, *Phys. Rev.* **D51** (1995) 4763, hep-ph/9410404.

[303] P. Hoyer and S. Peigne, *Phys. Rev.* **D59**, 034011 (1999), hep-ph/9806424.

[304] N. Marchal, S. Peigne and P. Hoyer, *Phys. Rev.* **D62**, 114001 (2000), hep-ph/0004234.

[305] P. Hoyer, N. Marchal and S. Peigne, hep-ph/0209365.

[306] R. Vogt, *Nucl. Phys.* **A700** (2002) 539, hep-ph/0107045.

[307] P. Hoyer, N. Marchal and S. Peigne, in preparation.

[308] HERA-B Report on Status and Prospects, DESY-PRC 00/04; M. Bruinsma, *'Prospects for J/ψ Suppression Measurements at HERA-B'*, poster presented at *Quark Matter*'01, the 15th International Conference on Ultra-Relativistic Nucleus–Nucleus Collisions, Jan. 2001.

[309] M.C. Abreu *et al.*, *Phys. Lett.* **B466** (1999) 408.

[310] J. Badier *et al.* (NA3 Collaboration), *Z. Phys.* **C20** (1983) 101.

[311] P. Bordalo *et al.* (NA10 Collaboration), *Phys. Lett.* **B193** (1987) 373.

[312] D.M. Alde *et al.*, *Phys. Rev. Lett.* **66** (1991) 2285.

[313] S. Gavin and M. Gyulassy, *Phys. Lett.* **B214** (1988) 241.

[314] J.P. Blaizot and J.Y. Ollitrault, *Phys. Lett.* **B217**, 392 (1989).

[315] J. Hufner, Y. Kurihara and H.J. Pirner, *Phys. Lett.* **B215** (1988) 218 [*Acta Phys. Slov.* **39** (1989) 281].

[316] P. Hoyer and S. Peigne, *Phys. Rev.* **D57**, 1864 (1998), hep-ph/9706486.

[317] S. Frixione, M.L. Mangano, P. Nason and G. Ridolfi, *Nucl. Phys.* **B431** (1994) 453.

[318] S. Frixione, M.L. Mangano, P. Nason and G. Ridolfi, *Adv. Ser. Direct. High Energy Phys.* **15** (1998) 609, hep-ph/9702287.

[319] R. Vogt (Hard Probe Collaboration), hep-ph/0111271.

[320] X.N. Wang, *Phys. Rev. Lett.* **81** (1998) 2655, hep-ph/9804384.

[321] P. Chiappetta and H.J. Pirner, *Nucl. Phys.* **B291** (1987) 765.

[322] S. Gavin and R. Vogt, hep-ph/9610432.

[323] P.L. McGaughey *et al.*, *Int. J. Mod. Phys.* **A10** (1995) 2999, hep-ph/9411438.

[324] E. Lippmaa *et al.* (FELIX Collaboration), *'FELIX: A full acceptance detector at the LHC'*, CERN-LHCC-97-45; A.N. Ageev *et al.*, *J. Phys.* **G28** (2002) R117.

[325] L. Frankfurt, G.A. Miller and M. Strikman, *Phys. Rev. Lett.* **71** (1993) 2859, hep-ph/9309285.

[326] L. Frankfurt, V. Guzey and M. Strikman, *J. Phys.* **G27** (2001) R23, hep-ph/0010248;
L. Frankfurt, V. Guzey, M. McDermott and M. Strikman, hep-ph/0104252.

[327] L. Frankfurt, W. Koepf, M. Strikman, *Phys. Rev.* **D54** (1996) 3194;
L.L. Frankfurt, M.F. McDermott and M. Strikman, *JHEP* **02** (1999) 002, hep-ph/9812316.

[328] R.P. Feynman, *'Photon–Hadron Interactions'*, Reading, MA, Benjamin, 1972.

[329] L. Alvero, J.C. Collins, M. Strikman and J.J. Whitmore, *Phys. Rev.* **D57** (1998) 4063, hep-ph/9710490.

[330] L. Frankfurt, V. Guzey, M. McDermott and M. Strikman, *Phys. Rev. Lett.* **87** (2001) 192301, hep-ph/0104154.

[331] V.N. Gribov, *JETP* **30** (1970) 709 [*Zh. Eksp. Teor. Fiz.* **57** (1969) 1306].

[332] H. Abramowicz, L. Frankfurt, M. Strikman, published in SLAC Summer Inst.1994:539-574.

[333] H. Abramowicz and A. Caldwell, *Rev. Mod. Phys.* **71** (1999) 1275, hep-ex/9903037.

[334] F. Gelis and J. Jalilian-Marian, *Phys. Rev.* **D66** (2002) 094014, hep-ph/0208141.

[335] C. Goebel, F. Halzen and D.M. Scott, *Phys. Rev.* **D22** (1980) 2789;
N. Paver and D. Treleani, *Nuovo Cim.* **A70** (1982) 215;
B. Humpert, *Phys. Lett.* **B131** (1983) 461;
B. Humpert and R. Odorico, *Phys. Lett.* **B154** (1985) 211;
T. Sjostrand and M. van Zijl, *Phys. Rev.* **D36** (1987) 2019.

[336] T. Akesson *et al.* (Axial Field Spectrometer Collaboration), *Z. Phys.* **C34** (1987) 163;
J. Alitti *et al.* (UA2 Collaboration), *Phys. Lett.* **B268** (1991) 145;
F. Abe *et al.* (CDF Collaboration), *Phys. Rev.* **D47** (1993) 4857.

[337] M. Strikman and D. Treleani, *Phys. Rev. Lett.* **88** (2002) 031801, hep-ph/0111468.

[338] L.L. Frankfurt and M.I. Strikman, *Nucl. Phys.* **B250** (1985) 143.

[339] A. Berera *et al.*, *Phys. Lett.* **403** (1997) 1.

[340] Yu. Dokshitzer, L. Frankfurt and M. Strikman, in preparation.

[341] A. Dumitru, L. Gerland and M. Strikman, *Phys. Rev. Lett.* **90** (2003) 092301, hep-ph/0211324.

[342] L. Frankfurt and M. Strikman, *Phys. Rep.* **76** (1981) 215.

[343] E.M. Aitala *et al.* (E791 Collaboration), *Phys. Rev. Lett.* **86** (2001) 4773, *Phys. Rev. Lett.***86** (2001) 4768.

[344] L. Frankfurt, G.A. Miller and M. Strikman, *Phys. Lett.* **B304** (1993) 1, hep-ph/9305228.

[345] L. Frankfurt, G.A. Miller and M. Strikman, *Phys. Rev.* **D65** (2002) 094015, hep-ph/0010297.

[346] S.J. Brodsky, L. Frankfurt, J.F. Gunion, A.H. Mueller and M. Strikman, *Phys. Rev.* **D50** (1994) 3134, hep-ph/9402283.

[347] L. Frankfurt and M. Strikman, hep-ph/9806536.

[348] L. Frankfurt and M. Strikman, *Phys. Rev.* **D66** (2002) 031502, hep-ph/0205223.

[349] L.L. Frankfurt, G.A. Miller and M. Strikman, *Ann. Rev. Nucl. Part. Sci.* **44** (1994) 501, hep-ph/9407274.

[350] L. Frankfurt and M. Strikman, *Phys. Rev.* **D67** (2003) 017502, hep-ph/0208252.